ABSTRACT

PENG, QING. Nanoscale Engineering Materials with Supercritical Fluid and Atomic Layer Deposition. (Under the direction of Gregory N. Parsons.)

With the development of material science and technology, modification of substrates, which have random geometry and high aspect ratio three dimensional (3D) complex structures, with desired functional, reactive and stable coatings becomes important and challenging. The ability to fabricate mono- or multi-layers of functional materials with precisely controlled dimensions, finely tuned composition and molecular structures, attracts significant interests in materials science and is the key to construct such devices and structures at nano- and micro- scale with desired properties. In this study, supercritical carbon dioxide ($scCO_2$) has been studied as an alternative route for modifying substrates due to the unique gas-like (low viscosity, high diffusivity and zero surface tension) and liquid-like properties (high density). 1) The reaction kinetics of metal oxides thin film deposition from pyrolysis of metal organics in $scCO_2$ was studied in detail. This method was demonstrated as a powerful technique to coat oxides, including Al_2O_3, Ga_2O_3 and others, into 3D high aspect ratio complex structure of carbon nanotubes (CNTs) forest. 2) The low temperature $scCO_2$ based hydrogenolysis process was developed as a useful way to functionalize aligned CNTs forest with dense Nickel nanoparticles. On the second part of this work, atomic layer deposition (ALD) /molecular layer deposition (MLD), as a vapor phase, stepwise and self-limiting vacuum based deposition process, was demonstrated as a powerful way to form highly conformal and uniform film onto substrates, even into highly complex 3D complex structures. In this study, 4) Metal oxide ALD is applied onto 3D electrospun polymer microfiber mats template to illustrate an effective and robust strategy to fabricate long and uniform metal

oxide microtubes with precisely controllable wall thickness. Designer tubes of various sizes and different materials were demonstrated by using this method. 5) By further extending this technique, complex coaxial Al_2O_3/ZnO/Al_2O_3 multilayed microtubular structure is fabricated, which provides an unique platform to study the solid state reaction and diffusion process (Kirkendall Effect) between Al_2O_3 shells and the confined middle ZnO layers by annealing the samples at 700 ˚C. 6) The extension of ALD-MLD process of polyamides, zinc hybrid, aminosilane self assembly monolayers were studied by various techniques to illustrate the surface reaction mechanism.

Nanoscale Engineering Materials by Supercritical Fluid and Atomic Layer Deposition

by
Qing Peng

A dissertation submitted to the Graduate Faculty of
North Carolina State University
In partial fulfillment of the
Requirements for the Degree of
Doctor of Philosophy

Chemical Engineering

Raleigh, North Carolina

2009

APPROVED BY:

_____	_____
Dr. Ruben G. Carbonell	Dr. Saad A. Khan
_____	_____
Dr. Jan Genzer	Dr. Gregory N. Parsons Chair of Advisory committee

DEDICATION

This dissertation is dedicated to my wife, Haiyan Liu,

my daughter, Emily Y. Peng,

my parents, Huanxin Peng and Jinyuan He,

and my sister Li Peng for all their love.

BIOGRAPHY

Qing Peng was born in Xining City, Qinghai Province, P. R. China on 1978. He received his B.S. and M.S. degrees in 2001 and 2004 from East China University of Science and Technology (ECUST). On the way to his Ph.D. in the Department of Chemical and Biomolecular Engineering at North Carolina State University, he received his second Master's degree in Chemical Engineering in May 2006. He will join Argonne National Laboratory as a Postdoc after graduation.

ACKNOWLEDGEMENTS

I would like to acknowledge my advisor Dr. Gregory N. Parsons, for his strong support throughout the whole research process, for the freedom he provided me to explore the unknown scientific world, for his tireless discussion about the detail problems.

I would also like to acknowledge that the past and present members in Dr. Parsons' group, Dr. Kie Jin Park, Jeong-Seok Na, Joseph C. Spagnola, Dr. G. Kevin Hyde, Bo Gong, Dr. Scarel Giovanna, Dr. Daisuke Hojo, Dr. David Terry, Dr. Changwoong Chu, Dr. Gougousi Theodosia, Dr. Dipak Barua, Dr. Jason Kelly, Dr. Kim Roberts for their thoughtful discussions and collaborations.

I would like to acknowledge the collaborators from the Chemical and Biomolecular Engineering Department, Dr. Saad A. Khan, Dr. Richard M. Spontak, Dr. Carl D. Saquing, Dr. Xiao-Yu Sun.

I am grateful to Ali Evren Ozcam, Shafi Mahmud Arifuzzaman and Dr. Jan Genzer, Dr. Kirill Efimenko for spectroscopic ellipsometry measurements, Jeong-Seok Na for AFM measurements, Seymen Aygun, Michelle D. Casper and Dr. J. P. Maria for XRD measurement, and Dr. Jan Genzer and Dr. Christopher Gorman for helpful discussions.

I acknowledge my committee members, Dr. Ruben G. Carbonell, Dr. Jan Genzer, Dr. Saad A. Khan, Dr. Michael Dickey for their support and excellent mentoring. Special thanks to Kit Yeung for being a good friend and helping me maintain my reaction system.

TABLE OF CONTENTS

LIST OF TABLES ..... **ix**

LIST OF FIGURES ..... **x**

CHAPTER 1. Introduction **1**

1.1 Liquid solvent based routes 1

1.2 Supercritical Carbon Dioxides based Process 4

1.3. Atomic layer deposition and molecular layer deposition 8

REFERENCES 18

CHAPTER 2. Experimental Tools **40**

2.1 Supercritical carbon dioxide based process 40

2.2 Atomic layer deposition/Molecular layer deposition 43

2.3 Characterization Methods 47

REFERENCES 50

CHAPTER 3. Overview of Key Results of Dissertation and Author's Contributions **54**

3.1 Low-temperature metal oxide thin film deposition and reaction kinetics in supercritical carbon dioxide 54

3.2 Conformal metal oxide coatings on nanotubes by direct low-temperature metal-organic pyrolysis in supercritical carbon dioxide 56

3.3 Self-catalyzed hydrogenolysis of Nickelocene: functional metal coating of three-dimensional nanosystems at low temperature 57

3.4 Atomic layer deposition on electrospun polymer fibers as a direct route to Al_2O_3 microtubes with precise wall thickness control 57

3.5 Bi-directional Kirkendall effect in coaxial microtube nanolaminate assemblies fabricated by atomic layer deposition 58

3.6 Metal organic hybrid polymer thin films formed by molecular layer deposition 59

3.7 Polyamide thin film and amino silane self-assembled monolayer formed by molecular layer deposition 61

CHAPTER 4. Summary and Outlook **85**

4.1 Summary and Outlook for Supercritical Carbon Dioxide Based Process 85
4.2 Summary and Outlook for Atomic Layer Deposition 86
4.3 Summary and Outlook for Molecular Layer Deposition 87
REFERENCES 90
CHAPTER 5. Low-Temperature Metal Oxide Film Deposition and Reaction Kinetics in Supercritical Carbon Dioxide 94
5.1 Introduction 95
5.2 Experiment 97
5.3 Results 100
5.4 Discussion 105
5.5 Summary and Conclusions 109
5.6 Acknowledgment 110
REFERENCES 113
CHAPTER 6. Conformal Metal Oxide Coatings on Nanotubes by Direct Low-Temperature Metal-Organic Pyrolysis in Supercritical Carbon Dioxide 122
6.1 Introduction 123
6.2 Experiment 124
6.3 Results and discussion 126
6.4 Conclusion 130
6.5 Acknowledgement 130
REFERENCES 132
CHAPTER 7. Self-Catalyzed Hydrogenolysis of Nickelocene: Functional Metal Coating of Three-Dimensional Nanosystems at Low Temperature 140
7.1 Introduction 141
7.2 Experiment 142
7.3 Results and Discussion 144
7.4 Conclusions 147
7.5 Acknowledgments 147
REFERENCES 148

CHAPTER 8. Atomic Layer Deposition on Electrospun Polymer Fibers as a Direct Route to Al_2O_3 Microtubes with Precise Wall Thickness Control 155

8.1 Introduction 156

8.2. Experiment 158

8.3 Experiment results and discussion 159

8.4 Conclusion 162

8.5 Acknowledgments 162

REFERENCES 164

CHAPTER 9. Bi-Directional Kirkendall Effect in Coaxial Microtube Nanolaminate Assemblies Fabricated by Atomic Layer Deposition 172

9.1 Introduction 173

9.2 Experiment methods 174

9.3 Results and discussions 176

9.4 Conclusion 187

9.5 Acknowledgments 188

REFERENCES 189

Chapter 10. "Zincone" Zinc Oxide–Organic Hybrid Polymer Thin Films formed by Molecular Layer Deposition 203

10.1 Introduction 205

10.2 Experimental 207

10.3 Experimental Results 211

10.4 Discussion 223

10.5 Conclusions 226

10.6 Acknowledgments 227

REFERENCES 228

Chapter 11. Surface Functionalization with Aminosilane by Atomic Layer Deposition 247

11.1 Introduction 249

11.2 Experiments 250

11.3 Experiment results 253

11.4 Discussion 260
11.5 Conclusions 264
11.6 Acknowledgement 265
REFERENCES 266

LIST OF TABLES

Table 3.1 Experiment results of $scCO_2$-based deposition from pyrolytic reaction of different metal organics 65

Table 5.1 Experiment results of $scCO_2$-based deposition from pyrolytic reaction of different metal organics 120

Table 9.1 Characteristic dimensions of initial ALD layers and post-reaction spinel layers and Kirkendall gaps. 193

Table 10.1 Summary of mass uptake results obtained from QCM analysis during various ALD and MLD half–cycles on starting surfaces of interest. 246

Table 11.1 Infrared spectral assignment of APTES functionalized Al_2O_3 ALD film and the surface generated after TMA and H_2O half cycles in Al_2O_3 ALD process. 273

LIST OF FIGURES

Figure 1.1 The scheme of the Langmuir- Blodgett (LB) thin film fabrication process, A) amphiphilc molecules at the air/water interface. B) Substrate pulled out, hydrophilic group absorbed onto substrate. C) Substrate pushed into water, hydrophobic group attached onto hydrophobic surface, D) several layer LB films 35

Figure 1.2 The scheme of the layer by layer thin film deposition, A) process of LBL film fabrication, 1) solution of positive polyelectrolyte, 2) pure deionized water, 3) solution of negative polyelectrolyte, 4) pure deionized water. B) the structure of LBL films. 36

Figure 1.3 Schematic diagram of vapor-phase, self-limiting atomic layer deposition (ALD) illustrating the cyclic process by which an Al_2O_3 surface coating is controllably constructed layer-by-layer from TMA and H_2O precursors..... 37

Figure 1.4 A representative SEM image of the electropun polyvinyl alcohol fiber matrix. 38

Figure 1.5 Schematic diagram of vapor-phase, self-limiting molecular layer deposition (MLD) illustrating the cyclic process from two bifunctional reactants, which could be extended into other types of multiple functionalities molecules. 39

Figure 2.1 Schematic diagram of the experimental apparatus. The inner volume of the reactor is ~ 110 mL. The reactor wall temperature is typically held at 100 ^oC. The sample is located on a block that is heated independently from the reactor chamber wall. 51

Figure 2.2 The diagram of reaction system. H_2 is mixed with $scCO_2$ in the manifold to form uniform solution. The temperature of the reactor and manifold are controlled by feedback thermal couples individually. The reaction system can be observed through the sapphire windows. 52

Figure 2.3 A schematic view of the viscous flow ALD/MLD reactor. The precursors are delivered into the reactor with Ar carrier gas. On the reactor exhaust line, computer controlled gate values are used to direct the exhaust from the EG pulse into a liquid nitrogen trap before entering the pump. 53

Figure 3.1 Apparent reaction kinetics of $scCO_2$-based deposition of Al_2O_3 films from pyrolytic reaction of $Al(acac)_3$ with initial concentration of 170 μmol/L. The slopes of the lines indicate that the overall energy barrier for Al_2O_3 deposition is 68±6 kJ/mol. And the apparent kinetics of $scCO_2$-based Ga_2O_3 deposition from pyrolysis of $Ga(acac)_3$ at initial concentration of 230 μmol/L. The kinetic barrier of Ga_2O_3 deposition is 84±7 kJ/mol. The solid lines represent linear regressions of the data points. 63

Scheme 3.1 A simplified reaction mechanism for pyrolysis reaction of $Al(acac)_3$. The * denotes the postulated polar transition state. 64

Figure 3.2 (a) TEM image of a single pristine MWCNT. (b) TEM image of MWCNTs coated by gallium oxide from thermal decomposition of $Ga(acac)_3$ at 160 °C and 23 MPa-24 MPa for 7 min. The arrow inside (b) shows the part of MWCNTs having no oxide coating. (c) TEM image of MWCNTs coated by gallium oxide from thermal decomposition of $Ga(acac)_3$ at 200 °C and 28 MPa for 1.5 min. (d) Higher magnification TEM image of MWCNTs coated by gallium oxide from thermal decomposition of $Ga(acac)_3$ at 200 °C and 28 MPa for 1.5 min. (e) A typical EDS spectrum of oxide coated MWCNTs. The gallium oxide deposition experiment was carried out at 200 °C, 28-32 MPa for 1.5 min. The Ga and majority O peaks result from the gallium oxide coating, and the major carbon signal is ascribed to the MWCNTs with some contribution from carbon impurities and adventitious carbon. The tiny Cu peak is from the TEM grid. 66

Figure 3.3 (a) FESEM image of untreated pristine MWCNTs. The diameters of the MWCNTs are in the range of 10-30 nm. (b) FESEM image of MWCNTs coated by gallium oxide from pyrolysis of $Ga(acac)_3$ at 200 °C, 28-30 MPa for 10mins. The diameters of the MWCNTs are in the range of 60-100 nm The arrow in (b) indicates that the coating of gallium oxide can replicate the small helix feature of MWCNTs. (c) FESEM image of gallium oxide coated MWCNTs with relatively uniform Ru coating on the surface by atomic layer deposition from reaction between $Ru(Cp)_2$ and O_2 at 325 °C for 150 cycles. (d) A typical EDS spectrum of oxide-coated MWCNTs with Ru ALD coating. The significant Ru peak is shown. The peak of Ga and O come from the gallium oxide under the Ru, and the tiny C peak probably comes from the carbon nanotube core, adventitious carbon from air and the as-deposited films 67

Figure 3.4 (a) FESEM image of pristine MWCNTs. (b) FESEM image of the Ni nanoparticles decorated MWCNTs, which was treated in the $scCO_2$ based direct hydrogenolysis reaction between $Ni(Cp)_2$ and H_2 at 70 °C. (c) A higher resolution SEM image of the Ni nanoparticles anchored MWCNTs. (d) A typical TEM image of Ni nanoparticles decorated MWCNTs. 68

Scheme 3.2 The reaction scheme of hydrogenolysis of Nicklocene without catalyst. Step (1) is a slower reaction step in order to form Ni nuclei from homogenous hydrogenolysisi of Nicklocene. Once Ni particles are generated, they will catalyze the heterogeneous hydrogenolysis reaction of Nicklocene on Ni particles with a much faster reaction rate..... 69

Figure 3.5 Wall thickness of Al_2O_3 microtubes prepared on electrospun PVA fibers (○) and measured by TEM as a function of ALD cycle number. Included for comparison is the Al_2O_3 film thickness on a planar Si substrate (●) measured by ellipsometry. The solid lines denote linear regressions of the data points. The corresponding average growth rates of Al_2O_3 are

about 0.08 nm/cycle on the electrospun fibers and 0.07 nm/cycle on the Si substrate. Error bars (±1 standard deviation) deduced from analysis of 25 thickness measurements from each specimen are smaller than the symbols shown. 70

Figure 3.6 (a) FESEM image of an Al_2O_3 microtube in which ALD was performed on electrospun PVA fibers for 300 cycles at 45˚C. The arrow indicates a circle on the inside wall of the resultant microtube. (b) TEM image of the corresponding Al_2O_3 microtube illustrating the wall thickness. (c) FESEM and (d) TEM images of Al_2O_3 microtubes fabricated by ALD for 150 cycles at 45 ˚C. A wall thickness measurement is included in (d). In all cases, the electrospun PVA fiber templates were removed by heating in air at 400 ˚C for 24 h..... 71

Figure 3.7 (a) FESEM image of polyethylene oxide (PEO) electrospun fiber matrix. (b) FESEM images of polyethylene oxide (PEO) electrospun fiber after Al_2O_3 coating for 150 cycles at 35 ˚C. The top layers of PEO fibers are fused together to form films (solid arrow) and ALD of Al_2O_3 are deposited onto the fused fiber mat as indicated by the (dash arrow). 72

Figure 3.8 Schematic diagram of the procedure developed here for the fabrication of coaxial $ZnAl_2O_4$ microtube-in-microtube coaxial assemblies: (a) electrospinning is used to produce PVA microfibers; (b) a thin, conformal Al_2O_3 coating is applied to the PVA fibers by low-temperature ALD; (c) a successive ZnO coating is applied by ALD; (d) a second Al_2O_3 coating is applied by ALD, resulting in trilayered PVA/Al_2O_3/ZnO/Al_2O_3 microcables; (e) the PVA core is removed by calcination at 450 °C in air for 12 h; (f) the resultant Al_2O_3/ZnO/Al_2O_3 coaxial microtubes are annealed at 700˚C to form coaxial $ZnAl_2O_4$ microtubes separated by a nanometer-scale gap resulting from accumulation of Kirkendall voids. (g) White arrows show the direction of vacancy diffusion for a typical nanoscale Kirkendall-effect experiment in which Al_2O_3 is coated onto a ZnO crystal (left), as well as for the experimental procedure described here, where diffusion occurs in two directions to produce an internal nanoscale gap (right). 73

Figure 3.9 Representative TEM images of Al_2O_3/ZnO/Al_2O_3 microtubes formed by ALD on PVA microfibers. The images in (a) and (b) were obtained after annealing at 450˚C in air. The image in (b) permits direct visualization of the trilayered morphology consisting of a dark polycrystalline ZnO middle layer and lighter amorphous Al_2O_3 shells. The images in (c) and (d) were obtained after annealing at 700 °C for 12 h. Light spots (arrows in c and d) indicate void formed within the tubular structure. Unreacted excess ZnO partitions between the inner and outer shells. 74

Figure 3.10 TEM images of (a) Al_2O_3/ZnO/Al_2O_3 microtubes (18/10/25 nm) after annealing in air at 450 °C. It shows the thin dark ZnO middle layer sandwiched between two lighter Al_2O_3 layers. b) after further annealing at 700 °C for 12 h. The arrows in (b) identify isolated

pieces of the inner or outer shells as a consequence of microtube fracture. (c) $Al_2O_3/ZnO/Al_2O_3$ microtubes (18/21/39nm) after annealing in air at 450 °C, d) after further annealing at 700 °C for 12 h. (e) STEM image of the cross section view of $Al_2O_3/ZnO/Al_2O_3$ microtubes (35/30/38 nm) after annealing at 450 °C in air. The arrow points to the middle ZnO layer. (f) The tubes from (e) after further annealing at 700 °C for 12 h. The arrow inside indicates the formation of a thin gap between two polycrystalline $ZnAl_2O_4$ layers. 75

Figure 3.11 ALD layer thicknesses of ZnO and Al_2O_3 deposited on planar silicon wafers (measured by ellipsometry, open symbols) and microfibers (measured by TEM, filled symbols) after annealing at 450°C in air. Included is the Kirkendall gap thickness from three $Al_2O_3/ZnO/Al_2O_3$ microtubular specimen series (with different shell thicknesses 18/10/25 nm, 18/21/39 nm, 35/30/38 nm) annealed at 700°C and plotted as a function of the ALD cycle number for the ZnO layer. The error bars represent one standard deviation in the data. 76

Figure 3.12 In-situ QCM results at 120˚C showing the effect of EG exposure on the -$OZn(C_2H_5)_{(s)}$ saturated surface produced during ZnO ALD. The DEZ dose is indicated by the dotted line, and the H_2O dose is indicated by the dashed line. The EG dose is shown with the shaded solid line. The first EG exposure result in mass uptake and surface saturation. The EG exposure results in significantly decreased mass uptake for subsequent DEZ exposure steps. 77

Figure 3.13 In-situ QCM results at 120˚C during steady–state molecular layer deposition. The DEZ dose is indicated by the dotted line, and the EG dose is shown with the shaded solid line. After an EG/Ar half cycle, the DEZ/Ar (2/88 s) half–cycle was repeated 3 times, resulting in mass uptake followed by approximately equivalent mass loss, indicative of DEZ physisorption/desorption. 78

Figure 3.14 FTIR spectra collected from an example Zn-hybrid MLD film deposited using 800 cycles at 120 ˚C: (a) after immediate transfer to dry air; (b) in dry air for 3 days; (c) after exposure to ambient for 1 h; (d) after ~ 12 h in ambient; and (e) after annealing in ambient at 100 ˚C for ~ 2 h. Spectrum (f) is obtained from a ~ 45 nm thick ALD ZnO film deposited using 200 cycles at 120 ˚C. 79

Figure 3.15 A transmission electron micrograph obtained from a hydrolyzed Zn -hybrid film deposited at 165 ˚C for 528 cycles onto two Al_2O_3 microtubes. The white lines depict the outline of the starting Al_2O_3 shell, and the right side of the image shows a region where the tube is broken allowing plan–view through the Zn–hybrid/Al_2O_3/Zn–hybrid laminate. The hydrolyzed Zn–hybrid MLD film is conformal and uniform with thickness ~20 nm. The white arrow indicates a point with high contrast suggesting through–holes present in the hydrolyzed film. 80

Figure 3.16 A typical FTIR spectrum of alkyl-aromatic polyamide deposited at 85 ºC for 150 cycles with thickness ~280 nm. The spectrum shows the characteristic peaks of the polyamide, (N-H stretching mode at 3310 cm^{-1}, C=O stretching mode at 1638 cm^{-1} and N-H bending mode at 1543 cm^{-1}). 81

Figure 3.17 A typical near edge X-ray adsorption fine structure (NEXAFS) spectrum of alkyl-aromatic polyamide from different incident angles. The film deposited at 85ºC for 100 cycles with film thickness around 21nm. The spectrum shows chemical information from phenyl group and polyamide C=O bonding. According to the spectrum, the polyamide molecules are aligned and tilted quite a bit to the substrate normal as shown by the inset figure of molecule. 82

Figure 3.18 In-situ QCM measurement of mass uptake of atomic layer deposition of APTES/H_2O cycles (2/40/2/40 s) on Al_2O_3 ALD film. It shows steady state Al_2O_3 ALD process (2/40/2/40 s) at 120 ˚C and 150 ˚C and the sequential ALD process of APTES on the Al-OH terminated in-situ generated Al_2O_3 ALD film. At both temperatures, the first of the APTES/H_2O ALD cycle counts more than 50% of total mass uptake of SAM of APTES on the Al_2O_3 ALD film. 83

Figure 3.19 Representative in-situ FTIR spectra after sequential half cycles of TMA, H_2O, APTES and H_2O onto the Al-OH terminated Al_2O_3 ALD film coated anodic aluminum oxide substrate at 100 ˚C. Spectra were taken after more than 1mins purge time to make sure that all physical absorbed molecules were removed. 84

Figure 5.1 Schematic diagram of the experimental apparatus. The inner volume of the reactor is ~ 110 mL. The reactor wall temperature is typically held at 100 ^oC. The sample is located on a block that is heated independently from the reactor chamber wall. 114

Figure 5.2 Transmission FTIR spectra for an Al_2O_3 film deposited from pyrolysis of $Al(acac)_3$ at 150 °C and 25-26 MPa on a Si substrate for 40 mins with film thickness ~ 23 nm. Before anneal: spectrum taken after deposition. After anneal: spectrum taken after the film was annealed at 600 °C in air for 15 mins. 115

Figure 5.3 (a) Auger Electron Spectroscopy (AES) survey scan of Al_2O_3 and Ga_2O_3 films. Ga_2O_3 was deposited from pyrolysis of $Ga(acac)_3$ at 200 °C and 28-32 MPa, for 10 mins, resulting in a thickness of ~ 150 nm. Al_2O_3 was deposited from pyrolysis of $Al(acac)_3$ at 185 °C and 25-26 MPa for 50 mins, resulting in a thickness of ~ 100 nm. (b) The detailed AES spectrum of the Ga-LMM peaks. (c) The detailed AES spectrum of the Al-KLL peaks. The positions of Ga-LMM and Al-KLL peaks are consistent with the fully oxidized status of Ga and Al. 116

Figure 5.4 The Al_2O_3 film thickness measured as a function of deposition time at different reaction temperatures during the $scCO_2$-based pyrolysis of $Al(acac)_3$ with initial precursor

concentration ~ 170 μmol/L. The straight lines are linear regressions and the curved lines are guides for the eye. At high temperatures (200 °C and 250 °C) for short deposition time (<5 mins), the films are observed to grow linearly with reaction time, followed by saturation of the film thickness at longer periods. At low temperatures (150 °C, 180 °C and 185 °C), the linear growth rate is observed for longer reaction times (measured up to 50 mins)..... 117

Figure 5.5 The effect of precursor concentration in the reaction system on the deposition rate of Al_2O_3 films in $scCO_2$-based process from pyrolysis of $Al(acac)_3$ at 250 °C. The solid line denotes a linear regression of the data points. The linear fit reveals that the growth rate is determined by the precursor concentration in the reaction system..... 118

Figure 5.6 Apparent reaction kinetics of $scCO_2$-based deposition of Al_2O_3 films from pyrolytic reaction of $Al(acac)_3$ with initial concentration of 170 μmol/L. The slopes of the lines indicate that the overall energy barrier for Al_2O_3 deposition is 68±6 kJ/mol. And the apparent kinetics of $scCO_2$-based Ga_2O_3 deposition from pyrolysis of $Ga(acac)_3$ at initial concentration of 230 μmol/L. The kinetic barrier of Ga_2O_3 deposition is 84±7 kJ/mol. The solid lines represent linear regressions of the data points..... 119

Scheme 5.1 A simplified reaction mechanism for pyrolysis reaction of $Al(acac)_3$. The * denotes the postulated polar transition state. 121

Figure 6.1 Schematic diagram of the experiment apparatus. Power cable was used to provide electricity for cartridge heaters in the heating block. The temperatures of sample and supercritical CO_2 solution were heated individually by different heaters and controlled by using different thermocouples. The inner volume of the reactor is around 110mL. 135

Figure 6.2 AES spectrum of untreated pristine MWCNTs (top spectrum) grown by catalytic chemical vapor deposition process at 500°C, with Fe (0.5nm)/Al_2O_3(10nm) as the catalyst on thermally grown silicon oxide. Gallium oxide coated MWCNTs (bottom spectrum) fabricated by thermal decomposition of $Ga(acac)_3$ in $scCO_2$ process at 200°C, 28-32MPa for 10mins..... 136

Figure 6.3 (a) FESEM image of untreated pristine MWCNTs. The diameters of the pristine MWCNTs are in the range of 20-60nm. (b) FESEM image of gallium oxide-coated MWCNTs. The gallium oxide coating was deposited by thermal decomposition of $Ga(acac)_3$ in $scCO_2$ process at 200°C, 28-32MPa for 10mins. The diameters of the coated MWCNTs are in the range of 70-130nm, which indicates the average thickness of the gallium oxide coating is around 30nm for 10mins. 137

Figure 6.4 (a) TEM image of a single pristine MWCNT. (b) TEM image of MWCNTs coated by gallium oxide from thermal decomposition of $Ga(acac)_3$ at 160°C and 23MPa-24MPa for 7 mins. The arrow inside (b) shows the part of MWCNTs having no oxide coating. (c) TEM image of MWCNTs coated by gallium oxide from thermal decomposition of

$Ga(acac)_3$ at 200°C and 28MPa for 1.5 mins. (d) Higher magnification TEM image of MWCNTs coated by gallium oxide from thermal decomposition of $Ga(acac)_3$ at 200°C and 28MPa for 1.5 mins. (e) A typical EDS spectrum of oxide coated MWCNTs. The gallium oxide deposition experiment was carried out at 200°C, 28-32MPa for 1.5 mins. The Ga and majority O peaks result from the gallium oxide coating, and the major carbon signal is ascribed to the MWCNTs with some contribution from carbon impurities and adventitious carbon. The tiny Cu peak is from the TEM grid. 138

Figure 6.5 (a) FESEM image of untreated pristine MWCNTs. The diameters of the MWCNTs are in the range of 10-30nm. (b) FESEM image of MWCNTs coated by gallium oxide from pyrolysis of $Ga(acac)_3$ at 200°C, 28-30MPa for 10mins. The diameters of the MWCNTs are in the range of 60-100nm The arrow in (b) indicates that the coating of gallium oxide can replicate the small helix feature of MWCNTs. (c) FESEM image of gallium oxide coated MWCNTs with relatively uniform Ru coating on the surface by atomic layer deposition from reaction between $Ru(Cp)_2$ and O_2 at 325°C for 150cycles. (d) A typical EDS spectrum of oxide-coated MWCNTs with Ru ALD coating. The significant Ru peak is shown. The peak of Ga and O come from the gallium oxide under the Ru, and the tiny C peak probably comes from the carbon nanotube core, adventitious carbon from air and the as-deposited films. 139

Figure 7.1 The diagram of reaction system. H_2 is mixed with $scCO_2$ in the manifold to form uniform solution. The temperature of the reactor and manifold are controlled by feedback thermal couples individually. The reaction system can be observed through the sapphire windows. 150

Figure 7.2 (a) A photo image of stable $Ni(Cp)_2$ in $scCO_2$ solution (Green) at 70 °C. (b) A photo image of the solution after 7-8 h incubation time (Orange). 151

Figure 7.3 (a) FESEM image of pristine MWCNTs. (b) FESEM image of the Ni nanoparticles decorated MWCNTs after treated in the $scCO_2$ based direct hydrogenolysis reaction between $Ni(Cp)_2$ and H_2 at 70 °C. (c) A typical TEM image of the Ni nanoparticles anchored MWCNTs. (d) High Resolution TEM image of Ni nanoparticles decorated MWCNTs. 152

Figure 7.4 EDS spectrum of Ni nanoparticles decorated MWCNTs 153

Figure 7.5 (a) A photo image of clean glass bottle which is transparent. (b) A photo image of glass bottle coated by Ni thin film by the direct low temperature supercritical carbon dioxide based hydrogenation process of Ni $(Cp)_2$ at 70 °C. The gold color film is Ni. (c) A photo image of clean sapphire window which is transparent. (d) A photo image of sapphire window after Ni deposition from the direct low temperature supercritical carbon dioxide based hyrogenation process of $Ni(Cp)_2$ at 70 °C. 154

Figure 8.1 Schematic diagram of vapor-phase, self-limiting atomic layer deposition (ALD) illustrating the cyclic process by which an Al_2O_3 surface coating is controllably constructed layer-by-layer from TMA and H_2O precursors..... 167

Figure 8.2 (a) FESEM image of electrospun PVA fibers. (b, c) FESEM images of Al_2O_3 microtube replicas prepared by ALD wherein the Al_2O_3 coating was deposited for 475 cycles at 45˚C. (d) TEM image of a corresponding Al_2O_3 microtube. The arrow in (d) identifies a peripheral circle formed inside the microtube near an apparent neck in the fiber template. 168

Figure 8.3 (a) FESEM image of an Al_2O_3 microtube formed when ALD was performed on electrospun PVA fibers for 300 cycles at 45˚C. The arrow indicates a circle on the inside wall of the resultant microtube. (b) TEM image of the corresponding Al_2O_3 microtube illustrating the wall thickness. (c) FESEM and (d) TEM images of Al_2O_3 microtubes fabricated by ALD for 150 cycles at 45˚C. A wall thickness measurement is included in (d). In all cases, the electrospun PVA fiber templates were removed by heating in air at 400˚C for 24 h..... 169

Figure 8.4 Wall thickness of Al_2O_3 microtubes prepared on electrospun PVA fibers (○) and measured by TEM as a function of ALD cycle number. Included for comparison is the Al_2O_3 film thickness on a planar Si substrate (●) measured by ellipsometry. The solid lines denote linear regressions of the data points. The corresponding average growth rates of Al_2O_3 are about 0.08 nm/cycle on the electrospun fibers and 0.07 nm/cycle on the Si substrate. Error bars (±1 standard deviation) deduced from analysis of 25 thickness measurements from each specimen are smaller than the symbols shown. 170

Figure 8.5 Representative EDS spectra acquired from the Al_2O_3 microtubes generated by ALD on electrospun polymer fibers after different cycle numbers (labeled). Note the presence of Al and O signals from Al_2O_3, as well as the absence of a discernible C peak from the polymer precursor (the instrument employed is capable of detecting C), after thermal treatment in air at 400°C for 24 h. The Cu signal is a consequence of the TEM grid and can be disregarded. The expected position for a signal due to C is also identified..... 171

Figure 9.1 Schematic diagram of the procedure developed here for the fabrication of coaxial $ZnAl_2O_4$ microtube-in-microtube coaxial assemblies: (a) electrospinning is used to produce PVA microfibers; (b) a thin, conformal Al_2O_3 coating is applied to the PVA fibers by low-temperature ALD; (c) a successive ZnO coating is applied by ALD; (d) a second Al_2O_3 coating is applied by ALD, resulting in trilayered PVA/Al_2O_3/ZnO/Al_2O_3 microcables; (e) the PVA core is removed by calcination at 450°C in air for 12 h; (f) the resultant Al_2O_3/ZnO/Al_2O_3 coaxial microtubes are annealed at 700˚C to form coaxial $ZnAl_2O_4$ microtubes separated by a nanometer-scale gap resulting from accumulation of Kirkendall voids. (g) White arrows show the direction of vacancy diffusion for a typical nanoscale

Kirkendall-effect experiment in which Al_2O_3 is coated onto a ZnO crystal (left), as well as for the experimental procedure described here, where diffusion occurs in two directions to produce an internal nanoscale gap (right). 194

Figure 9.2 SEM (a and b) images of PVA electrospun fibers coated with an Al_2O_3(inner)/ZnO(outer) bilayer deposited by low-temperature ALD. Film thicknesses and the number of ALD cycles used in this and subsequent specimens are provided in Table 1. The SEM image in (b) shows a single PVA fiber with the coaxial bi-layer coating (Al_2O_3, solid arrow; ZnO, dashed arrow). TEM (c and d) image of the coaxial Al_2O_3/ZnO microtubes obtained after removal of the PVA by dissolution in water, which is displayed in (c), whereas microtubes produced after PVA calcinations, which are evident in (d). 195

Figure 9.3 Representative TEM images of Al_2O_3/ZnO/Al_2O_3 microtubes formed by ALD on PVA microfibers. The images in (a) and (b) were obtained after annealing at 450˚C in air. The image in (b) permits direct visualization of the trilayered morphology consisting of a dark polycrystalline ZnO middle layer and lighter amorphous Al_2O_3 shells. The images in (c) and (d) were obtained after annealing at 700°C for 12 h. Light spots (arrows in c and d) indicate void formed within the tubular structure. Unreacted excess ZnO partitions between the inner and outer shells. 196

Figure 9.4 TEM images of Al_2O_3/ZnO/Al_2O_3 microtubes: (a), (b) after annealing in air at 450°C; The HRTEM image in (b) shows the thin dark ZnO middle layer sandwiched between two lighter Al_2O_3 layers. (c) – (f) after further annealing at 700°C for 12 h. Compared to samples in Figure 9.3, these samples contained a thinner (~10 nm) ZnO layer, with a thicker (~25 nm) outer Al_2O_3 layer. The arrows in (d) identify isolated pieces of the inner or outer shells as a consequence of microtube fracture. In (e) and (f), HRTEM images reveal a light middle layer located between two darker layers, indicating the formation of a thin gap between two polycrystalline $ZnAl_2O_4$ layers. 197

Figure 9.5 TEM images of Al_2O_3/ZnO/Al_2O_3 microtubes similar to those shown in Figure 9.4, with thicker ZnO (~21 nm) and outer Al_2O_3 (~39 nm) layers: (a), (b) annealed at 450˚C in air; (c), (d) annealed at 700°C for 12 h. Image contrast (and reversal) is identical to that observed in Figure 9.4. A continuous Kirkendall gap is evident in (d). 198

Figure 9.6 HRTEM images of a) a section of isolated inner tube wall, showing polycrystalline structures, b) a part of inner tube shell showing polycrystalline $ZnAl_2O_4$ and amorphous Al_2O_3 region (within the yellow line region), c) a section of outer tube wall consisting mainly of $ZnAl_2O_4$ crystal, d) a section of outer tube wall having $ZnAl_2O_4$ crystalline and amorphous Al_2O_3. The inner and outer microtubes obtained from the sample batch shown in Figure 9.4 after 700°C for 12 h. Lattice spacing is 0.46 and 0.28 nm corresponding to the 111 and 220 planes of $ZnAl_2O_4$ respectively. 199

Figure 9.7 Typical TEM image of Al2O3/ZnO/Al2O3 microtubes (~18/10/44nm) annealed at 700°C for 12h. a) The broken tubes reveal clear physical separation and delineation between the inner and outer tubes. The image reveals roughness of the spinel layers along the length of the tube, on the surfaces adjacent to the Kirkendall void. A process break during the final Al_2O_3 coating step resulted in the thin line visible in the thick outer Al_2O_3 layer. b) HRTEM image of the tube set in panel a, showing the outer tube, hollow gap and inner tube. The lattice spacing and orientation are consistent with polycrystalline $ZnAl_2O_4$ distributed randomly in an amorphous Al_2O_3 matrix. The lattice signal becomes weaker along the radial direction toward the outer surface of the outer shell. The width of the hollow region between the tubes is consistent with that shown in Figure 9.4, with a similar starting thickness of ZnO. 200

Figure 9.8 XRD patterns of the coaxial microtubes portrayed in Figure 9.4: (a) after calcination at 450°C in air for 12 h, and (b) after annealing at 700°C for 12 h. The reflections marked in (a) correspond to the ZnO lattice, whereas those in (b) correspond to features associated with $ZnAl_2O_4$. There is no evidence of crystalline ZnO in the diffraction pattern acquired after high-temperature annealing, which is indicative of complete reaction consumption of the ZnO layer. 201

Figure 9.9 ALD layer thicknesses of ZnO and Al_2O_3 deposited on planar silicon wafers (measured by ellipsometry, open symbols) and microfibers (measured by TEM, filled symbols) after annealing at 450°C in air. Included is the Kirkendall gap thickness from two Al_2O_3/ZnO/Al_2O_3 microtubular specimen series (shown in Figure 9.4 and 9.5) annealed at 700°C and plotted as a function of the ALD cycle number for the ZnO layer. The error bars represent one standard deviation in the data. 202

Figure 10.1 A schematic view of the viscous flow ALD/MLD reactor. The precursors are delivered into the reactor with Ar carrier gas. On the reactor exhaust line, computer controlled gate values are used to direct the exhaust from the EG pulse into a liquid nitrogen trap before entering the pump. 232

Figure 10.2 (a), (b) In–situ QCM results for ZnO ALD at 120 ˚C using DEZ/Ar/H_2O/Ar exposure times of 2/42/4/42 seconds. Panel (a) shows linear mass gain for more than 130 ALD cycles. The average mass uptake rate is ~125 ng/cm^2•cycle with standard deviation of 3 ng/cm^2•cycle. Panel (b) shows an interrupted ZnO ALD sequence at 120˚C, showing the effect of three sequential DEZ/Ar (2/88 s) ALD half–cycle exposures. The DEZ dose time is indicated by the dotted line, and the H_2O dose is indicated by the dashed line. Repeating the DEZ exposure results in a small mass uptake, followed by a slow mass decrease, consistent with some reactant physisorption..... 233

Figure 10.3 In-situ QCM results at 120˚C showing the effect of EG exposure on the -$OZn(C_2H_5)_{(s)}$ saturated surface produced during ZnO ALD. Two data sets are shown from two separate experiments. The DEZ dose is indicated by the dotted line, and the H_2O dose is indicated by the dashed line. The EG dose is shown with the shaded solid line. The first EG exposure result in mass uptake and surface saturation. The EG exposure results in significantly decreased mass uptake for subsequent DEZ exposure steps. 234

Figure 10.4 In-situ QCM results at 120 ˚C showing the effect of EG exposure on the -$OZn(OH)_{(s)}$ saturated surface produced during ZnO ALD. The DEZ dose is indicated by the dotted line, and the H_2O dose is indicated by the dashed line. The EG dose is shown with the shaded solid line. Exposing the –OH terminate surface to EG results in a mass uptake of ~33 ng/cm^2. 235

Figure 10.5 In-situ QCM results at 120˚C during steady–state molecular layer deposition. The DEZ dose is indicated by the dotted line, and the EG dose is shown with the shaded solid line. After an EG/Ar half cycle, the DEZ/Ar (2/88 s) half–cycle was repeated 3 times, resulting in mass uptake followed by approximately equivalent mass loss, indicative of DEZ physisorption/desorption. 236

Figure 10.6 In-situ QCM results at 120˚C during steady–state molecular layer deposition using the same conditions shown in Figure 5. After a DEZ/Ar half cycle, the EG/Ar (4/86 s) half–cycle was repeated 2 times, resulting in mass uptake followed by approximately equivalent mass loss, indicative of reactant physisorption/desorption. No net mass gain is observed during the repeated EG/Ar half cycles. 237

Figure 10.7 In-situ QCM results at various temperatures during steady–state molecular layer deposition using DEZ/Ar/EG/Ar: 2/42/4/42 s. The mass uptake rate decreased with increasing temperature, resulting in an average mass uptake of ~24.3 $ng/(cm^2 \bullet cycle)$ at 120˚C and ~17.4 $ng/(cm^2 \bullet cycle)$ at 165˚C. Data was not collected during film nucleation, so data from an arbitrary starting time was normalized to the origin. 238

Figure 10.8 A plot of the net mass uptake rate at versus deposition temperature for various Ar purge times: DEZ/Ar/EG/Ar = 2/n/4/n s, where n is 12, 22, 32, or 42 seconds. The mass uptake rate of Zn hybrid MLD decreases with the increasing the purge time and the reaction temperature. The error bars were deduced from the corresponding QCM measurements, and the lines are a guide for the eye. The data at 32 and 42 s are statistically indistinguishable for all studied temperatures. 239

Figure 10.9 FTIR spectra collected from an example Zn-hybrid MLD film deposited using 800 cycles at 120˚C: (a) after immediate transfer to dry air; (b) in dry air for 3 days; (c) after exposure to ambient for 1 h; (d) after ~ 12 h in ambient; and (e) after annealing in ambient at

100 ˚C for ~ 2 h. Spectrum (f) is obtained from a ~ 45 nm thick ALD ZnO film deposited using 200 cycles at 120 ˚C. 240

Figure 10.10 FTIR spectra obtained from three Zn-hybrid MLD films deposited at 120°C using different numbers of MLD cycles. All samples received a similar brief ambient exposure before analysis. The intensity of the characteristic EG peaks increase with the number of deposition cycles. 241

Figure 10.11 Film thickness of hydrolyzed Zn-hybrid films obtained from spectroscopic ellipsometry, plotted versus number of MLD cycles for films deposited on oxidized silicon. The typical uncertainty in each measurement is ~1–2%. The solid lines give linear fits corresponding to a deposition rate of 0.57 Å/cycle at 120°C (■) and 0.39 Å/cycle at 165°C (●). 242

Figure 10.12 a), b) O1s and C1s XPS spectra collected from a hydrolyzed MLD Zn- hybrid film (~45 nm, 800 cycles, at 120˚C). The O1s signal shows features at 531.5 eV 529.7 eV corresponding to zinc hydroxide (54.5%) and zinc oxide (45.5%) respectively. The C1s signal includes components 284.6 eV, 285.7 eV and 289.4 eV related to –C–H_2, –C–OH and –O–C=O respectively. c), d) O1s and C1s XPS spectra collected from an ALD ZnO film (~45 nm, 200 cycles, at 120˚C). The carbon content is ~2 atomic %. Ar sputtering (5 KeV for 3 min) was used to remove surface contamination before spectra collection. Gaussian curve fits are included. 243

Figure 10.13 Image (a) is a scanning force micrograph of a MLD Zn-hybrid film deposited at 120 ˚C for 800 cycles after prolonged air exposure. The film thickness is ~45 nm and root mean square (RMS) roughness is 0.8 nm. The surface features with diameter of 20–30 nm are cavities or holes in the film. Image (b) was acquired after annealing the film in image (a) in ambient for 2 h at 100 ˚C. The film thickness decreased to ~30 nm and RMS increased to 1.4 nm. The surface appears more homogeneous without obvious voids or holes at the scale imaged. 244

Figure 10.14 A transmission electron micrograph obtained from a hydrolyzed Zn -hybrid film deposited at 165°C for 528 cycles onto two Al_2O_3 microtubes. The white lines depict the outline of the starting Al_2O_3 shell, and the right side of the image shows a region where the tube is broken allowing plan–view through the Zn–hybrid/Al_2O_3/Zn–hybrid laminate. The hydrolyzed Zn–hybrid MLD film is conformal and uniform with thickness ~20 nm. The white arrow indicates a point with high contrast suggesting through–holes present in the hydrolyzed film. 245

Figure 11.1 In-situ QCM measurement of APTES/ H_2O ALD (2/40/2/40 s) on Al_2O_3 ALD film. It shows steady state Al_2O_3 ALD process (2/40/2/40 s) at 120 ˚C, which has a mass uptake of ~35 ng/cm^2 for TMA dose, ~6 ng/cm^2 for H_2O dose. The mass uptake of the 1st

cycle of APTES on Al_2O_3 ALD film is ~68 ng/cm^2. The following 8 cycles of APTES/H_2O contribute ~20 ng/cm^2. The surface reaction is completed after 5 cycles. The following Al_2O_3 ALD on APTES covered surface has a smaller mass uptake than steady state growth rate of Al_2O_3 ALD. 270

Figure 11.2 In-situ QCM measurement at 150 ˚C: Al_2O_3 ALD, APTES/H_2O ALD cycles (2/40/2/40 s) on Al-OH terminated Al_2O_3 ALD film, Al_2O_3 ALD on APTES covered surface. It shows steady state Al_2O_3 ALD process (2/40/2/40 s) at 150˚C, which has a mass uptake of ~35 ng/cm^2 for TMA dose, ~5 ng/cm^2 for H_2O dose. The mass uptake of the 1st cycle of APTES on Al_2O_3 ALD film is ~78 ng/cm^2. The mass uptake from 11 cycles of APTES/H_2O is saturated at ~138 ng/cm^2. The mass uptake of TMA on the APTES covered surface is ~28 ng/cm^2, which is smaller than the steady state mass uptake rate of Al_2O_3 ALD. 271

Figure 11.3 Representative in-situ FTIR spectra of the Al_2O_3 ALD film (with Al-OH surface bonded ligands) coated AAO substrate at 100 ˚C: A) after sequential TMA half cycle, H_2O half cycle, APTES half cycle, then the H_2O half cycle. B) The No. 2 to No. 4 cycles of APTES/H_2O after the 1st cycle of APTES/H_2O. C) The No. 10 cycle of APTES/H_2O, followed by TMA and H_2O dose at same temperature. All spectra were taken after more than 1mins purge time to make sure that all physical absorbed molecules were removed. 272

Figure 11.4 XPS analysis of Al_2O_3 ALD film (deposited at 120 ˚C) with 10 cycles of APTES/H_2O (2/40/2/40 s) at 120 ˚C. A) The survey scan of the APTES functionalized Al_2O_3 film. The N atomic concentration is ~2.5 %, which is similar as the Si atomic ratio in the film. It shows that N 1s peak in the film. B) The detail scan of the N 1s peaks (in black), which is fitted with Gaussian curve. According to the fitting, there are two components of Nitrogen were observed in the APTES monolayer. 274

Figure 11.5 a) The nonwoven polypropylene fiber matrix coated by Al_2O_3 ALD 100 cycles and 10 cycles of APTES/H_2O ALD process at 120 ˚C. b) The replica resulted by removing template of nonwoven PP fiber matrix through annealing in air at 500 ˚C for 24 hours. c) The overall view of the PP fibers with 40 nm Au NP attachment. The resulted fibers from (a) were dipped into the 40nm Au colloid solutions for 24 hours. d) The higher magnification view of PP fibers coated with Au NPs. 275

Figure 11.6 In-situ QCM measurement of APTES/H_2O cycles (2/40/2/40 s) on ZnO ALD films. The mass uptake of the 1st pulse of APTES on ZnO ALD film is around 60ng/cm^2. There is a small net mass decrease in the 1st water half cycle. Virtually there is no mass uptake in the following 5 cycles of APTES/H_2O. Steady state ZnO ALD process have a mass uptake ~ 120 ng/cm^2 for each cycle. 276

Figure 11.7 In-situ QCM measurement of mass uptake of APTES/H_2O ALD cycles (2/40/2/40 s) on Al-CH_3 terminated Al_2O_3 ALD film. It shows steady state Al_2O_3 ALD

process (2/40/2/40 s) at 150 ˚C, which has a mass uptake of ~35 ng/cm^2 for TMA dose, ~5 ng/cm^2 for H_2O dose. APTES on the Al-OH terminated Al_2O_3 ALD film. The mass uptake of the 1st cycle of APTES on Al_2O_3 ALD film is around ~78ng/cm^2. The following 9 cycles of APTES/H_2O contribute around ~55ng/cm^2. The surface reaction is completed after 10 cycles. B) Representative in-situ FTIR spectra of the Al_2O_3 ALD film coated AAO substrate at 100 ˚C: A) after chemical absorption of TMA, H_2O in the Al_2O_3 ALD process, after APTES, H_2O onto the Al-CH_3 terminated Al_2O_3 ALD film. 277

Scheme 11.1 Reaction scheme of the APTES on the Al-OH terminated Al_2O_3 ALD film surface. It is possible the one, two or even three of the ethoxyl ligands reacted with -OH groups through a hydrolytic sol-gel reaction to form Si-O-Al bondings. The following H_2O pulsing step will hydrolyze the unreacted ethoxy groups and generate new -OH groups for hydrolysis reaction with the following APTES pulse. By repeating this APTES/H_2O ALD process, the surface will be covered by a monolayer of APTES with -NH_2 terminal group. 278

Scheme 11.2 Reaction scheme of the APTES on the Al-CH_3 terminated Al_2O_3 ALD film surface. It is possible the one, two or even three of the ethoxyl ligands reacted with Al-CH_3 through an nonhydrolytic sol-gel reaction to form Si-O-Al bonding. The following H_2O dose step will convert the unreacted ethoxy group and CH_3 ligands to –OH ligands, which will be available for the hydrolysis reaction with the next pulse of APTES. By repeating the APTES/H_2O ALD cycles, the Al_2O_3 ALD film surface will be eventually covered by one monolayer of APTES SAM with NH_2 terminals. 279

CHAPTER 1. Introduction

For different applications, including energy related,[1-6] biomedical,[7-9] catalytic,[10-12] electronic,[13-16] photonic fields,[17-19] and nanoscience and technologies,[15, 20, 21] it is important to modify the interior and exterior of substrates, which have high aspect ratio three dimensional (3D) complex structures, with desired functional, reactive and stable coatings. The ability to fabricate mono- or multi-layers of functional materials with precisely-controlled dimensions, finely-tuned composition and molecular structures, has attracted significant interest in materials science[22-28]and is the key to construct such materials and structures at the nano- and micro-scale with desired properties. A variety of different techniques for constructing mono- and multi-layers functional materials into various substrates, especially those with high aspect ratio three dimensional (3D) complex structures, has been developed. They are generally categorized into three different types based on the fabrication mediums: liquid solvent based route, supercritical fluid based route and solvent free route (vacuum). An overview of those processes will be presented in the following text.

1.1 Liquid solvent based routes and related disadvantages

In the liquid solvent based processes, the fabrication of mono or multi-layer functional coatings is carried out in solution, in which the precursor solute is dissolved in a solvent such as water or inorganic solvent. Example techniques include sol-gel chemistry,[25, 29, 30] Langmuir- Blodgett (LB) technique,[31] Layer by layer (LBL) assembly technique,[24] spin-coating,[32] electrodeposition[33] etc, which are summarized below.

1.1.1 Sol-gel chemistry

Sol-gel chemistry has been widely used for thin film deposition of metal oxides, multi-components materials and organic-inorganic hybrid materials from either hydrolytic or nonhydrolytic chemistry.[25, 29, 30] Due to the homogeneous reaction process of most sol-gel technique, it is difficult for it to form uniform and conformal thin coating on/into substrates with complex structure. Moreover it is very difficult and complex to control the coating thickness. The reason is that the coating layer thickness is determined by precursor concentrations, reaction temperature, diffusion of reactants etc. Although the surface sol-gel process was developed[34-36] to achieve better control of the thickness, the process suffered from slow growth rate, long process time, multiple layers growth per cycle and impurities incorporation.[34-36] Due to the liquid solvent environment, nonconformal coating induced by capillary force is common for processing of 3D complex structures.

1.1.2 Langmuir- Blodgett (LB) technique

Langmuir-Blodgett (LB) technique is one of the earliest techniques used to form thin film coatings. The basic concept of this idea is to transfer organized monolayers of amphiphilic molecules from the air-water interface to a solid substrate surface through hydrophobic and hydrophilic interactions as shown in Figure 1.1.[31] This simple technique has mostly been used for amphiphilic molecules and is not directly adaptable to other material systems. The molecular layers are assembled together by weaker hydrophobic and hydrophilic forces compared with covalent bonding. Consequently, the mechanical properties of LB films are generally not good. More importantly, it is hard to form conformal film

coating in complex 3D structures with this technique. At the same time, organic solvent, water or other contaminants can be easily brought into the as-formed film.

1.1.3 Layer by layer (LBL) assembly technique

LBL assembly technique, as shown in Figure 1.2, is a modified LB approach, in which the reactants with complementary charges adsorb onto substrates alternatively to form integrated thin films through electrostatic force.[24, 37-52] A variety of functional polyelectrolytes (including functionalized polymers, nanoparticles, biomolecules etc) could be incorporated into the film to enable multiple functionalities including photoluminescence, electroluminescence and mechanical, optical and electronic properties.[24, 37-52] Combined with patterning and templating techniques, LBL has been applied to form different complex nanostructures.[53-56] Although LBL is a versatile technique, there are a lot of limitations of the LBL technique. For instance, it is not easy to form uniform and conformal films over large scale, especially onto the 3D complex structures. LBL films have to be formed by electrostatic force and the components have to be polyelectrolytes. It is easy to bring contaminants into films, which is common for the solvent based process as well.

1.1.4 Electrodeposition

Electrodeposition is an important solvent based coating technique and is widely used in the electronics industry. The principle of electrodeposition is analogous to a galvanic cell acting in reverse. The item to be coated is placed into a solution containing one or more metal salts. The item is connected to an electrical circuit as the cathode while another electrode of the same metal in the metal salt acts as the anode. While electrical current is

passed through the circuit, metal ions in the solution take up excess electrons and form a layer of metal on the item surface. Metalic thin films such as Cu, Ag, Au, Zn, Ni or alloys [33, 57-66] can be synthesized by this way. Several organic thin films like polypyrrole or polythiophene were also formed by this method.[67-70] Combined with patterning and templating techniques, different nanostructures have been fabricated by electrodeposition process.[57, 58, 60, 71-73] While electrodeposition is a low-cost, room temperature process, . it is difficult for electrodeposition to form uniform coating on nonconductive substrates.

1.1.5 Challenges for liquid solvent based routes

As mentioned in this section, it is difficult for those liquid solvent based deposition processes to form uniform and conformal coating of functional materials with well defined properties, due to the i) intrinsic limitations including capillary force and surface tension, ii) solvent contamination, iii) complex reaction environment. The situation is serious for uniform modification of the three dimensional substrate with complex structures. In order to circumvent those intrinsic problems, supercritical fluid, which has low surface tension and liquid like density has been investigated as an alternative deposition environment.

1.2 Supercritical fluids based process

Due to the unique gas-like (low viscosity, high diffusivity, zero surface tension) and liquid-like properties (high density), supercritical fluids have been studied as an alternative medium for fabrication of nanoscale functional coatings. Thin films of number of metals (Au, Ni, Cu, Co, Pd, Pt etc),[74-82] metal oxides (TiO_2, Al_2O_3, Ga_2O_3, HfO_2 etc)[78, 83-87] and others have been synthesized in supercritical fluids. Supercritical carbon dioxide ($scCO_2$) is

especially of interest because it has an easily accessible critical point and is environmentally benign.

1.2.1. Properties of supercritical carbon dioxide

$ScCO_2$ is a clean solvent with unique properties, such as gas-like high diffusivity, low viscosity, zero surface tension, liquid-like high density and chemically inertness at temperature lower than 600 ˚C.[88-90] The high diffusivity and low viscosity of $scCO_2$ is important for overcoming the limitation of mass transport in nanometer or sub-nanometer confined surface geometries. Zero surface tension of $scCO_2$ enables it to permeate and wet the deposition surface with high aspect ratio 3D complex structures without damaging those structures. On the other hand, the high density of $scCO_2$ assists the dissolution of precursors (metal organic species, monomer etc), and helps remove reaction byproducts and impurities from the deposition surface to decrease contaminants in resulting films. Moreover compared with supercritical water, supercritical ammonia, $scCO_2$ has a readily accessible critical point (Tc=31 ˚C, Pc=7.38 MPa). Because of those interesting properties, supercritical carbon dioxide has been widely studied for material fabrication process.[88, 91]

1.2.2 Applications of supercritical carbon dioxide in materials fabrication and functionalization

By taking advantage of high solubility of precursors and hydrogen in $scCO_2$, Watkins and his coworkers[82, 90, 92, 93] developed a chemical fluid deposition process (CFD) using $scCO_2$ as the solvent to deposit metal thin films such as Cu, Ni, Co, Au, Pd and Pt on silicon and polymer substrates. CFD is comparable with the corresponding vacuum process,

chemical vapor deposition, except that CFD can grow metal films of higher purity at relatively lower temperature with faster growth rate.[74, 90, 94] Detail reaction kinetics of deposition of Cu thin film from (2,2,7-trimethyloctane -3,5-dionato) copper(II) with hydrogen has been studied by Zong etc.[92] Kinetics of copper deposition from $Cu(hfac)_2$ in $scCO_2$ process has been shown by Kondoh's group and lower deposition temperature compared with CVD process have been reported.[81] Ru deposition has also been demonstrated for the $scCO_2$ based thin film deposition technology by Kondoh et al.[79] Although $scCO_2$ based metal oxides thin film deposition has not been studied as much as metal deposition, there are some works reported. Metal oxides including Al_2O_3, Ga_2O_3, HfO_x, Fe_2O_3, SiO_2, TiO_2 and other inorganic thin films including silicates has been studied by Parsons[86, 87] and several other groups.[84, 88, 95-100] Parsons group also studied $scCO_2$ based low temperature deposition of a wide range of metal oxides thin films[86, 87] and showed the cyclic type deposition process in $scCO_2$ environment.[87] Beside inorganic materials, deposition of organic materials such as polymer thin films[101] and self-assembly monolayer (SAMs)[76] have also been studied for $scCO_2$ system. Covalent assembly of ultra thin organic films, such as oligoimide, by using $scCO_2$ as a solvent was reported by Srinivasan etc.[102-104] In contrast to the conventional solvent based process, $scCO_2$ based process eliminates the post-treatment for solvent removal and facilitates transportation of molecules.[102, 103] Carbonell and his coworkers developed a liquid-CO_2 free meniscus process[105] to coat substrates with different organics, such as sucrose octaacetate (SOA).[106] SAMs have also been fabricated in $scCO_2$ environment. McCarthy's group[107] and other groups[108, 109] studied formation of a wide range of silane SAMs on silicon in the $scCO_2$-based process. Organic silane SAMs formation on

Al_2O_3[110, 111] and TiO_2[111] in $scCO_2$ process has also been reported and the substrate chemistry for SAMs formation in $scCO_2$ process has been discussed.[111]

Owing to the penetration ability and zero surface tension of $scCO_2$, SAMs of silanes have been formed in the buried interface between silicon and polymer layers[112-114] to improve interfacial mechanical properties in the $scCO_2$ process. SAMs were also successfully formed in 3D complex porous structures including porous silica[115] and nanoparticles.[110] By applying the $scCO_2$ process[116] onto porous silicates as the substrate, Cu, Fe_2O_3, Co nanowires and nanotubes were synthesized. Moreover, a block copolymer was used as template to fabricate porous silica film in $scCO_2$.[84, 98, 99] As an antisolvent, $scCO_2$ has also been used to coat carbon nanotubes of high aspect ratio with Eu_2O_3, Fe_2O_3 and Co_2O_3 thin film coatings on CNTs.[83, 95, 97] Nanostructures of metals including Ru,[79, 117] Cu,[79, 117] Pd[117] and Au[74] were generated by applying $scCO_2$ based process onto 3D complex structures. Moreover, Watkins, McCarthy and other groups synthesized nanocomposites of metal nanoparticles or polymer materials into a polymer or inorganic 3D matrix.[118-129] As demonstrated in various examples, $scCO_2$ fluid is a good solvent environment for modifying substrates, including the ones with 3D complex structures, with functional materials.

1.2.3 The challenges and opportunities of supercritical carbon dioxide process

Due to the harsh reaction environment (high pressure and high temperature), it is difficult to use the *in-situ* monitoring techniques to study the reaction mechanisms, especially the surface reaction, involved in the $scCO_2$ process. Very little research has addressed reaction mechanisms of the $scCO_2$ based deposition process. Other than that, $scCO_2$ is still a

promising technique for incorporating functional coatings of a wide range of materials into complex structures. It is a good solvent for wetting and penetrating into the 3D highly porous substrates to modify them with desired functionalities and without breaking down the structure of the substrate. However, the CFD process was mainly focused on the metal deposition.[74, 82, 90, 92-94] Very few research focused onto the metal oxides deposition, which has wide range applications. In our work, a strategy for studying the deposition kinetics of Al_2O_3 and Ga_2O_3 was developed(Chapter 5),[130] especially the role of $scCO_2$ in the deposition kinetics. The pyrolysis chemistry of metal organics in supercritical carbon dioxides, was demonstrated as a powerful technique to coat oxides such as Al_2O_3 and Ga_2O_3 into 3D high aspect ratio complex structure of CNT forest (Chapter 6).[131] Furthermore, the low temperature $scCO_2$ based hydrogenolysis process was developed as a useful way to functionalize aligned CNTs forest with dense Ni nanoparticles (Chapter 7).[132] The longer incubation time is needed in the CFD process of Ni thin film deposition from hydrogenolysis of Nicklocene without catalyst.

1.3. Atomic layer deposition and molecular layer deposition

For functional coating of inorganics including metals and metal oxides, the major deposition process is vacuum-based solvent-free techniques including physical vapor deposition (PVD),[26, 133] chemical vapor deposition (CVD)[134, 135] and atomic layer deposition (ALD). High quality film can be deposited through PVD process.[26, 133] However, PVD technique is not good for coating high aspect ratio structures and coating for complex structure materials because of the *line-of-sight* deposition angle issue. Moreover, it is difficult to form uniform conformal films over large scale.[26]

CVD can solve some problems that exist in PVD.[136-138] CVD can form conformal coverage film onto surface with complex structures.[139] During the typical CVD process, source molecules will be vaporized and transported to the substrates and react with other reagents such as H_2, O_2, H_2O_2, NH_3, etc to form metal, metal oxide or nitride films.[140] Plasma activation can be used to facilitate the deposition process.[141] CVD process has been widely used to coat functional materials,[140] for application in fields of electronics, optoelectronics, ferroelectrics, wear-resistant and corrosion-resistant application, fiber and powder applications and nanotechnologies.[20]

However as the dimensions of devices scale down, there is a need to deposit ultra thin conformal films at relatively lower temperature onto large substrate with complex structures. AS noted, tt is difficult for both CVD and PVD process to accomplish it.[14, 142-146] In addition, active materials that integrate different constituents at the molecular scale or multiple layers with well-controlled thickness and structures are growing in interest, for applications including hybrid semiconductors,[147] high surface area gas storage, and flexible gas transport barriers. For many applications such as optics,[148] photovoltaic cells,[4, 149]sensor systems,[150, 151] and nanogenerators,[152, 153] highly conformal coatings on high surface area structures, including fiber–based substrates,[150, 151, 153] enable three dimensional designs with function and strategic performance enhancement over typical planar or semi-planar constructs. In order to form functional materials thin coating onto substrates with desired properties, the coating layer needs to have the properties: conformity, uniform, precisely controlled thickness and no pin hole. For 3D substrates with highly complex structure, processes with self-limited deposition behavior, for example atomic layer deposition and

molecular layer deposition, are necessary to achieve conformal and uniform coating layer.[5]

1.3.1 Overview of atomic layer deposition

In the 1970s, atomic layer deposition (ALD) was developed by Dr. Suntola.[154] Most ALD processes consist of two self-limiting growth steps by alternating dose of chemical species onto the substrate as shown in Figure 1.3.[14, 28, 142, 143] The separation of two reactants reduces the possible gas phase reaction that can form particles to produce granular film, which is observed in CVD process. It is worthy to mention that: majority of ALD processes were carried out in gas phase, which eliminate the limitations from solvent process including capillary force, contamination from solvent and tedious washing steps. The gas phase reactants in ALD could also fill all substrate void space independent of substrate geometry and circumvent the requirement of line-of-sight to the substrate. In ALD process, the surface reaction will stop after consuming all of the reactive sites on the surface during the half cycle of each reactant. Because of this self-limiting characteristics, ALD process can satisfy the requirement of modern thin film deposition development to form highly conformal and uniform film with atomic level control on different structures with 3D complex geometries.[14, 143-146] Thin films of different materials, including metals,[14] metal oxides,[144, 145, 155-158] metal nitrides[14], have been readily deposited by ALD process. Combined with patterning techniques, ALD has been applied to deposit patterned thin films of Ru,[159] Rd[160] and Ir[161].

Although ALD was initially developed for applications in the field of electronic materials,[14, 143-146] ALD has been widely used to modify 3D substrates with high aspect ratio structures (such as anodic aluminum oxide,[162] silica,[163] carbon nanotube,[15, 16, 164, 165

biomolecules,[166] cotton[10, 167] and photonic crystal structures[17, 18]), with precisely controlled thickness andchemical and physical properties due to the self-limiting deposition behavior. The applications of ALD onto those 3D high aspect ratio structures have enabled applications in a variety of fields such as MEMS,[168, 169]optoelectronics,[170] nanofluidics,[171] biomedicine, nano-materials fabrication,[21, 172] energy[2, 4, 6] and catalyst[10, 12] .

1.3.2 Challenges and opportunities of atomic layer deposition

As a gas phase deposition process for inorganic materials, the chemistries of ALD are mainly adopted from chemical vapor deposition and solution based sol-gel chemistry. Compared with these two techniques, ALD offers the capability to deposit highly conformal and uniform film with precisely controlled film thickness as mentioned earlier.

Although wide range of materials could be deposited by ALD process, there are still desire for new ALD chemistry of novel important materials (such as Si, Ge, M_xTe, M_xSe).[142, 173] These new chemistries mainly rely on metal organic chemistry[142, 174, 175] and sol-gel chemistry [144, 176]development for suitable precursor and self-limiting process. Another challenge for ALD process is the low deposition rate (<500 nm/h),[142] which makes ALD process not suitable for thick film deposition (>1 μm), although there are some trials that have been made to solve this problem.[177, 178] Morever, the synthesis of a material with well controlled crystal stucture is still a big challenge for ALD process. Currently, the majority of ALD processes are carried out at temperature range from100 ˚C to 500 ˚C or above, which is not applicable for temperature sensitive materials. Low temperature ALD process of Al_2O_3,[21,22] ZnO,[179, 180] TiO_2[8] and TiN[24] opened opportunities for coating polymers and other

thermal sensitive molecules by reducing thermal damage. More low temperature ALD processes still need to be explored. Due to the expanding substrates used in ALD process, the nucleation and growth behavior of ALD films on different substrates is also a challenge. Moreover, for the ALD process of noble metals or other expensive materials, the utility of precursors is important and worth further study because it is critical for the practical applications. Although ALD is capable of forming conformal and uniform coatings onto some complex substrates in the current study range, further study is needed to confirm the conformality of ALD coating when applied onto extremely high aspect ratio structures with high surface area and small pore openings in large scale due to the limitations imposed by molecule diffusion in the very confined geometry.

The prospects of ALD process are very promising and encouraging. New chemistries are under development. Even with different challenges, ALD technique is finding its own unique fitting into different research and application fields including bio, energy and nanomaterial. For example, ALD could modify the surface chemical properties with nano/subnano meter coating to enable different novel functionalities.[2, 171] ALD applications in nanomaterials fabrication would enable people to explore the size dependable properties such as mechanics, electronics and magnetic.[181-183] As the application of ALD process expands into other fields, the corresponding materials properties need to be carefully characterized.

In this work, ALD has been applied to matrices of electrospun polymer fibers, which are complex three dimensional structures and thermal sensitive as shown in Figure 1.4, to form Al_2O_3, $Al_2O_3/ZnO/Al_2O_3$ nanolaminate coatings with smooth wall surfaces and

precisely controlled wall thickness. Nanostructure resulted from the coated fiber mat through different thermal treatment were studied.

1.3.3 Overview of molecular layer deposition

Molecular layer deposition (MLD) is a special extension of atomic layer deposition.[184-186] ALD is mainly used for inorganic material thin film fabrication, MLD process is mainly used to deposit thin film of organic polymeric materials and organic-inorganic hybrid materials. Vapor phase deposition (VPD) techniques have also been used for organic thin film deposition. Thin films of metal phthalocyanines,[187, 188] polymerized amino acids,[189] silanes,[190, 191] polypyrrole,[192] poly(Vinyliene fluoride),[193] poly(p-xylenes)[194] conjugated polymers[195] have been successfully formed by VPD. However, just as in inorganic PVD and CVD process, it is difficult for VPD process to form conformal coating with precisely controlled thickness onto substrates with 3D complex structure on large scale.

The concept of molecular layer deposition is shown in Figure 1.5.[196] Reactants A and B with multiple functionalities will be exposed to the substrate, which has active sites on the surface, alternatively and cyclically. Between each dosing of reactants, a purging step was used to remove excess precursors and byproducts. By repeating this process, -A-B-A-B- type polymer thin films can be formed onto the substrate. Due to the intrinsic self-limiting deposition behavior, MLD is becoming critical in advanced materials development in order to achieve better chemical, structure and film thickness control over large scale for organic and hybrid materials than many current processes such as CVD, PVD and solvent based techniques. Currently, several different types of polymer thin films have been formed through the stepwise polymerization chemistry by MLD, such as polyamide,[197,

[198]polyimide,[185, 186, 199-202] polyurea[185] and polyester[185].

Hybrid materials (metal organic framework and coordination polymers) have unique properties. However, it is difficult to organize them into thin nanoscale coatings.[203-205] Recently MLD has been extended to fabricate hybrid materials. For example, Nilsen et. al.[184, 206] have studied the molecular layer deposition of different hybrid materials with a range of bi-functional and tri-functional carboxylic acids (including oxylic acid, malanic acid, 1,4 benzene dicarboxylic acid and 1,2 benzene dicarboxylic acid etc) and trimethyl aluminum in MLD process. Dameron et al.[207] reported several diols (ethylene glycol, 1,4 butane diol,1,4 phenyl diol) with TMA (Trimethyl aluminum), and they found that the bifunctional organics produce a "double reaction" (i.e. both ends of the organic species with the Al–CH_3 terminated surface). Kim et al.[208] have examined ethylene diamine reactions with diisocyante in a UHV (Ultra High Vacuum) reactor system, and they have also seen evidence for the "double reaction" that impedes film growth. Lee et al[209-211] formed a Ti-based and Al- based hybrid film using an ozone exposure step to activate an alkane monolayer, followed by Ti and Al precursor exposure.

Several other early reports[103, 186, 196-198, 202, 212] also present work on polymer MLD processes, with few details regarding film reaction mechanisms. Du and his coworks[213] have studied surface reactions involved in polyamide deposition from acid chloride bifunctional organics and various diamines. Similar surface reactions were investigated by Adamczyk [214] to form poly-phenyl amide films. More complex "A–B–C" reaction chemistries[184] have also been presented using repeating cycles of trimethylaluminum, followed by ethanolamine, then maleic anhydride. Film growth was achieved, but the rates suggested that additional growth

mechanisms were active which promoted excess film growth. Moreover different new chemistries are explored for MLD process.[184]

1.3.4 Challenges and opportunities in molecular layer deposition

The surface chemistries (organic chemistry, coordinating chemistry, polymerization chemistry) involved in molecular layer deposition were mainly studied in solvent-based processes. Although some experiments have been carried out in vacuum-based MLD growth mode for polymers and hybrids, these research are still in their infancy compared with solvent-based process. There are several challenges involved in the MLD process. First of all, due to the vacuum-based process, the organic reactants involved in the MLD process have to have adequate vapor pressure under the reaction temperature in order to get enough reactant into the reactor. Generally one could increase vapor pressure by increasing reaction temperature. However due to the thermal instability of the organic reactants, they would decompose above certain temperature. Moreover at high reaction temperature, the adhesive force between the substrate and reactant will decrease, which will result in decreased growth rate. Second of all, the reaction rate between the two reactants needs to be fast. According to the MLD scheme, it is almost impossible, at least practically, to keep the reactants in the chamber for hours in order to get one monolayer saturated reaction in the MLD process. Of course the reaction rate could be speed up by increasing reaction temperature, but again the room for temperature increase is limited by the thermal decomposition property of the organic monomers and the resulted products. Third of all, majority of the reaction of organic chemistry needs catalysts. It is difficult to perform catalysis reaction under gas phase in the MLD process. Fourth of all, the solvent effect in the solvent-based process, which is crucial

for the reaction rate and reaction path way, is absent in the vacuum-based process. Moreover, the solvent in solution-based processes provide a three dimensional growth environment so that complex three dimensional porous and hybrid materials can be fabricated. This three dimensional growth environment is absent for MLD process due to the self-limited two dimensional growth mode.

Nevertheless, there is a still bright future for MLD processing. For instance, organic-inorganic materials with controlled interface chemistry, thickness, chemical properties and physical properties can be synthesized by using MLD and ALD process together. These novel organic-inorganic materials would be equipped with advanced properties, many of which are undetermined to date. The MLD process is a promising technique for fabricating polymer and hybrid materials into conformal and uniform film with controlled properties. By carefully manipulating with molecular force, thermal dynamics, lattice properties, it is possible to synthesize high aligned and organized crystals of polymer and hybrid materials. Moreover, due to the cleaner and simplified environment in vacuum, it is easier to explore the underlying surface chemistry for the reactions.

In this work, the *in-situ* techniques including quartz crystal microbalance (QCM) and Fourier transform infrared (FT-IR) spectroscopy are used to explore the surface reaction mechanism involved in the hybrid material MLD process. In particular the transition from metal oxide ALD to metal hybrid MLD is studied carefully. Different techniques including X-ray Diffraction and Near Edge X-ray Absorption Fine Structure were employed to explore the molecular structures of the depositions. The resulted molecular structure of the resulted hybrid materials and the deposition behavior of self-assembly monolayer on the ALD metal

oxides by MLD were also studied.

REFERENCES

1. Taylor, A. D.; Michel, M.; Sekol, R. C.; Kizuka, J. M.; Kotov, N. A.; Thompson, L. T., *Advanced Functional Materials* **18,** 3003-3009 (2008).
2. Martinson, A. B. F.; Elam, J. W.; Liu, J.; Pellin, M. J.; Marks, T. J.; Hupp, J. T., *Nano Letters* **8,** 2862-2866 (2008).
3. Hamann, T. W.; Martinson, A. B. F.; Elam, J. W.; Pellin, M. J.; Hupp, J. T., *Journal of Physical Chemistry C* **112,** 10303-10307 (2008).
4. Hamann, T. W.; Martinson, A. B. E.; Elam, J. W.; Pellin, M. J.; Hupp, J. T., *Advanced Materials* **20,** 1560-+ (2008).
5. Rolison, D. R.; Long, R. W.; Lytle, J. C.; Fischer, A. E.; Rhodes, C. P.; McEvoy, T. M.; Bourga, M. E.; Lubers, A. M., *Chemical Society Reviews* **38,** 226-252 (2009).
6. Law, M.; Greene, L. E.; Radenovic, A.; Kuykendall, T.; Liphardt, J.; Yang, P. D., *Journal of Physical Chemistry B* **110,** 22652-22663 (2006).
7. Lee, J.; Cuddihy, M. J.; Kotov, N. A., *Tissue Engineering Part B-Reviews* **14,** 61-86 (2008).
8. Tang, Z. Y.; Wang, Y.; Podsiadlo, P.; Kotov, N. A., *Advanced Materials* **18,** 3203-3224 (2006).
9. Huang, J. G.; Ichinose, I.; Kunitake, T., *Angewandte Chemie-International Edition* **45,** 2883-2886 (2006).
10. Kemell, M.; Pore, V.; Ritala, M.; Leskela, M.; Linden, M., *Journal of the American Chemical Society* **127,** 14178-14179 (2005).
11. Baiker, A., *Chemical Reviews* **99,** 453-473 (1999).

12. King, J. S.; Wittstock, A.; Biener, J.; Kucheyev, S. O.; Wang, Y. M.; Baumann, T. F.; Giri, S. K.; Hamza, A. V.; Baeumer, M.; Bent, S. F., *Nano Letters* **8,** 2405-2409 (2008).

13. Javey, A.; Kim, H.; Brink, M.; Wang, Q.; Ural, A.; Guo, J.; McIntyre, P.; McEuen, P.; Lundstrom, M.; Dai, H. J., *Nature Materials* **1,** 241-246 (2002).

14. Kim, H., *Journal Of Vacuum Science & Technology B* **21,** 2231-2261 (2003).

15. Kim, H.; McIntyre, P. C., *Journal Of The Korean Physical Society* **48,** 5-17 (2006).

16. Farmer, D. B.; Gordon, R. G., *Nano Letters* **6,** 699-703 (2006).

17. King, J. S.; Graugnard, E.; Summers, C. J., *Advanced Materials* **17,** 1010-+ (2005).

18. King, J. S.; Neff, C. W.; Summers, C. J.; Park, W.; Blomquist, S.; Forsythe, E.; Morton, D., *Applied Physics Letters* **83,** 2566-2568 (2003).

19. King, J. S.; Heineman, D.; Graugnard, E.; Summers, C. J. In *Atomic layer deposition in porous structures: 3D photonic crystals*, 2005; 2005; pp 511-516.

20. Xia, Y. N.; Yang, P. D.; Sun, Y. G.; Wu, Y. Y.; Mayers, B.; Gates, B.; Yin, Y. D.; Kim, F.; Yan, Y. Q., *Advanced Materials* **15,** 353-389 (2003).

21. Jeong, D.; Lee, J.; Shin, H.; Lee, J.; Kim, J.; Sung, M., *Journal Of The Korean Physical Society* **45,** 1249-1252 (2004).

22. Forrest, S. R., *Chemical Reviews* **97,** 1793-1896 (1997).

23. Bain, C. D.; Troughton, E. B.; Tao, Y. T.; Evall, J.; Whitesides, G. M.; Nuzzo, R. G., *Journal of the American Chemical Society* **111,** 321-335 (1989).

24. Hammond, P. T., *Advanced Materials* **16,** 1271-1293 (2004).

25. Hench, L. L.; West, J. K., *Chemical Reviews* **90,** 33-72 (1990).

26. Mahan, J. E.*, Physical vapor deposition of thin films,* Wiley, New York (2000).

27. Parsons, G. N.*, Integrated Molecular Layer deposition and atomic layer deposition of organic and inorganic thin films*, NSF Proposal (2006).

28. Gordon, R. G., *Abstracts Of Papers Of The American Chemical Society* **227,** U553-U554 (2004).

29. Sanchez, C.; Ribot, F., *New Journal of Chemistry* **18,** 1007-1047 (1994).

30. Livage, J.; Henry, M.; Sanchez, C., *Progress in Solid State Chemistry* **18,** 259-341 (1988).

31. Zasadzinski, J. A.; Viswanathan, R.; Madsen, L.; Garnaes, J.; Schwartz, D. K., *Science* **263,** 1726-1733 (1994).

32. Drury, C. J.; Mutsaers, C. M. J.; Hart, C. M.; Matters, M.; de Leeuw, D. M., *Applied Physics Letters* **73,** 108-110 (1998).

33. Andricacos, P. C.; Arana, C.; Tabib, J.; Dukovic, J.; Romankiw, L. T., *Journal Of The Electrochemical Society* **136,** 1336-1340 (1989).

34. Ichinose, I.; Senzu, H.; Kunitake, T., *Chemistry of Materials* **9,** 1296-& (1997).

35. Brunner, H.; Vallant, T.; Mayer, U.; Hoffmann, H., *Langmuir* **12,** 4614-4617 (1996).

36. Tillman, N.; Ulman, A.; Penner, T. L., *Langmuir* **5,** 101-111 (1989).

37. Decher, G.; Lehr, B.; Lowack, K.; Lvov, Y.; Schmitt, J., *Biosensors & Bioelectronics* **9,** 677-684 (1994).

38. Decher, G.; Hong, J. D., *Berichte Der Bunsen-Gesellschaft-Physical Chemistry Chemical Physics* **95,** 1430-1434 (1991).

39. Decher, G.; Hong, J. D., *Makromolekulare Chemie-Macromolecular Symposia* **46,** 321-327 (1991).

40. Decher, G., *Science* **277,** 1232-1237 (1997).

41. Sullivan, D. M.; Bruening, M. L., *Chemistry Of Materials* **15,** 281-287 (2003).

42. Levasalmi, J. M.; McCarthy, T. J., *Macromolecules* **30,** 1752-1757 (1997).

43. Stanton, B. W.; Harris, J. J.; Miller, M. D.; Bruening, M. L., *Langmuir* **19,** 7038-7042 (2003).

44. Farhat, T. R.; Schlenoff, J. B., *Langmuir* **17,** 1184-1192 (2001).

45. Constantine, C. A.; Gattas-Asfura, K. M.; Mello, S. V.; Crespo, G.; Rastogi, V.; Cheng, T. C.; DeFrank, J. J.; Leblanc, R. M., *Langmuir* **19,** 9863-9867 (2003).

46. Constantine, C. A.; Mello, S. V.; Dupont, A.; Cao, X. H.; Santos, D.; Oliveira, O. N.; Strixino, F. T.; Pereira, E. C.; Cheng, T. C.; Defrank, J. J.; Leblanc, R. M., *Journal Of The American Chemical Society* **125,** 1805-1809 (2003).

47. Yu, A. M.; Liang, Z. J.; Cho, J. H.; Caruso, F., *Nano Letters* **3,** 1203-1207 (2003).

48. Liu, S. Q.; Kurth, D. G.; Mohwald, H.; Volkmer, D., *Advanced Materials* **14,** 225-+ (2002).

49. DeLongchamp, D.; Hammond, P. T., *Advanced Materials* **13,** 1455-+ (2001).

50. DeLongchamp, D. M.; Hammond, P. T., *Langmuir* **20,** 5403-5411 (2004).

51. Mamedov, A. A.; Kotov, N. A.; Prato, M.; Guldi, D. M.; Wicksted, J. P.; Hirsch, A., *Nature Materials* **1,** 190-194 (2002).

52. Choi, J. Y.; Rubner, M. F., *Journal Of Macromolecular Science-Pure And Applied Chemistry* **38,** 1191-1206 (2001).

53. Liang, Z. J.; Susha, A. S.; Yu, A. M.; Caruso, F., *Advanced Materials* **15,** 1849-1853 (2003).

54. Jiang, X. P.; Hammond, P. T., *Langmuir* **16,** 8501-8509 (2000).

55. Clark, S. L.; Hammond, P. T., *Advanced Materials* **10,** 1515-+ (1998).

56. Clark, S. L.; Montague, M. F.; Hammond, P. T., *Macromolecules* **30,** 7237-7244 (1997).

57. Yin, A. J.; Li, J.; Jian, W.; Bennett, A. J.; Xu, J. M., *Applied Physics Letters* **79,** 1039-1041 (2001).

58. Prieto, A. L.; Sander, M. S.; Martin-Gonzalez, M. S.; Gronsky, R.; Sands, T.; Stacy, A. M., *Journal Of The American Chemical Society* **123,** 7160-7161 (2001).

59. Moffat, T. P.; Bonevich, J. E.; Huber, W. H.; Stanishevsky, A.; Kelly, D. R.; Stafford, G. R.; Josell, D., *Journal Of The Electrochemical Society* **147,** 4524-4535 (2000).

60. Nielsch, K.; Muller, F.; Li, A. P.; Gosele, U., *Advanced Materials* **12,** 582-586 (2000).

61. Pauporte, T.; Lincot, D., *Applied Physics Letters* **75,** 3817-3819 (1999).

62. Shirkhanzadeh, M., *Journal Of Materials Science Letters* **10,** 1415-1417 (1991).

63. Kost, K. M.; Bartak, D. E.; Kazee, B.; Kuwana, T., *Analytical Chemistry* **60,** 2379-2384 (1988).

64. Matsushita, M.; Sano, M.; Hayakawa, Y.; Honjo, H.; Sawada, Y., *Physical Review Letters* **53,** 286-289 (1984).

65. Higashi, K.; Fukushima, H.; Urakawa, T.; Adaniya, T.; Matsudo, K., *Journal Of The Electrochemical Society* **128,** 2081-2085 (1981).

66. Cheh, H. Y., *Journal Of The Electrochemical Society* **118,** 551-& (1971).

67. Beck, F., *Electrochimica Acta* **33,** 839-850 (1988).

68. Beck, F.; Oberst, M., *Makromolekulare Chemie-Macromolecular Symposia* **8,** 97-125 (1987).

69. Asavapiriyanont, S.; Chandler, G. K.; Gunawardena, G. A.; Pletcher, D., *Journal Of Electroanalytical Chemistry* **177,** 229-244 (1984).

70. Andricacos, P. C.; Uzoh, C.; Dukovic, J. O.; Horkans, J.; Deligianni, H., *Ibm Journal Of Research And Development* **42,** 567-574 (1998).

71. Zach, M. P.; Ng, K. H.; Penner, R. M., *Science* **290,** 2120-2123 (2000).

72. Thurn-Albrecht, T.; Schotter, J.; Kastle, C. A.; Emley, N.; Shibauchi, T.; Krusin-Elbaum, L.; Guarini, K.; Black, C. T.; Tuominen, M. T.; Russell, T. P., *Science* **290,** 2126-2129 (2000).

73. Routkevitch, D.; Bigioni, T.; Moskovits, M.; Xu, J. M., *Journal Of Physical Chemistry* **100,** 14037-14047 (1996).

74. Cabanas, A.; Long, D. P.; Watkins, J. J., *Chemistry Of Materials* **16,** 2028-2033 (2004).

75. Cabanas, A.; Shan, X. Y.; Watkins, J. J., *Chemistry Of Materials* **15,** 2910-2916 (2003).

76. Cansell, F.; Aymonier, C.; Loppinet-Serani, A., *Current Opinion In Solid State & Materials Science* **7,** 331-340 (2003).

77. Cansell, F.; Chevalier, B.; Demourgues, A.; Etourneau, J.; Even, C.; Garrabos, Y.; Pessey, V.; Petit, S.; Tressaud, A.; Weill, F., *Journal Of Materials Chemistry* **9,** 67-75 (1999).

78. Hansen, B. N.; Hybertson, B. M.; Barkley, R. M.; Sievers, R. E., *Chemistry Of Materials* **4,** 749-752 (1992).

79. Kondoh, E., *Japanese Journal Of Applied Physics Part 1-Regular Papers Short Notes & Review Papers* **43,** 3928-3933 (2004).

80. Kondoh, E.; Kato, H., *Microelectronic Engineering* **64,** 495-499 (2002).

81. Kondoh, E.; Shigama, K., *Thin Solid Films* **491,** 228-234 (2005).

82. Long, D. P.; Blackburn, J. M.; Watkins, J. J., *Advanced Materials* **12,** 913-915 (2000).

83. Sun, Z. Y.; Yuan, H. Q.; Liu, Z. M.; Han, B. X.; Zhang, X. R., *Advanced Materials* **17,** 2993-+ (2005).

84. Pai, R. A.; Watkins, J. J., *Abstracts Of Papers Of The American Chemical Society* **225,** U136-U136 (2003).

85. Jones, C. A.; Zweber, A.; DeYoung, J. P.; McClain, J. B.; Carbonell, R.; DeSimone, J. M., *Critical Reviews In Solid State And Materials Sciences* **29,** 97-109 (2004).

86. Gougousi, T.; Barua, D.; Young, E. D.; Parsons, G. N., *Chemistry Of Materials* **17,** 5093-5100 (2005).

87. Barua, D.; Gougousi, T.; Young, E. D.; Parsons, G. N., *Applied Physics Letters* **88,** (2006).

88. Darr, J. A.; Poliakoff, M., *Chemical Reviews* **99,** 495-541 (1999).

89. O'Neil, A.; Watkins, J. J., *MRS Bulletin* **30,** 967-975 (2005).

90. Blackburn, J. M.; Long, D. P.; Cabanas, A.; Watkins, J. J., *Science* **294,** 141-145 (2001).

91. Xiang R. Yea, C. M. W., Yuehe Linb, James S. Young, Mark H. Engelhard, *Surface & Coatings Technology* **190,** 25-31 (2005).

92. Zong, Y. F.; Watkins, J. J., *Chemistry Of Materials* **17,** 560-565 (2005).

93. Watkins, J. J.; Blackburn, J. M.; McCarthy, T. J., *Chemistry Of Materials* **11,** 213-215 (1999).

94. Hunde, E. T.; Watkins, J. J., *Chemistry Of Materials* **16,** 498-503 (2004).

95. Fu, L.; Liu, Z. M.; Liu, Y. Q.; Han, B. X.; Hu, P. G.; Cao, L. C.; Zhu, D. B., *Advanced Materials* **17,** 217-+ (2005).

96. Wang, X. B.; Liu, Z. M.; Hu, P. A.; Liu, Y. Q.; Han, B. X.; Zhu, D. B., *Applied Physics A-Materials Science & Processing* **80,** 637-639 (2005).

97. Fu, L.; Liu, Z. M.; Liu, Y. Q.; Han, B. X.; Wang, J. Q.; Hu, P. G.; Cao, L. C.; Zhu, D. B., *Journal Of Physical Chemistry B* **108,** 13074-13078 (2004).

98. Pai, R. A.; Watkins, J. J., *Advanced Materials* **18,** 241-+ (2006).

99. Pai, R. A.; Humayun, R.; Schulberg, M. T.; Sengupta, A.; Sun, J. N.; Watkins, J. J., *Science* **303,** 507-510 (2004).

100. Hiroshi Uchida, A. O., Kiyoshi Itatani and Seiichiro Koda, *Japanese Journal of Applied Physics* **44,** 1901-1906 (2005).

101. Gallyamov, M. O.; Vinokur, R. A.; Nikitin, L. N.; Said-Galiyev, E. E.; Khokhlov, A. R.; Yaminsky, I. V.; Schaumburg, K., *Langmuir* **18,** 6928-6934 (2002).

102. Puniredd, S. R.; Srinivasan, M. P., *Langmuir* **21,** 7812-7822 (2005).

103. Zhang, F.; Jia, Z.; Srinivasan, M. P., *Langmuir* **21,** 3389-3395 (2005).

104. Puniredd, S. R.; Srinivasan, M. P., *Langmuir* **22,** 4092-4099 (2006).

105. Kim, J.; Carbonell, R. G., *Langmuir* **22,** 2117-2129 (2006).

106. Kim, J.; Novick, B. J.; DeSimone, J. M.; Carbonell, R. G., *Langmuir* **22,** 642-657 (2006).

107. Cao, C. T.; Fadeev, A. Y.; McCarthy, T. J., *Langmuir* **17,** 757-761 (2001).

108. Domingo, C.; Loste, E.; Fraile, J., *Journal Of Supercritical Fluids* **37,** 72-86 (2006).

109. Luscombe, C. K.; Li, H. W.; Huck, W. T. S.; Holmes, A. B., *Langmuir* **19,** 5273-5278 (2003).

110. Visintin, P. M.; Carbonell, R. G.; Schauer, C. K.; DeSimone, J. M., *Langmuir* **21,** 4816-4823 (2005).

111. Gu, W.; Tripp, C. P., *Langmuir* **22,** 5748-5752 (2006).

112. Jia, X. Q.; McCarthy, T. J., *Langmuir* **18,** 683-687 (2002).

113. Caskey, T.; Lesser, A. J.; McCarthy, T. J., *Polymer Engineering And Science* **41,** 2259-2265 (2001).

114. Jia, X. Q.; McCarthy, T. J., *Abstracts Of Papers Of The American Chemical Society* **220,** U273-U273 (2000).

115. Zemanian, T. S.; Fryxell, G. E.; Liu, J.; Mattigod, S.; Franz, J. A.; Nie, Z. M., *Langmuir* **17,** 8172-8177 (2001).

116. Crowley, T. A.; Ziegler, K. J.; Lyons, D. M.; Erts, D.; Olin, H.; Morris, M. A.; Holmes, J. D., *Chemistry Of Materials* **15,** 3518-3522 (2003).

117. Ye, X. R.; Lin, Y. H.; Wang, C. M.; Wai, C. M., *Advanced Materials* **15,** 316-319 (2003).

118. Watkins, J. J.; McCarthy, T. J., *Chemistry Of Materials* **7,** 1991-& (1995).

119. Watkins, J. J.; McCarthy, T. J., *Abstracts Of Papers Of The American Chemical Society* **210,** 84-PMSE (1995).

120. Watkins, J. J.; McCarthy, T. J., *Abstracts Of Papers Of The American Chemical Society* **208,** 97-POLY (1994).

121. Yoda, S.; Takebayashi, Y.; Sugeta, T.; Otake, K., *Journal Of Non-Crystalline Solids* **350,** 320-325 (2004).

122. Ohde, H.; Ohde, M.; Wai, C. M., *Chemical Communications***,** 930-931 (2004).

123. Tomasko, D. L.; Han, X. M.; Liu, D. H.; Gao, W. H., *Current Opinion In Solid State & Materials Science* **7,** 407-412 (2003).

124. Cooper, A. I., *Advanced Materials* **15,** 1049-1059 (2003).

125. Morley, K. S.; Marr, P. C.; Webb, P. B.; Berry, A. R.; Allison, F. J.; Moldovan, G.; Brown, P. D.; Howdle, S. M., *Journal Of Materials Chemistry* **12,** 1898-1905 (2002).

126. Corbierre, M. K.; Cameron, N. S.; Sutton, M.; Mochrie, S. G. J.; Lurio, L. B.; Ruhm, A.; Lennox, R. B., *Journal Of The American Chemical Society* **123,** 10411-10412 (2001).

127. Green, J. W.; Rubal, M. J.; Osman, B. M.; Welsch, R. L.; Cassidy, P. E.; Fitch, J. W.; Blanda, M. T., *Polymers For Advanced Technologies* **11,** 820-825 (2000).

128. Rosolovsky, J.; Boggess, R. K.; Rubira, A. F.; Taylor, L. T.; Stoakley, D. M.; StClair, A. K., *Journal Of Materials Research* **12,** 3127-3133 (1997).

129. Watkins, J. J.; McCarthy, T. J., *Macromolecules* **27,** 4845-4847 (1994).

130. Peng, Q.; Hojo, D.; Park, K. J.; Parsons, G. N., *Thin Solid Films* **516,** 4997-5003 (2008).

131. Peng, Q.; Spagnola, J. C.; Daisuke, H.; Park, K. J.; Parsons, G. N., *Journal of Vacuum Science & Technology B* **26,** 978-982 (2008).

132. Peng, Q.; Spagnola, J. C.; Parsons, G. N., *Journal of the Electrochemical Society* **155,** D580-D582 (2008).

133. Mattox, D. M., *Handbook of physical vapor deposition (PVD) processing* Noyes Publications: Westwood, N.J. , 1998.

134. Koh, W.; Ku, S. J.; Kim, Y., *Thin Solid Films* **304,** 222-224 (1997).

135. Hampden-smith, T. T. K. a. M. J., *The Chemistry of Metal CVD*. 1 ed.; VCH Weinheim; New York; Basel; Cambridge; Tokyo, 1994.

136. Hampdensmith, M. J.; Kodas, T. T., *Chemical Vapor Deposition* **1,** 8-23 (1995).

137. Spencer, J. T., Chemical-Vapor-Deposition Of Metal-Containing Thin-Film Materials From Organometallic Compounds. In *Progress In Inorganic Chemistry, Vol 41*, 1994; Vol. 41, pp 145-237.

138. Ludowise, M. J., *Journal Of Applied Physics* **58,** R31-R55 (1985).

139. Gladfelter, W. L., *Chemistry Of Materials* **5,** 1372-1388 (1993).

140. Pierson, H. O., *Handbook of chemical vapor deposition*. Noyes Publications: Norwich, 1999.

141. Jasinski, J. M.; Meyerson, B. S.; Scott, B. A., *Annual Review Of Physical Chemistry* **38,** 109-140 (1987).

142. Leskela, M.; Ritala, M., *Angewandte Chemie-International Edition* **42,** 5548-5554 (2003).

143. Leskela, M.; Ritala, M., *Thin Solid Films* **409,** 138-146 (2002).

144. Ritala, M.; Kukli, K.; Rahtu, A.; Raisanen, P. I.; Leskela, M.; Sajavaara, T.; Keinonen, J., *Science* **288,** 319-321 (2000).

145. Ritala, M.; Leskela, M.; Dekker, J. P.; Mutsaers, C.; Soininen, P. J.; Skarp, J., *Chemical Vapor Deposition* **5,** 7-9 (1999).

146. George, S. M.; Ott, A. W.; Klaus, J. W., *Journal Of Physical Chemistry* **100,** 13121-13131 (1996).

147. Mitzi, D. B.; Chondroudis, K.; Kagan, C. R., *Ibm Journal of Research and Development* **45,** 29-45 (2001).

148. Wang, J. J.; Deng, X. G.; Varghese, R.; Nikolov, A.; Sciortino, P.; Liu, F.; Chen, L.; Liu, X. M., *Journal of Vacuum Science and Technology B* **23,** 3209-3213 (2005).

149. Martinson, A. B. F.; Elam, J. W.; Hupp, J. T.; Pellin, M. J., *Nano Letters* **7,** 2183-2187 (2007).

150. Shim, B. S.; Chen, W.; Doty, C.; Xu, C. L.; Kotov, N. A., *Nano Letters* **8,** 4151-4157 (2008).

151. Virji, S.; Kojima, R.; Fowler, J. D.; Villanueva, J. G.; Kaner, R. B.; Weiller, B. H., *Nano Res* **2,** 135-142 (2009).

152. Wang, X. D.; Song, J. H.; Liu, J.; Wang, Z. L., *Science* **316,** 102-105 (2007).

153. Qin, Y.; Wang, X. D.; Wang, Z. L., *Nature* **451,** 809-U5 (2008).

154. T. Suntola, J. A., *U.S. Patent 4,057,430,* (1977).

155. Ritala, M.; Leskela, M.; Niinisto, L.; Haussalo, P., *Chemistry Of Materials* **5,** 1174-1181 (1993).

156. Sang, B. S.; Yamada, A.; Konagai, M., *Japanese Journal Of Applied Physics Part 2-Letters* **37,** L206-L208 (1998).

157. Ritala, M.; Leskela, M.; Nykanen, E.; Soininen, P.; Niinisto, L., *Thin Solid Films* **225,** 288-295 (1993).

158. George, S. M.; Sneh, O.; Dillon, A. C.; Wise, M. L.; Ott, A. W.; Okada, L. A.; Way, J. D., *Applied Surface Science* **82-3,** 460-467 (1994).

159. Park, K. J.; Doub, J. M.; Gougousi, T.; Parsons, G. N., *Applied Physics Letters* **86,** (2005).

160. Park, K. J.; Parsons, G. N., *Applied Physics Letters* **89,** (2006).

161. Farm, E.; Kemell, M.; Ritala, M.; Leskela, M., *Chemical Vapor Deposition* **12,** 415-+ (2006).

162. Elam, J. W.; Routkevitch, D.; Mardilovich, P. P.; George, S. M., *Chemistry Of Materials* **15,** 3507-3517 (2003).

163. de Rouffignac, P.; Li, Z. W.; Gordon, R. G., *Electrochemical And Solid State Letters* **7,** G306-G308 (2004).

164. Farmer, D. B.; Gordon, R. G., *Electrochemical And Solid State Letters* **8,** G89-G91 (2005).

165. Javey, A.; Guo, J.; Farmer, D. B.; Wang, Q.; Yenilmez, E.; Gordon, R. G.; Lundstrom, M.; Dai, H. J., *Nano Letters* **4,** 1319-1322 (2004).

166. Knez, M.; Kadri, A.; Wege, C.; Gosele, U.; Jeske, H.; Nielsch, K., *Nano Letters* **6,** 1172-1177 (2006).

167. Hyde, G. K.; Park, K. J.; Stewart, S. M.; Hinestroza, J. P.; Parsons, G. N., *Langmuir* **23,** 9844-9849 (2007).

168. Mayer, T. M.; Elam, J. W.; George, S. M.; Kotula, P. G.; Goeke, R. S., *Applied Physics Letters* **82,** 2883-2885 (2003).

169. Hoivik, N. D.; Elam, J. W.; Linderman, R. J.; Bright, V. M.; George, S. M.; Lee, Y. C. In *Atomic layer deposited protective coatings for micro-electromechanical systems*, 2003; 2003; pp 100-108.

170. Niinisto, L.; Paivasaari, J.; Niinisto, J.; Putkonen, M.; Nieminen, M., *Physica Status Solidi a-Applied Research* **201,** 1443-1452 (2004).

171. Chen, P.; Mitsui, T.; Farmer, D. B.; Golovchenko, J.; Gordon, R. G.; Branton, D., *Nano Letters* **4,** 1333-1337 (2004).

172. Ras, R. H. A.; Kemell, M.; de Wit, J.; Ritala, M.; ten Brinke, G.; Leskela, M.; Ikkala, O., *Advanced Materials* **19,** 102-+ (2007).

173. Pore, V.; Hatanpaa, T.; Ritala, M.; Leskela, M., *Journal of the American Chemical Society* **131,** 3478-+ (2009).

174. Lim, B. S.; Rahtu, A.; Gordon, R. G., *Nature Materials* **2,** 749-754 (2003).

175. Hoffmann, H., *Angewandte Chemie-International Edition* **48,** 2457-2459 (2009).

176. Mutin, P. H.; Vioux, A., *Chemistry of Materials* **21,** 582-596 (2009).

177. Hausmann, D.; Becker, J.; Wang, S. L.; Gordon, R. G., *Science* **298,** 402-406 (2002).

178. Burton, B. B.; Boleslawski, M. P.; Desombre, A. T.; George, S. M., *Chemistry of Materials* **20,** 7031-7043 (2008).

179. Lee, S. M.; Pippel, E.; Gosele, U.; Dresbach, C.; Qin, Y.; Chandran, C. V.; Brauniger, T.; Hause, G.; Knez, M., *Science* **324,** 488-492 (2009).

180. Peng, Q.; Sun, X. Y.; Spagnola, J. C.; Hyde, G. K.; Spontak, R. J.; Parsons, G. N., *Nano Letters* **7,** 719-722 (2007).

181. Nazzal, A.; Fu, H. X., *Journal of Computational and Theoretical Nanoscience* **6,** 1277-1289 (2009).

182. Luo, M.; Cheng, K.; Weng, W. J.; Song, C. L.; Du, P. Y.; Shen, G.; Xu, G.; Han, G. R., *Journal of Physics D-Applied Physics* **42,** (2009).

183. Napierska, D.; Thomassen, L. C. J.; Rabolli, V.; Lison, D.; Gonzalez, L.; Kirsch-Volders, M.; Martens, J. A.; Hoet, P. H., *Small* **5,** 846-853 (2009).

184. George, S. M.; Yoon, B.; Dameron, A. A., *Accounts of Chemical Research* **42,** 498-508 (2009).

185. Kubono, A.; Okui, N., *Progress In Polymer Science* **19,** 389-438 (1994).

186. Bitzer, T.; Richardson, N. V., *Applied Physics Letters* **71,** 662-664 (1997).

187. Back, G.; Hanada, T.; Yoshida, Y.; Takiguchi, H.; Abe, K.; Tanigaki, N.; Yase, Y., *Molecular Crystals And Liquid Crystals* **327,** 147-152 (1999).

188. Schlettwein, D.; Hesse, K.; Tada, H.; Mashiko, S.; Storm, U.; Binder, J., *Chemistry Of Materials* **12,** 989-995 (2000).

189. Chang, Y. C.; Frank, C. W., *Langmuir* **14,** 326-334 (1998).

190. Petri, D. F. S.; Wenz, G.; Schunk, P.; Schimmel, T., *Langmuir* **15,** 4520-4523 (1999).

191. Heiney, P. A.; Gruneberg, K.; Fang, J. Y.; Dulcey, C.; Shashidhar, R., *Langmuir* **16,** 2651-2657 (2000).

192. Mohammadi, A.; Hasan, M. A.; Liedberg, B.; Lundstrom, I.; Salaneck, W. R., *Synthetic Metals* **14,** 189-197 (1986).

193. Takeno, A.; Okui, N.; Hiruma, T.; Muraoka, M.; Umemoto, S.; Sakai, T., *Kobunshi Ronbunshu* **48,** 405-410 (1991).

194. Simon, P.; Mang, S.; Hasenhindl, A.; Gronski, W.; Greiner, A., *Macromolecules* **31,** 8775-8780 (1998).

195. Senkevich, J. J.; Woods, B. W.; Carrow, B. P.; Geil, R. D.; Rogers, B. R., *Chemical Vapor Deposition* **12,** 285-289 (2006).

196. Yoshimura, T.; Tatsuura, S.; Sotoyama, W., *Applied Physics Letters* **59,** 482-484 (1991).

197. Shao, H. L.; Umemoto, S.; Okui, N., *Abstracts Of Papers Of The American Chemical Society* **214,** 301-POLY (1997).

198. Shao, H. I.; Umemoto, S.; Kikutani, T.; Okui, N., *Polymer* **38,** 459-462 (1997).

199. Yoshimura, T.; Ito, S.; Nakayama, T.; Matsumoto, K., *Applied Physics Letters* **91,** (2007).

200. Yoshimura, T.; Terasawa, N.; Kazama, H.; Naito, Y.; Suzuki, Y.; Asama, K., *Thin Solid Films* **497,** 182-184 (2006).

201. Haq, S.; Richardson, N. V., *Journal of Physical Chemistry B* **103,** 5256-5265 (1999).

202. Bitzer, T.; Richardson, N. V., *Applied Surface Science* **145,** 339-343 (1999).

203. Szelagowska-Kunstman, K.; Cyganik, P.; Goryl, M.; Zacher, D.; Puterova, Z.; Fischer, R. A.; Szymonski, M., *Journal of the American Chemical Society* **130,** 14446-+ (2008).

204. Yoo, Y.; Jeong, H. K., *Chemical Communications*, 2441-2443 (2008).

205. Amezcua-Correa, A.; Yang, J.; Finlayson, C. E.; Peacock, A. C.; Hayes, J. R.; Sazio, P. J. A.; Baumberg, J. J.; Howdle, S. M., *Advanced Functional Materials* **17,** 2024-2030 (2007).

206. Peng, Q.; Gong, B.; VanGundy, R. M.; Parsons, G. N., *Chemistry of Materials* **21,** 820-830 (2009).

207. Dameron, A. A.; Seghete, D.; Burton, B. B.; Davidson, S. D.; Cavanagh, A. S.; Bertrand, J. A.; George, S. M., *Chemistry of Materials* **20,** 3315-3326 (2008).

208. Kim, A.; Filler, M. A.; Kim, S.; Bent, S. F., *Journal of the American Chemical Society* **127,** 6123-6132 (2005).

209. Lee, B. H.; Lee, K. H.; Im, S.; Sung, M. M., *Organic Electronics* **9,** 1146-1153 (2008).

210. Oh, M. S.; Lee, K.; Lee, K. H.; Cha, S. H.; Choi, J. M.; Lee, B. H.; Sung, M. M.; Im, S., *Advanced Functional Materials* **19,** 726-732 (2009).

211. Lee, B. H.; Ryu, M. K.; Choi, S. Y.; Lee, K. H.; Im, S.; Sung, M. M., *Journal of the American Chemical Society* **129,** 16034-16041 (2007).

212. Kubono, A.; Yuasa, N.; Shao, H. L.; Umemoto, S.; Okui, N., *Thin Solid Films* **289,** 107-111 (1996).

213. Du, Y.; George, S. M., *Journal of Physical Chemistry C* **111,** 8509-8517 (2007).

214. Adarnczyk, N. M.; Dameron, A. A.; George, S. M., *Langmuir* **24,** 2081-2089 (2008).

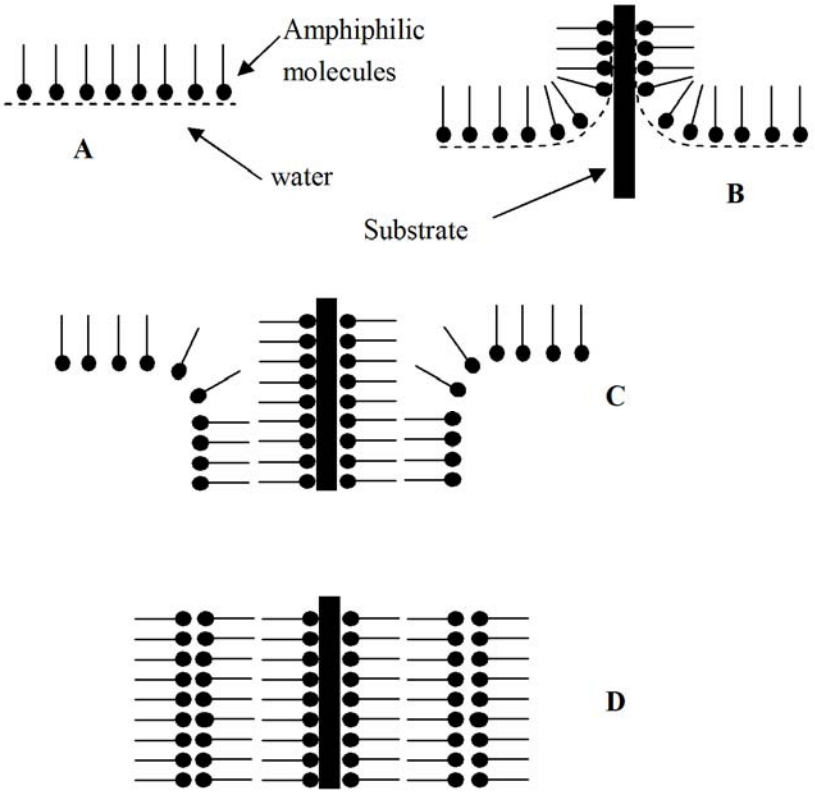


Figure 1.1 The scheme of the Langmuir- Blodgett (LB) thin film fabrication process, **A)** amphiphilc molecules at the air/water interface. **B)** Substrate pulled out, hydrophilic group absorbed onto substrate. **C)** Substrate pushed into water, hydrophobic group attached onto hydrophobic surface, **D)** several layer LB films

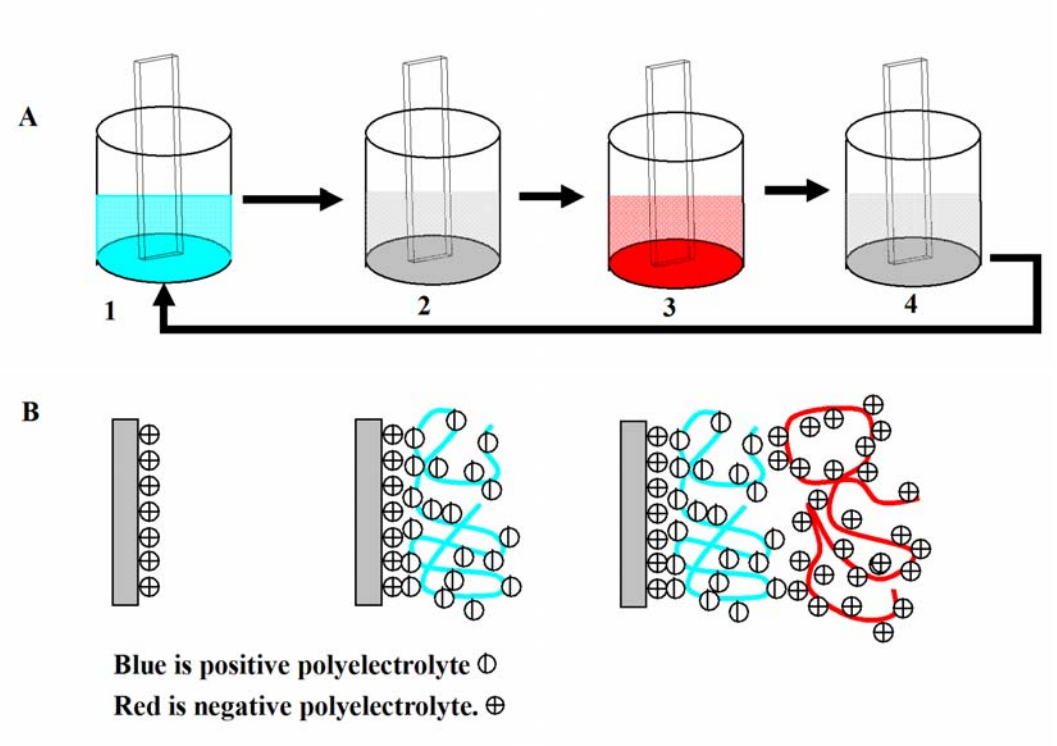


Figure 1.2 The scheme of the layer by layer thin film deposition, **A)** process of LBL film fabrication, 1) solution of positive polyelectrolyte, 2) pure deionized water, 3) solution of negative polyelectrolyte, 4) pure deionized water. **B)** the structure of LBL films.

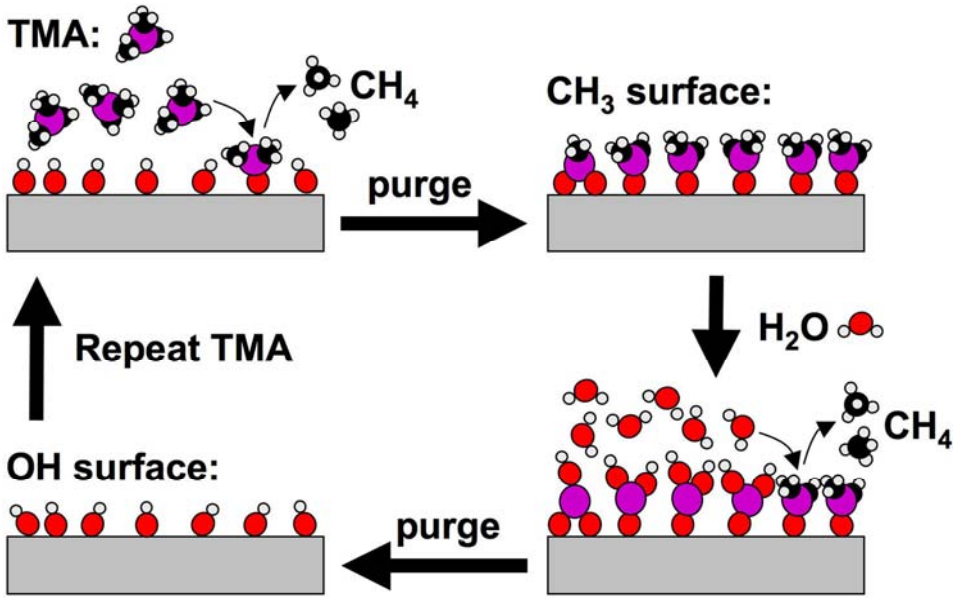


Figure 1.3 Schematic diagram of vapor-phase, self-limiting atomic layer deposition (ALD) illustrating the cyclic process by which an Al_2O_3 surface coating is controllably constructed layer-by-layer from TMA and H_2O precursors.

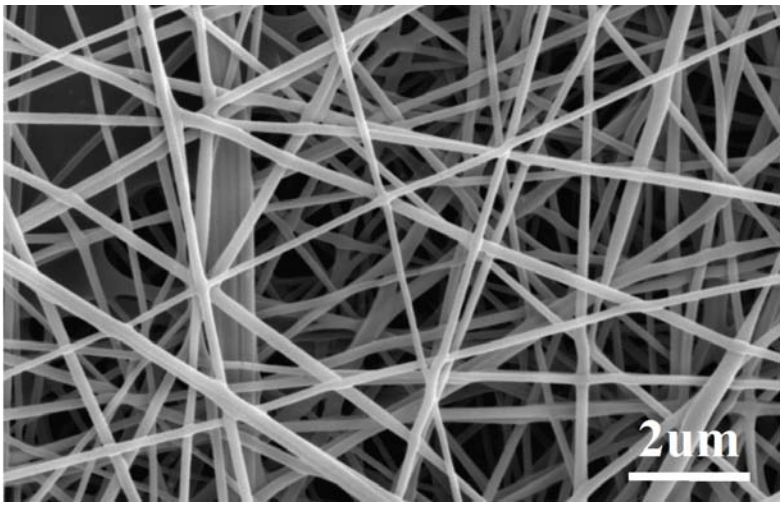


Figure 1.4 A representative SEM image of the electropun polyvinyl alcohol fiber matrix.

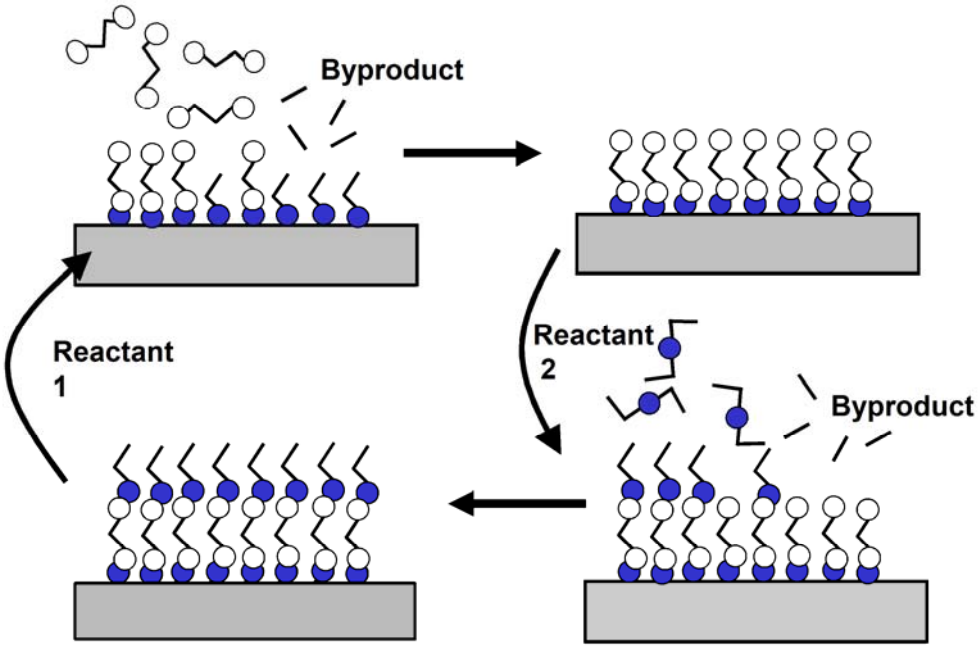


Figure 1.5 Schematic diagram of vapor-phase, self-limiting molecular layer deposition (MLD) illustrating the cyclic process from two bifunctional reactants, which could be extended into other types of multiple functionalities molecules.

CHAPTER 2. Experimental Tools

The experimental setups for both supercritical carbon dioxide based deposition technique and atomic layer deposition and its related processes are included in this section, as well as the analysis and characterization techniques performed during the thesis work.

2.1 Supercritical carbon dioxide based process

2.1.1 Metal oxides thin films deposition through pyrolysis of metal organics

Native oxide Si(100) wafers were used as substrates for deposition, and prepared by wet cleaning in BakerClean® JTB-100 solution (Mallinckrodt Baker Inc), followed by rinsing in deionized water, then drying in a N_2 flow.

Metal containing precursors utilized in this study including aluminum acetylacetonate (99 %) ($Al(acac)_3$) [$Al(C_5H_7O_2)_3$], $Ga(acac)_3$, $Fe(acac)_3$, $Zn(acac)_2$, $Zr(acac)_4$, $Co(acac)_3$, $Cr(acac)_3$, $Hf(acac)_4$, aluminum hexafluoroacetylacetonate ($Al(hfac)_3$) [$Al(C_5HO_2F_6)_3$] and $Zr(hfac)_4$, were used as received (Strem Chemicals). Coleman grade CO_2 (99.99 %) (National Welders) was used in the experiments.

Deposition reactions were carried out in a homemade stainless steel batch type reactor with a total volume of 110 milliliters as illustrated schematically in Figure 2.1.[1] In a typical experiment, a piece of pretreated native oxide Si substrate (~ 1 cm×1.5 cm) was fixed onto the heating block, which was attached to a gland fitting (Conax Buffalo Corp.), as shown in Figure 2.1. Three cartridge heaters (Tempco) were fit into the heating block, enabling substrate surface temperature to be controlled by using a feedback thermocouple fit through the gland fitting. A predetermined amount of precursor was weighed and placed in

the reactor with the substrate holder before sealing. Air was purged from the reactor by flowing low pressure CO_2 through a vent valve for 5 min at a temperature of ~ 70-100 °C. The reactor was then pressurized with CO_2 and heated to the predetermined set point (P=21 MPa, T=100 °C). Subsequently, the system was kept stable for 2 h to allow the precursor to dissolve. The typical precursor concentration was approximately 170 μmol/L for $Al(acac)_3$ and 230 μmol/L for $Ga(acac)_3$. For some experiments, to examine the effect of oxidizing species, oxygen or water was intentionally added to the reaction. For these experiments, after the precursor was loaded into the clean vessel, the vessel was purged with low pressure CO_2 for ~ 10 min to remove ambient air. The vessel was then filled with high purity dry air or a small known volume of deionized water and subsequently sealed and filled with high pressure CO_2. The concentration of oxidant was then estimated using the known volume of the system.

After the precursor dissolution time, the temperature of the substrate was increased to the growth temperature set point. This transition occurred typically within 1 min. After a predetermined reaction time, the cartridge heaters were turned off and the temperature of the substrate decreased to below 150 °C, typically within 1 min. For higher substrate temperatures, the reactor temperature was observed to increase above the set temperature of reactor wall (100 °C) during the first 20 min, but temperature generally stayed below ~ 190 °C. After the set deposition time, the effluent from the reactor was vented through an activated carbon bed, and fresh $scCO_2$ was used to purge the reactor to remove byproducts and remaining precursor out of system. The reactor was allowed to cool, and the samples were then removed from the reactor and characterized.

2.1.2 Metal oxides thin film deposition onto carbon nanotube forest through pyrolysis of metal organics

Multi-walled carbon nanotubes (MWCNTs) were grown by catalytic chemical vapor deposition (CVD) process in a homemade quartz reactor at 500 °C. Ethanol was used as the carbon source. Argon was used as a carrier gas and was bubbled through the ethanol at room temperature with a flow rate of 1.5 standard liters per minute (SLM). The catalyst layer Fe (0.5nm)/Al_2O_3(10nm) was formed on the thermal oxide silicon wafer (SiO_2(500nm)/Si) by using sequential e-beam evaporation. In a typical experiment, a Si substrate (size: ~1 cm×1.5 cm) having MWCNTs forest grown on it, was used as the deposition platform without further treatment.

The deposition process follows the same procedure as shown in section 2.1.1.

2.1.3 Nickel metal deposition from self-catalyzed hydrogenation process in $scCO_2$

Nickelocene [$Ni(Cp)_2$] (Strem Chemicals®) was used as the precursor and H_2 was used as the reducing agent. Coleman grade CO_2 (99.99%) and high purity H_2 (99.999%) (National Welders/Supply Company) were used without further purification.

The experiment was carried out in a 110 ml homemade high-pressure reactor as shown in Figure 2.2.[2] In a typical experiment, 70-90 mg $Ni(Cp)_2$ was loaded into the high pressure reactor, which was then sealed by sapphire windows on both sides, with a silicon wafer having MWCNTs forest grown on it. Following precursor loading, low-pressure fresh CO_2 was used to purge the system for 10 min (minute) at temperature ~ 70 ˚C in order to purge air out of the reactor. After purging, high-pressure CO_2 was fed into the reactor through a high-pressure syringe pump (Model 260D, Isco, Inc.). The temperature of the

$scCO_2$ solution was stabilized by a heating tape at the dissolving condition (T=70 ˚C, P=17 MPa) for 4 h (hours) to form a uniform solution. During $Ni(Cp)_2$ dissolution, H_2 was fed into another clean, air-free high-pressure manifold vessel (43 ml), to the pressure of ~ 3.5 MPa at 60 ˚C. The vessel was then further charged with fresh CO_2 using the high-pressure syringe pump to the pressure of ~ 34.5 MPa. This $H_2/scCO_2$ solution was kept stable at this condition for more than 2 h before injected into the high-pressure reactor. Upon $H_2/scCO_2$ injection, the pressure in the vessel dropped from ~ 34.5 to ~ 19.3 MPa, allowing the amount of H_2 fed into the reactor to be quantified. The H_2 injection process will be repeated to obtain a 50-100x molar excess of hydrogen relative to nickelocene in the reactor system. Upon the addition of H_2, the $scCO_2$ solution containing $Ni(Cp)_2$ maintained a green color and the reaction system was left undisturbed at 70 ˚C, 17-18 MPa for several hours. After 7-8 h substantial Ni film and particles deposition was observed (as described in the experimental results section). Following each experiment, the reactor was prepared for another reaction sequence by removing the Ni deposition on the vessel walls. The reactor was scrubbed then sonicated in water, followed by deionized (DI) water flush and N_2 flow dry.

2.2 Atomic layer deposition/Molecular layer deposition

2.2.1 Atomic layer deposition of metal oxides onto electrospun fibers

Fibers were electrospun from polyvinyl alcohol (PVA) (127 kDa and a degree of hydrolysis of 88%), and polyethylene oxide (PEO) (1 MDa) purchased from Aldrich and used without further purification.[3] A 7 wt% PVA aqueous solution and PEO solution of 30g/L was prepared by dissolving the polymers in deionized water (DI H_2O) and used as spinning solution. Electrospinning was performed using a parallel-plate setup described

elsewhere.[3] A stable jet was formed at a flow rate of 7 μl/min and an electric field of 1 kV/cm. PEO was electrospun with electric field of 0.8 kV cm^{-1} and a solution flow rate of 2-3 μL/min.

Al_2O_3 ALD was conducted at 45 ˚C and ~0.9 Torr. A modestly higher temperature (65 °C) was used for ZnO ALD, also performed at ~0.9 Torr. The reactants included two organometallic precursors - trimethylaluminum ($Al(CH_3)_3$, TMA, 98%, Strem®), diethyl zinc ($Zn(C_2H_5)_2$, DEZ, 96%, Strem®) and deionized water vapor (DI H_2O). High-purity Ar (99.999%) (National Welders Supply Co.) used as the purge and carrier gas was further purified by a gas filter (DRIERITE Gas Purifier) before entering the reaction system. The AD system used is similar to the reactor scheme shown in Figure 2.3, except there is no cold trap on the system. The temperature gradient of the whole reactor was maintained in order to prevent condensation of precursors in the reactor and delivery lines.

All the species were delivered as ambient-temperature vapors into a custom-built hot-wall viscous flow tube reactor. During Al_2O_3 ALD cycling, the TMA and DI H_2O were alternately introduced into the ALD chamber (base pressure ~10^{-6} Torr) in pulses of different times to saturate the surface reaction. Corresponding purge times were used for TMA and DI H_2O to remove all physical absorbed reactants and byproducts. For ZnO ALD deposition, DEZ and DI H_2O were likewise injected into the reactor in pulses of different times to saturate the surface reaction respectively. A satisfactory purge time was used to eliminate the gas phase reaction.

For ALD deposition on PVA microfiber mats, two pieces of silicon wafer (measuring ~1 cm × 1.5 cm, treated by JTB® Baker Clean, rinsed in DI water and then blown-dry with

N_2) were used as reference substrates for growth rate measurements on a planar surface under identical deposition conditions. A multi-components coaxial metal oxide coating was formed by performing ALD of different materials onto the fiber mat sequentially.

The metal oxides tubular structures were formed by removing the electrospun fiber template through either calcinating in air at 450 ˚C above for 24 hours or dissolving in DI H_2O for 24 hours.

The solid state reaction and diffusion process (Kirkendall Effect) was initialized by heating the coaxial tubings of (Al_2O_3/ZnO/Al_2O_3) at reaction temperature of 700 ˚C for more than 12 hours.

2.2.2 Molecular layer deposition of organics, hybrid and self assembly monolayers.

In the experiment of zinc hybrid materials molecular layer deposition (MLD), diethyl zinc ($Zn(C_2H_5)_2$) (96%) was obtained from Strem Chemicals Inc. and used without further treatment. Deionized water (DI H_2O) was used as the water source for ZnO ALD deposition. Anhydrous ethylene glycol, EG (OHC_2H_4OH) (99.8%) (Sigma-Aldrich) was used as the organic material source without further purification. For nylon thin film deposition, 1,4 butane diamine (BDA) (99%), 1,6 hexane diamine (DAH) (99%), terephthaloyl dichloride (TDC) (99%) and sebacoyl dichloride (SEDC) (99%) were purchased from Sigma-Aldrich and used without further purification. For the self-assembly monolayer deposition, 3-aminopropyltriethoxysilane (APTES, 99%) was used as the precursor for amino silane self-assembly monolayer deposition.

Molecular layer deposition of organics, hybrid materials and self-assembly monolayer were carried out in the same homemade viscous flow vacuum reactor as the previously

described ALD processing. A representative schematic of the deposition equipment is shown in Figure 2.3. The sample substrates and the quartz crystal microbalance (QCM) crystal were heated by convection and radiation from the heated reactor wall. High purity Ar (99.999%) (National Welders Supply Co.) used as the purge gas and carrier gas for reactants was further purified by using a gas filter (DRIERITE Gas Purifier) before entering the reaction system. The flow rate of Ar carrier gas was controlled by mass flow meters. The process pressure was monitored by a Baratron pressure gauge (MKS Instrument Inc.). The reaction system was pumped using a rotary mechanical pump. For the reactants with higher vapor pressure, such as TMA, DEZ H_2O, APTES, Diamines and EG (Ethylene glycol), the reactants were delivered into the reactor by injecting the reactant vapor into Ar carrier gas through a computer–controlled ALD solenoid valve. For reactants with low vapor pressure (<1 torr) at approximately the reaction temperature, such as dicarboxylic chlorides, the precursors were delivered into the reactor by Ar bubbling. The reactant dose amount was adjusted by either changing pulse time or heating temperature in order to achieve saturated surface reaction. Different purge times were used to eliminate the gas phase reaction between precursors.

In order to increase the mechanical pumn operation longevity, the organics and metal organic precursors were pumped through separate exhaust lines, which were controlled individually using computer-controlled gate valves. Organic precursors (including APTES, Diamines, EG, Dicarboxylic chlorides) were isolated using liquid N_2 trap before entering the pump. DEZ, TMA and H_2O were pumped directly to the pump.

As illustrated by the reactor schematic for the zinc hybrid deposition in Figure 2.3,[4] the reactor was designed to allow simple transitions between deposition of ZnO ALD and

MLD of zincone materials by switching easily between H_2O and EG reactant flow. For nylon thin film, APTES self-assembly monolayer and other materials deposition similar deposition system were used except the precursor delivery lines were designed in different way in order to provide adequate material to achieve saturation growth.

2.3. Characterization Methods

2.3.1 *In-situ* Quartz Crystal Microbalance

In-situ QCM is installed onto the vacuum ALD deposition reactor system through the inlet of the reactor as show in Figure 2.3. Polished QCM crystal sensors with Au coating (Colorado Crystal Corp.) were mounted in the Maxtek BSH-150 bakeable sensor head. The sensor head was modified to allow ~10 sccm of Ar flow over the back side of the sensor, and the crystal was sealed to the QCM housing using conductive epoxy in order to prevent material from depositing onto the backside of the crystal surface. The mass change signals were detected by a monitor (Maxtek TM-400), and recorded using a home designed LABVIEW program. The QCM detect the mass change by measuring the change in frequency of a quartz crystal resonator, as illustrated by the eq. 2.1. The resonance is disturbed by the addition or removal of a small mass due to material growth, residue remove or etching process. As shown by eq.2.2, ***C*** is a crystal-dependent sensitivity factor that includes the fundamental resonant frequency (f_0), the surface area (A), the density (ρ) and the shear modulus (μ):[5]

$$\Delta f = -C \times \Delta m \qquad \text{eq. 2.1}$$

$$C = 2 f_0^2 / (A(\mu\rho)^{0.5}) \qquad \text{eq. 2.2}$$

2.3.2 Chemical composition analysis tools

Auger electron spectroscopy (AES) and x-ray photoelectron spectroscopy (XPS) are used to determine the chemical composition and impurities on the surface of the deposited film. AES was conducted by using a 5 keV primary electron gun. The XPS analysis was conducted with monochromatic Al Kα source operate at 15kV on a Kratos Analytical Axis Ultra equipment. For all samples, the C-1s peak (representing the binding energy of C–H and C–C) was normalized to 284.6 eV for reference. For the survey and detail scans, 160 and 20 eV were used for the pass energy respectively. In some instances, the sample surfaces were cleaned in–situ by Ar sputtering at 5 kV for 3 min.

Fourier transform infrared spectroscopy (FT-IR) is used to probe the chemical bondings of synthesized material. A ThermoNicolet IR bench with a deuterated triglycine sulfate detector (KBr bean splitter) was used in transmission mode with 2048 scans at 4 cm^{-1} resolution. The measuring chamber was continuously purged with purified dry air. A background spectrum was collected using the starting Si wafer before deposition.

2.3.3 Material morphology analysis tools

Surface morphology of thin films, which are deposited onto planar Si substrates, was analyzed by a Nanoscope IIIa atomic force microscope (Digital Instruments) operated in tapping mode with a scanning frequency of 0.5 Hz.

Transmission electron microscopy (TEM) and scanning electron microscopy (SEM) are used to probe the morphology of materials. Generally the TEM was operated at 200 keV. SEM was operated at 5 keV. For TEM measurements, several droplets of the dispersion

ethanol solution of nanomaterials was placed onto the carbon film coated TEM grid for analysis.

2.3.4 Crystal structure analysis

X-ray diffraction (XRD) spectra of materials were obtained using a Bruker AXS D-5000 x-ray diffractometer equipped with GADDS area detector. All measurements were taken by using a generator with a voltage of 40 kV and a current of 30 mA.

2.3.5 Thickness of the deposition

Film thickness of deposition was measured by ellipsometry. For the materials with well-known optical parameters, such as Al_2O_3, ZnO etc, fixed angle ellipsometry was used. For materials with unknown optical properties, for example zinc based hybrid materials, the variable-angle spectroscopic ellipsometry (J. A. Woollam). Measurement was carried out over a spectrum from 400 to 1100 nm using incident angles of 65, 70, and 75 degrees. A three-layer Cauchy model (hybrid/nativeSiO_2/Si) was used to fit the experiment data to derive the refractive index and film thickness. In the model, thickness of native oxide and Si substrate were set at 15 Å and 1 mm, respectively. The film thicknesses were confirmed by TEM or SEM.

REFERENCES

1. Peng, Q.; Hojo, D.; Park, K. J.; Parsons, G. N., *Thin Solid Films* **516,** 4997-5003 (2008).
2. Peng, Q.; Spagnola, J. C.; Parsons, G. N., *Journal of the Electrochemical Society* **155,** D580-D582 (2008).
3. Sun, X. Y.; Shankar, R.; Borner, H. G.; Ghosh, T. K.; Spontak, R. J., *Advanced Materials* **19,** 87-89 (2007).
4. Peng, Q.; Gong, B.; VanGundy, R. M.; Parsons, G. N., *Chemistry of Materials* **21,** 820-830 (2009).
5. Elam, J. W.; Groner, M. D.; George, S. M., *Review of Scientific Instruments* **73,** 2981-2987 (2002).

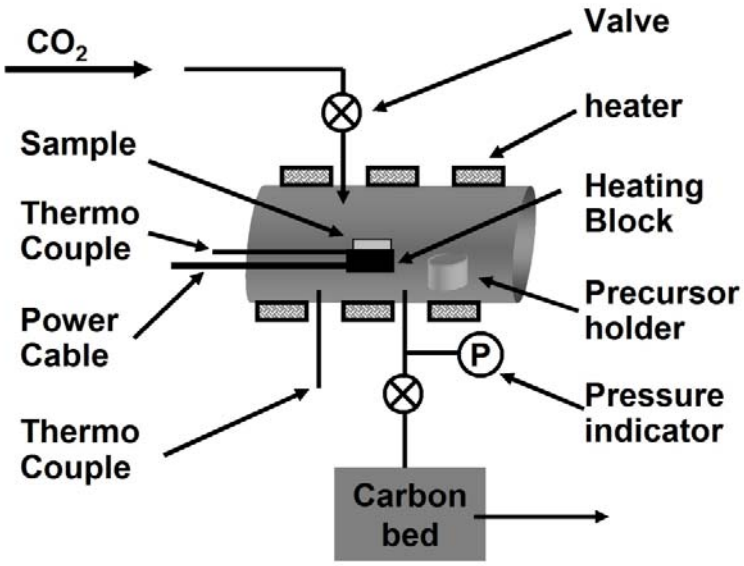


Figure 2.1 Schematic diagram of the experimental apparatus. The inner volume of the reactor is ~ 110 mL. The reactor wall temperature is typically held at 100 ^{o}C. The sample is located on a block that is heated independently from the reactor chamber wall.

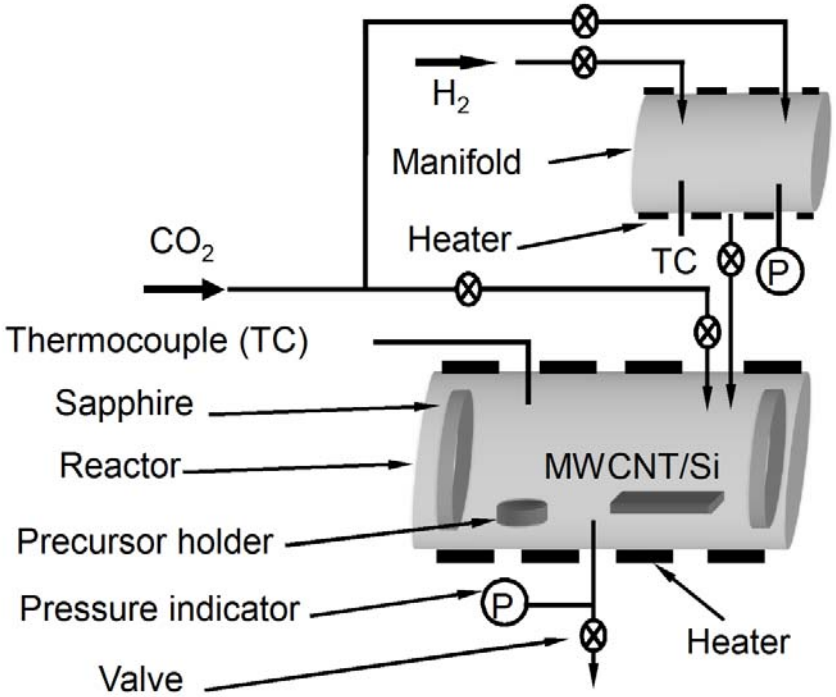


Figure 2.2. The diagram of reaction system. H_2 is mixed with $scCO_2$ in the manifold to form uniform solution. The temperature of the reactor and manifold are controlled by feedback thermal couples individually. The reaction system can be observed through the sapphire windows.

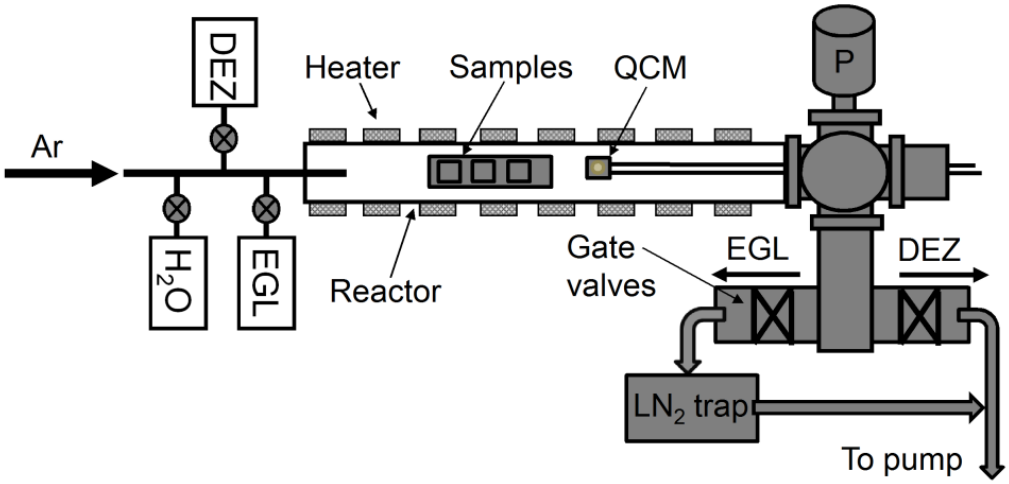


Figure 2.3. A schematic view of the viscous flow ALD/MLD reactor. The precursors are delivered into the reactor with Ar carrier gas. On the reactor exhaust line, computer controlled gate values are used to direct the exhaust from the EG pulse into a liquid nitrogen trap before entering the pump.

CHAPTER 3. Overview of Key Results of Dissertation and Author's Contributions

The first part of this dissertation has been focused on understanding the surface reaction, nucleation phenomena, deposition kinetics involved in the supercritical carbon dioxide based deposition process and its applications in modifying substrates with three dimensional structures. The kinetics of metal oxide thin film deposition process through pyrolysis of metal organics in $scCO_2$ was studied in detail. This process is applied to modify complex 3D carbon nanotube forests without breaking the original structure. Moreover, the nucleation mechanism of Ni nanoparticles from hydrogenolysis of metal organics was studied and used to modify the carbon nanotube forest.

The second part of this dissertation explores the application of atomic layer deposition process on polymer fiber matrix in order to facile way of nanostructure fabrication with precisely tuned dimensions. Through this technique, coaxial $Al_2O_3/ZnO/Al_2O_3$ microtubes were fabricated and used as a platform for the study of bi-directional Kirkendall effect. Moreover, an extension of atomic layer deposition process, named as molecular layer deposition, was explored to deposit new materials including nylons, hybrid, self-assembly monolayer. The detailed surface reaction mechanism involved in those novel new material deposition processes were studied in detail.

3.1 Low-temperature metal oxide thin film deposition and reaction kinetics in supercritical carbon dioxide

3.1.1 Key results

An effective method is developed for low temperature metal oxide deposition through thermal decomposition of metal diketonates in supercritical carbon dioxide ($scCO_2$) solvent.

The rates of thermal decomposition of $Al(acac)_3$ (Aluminum acetyl acetonate) and $Ga(acac)_3$ (Gallium acetyl acetonate) in $scCO_2$ to form conformal Al_2O_3 and Ga_2O_3 thin films on planar surfaces were investigated and shown in Figure 3.1. The thermal decomposition reactions of $Al(acac)_3$ and $Ga(acac)_3$ were found to be initialized at ~ 150 °C and 160 °C respectively, in $scCO_2$ solvent compared to ~ 250 °C and 360 °C in analogous vacuum-based processes. As determined by the temperature dependent growth rates of metal oxide thin films (as shown in Figure 3.1), the apparent activation energy for the thermal decomposition of $Al(acac)_3$ in $scCO_2$ is ~ 68 ± 6 kJ/mol, in comparison with 80-100 kJ/mol observed for the corresponding vacuum-based thermal decomposition reaction. The enhanced thermal decomposition rate in $scCO_2$ is ascribed to the high density solvent, which effectively reduces the energy of the polar transition states in the reaction pathway as shown in Scheme 3.1. Preliminary results of thin film deposition of other metal oxides including ZrO_x, FeO_x, Co_2O_3, Cr_2O_3, HfO_x from thermal decomposition of metal diketonates or fluorinated diketonates in $scCO_2$ are also presented in Table 3.1

3.1.2 Author's contribution

The author designed the research plan together with Dr. Gregory N. Parsons and performed the majority of the metal oxide deposition experiments and characterization measurements with help from coauthors. The author and Dr. Parsons interpreted the results with the co-authors. The author wrote the manuscripts with Dr. Gregory N. Parsons.

3.2 Conformal metal oxide coatings on nanotubes by direct low-temperature metal-organic pyrolysis in supercritical carbon dioxide

3.2.1 Key results

The low temperature (< 200 °C) thermal decomposition of metal organic precursors dissolved in supercritical carbon dioxide ($scCO_2$) were demonstrated as an effective method to deposit conformal metal oxide films with tunable thickness into dense three dimensional networks. Results, as shown in Figure 3.2, specifically show that the thermal decomposition of gallium acetylacetonate in $scCO_2$ leads to conformal coatings of gallium oxide on multi-walled carbon nanotube forests with a fast deposition rate (~3-4 nm/min), without the need for any co-solvent. Moreover, as-formed metal oxide/nanotube structures can be further coated by metal atomic layer deposition to produce nanotube/oxide/metal nano-composites as presented in Figure 3.3.

3.2.2 Author's contribution

The author designed the research plan together with Dr. Gregory N. Parsons and performed all the metal oxide deposition experiments and carried out the thickness measurement. Joseph C. Spagnola prepared carbon nanotube forest samples and Dr. Kiejin Park did the ruthenium atomic layer deposition experiment. The author and Dr. Gregory N. Parsons interpreted the results. The author wrote the manuscripts. Dr. Gregory N. Parsons revised it.

3.3 Self-catalyzed hydrogenolysis of Nickelocene: functional metal coating of three-dimensional nanosystems at low temperature

3.3.1 Key results

Hydrogenolysis of Nickelocene can take place through a self-catalyzed process at low temperature (< 70 ˚C) in supercritical carbon dioxide to generate relatively uniform dispersed Ni (nickel) metal particles onto carbon nanotubes forests (as shown in Figure 3.4) as well as Ni films on flat surfaces. The ability to form metal particles or films without a local catalyst at this low temperature is significant because it provides further insight into mechanisms of Ni deposition reactions (as shown in scheme 3.2) and it enables a new route of low temperature metal coating on a range of non-metal substrate materials with complex topography and nanostructure, for example to form Ni/polymer magnetic nanocomposites.

3.3.2 Author's contribution

The author designed the research plan together with Dr. Gregory N. Parsons and performed the metal hydrogenolysis experiments. Joseph C. Spagnola prepared carbon nanotube forest samples. The author interpreted the results and wrote the manuscripts with Dr. Gregory N. Parsons' revision.

3.4 Atomic layer deposition on electrospun polymer fibers as a direct route to Al_2O_3 microtubes with precise wall thickness control

3.4.1 Key results

In this work, atomic layer deposition (ALD) on electrospun polymer fibers (poly vinyl alcohol) was employed as a direct means by which to construct inorganic microtubes with well-defined nanoscale walls composed of Al_2O_3 after the templating polymer is

removed. As shown in Figure 3.5, the wall thickness of the tubes can be precisely tuned by adjusting cycle numbers. Moreover, as demonstrated by the transmission electron microcspopy and scanning electron microscopy measurement, the ALD coatings are very smooth and uniform throughout the electrospun fiber mat as illustrated in Figure 3.6. The results reported here indicate that this strategy provides an attractive, high-fidelity and low-cost route to inorganic microtubes, as well as nanoscale tubes and other complex shapes. The polyethylene oxide (PEO) electrospun fibers were also used as the template for Al_2O_3 ALD coating. However due to the thermal instability of PEO nanofibers, the morphology of the fiber mat is destroyed during the deposition as shown in Figure 3.7.

3.4.2 Author's contribution

The author designed the research plan together with Dr. Gregory N. Parsons and performed the atomic layer deposition experiments. Dr. Xiaoyu Sun prepared the electrospun fiber. Joseph C. Spagnola and Dr. G. Kevin Hyde helped with SEM and TEM imaging. The author interpreted the results and wrote the manuscripts. Dr. Gregory N. Parsons and Dr. Richard J. Spontak revised the manuscript.

3.5 Bi-directional Kirkendall effect in coaxial microtube nanolaminate assemblies fabricated by atomic layer deposition

3.5.1 Key results

In this work, low-temperature atomic layer deposition (ALD) of Al_2O_3 and ZnO was demonstrate as a effective method for the fabrication of complex coaxial multilayered microtubes with precise control of the starting film thicknesses and relative composition. Different coaxial tubes of ZnO, Al_2O_3/ZnO, Al_2O_3/ZnO/Al_2O_3 with tunable shell thicknesses

were fabricated. The solid-state reaction within a coaxial Al_2O_3/ZnO/Al_2O_3 multilayered microtubular structure were demonstrate as an idea system to prepare discrete microtube-in-microtube $ZnAl_2O_4$ spinel assemblies through a Kirkendall void production mechanism at 700 °C. In contrast with previous studies of the nano-scale Kirkendall effect, the reaction observed here proceeds through a bi-directional vacancy diffusion mechanism wherein ZnO species diffuse into inner- and outer-Al_2O_3 concentric layers as illustrate in Figure 3.8. thereby resulting in vacancy supersaturation and void production between two isolated spinel microtubes. When a molar excess of ZnO is present between two Al_2O_3 layers, electron microscopy images reveal incomplete ZnO consumption after annealing at 700 °C, as shown in Figure 3.9. At higher initial Al_2O_3 mole fractions, however, complete reaction with ZnO is observed as presented in Figure 3.10. The size of the Kirkendall gap between isolated spinel microtubes appears to be directly influenced by the thickness of the ZnO layer, as shown in Figure 3.11.

3.5.2 Author's contribution

The author designed the research plan together with Dr. Gregory N. Parsons and performed the atomic layer deposition experiments. Dr. Xiaoyu Sun prepared the electrospun fiber. Joseph C. Spagnola helped with SEM imaging. The author interpreted the results and wrote the manuscripts. Dr. Gregory N. Parsons and Dr. Richard J. Spontak revised it.

3.6 Metal organic hybrid polymer thin films formed by molecular layer deposition

3.6.1 Key results

In this work, hybrid organic–inorganic polymer thin films of the form (–O–Zn–O–C_2H_4–)$_n$, have been deposited from diethyl zinc and ethylene glycol (EG) using molecular

layer deposition (MLD) over a range of substrate temperatures between 100 and 170 °C. *In situ* quartz crystal microbalance (QCM) was used to studied the transition from zinc oxide atomic layer deposition to zinc hybrid deposition as shown in Figure 3.12. *In situ* QCM analysis in Figure 3.13 indicated that the sequential surface reactions of diethyl zinc and ethylene glycol are sufficiently self-limiting and saturating to enable well–controlled MLD growth. Quantitative analysis of *in situ* quartz crystal microbalance and film thickness results indicate that ethylene glycol molecules can undergo a "double reaction" where the -OH groups on both ends of the diol react with available $–Zn–C_2H_5$ surface sites to produce a relatively inert bridging alkane. The mass uptake per MLD cycle during Zn–hybrid film deposition decreased with increasing reaction temperature. Infrared transmission shows that Zn–organic hybrid films are a mixture of metal-oxygen bonding and carbon bonding and are stable in dry air as shown in Figure 3.14. However, the as-deposited ZnO-hybrid material could be hydrolyzed by H_2O (for example, in ambient) resulting in films consisting of zinc oxide and zinc hydroxide with some carbon remnants as presented in Figure 3.14. Spectroscopic ellipsometry indicated that the thickness of hydrolyzed films increased linearly with reaction cycles, and scanning probe and transmission electron microscopy images show the hydrolyzed Zn hybrid film coating is uniform and conformal. The transmission electron micrographs in Figure 3.15 also show the hydrolyzed Zn-hybrid films contain nano-scale porosity. These results suggest new pathways to fabricate organic–inorganic hybrid materials, including metal–organic framework structures.

3.6.2 Author's contribution

The author designed the research plan together with Dr. Gregory N. Parsons and performed the deposition experiments. Bo Gong helped with the deposition experiment. Ryan M. VanGundy worked on the Labview program for the QCM experiment. The author interpreted the results with Dr. Gregory N. Parsons. The author wrote the manuscripts. Dr. Gregory N. Parsons revised it.

3.7 Polyamide thin film and amino silane self-assembled monolayer formed by molecular layer deposition

3.7.1 Key results

Polyamides thin films from diamines and dicarboxylic chlorides were synthesized by molecular layer deposition in this work. The FT-IR analysis verified the chemical composition of the polyamide film as shown in Figure 3.16. In the as-formed the polyamide film, the molecular chains are generally laying down on the substrate surface related to substrate surface normal as shown by Near Edge X-ray Fine Structure (NEXAFS) in Figure 3.17.

The deposition behavior of ALD of aminosilane (specifically γ-aminopropyl triethoxysilane: APTES) with H_2O on the *in situ* generated Al_2O_3 ALD film is monitored by *in situ* quartz crystal microbalance (QCM) at different deposition temperatures (120 and 150 ˚C) as shown in Figure 3.18. The *in situ* QCM data shows that on Al-OH surface, the mass uptake from APTES/H_2O ALD is saturated after ~ 10 cycles. Moreover, *in situ* QCM measurement also confirmed that APTES could react with Al-CH_3 terminated Al_2O_3 ALD film surface. The detailed analysis from *in situ* FT-IR presented in Figure 3.19, which

illustrates the surface reaction chemistry and confirmed the reaction between APTES and surface bonded Al-OH ligands. The *ex situ* x-ray photoelectron spectroscopy measurement confirmed the N components on the Si substrate after 100 cycles Al_2O_3 ALD and 10 cycles of APTES/H_2O, which is approximately 2.5 atomic % at a reaction temperature of 120 ˚C. The sequential low-temperature atomic layer deposition of metal oxides and amino silane self-assembly monolayer (SAM), is demonstrated as a promising method for surface modification onto inert substrate such as polypropylene nonwoven fiber matrix.

3.7.2 Author's contribution

The author designed the research plan together with Dr. Gregory N. Parsons and performed the deposition experiments and most of characterization work. Bo Gong helped with the in-situ FTIR analysis. The author interpreted the results and wrote the manuscripts. Dr. Gregory N. Parsons revised it.

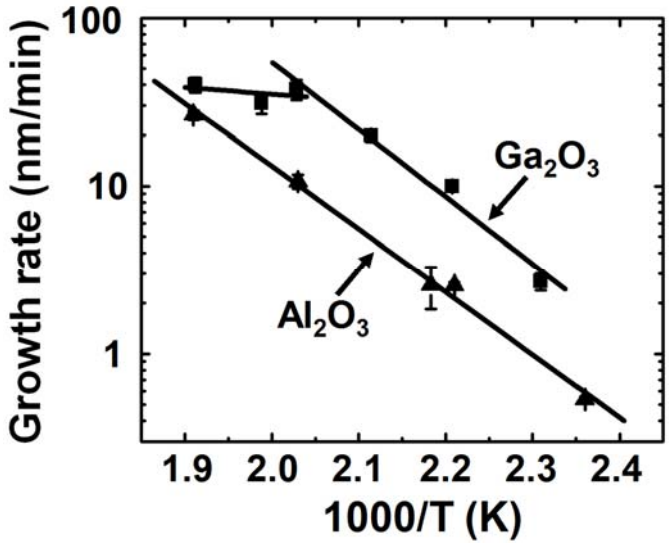
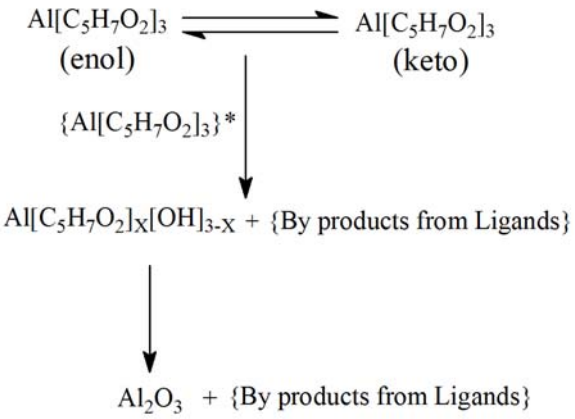


Figure 3.1 Apparent reaction kinetics of $scCO_2$-based deposition of Al_2O_3 films from pyrolytic reaction of $Al(acac)_3$ with initial concentration of 170 µmol/L. The slopes of the lines indicate that the overall energy barrier for Al_2O_3 deposition is 68±6 kJ/mol. And the apparent kinetics of $scCO_2$-based Ga_2O_3 deposition from pyrolysis of $Ga(acac)_3$ at initial concentration of 230 µmol/L. The kinetic barrier of Ga_2O_3 deposition is 84±7 kJ/mol. The solid lines represent linear regressions of the data points.



Scheme 3.1 A simplified reaction mechanism for pyrolysis reaction of $Al(acac)_3$. The * denotes the postulated polar transition state.

Table 3.1 Experiment results of $scCO_2$-based deposition from pyrolytic reaction of different metal organics

Precursor[A]	**Amount**	**Solubility**	**Reaction T**	**Thickness/ Growth time**[C]
$Al(hfac)_3$[B]	26.7 mg	Dissolved well	310 ºC	~ 650 nm/13 min
$Fe(acac)_3$	8.9 mg	Residue left	250 ºC	~ 110 nm/15 min
$Cr(acac)_3$	18.9 mg	Dissolve well	260 ºC	~ 20 nm/32 min
$Co(acac)_3$	6.9 mg	Hard to dissolve	250 ºC	< 10 nm/30 min
$Zr(acac)_4$	15.0 mg	Hard to dissolve	310 ºC	< 10 nm/30 min
$Zr(hfac)_4$	15.3 mg	Residue left	200 ºC	~ 75 nm/23 min
			310 ºC	~ 230 nm/5 min
$Zn(acac)_2$	8.0 mg	Hard to dissolve	200 ºC	No film
$Hf(acac)_4$	25.6 mg	Hard to dissolve	305 ºC	< 10nm/30 min

[A] All of these precursors dissolved at 100 °C, ~21 MPa;
[B] hfac: Fluorinated acetyl acetonate;
[C] For all as-deposited films, AES measurement shows corresponding Metal peak, O peak, C peak.

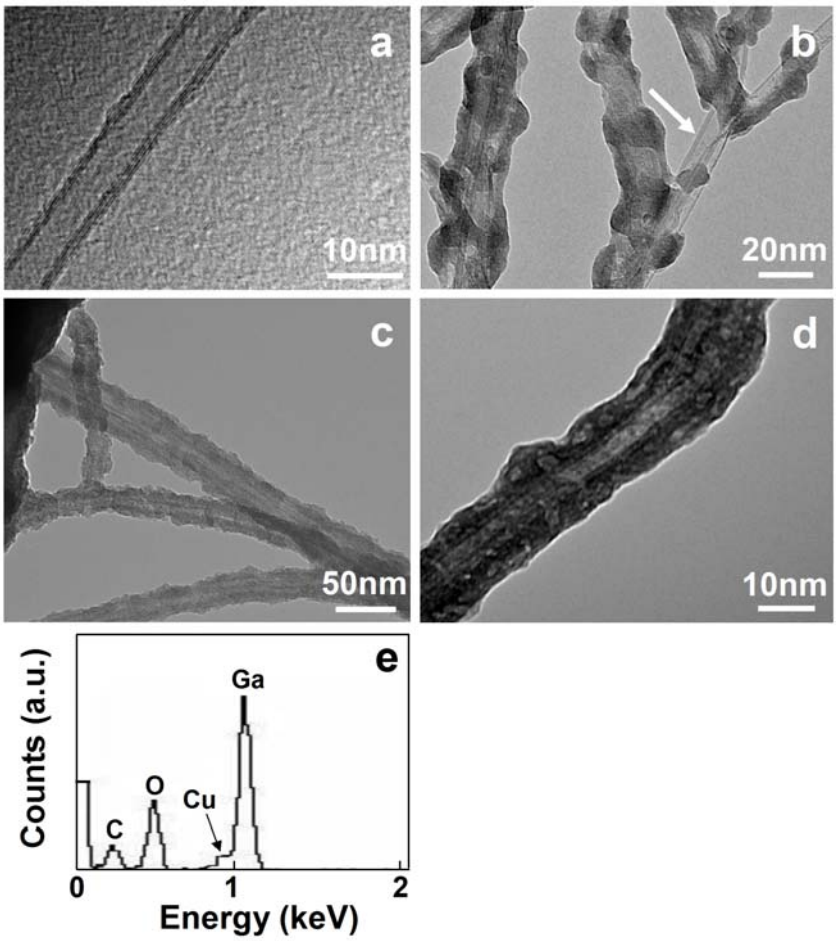


Figure 3.2 (a) TEM image of a single pristine MWCNT. (b) TEM image of MWCNTs coated by gallium oxide from thermal decomposition of $Ga(acac)_3$ at 160 °C and 23 MPa-24 MPa for 7 min. The arrow inside (b) shows the part of MWCNTs having no oxide coating. (c) TEM image of MWCNTs coated by gallium oxide from thermal decomposition of $Ga(acac)_3$ at 200 °C and 28 MPa for 1.5 min. (d) Higher magnification TEM image of MWCNTs coated by gallium oxide from thermal decomposition of $Ga(acac)_3$ at 200 °C and 28 MPa for 1.5 min. (e) A typical EDS spectrum of oxide coated MWCNTs. The gallium oxide deposition experiment was carried out at 200 °C, 28-32 MPa for 1.5 min. The Ga and majority O peaks result from the gallium oxide coating, and the major carbon signal is ascribed to the MWCNTs with some contribution from carbon impurities and adventitious carbon. The tiny Cu peak is from the TEM grid.

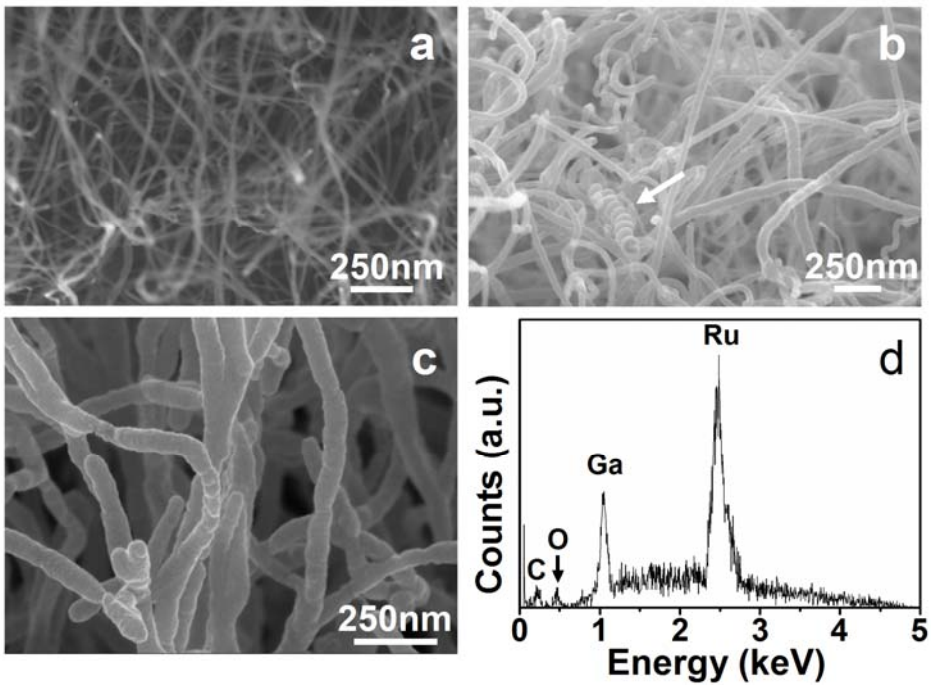


Figure 3.3 (a)FESEM image of untreated pristine MWCNTs. The diameters of the MWCNTs are in the range of 10-30 nm. (b) FESEM image of MWCNTs coated by gallium oxide from pyrolysis of $Ga(acac)_3$ at 200 °C, 28-30 MPa for 10mins. The diameters of the MWCNTs are in the range of 60-100 nm The arrow in (b) indicates that the coating of gallium oxide can replicate the small helix feature of MWCNTs. (c) FESEM image of gallium oxide coated MWCNTs with relatively uniform Ru coating on the surface by atomic layer deposition from reaction between $Ru(Cp)_2$ and O_2 at 325 °C for 150 cycles. (d) A typical EDS spectrum of oxide-coated MWCNTs with Ru ALD coating. The significant Ru peak is shown. The peak of Ga and O come from the gallium oxide under the Ru, and the tiny C peak probably comes from the carbon nanotube core, adventitious carbon from air and the as-deposited films

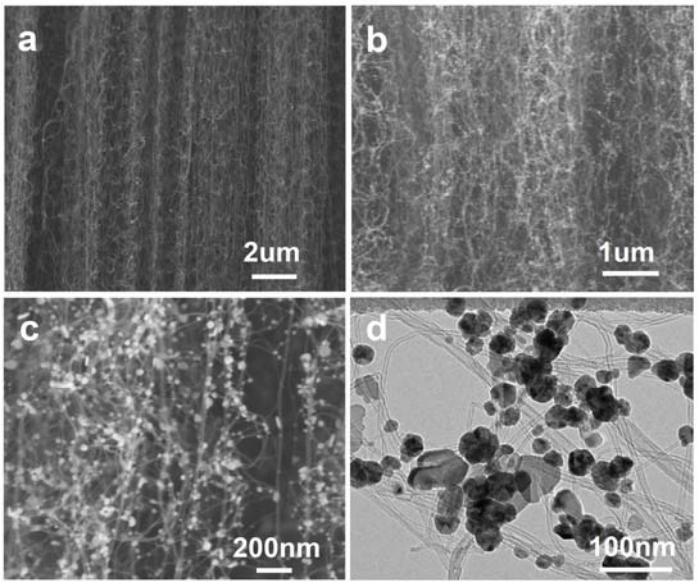
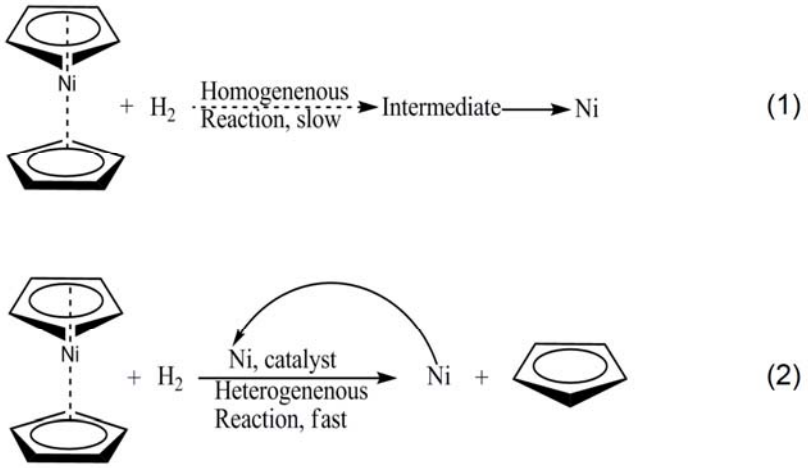


Figure 3.4 (a) FESEM image of pristine MWCNTs. (b) FESEM image of the Ni nanoparticles decorated MWCNTs, which was treated in the $scCO_2$ based direct hydrogenolysis reaction between $Ni(Cp)_2$ and H_2 at 70 °C. (c) A higher resolution SEM image of the Ni nanoparticles anchored MWCNTs. (d) A typical TEM image of Ni nanoparticles decorated MWCNTs.



Scheme 3.2 The reaction scheme of hydrogenolysis of Nicklocene without catalyst. Step (1) is a slower reaction step in order to form Ni nuclei from homogenous hydrogenolysisi of Nicklocene. Once Ni particles are generated, they will catalyze the heterogeneous hydrogenolysis reaction of Nicklocene on Ni particles with a much faster reaction rate.

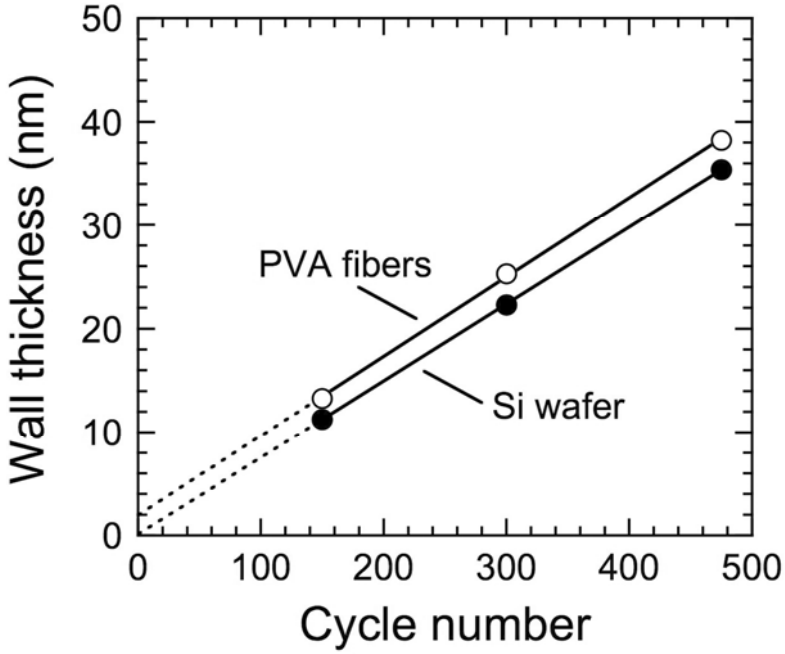


Figure 3.5 Wall thickness of Al_2O_3 microtubes prepared on electrospun PVA fibers (○) and measured by TEM as a function of ALD cycle number. Included for comparison is the Al_2O_3 film thickness on a planar Si substrate (●) measured by ellipsometry. The solid lines denote linear regressions of the data points. The corresponding average growth rates of Al_2O_3 are about 0.08 nm/cycle on the electrospun fibers and 0.07 nm/cycle on the Si substrate. Error bars (±1 standard deviation) deduced from analysis of 25 thickness measurements from each specimen are smaller than the symbols shown.

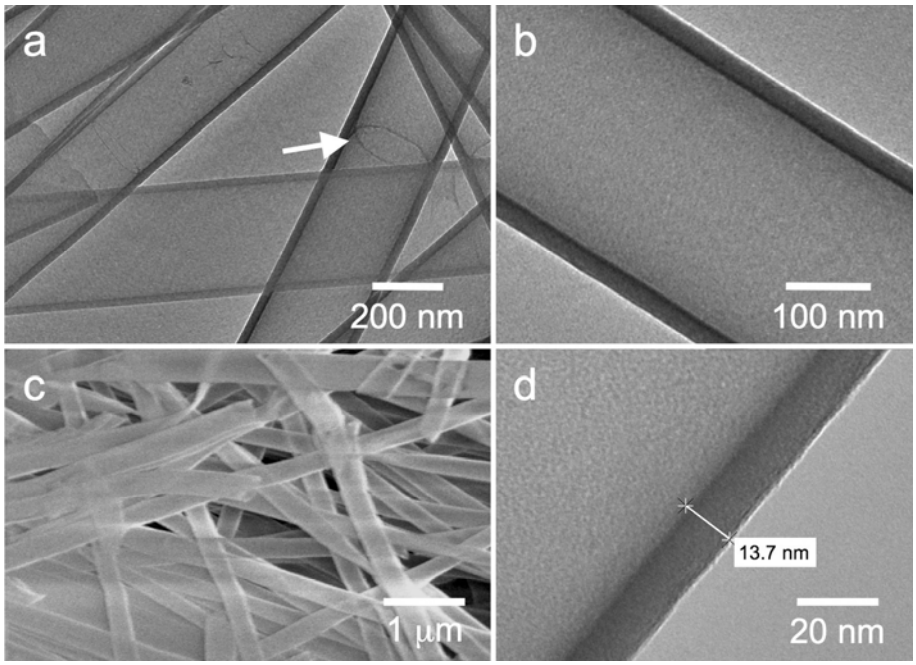


Figure 3.6 (a) FESEM image of an Al_2O_3 microtube in which ALD was performed on electrospun PVA fibers for 300 cycles at 45˚C. The arrow indicates a circle on the inside wall of the resultant microtube. (b) TEM image of the corresponding Al_2O_3 microtube illustrating the wall thickness. (c) FESEM and (d) TEM images of Al_2O_3 microtubes fabricated by ALD for 150 cycles at 45 ˚C. A wall thickness measurement is included in (d). In all cases, the electrospun PVA fiber templates were removed by heating in air at 400 ˚C for 24 h.

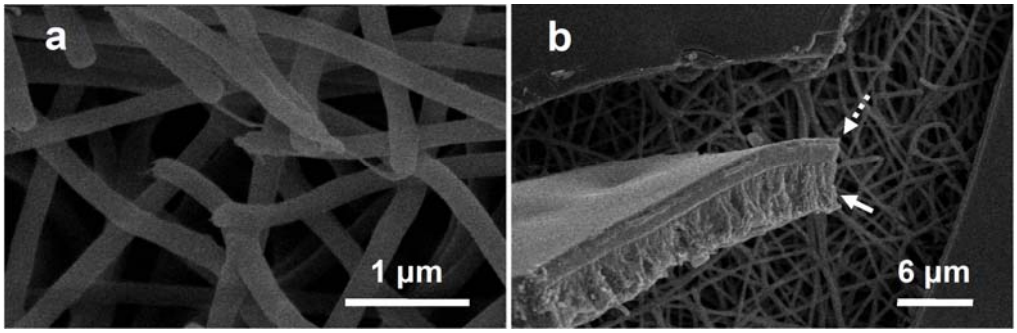


Figure 3.7 (a) FESEM image of polyethylene oxide (PEO) electrospun fiber matrix. (b) FESEM images of polyethylene oxide (PEO) electrospun fiber after Al_2O_3 coating for 150 cycles at 35 ˚C. The top layers of PEO fibers are fused together to form films (solid arrow) and ALD of Al_2O_3 are deposited onto the fused fiber mat as indicated by the (dash arrow).

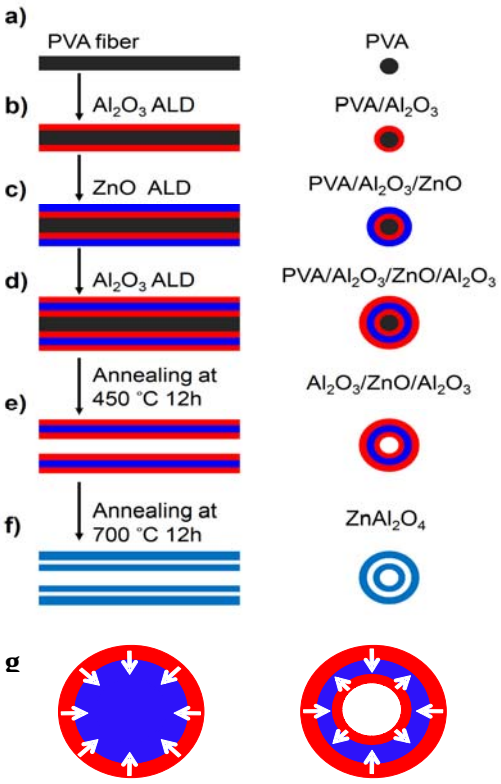


Figure 3.8 Schematic diagram of the procedure developed here for the fabrication of coaxial $ZnAl_2O_4$ microtube-in-microtube coaxial assemblies: (a) electrospinning is used to produce PVA microfibers; (b) a thin, conformal Al_2O_3 coating is applied to the PVA fibers by low-temperature ALD; (c) a successive ZnO coating is applied by ALD; (d) a second Al_2O_3 coating is applied by ALD, resulting in trilayered $PVA/Al_2O_3/ZnO/Al_2O_3$ microcables; (e) the PVA core is removed by calcination at 450 °C in air for 12 h; (f) the resultant $Al_2O_3/ZnO/Al_2O_3$ coaxial microtubes are annealed at 700˚C to form coaxial $ZnAl_2O_4$ microtubes separated by a nanometer-scale gap resulting from accumulation of Kirkendall voids. (g) White arrows show the direction of vacancy diffusion for a typical nanoscale Kirkendall-effect experiment in which Al_2O_3 is coated onto a ZnO crystal (left), as well as for the experimental procedure described here, where diffusion occurs in two directions to produce an internal nanoscale gap (right).

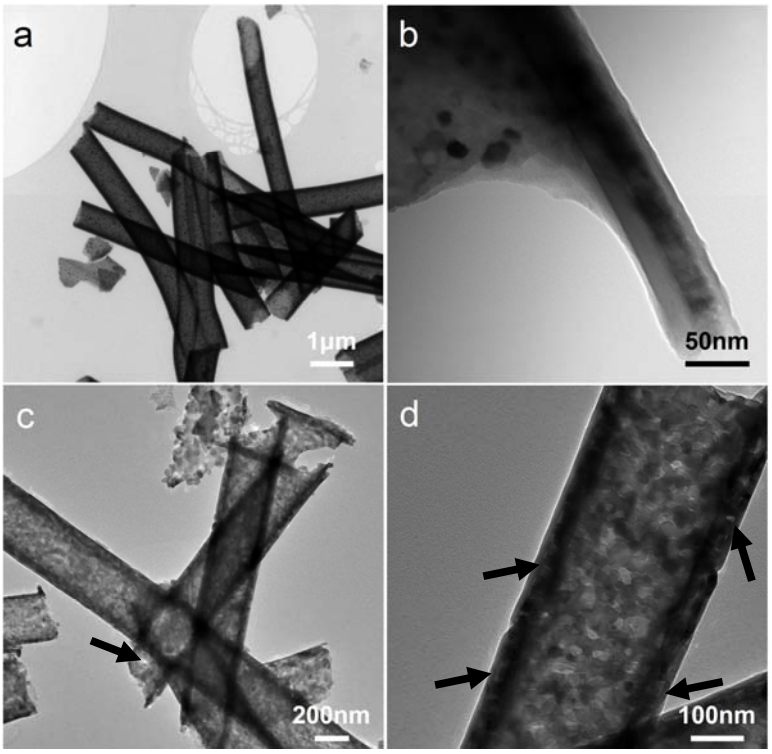


Figure 3.9 Representative TEM images of $Al_2O_3/ZnO/Al_2O_3$ microtubes formed by ALD on PVA microfibers. The images in (a) and (b) were obtained after annealing at 450˚C in air. The image in (b) permits direct visualization of the trilayered morphology consisting of a dark polycrystalline ZnO middle layer and lighter amorphous Al_2O_3 shells. The images in (c) and (d) were obtained after annealing at 700 °C for 12 h. Light spots (arrows in c and d) indicate void formed within the tubular structure. Unreacted excess ZnO partitions between the inner and outer shells.

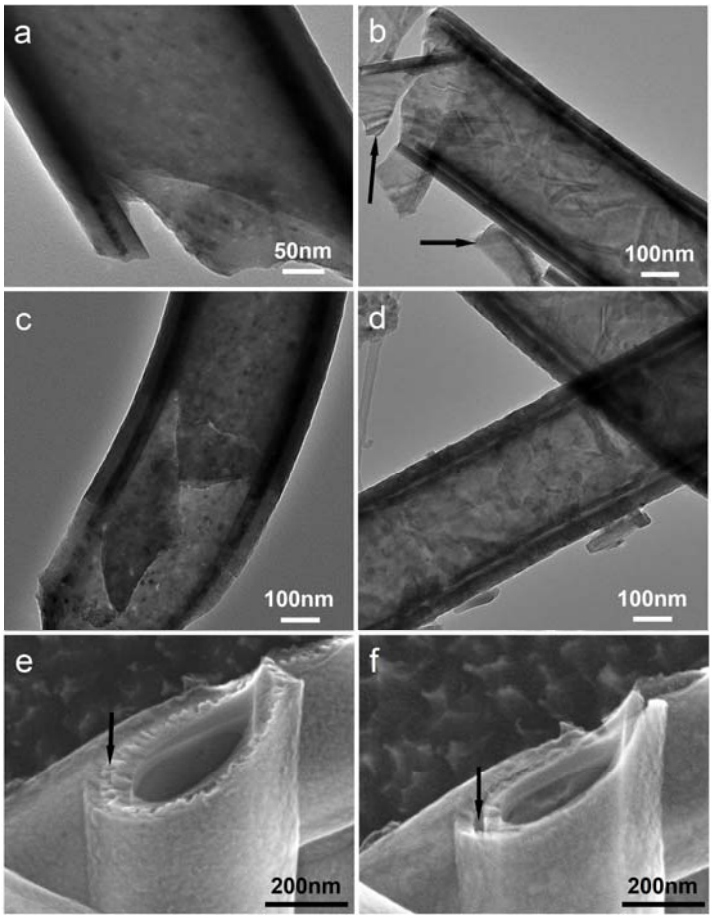


Figure 3.10 TEM images of (a) $Al_2O_3/ZnO/Al_2O_3$ microtubes (18/10/25 nm) after annealing in air at 450 °C. It shows the thin dark ZnO middle layer sandwiched between two lighter Al_2O_3 layers. b) after further annealing sample (a) at 700 °C for 12 h hollow middle gap in light contrast shown up instead. The arrows in (b) identify isolated pieces of the inner or outer shells as a consequence of microtube fracture. (c) $Al_2O_3/ZnO/Al_2O_3$ microtubes (18/21/39nm) after annealing in air at 450 °C, d) after further annealing at 700 °C for 12 h. (e) STEM image of the cross section view of $Al_2O_3/ZnO/Al_2O_3$ microtubes (35/30/38 nm) after annealing at 450 °C in air. The arrow points to the middle ZnO layer. (f) The tubes from (e) after further annealing at 700 °C for 12 h. The arrow inside indicates the formation of a thin gap between two polycrystalline $ZnAl_2O_4$ layers.

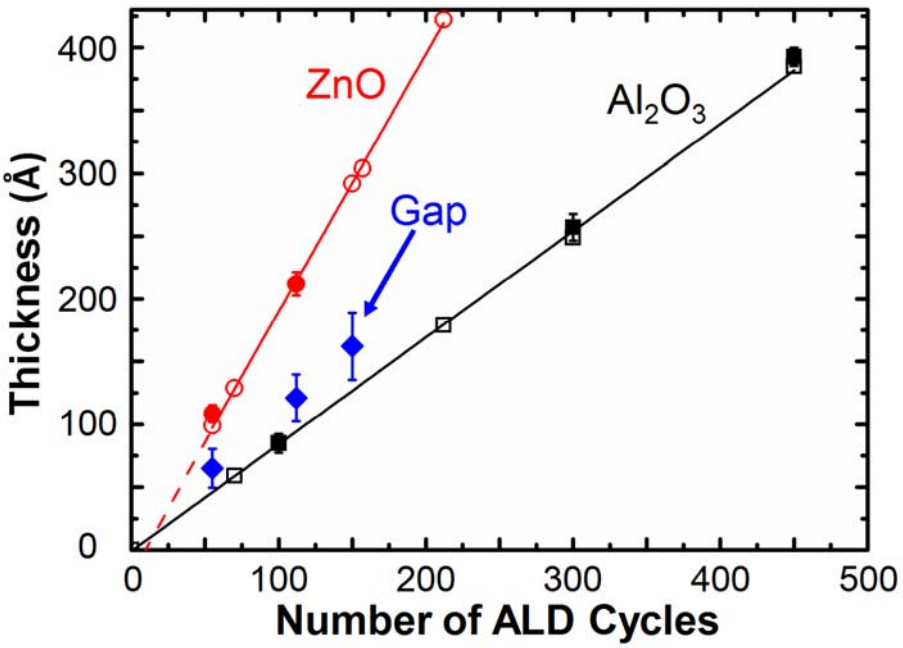


Figure 3.11 ALD layer thicknesses of ZnO and Al_2O_3 deposited on planar silicon wafers (measured by ellipsometry, open symbols) and microfibers (measured by TEM, filled symbols) after annealing at 450°C in air. Included is the Kirkendall gap thickness from three Al_2O_3/ZnO/Al_2O_3 microtubular specimen series (with different shell thicknesses 18/10/25 nm, 18/21/39 nm, 35/30/38 nm) annealed at 700°C and plotted as a function of the ALD cycle number for the ZnO layer. The error bars represent one standard deviation in the data.

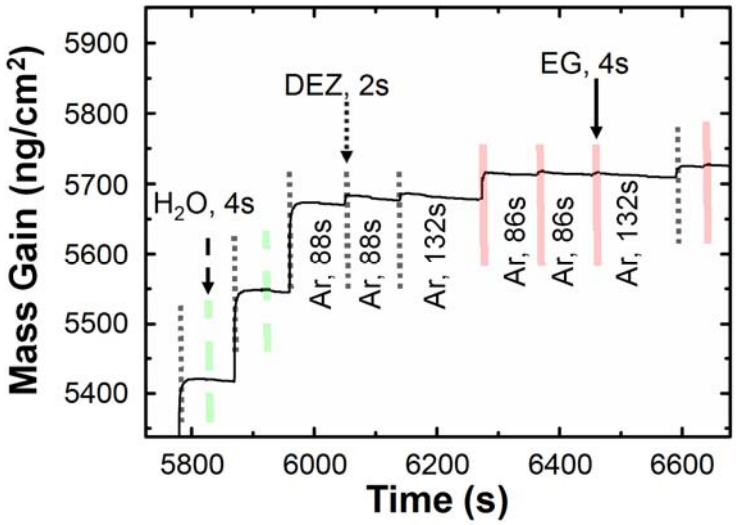


Figure 3.12 In-situ QCM results at 120˚C showing the effect of EG exposure on the -$OZn(C_2H_5)_{(s)}$ saturated surface produced during ZnO ALD. The DEZ dose is indicated by the dotted line, and the H_2O dose is indicated by the dashed line. The EG dose is shown with the shaded solid line. The first EG exposure result in mass uptake and surface saturation. The EG exposure results in significantly decreased mass uptake for subsequent DEZ exposure steps.

`

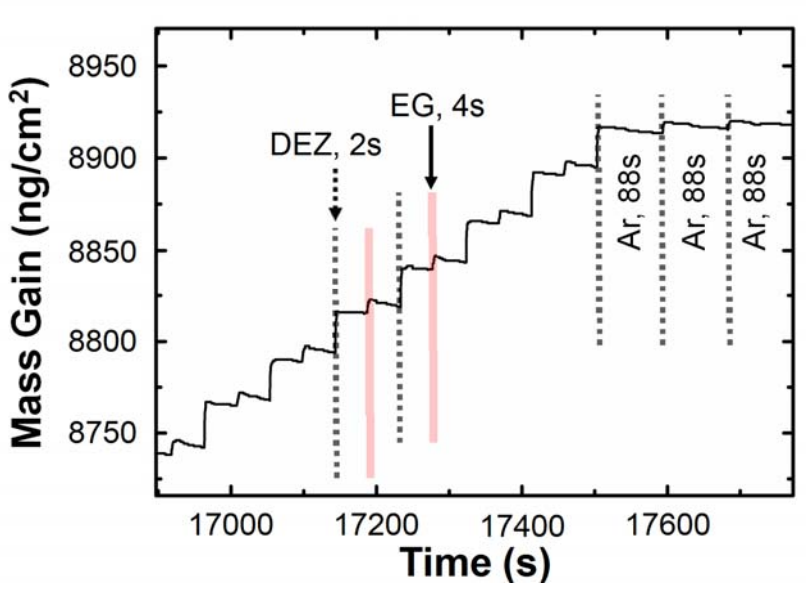


Figure 3.13 In-situ QCM results at 120˚C during steady–state molecular layer deposition. The DEZ dose is indicated by the dotted line, and the EG dose is shown with the shaded solid line. After an EG/Ar half cycle, the DEZ/Ar (2/88 s) half–cycle was repeated 3 times, resulting in mass uptake followed by approximately equivalent mass loss, indicative of DEZ physisorption/desorption.

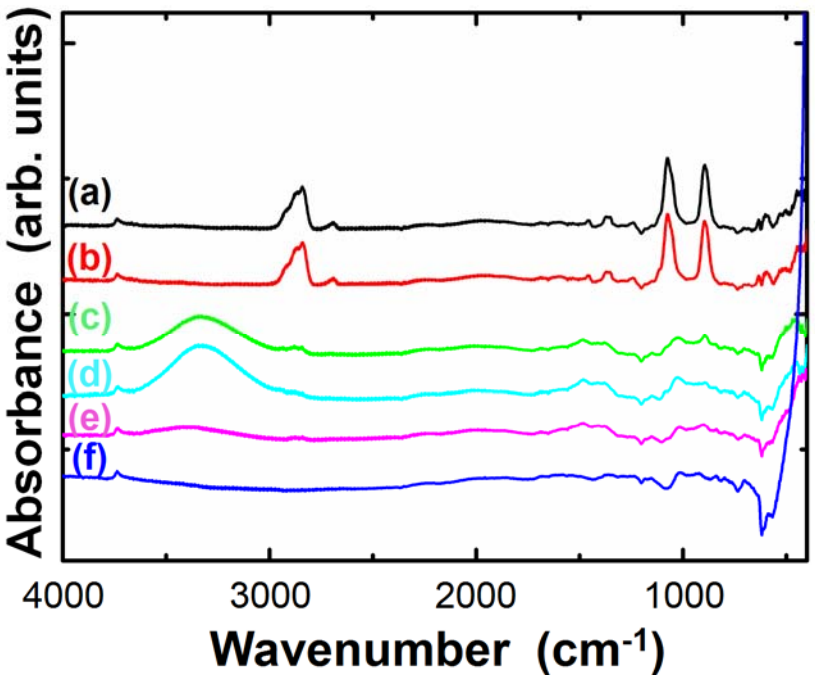


Figure 3.14 FTIR spectra collected from an example Zn-hybrid MLD film deposited using 800 cycles at 120 ˚C: (a) after immediate transfer to dry air; (b) in dry air for 3 days; (c) after exposure to ambient for 1 h; (d) after ~ 12 h in ambient; and (e) after annealing in ambient at 100 ˚C for ~ 2 h. Spectrum (f) is obtained from a ~ 45 nm thick ALD ZnO film deposited using 200 cycles at 120 ˚C.

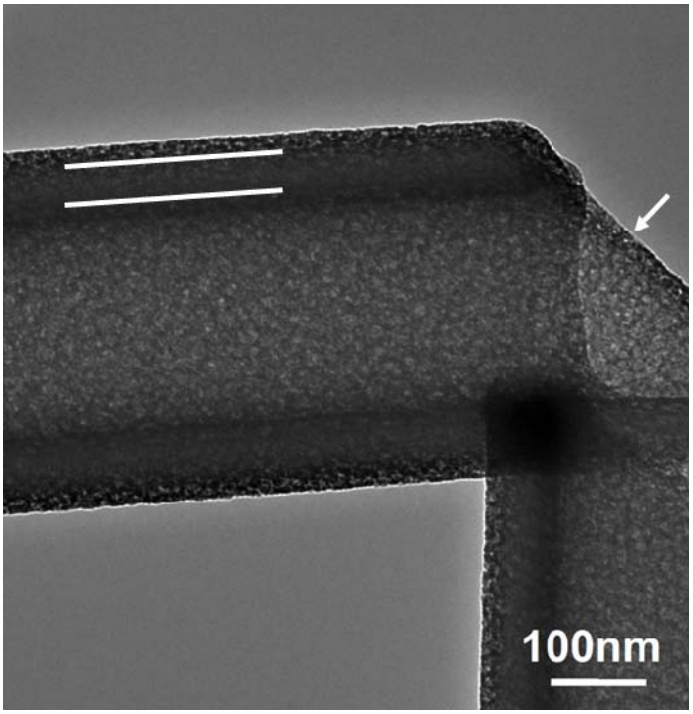


Figure 3.15 A transmission electron micrograph obtained from a hydrolyzed Zn - hybrid film deposited at 165 ˚C for 528 cycles onto two Al_2O_3 microtubes. The white lines depict the outline of the starting Al_2O_3 shell, and the right side of the image shows a region where the tube is broken allowing plan–view through the Zn–hybrid/Al_2O_3/Zn–hybrid laminate. The hydrolyzed Zn–hybrid MLD film is conformal and uniform with thickness ~20 nm. The white arrow indicates a point with high contrast suggesting through–holes present in the hydrolyzed film.

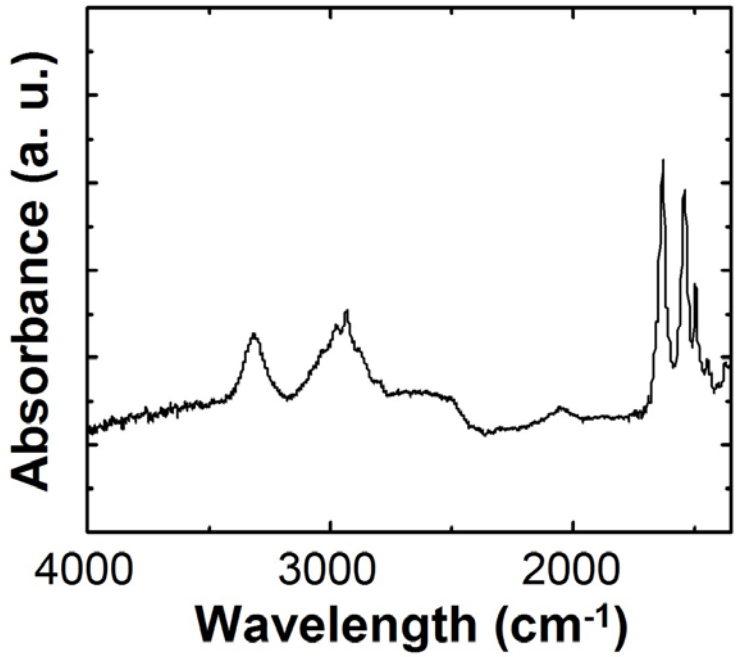


Figure 3.16 A typical FTIR spectrum of alkyl-aromatic polyamide deposited at 85 ºC for 150 cycles with thickness ~280 nm. The spectrum shows the characteristic peaks of the polyamide, (N-H stretching mode at 3310 cm^{-1}, C=O stretching mode at 1638 cm^{-1} and N-H bending mode at 1543 cm^{-1}).

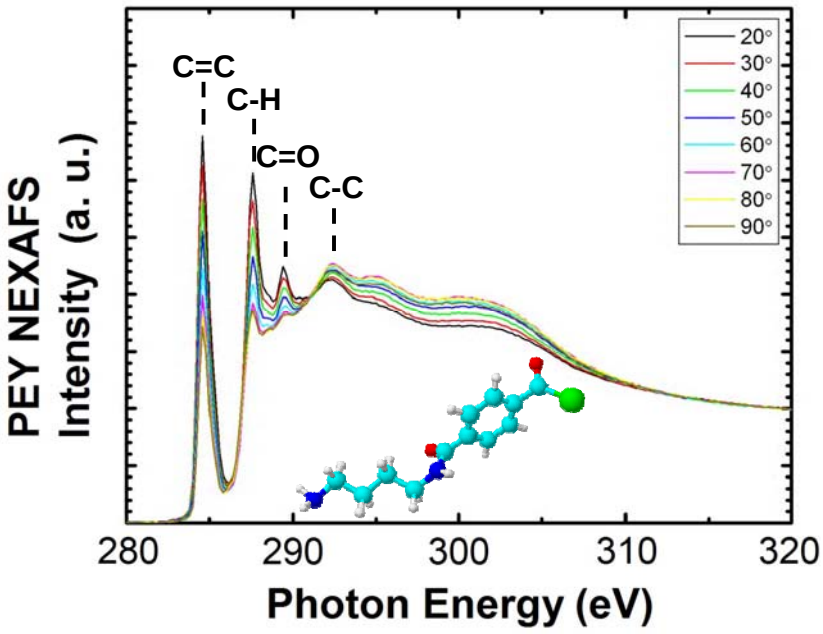


Figure 3.17 A typical near edge X-ray adsorption fine structure (NEXAFS) spectrum of alkyl-aromatic polyamide from different incident angles. The film deposited at 85ºC for 100 cycles with film thickness around 21nm. The spectrum shows chemical information from phenyl group and polyamide C=O bonding. According to the spectrum, the polyamide molecules are aligned and tilted quite a bit to the substrate normal as shown by the inset figure of molecule.

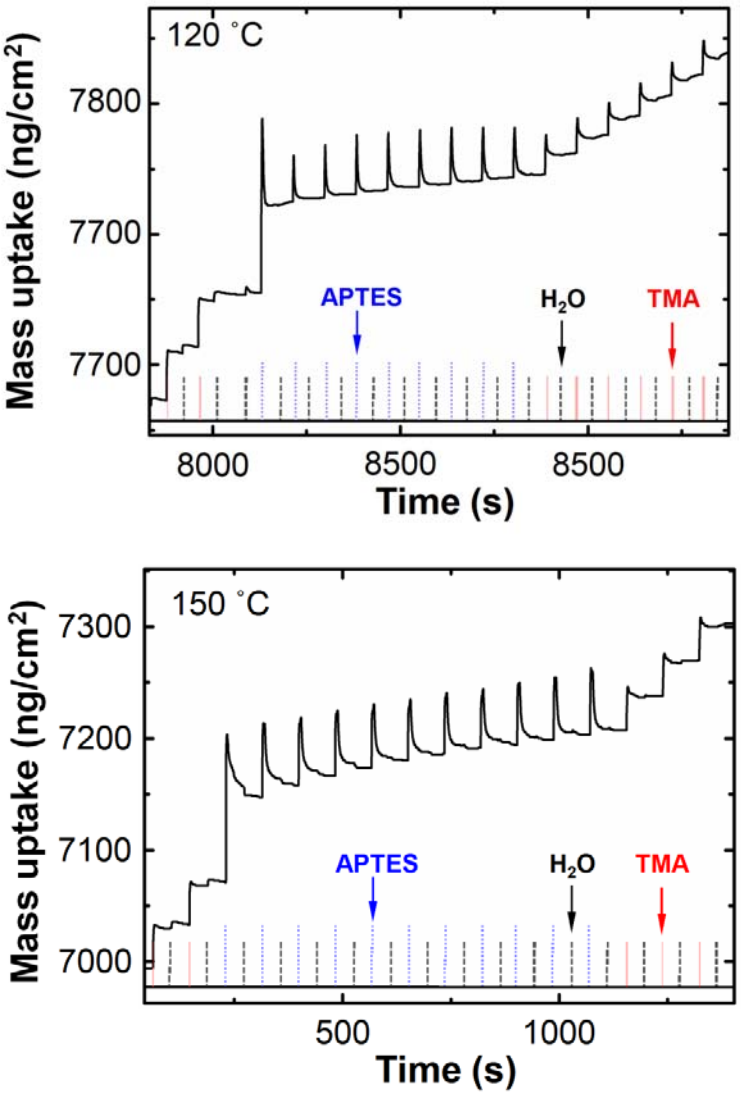


Figure 3.18 In-situ QCM measurement of mass uptake of atomic layer deposition of APTES/H_2O cycles (2/40/2/40 s) on Al_2O_3 ALD film. It shows steady state Al_2O_3 ALD process (2/40/2/40 s) at 120 ˚C and 150 ˚C and the sequential ALD process of APTES on the Al-OH terminated in-situ generated Al_2O_3 ALD film. At both temperatures, the first of the APTES/H_2O ALD cycle counts more than 50% of total mass uptake of SAM of APTES on the Al_2O_3 ALD film.

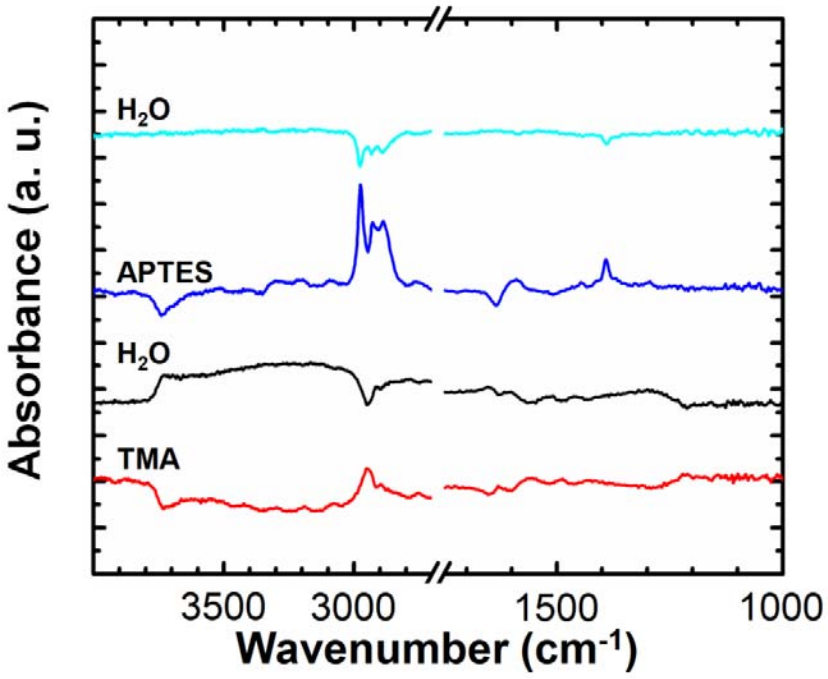


Figure 3.19 Representative in-situ FTIR spectra after sequential half cycles of TMA, H_2O, APTES and H_2O onto the Al-OH terminated Al_2O_3 ALD film coated anodic aluminum oxide substrate at 100 ˚C. Spectra were taken after more than 1mins purge time to make sure that all physical absorbed molecules were removed.

CHAPTER 4. Summary and Outlook

4.1 Summary and Outlook for Supercritical Carbon Dioxide Based Process

As illustrated in previous chapters, supercritical carbon dioxide has been used as the solvent for coating of metal[1] and metal oxides[2, 3] into the high aspect ratio, three dimensional structures of carbon nanotubes forest successfully.[4-14] However there are some shortcomings of supercritical fluid based process. Due to the high pressure and high temperature supercritical fluid environment, it is difficult for scientists to do in-situ monitor and analysis of the supercritical based process, which is critical for understanding and optimizing the process. In the future, the developments and applications of in-situ analytical tools for $scCO_2$ process would be a promising research field. Moreover due to harsh experiment conditions, the batch-type reactor systems are normally used for the $scCO_2$ process. The residue and byproducts from reaction cannot be removed continuously during the process. The process scale is also limited. The development of continuous $scCO_2$ process will attract some interest in the future. Due to the zero surface tension and good penetration ability of $scCO_2$, it could also find unique applications in following fields, 1) It would be good for $scCO_2$ to wet complex high aspect ratio substrates and modify the surface with advanced functionalities. 2) It could be used as cosolvent to decrease the viscosity of the materials, increase the heat transfer, mass diffusivity and rheological properties of the substrate and enable better processing properties. 3) As a solvent, $scCO_2$ could also be used for loading metal organic

precursor into the porous material to generate well dispersed heterogeneous catalyst materials.

4.2 Summary and Outlook for Atomic Layer Deposition

It has been demonstrated that low temperature ALD is a powerful way to coat polyvinyl alcohol electrospun fibers with uniform Al_2O_3 and $Al_2O_3/ZnO/Al_2O_3$ coating, which could be converted into complex nanostructures with thermal treatment.[15, 16] By judiciously adjusting the electrospinning parameters, the diameter, alignment and structure of the templates can be further tuned as desired.[17] In similar fashion, the ALD process could be extended to synthesize designer microtubes of other materials such as TiO_2,[18] more complex materials,[19] and others.

Because ALD is a self-limiting vapor-phase process, it can be easily adapted to construct, via reactive layering, large numbers of tube structures with nanoscale-precision dimensions and controlled composition with template technique. It opens a possibility to study the size dependent properties including magnetism,[20] mechanics,[21] electronics,[22]optics[23] and biomedicine,[24] associated with those nanomaterials. This technique is also promising for synthesizing more complex composite nanomaterials, for example coaxial nanotubules with shells having different functionalities.[25] Atomic layer deposition could also be performed onto inert surfaces (for example, polystyrene, polyethylene, polyimide, polypropylene, Teflon, etc) without reactive sites.[26-29] This unique nucleation and growth behavior of ALD growth of metal oxide films enable the incorporation of the metal

hydroxide ligands onto the inert substrate, which would be accessible by the following silane treatment for further surface engineering. Combined with the capability of coating substrates with complex structure, ALD process is promising for surface modification of complex substrates, for example the electrospun fibers, nanowoven fibers and other inert porous solid substrates. Moreover, the applications of ALD in micro/nano fluidics is another promising new field. The ALD process could incorporate different functionalities into the complex microfluidics channels. For example, ALD of ZnO and TiO_2 into microfluidics channel brings the optical catalytic properties into the channels. ALD of Pd, Pt, Ru etc into micro/nano fluidics will bring noble catalyst into the channel. W coating formed by ALD into microfluidic channel will enable local heating of the fluidics device. More advanced applications of ALD into micro/nanofluidics are possible with judicious tuning process parameters of the ALD. ALD of silanes monolayers would become a hot field to form dense monolayer of silane with desired functionality into substrates with 3D complex high aspect ratio structures.

4.3 Summary and Outlook for Molecular Layer Deposition

MLD process was demonstrated as a powerful way for fabrication of nylon, polyimide[30, 31] and Zinc based hybrid materials thin films.[32] For Zinc hybrid material, MLD was demonstrated as a good way to form uniform coating into complex structures.[32] The deposition behavior and surface chemistry were elucidated by using in-situ and ex-situ

techniques. The Zinc hybrid depositions depend strongly on the reaction temperatures. Those preliminary results stimulate some future research directions, which are listed in the following text.

At current research status, hybrid materials resulted from MLD process is still not stable in moisture environment as shown by the Zinc and Al based hybrid materials.[32, 33] However, the field of the MLD attract a lot of interests and many unknown questions needed to be explored. 1) New chemistries for MLD process need to be explored in order to find materials with stable and novel properties for the further applications. The chemistry of long chain organic silanes with ozone is a good direction to pursue.[34] Other organic silane related chemistries are also promising for stable hybrid materials with Si-O-C based matrix.[33] 2) By selectively removing the organic components through UV-Ozone treatment or thermal oxidation process, the MLD hybrid materials could be used as potential precursors for porous inorganic matrix. During the removing process, the collapse of the matrix would be big hindrance for the successful fabrication of porous structures. 3) Moreover, the combination of MLD and ALD could provide a strong tool for synthesis of organic/inorganic hybrid structure and nanolaminates with atomic level control of composition and structure. 4) MLD could be extended to form thin film of biomolecules,[35, 36] such as peptides etc. Combined with patterning technique, such as lithography,[35] microcontact techniques,[37, 38] higher density of patterned polymer thin film would be formed on substrates by using the MLD technique. 5)

Due to the self-limiting deposition behavior, MLD is a potential technique to modify the surface properties of 3D complex structures (such as carbon nanotubes (CNTs)[39]) with ultrathin uniform film of organics with control of thickness, chemistry. 6) The deposition mechanism of MLD process is crucial for applications. It is important to use different in-situ techniques to study the material properties. Combination of in-situ analysis (XPS, FTIR for chemistry, STM for ligand structure on the surface, QCM for the adsorption and desorption behavior etc) would give more insight of the MLD deposition behavior. Those information will provide basis for theoretical modeling of the MLD deposition process.

REFERENCES

1. Peng, Q.; Spagnola, J. C.; Parsons, G. N., *Journal of the Electrochemical Society* **155,** D580-D582 (2008).

2. Peng, Q.; Hojo, D.; Park, K. J.; Parsons, G. N., *Thin Solid Films* **516,** 4997-5003 (2008).

3. Peng, Q.; Spagnola, J. C.; Daisuke, H.; Park, K. J.; Parsons, G. N., *Journal of Vacuum Science & Technology B* **26,** 978-982 (2008).

4. Cabanas, A.; Long, D. P.; Watkins, J. J., *Chemistry Of Materials* **16,** 2028-2033 (2004).

5. Cansell, F.; Aymonier, C.; Loppinet-Serani, A., *Current Opinion In Solid State & Materials Science* **7,** 331-340 (2003).

6. Desmoulins-Krawiec, S.; Aymonier, C.; Loppinet-Serani, A.; Weill, F.; Gorsse, S.; Etourneau, J.; Cansell, F., *Journal Of Materials Chemistry* **14,** 228-232 (2004).

7. Long, D. P.; Blackburn, J. M.; Watkins, J. J., *Advanced Materials* **12,** 913-915 (2000).

8. Fu, L.; Liu, Z. M.; Liu, Y. Q.; Han, B. X.; Hu, P. G.; Cao, L. C.; Zhu, D. B., *Advanced Materials* **17,** 217-+ (2005).

9. Fu, L.; Liu, Z. M.; Liu, Y. Q.; Han, B. X.; Wang, J. Q.; Hu, P. G.; Cao, L. C.; Zhu, D. B., *Journal Of Physical Chemistry B* **108,** 13074-13078 (2004).

10. Crowley, T. A.; Ziegler, K. J.; Lyons, D. M.; Erts, D.; Olin, H.; Morris, M. A.;

Holmes, J. D., *Chemistry Of Materials* **15,** 3518-3522 (2003).

11. Pai, R. A.; Watkins, J. J., *Abstracts Of Papers Of The American Chemical Society* **225,** U136-U136 (2003).

12. Pai, R. A.; Humayun, R.; Schulberg, M. T.; Sengupta, A.; Sun, J. N.; Watkins, J. J., *Science* **303,** 507-510 (2004).

13. Ye, X. R.; Lin, Y. H.; Wang, C. M.; Engelhard, M. H.; Wang, Y.; Wai, C. M., *Journal Of Materials Chemistry* **14,** 908-913 (2004).

14. Ye, X. R.; Lin, Y. H.; Wang, C. M.; Wai, C. M., *Advanced Materials* **15,** 316-319 (2003).

15. Peng, Q.; Sun, X. Y.; Spagnola, J. C.; Hyde, G. K.; Spontak, R. J.; Parsons, G. N., *Nano Letters* **7,** 719-722 (2007).

16. Peng, Q.; Sun, X. Y.; Spagnola, J. C.; Saquing, C.; Khan, S. A.; Spontak, R. J.; Parsons, G. N., *Acs Nano* **3,** 546-554 (2009).

17. Li, D.; Xia, Y. N., *Advanced Materials* **16,** 1151-1170 (2004).

18. Kim, G. M.; Lee, S. M.; Michler, G. H.; Roggendorf, H.; Gosele, U.; Knez, M., *Chemistry of Materials* **20,** 3085-3091 (2008).

19. Santala, E.; Kemell, M.; Leskela, M.; Ritala, M., *Nanotechnology* **20,** (2009).

20. Bachmann, J.; Jing, J.; Knez, M.; Barth, S.; Shen, H.; Mathur, S.; Gosele, U.; Nielsch, K., *Journal of the American Chemical Society* **129,** 9554-+ (2007).

21. Lee, S. M.; Pippel, E.; Gosele, U.; Dresbach, C.; Qin, Y.; Chandran, C. V.; Brauniger, T.; Hause, G.; Knez, M., *Science* **324,** 488-492 (2009).

22. Nazzal, A.; Fu, H. X., *Journal of Computational and Theoretical Nanoscience* **6,** 1277-1289 (2009).

23. Luo, M.; Cheng, K.; Weng, W. J.; Song, C. L.; Du, P. Y.; Shen, G.; Xu, G.; Han, G. R., *Journal of Physics D-Applied Physics* **42,** (2009).

24. Napierska, D.; Thomassen, L. C. J.; Rabolli, V.; Lison, D.; Gonzalez, L.; Kirsch-Volders, M.; Martens, J. A.; Hoet, P. H., *Small* **5,** 846-853 (2009).

25. Mitchell, D. T.; Lee, S. B.; Trofin, L.; Li, N. C.; Nevanen, T. K.; Soderlund, H.; Martin, C. R., *Journal of the American Chemical Society* **124,** 11864-11865 (2002).

26. Kemell, M.; Farm, E.; Ritala, M.; Leskela, M., *European Polymer Journal* **44,** 3564-3570 (2008).

27. Wilson, C. A.; Grubbs, R. K.; George, S. M., *Chemistry of Materials* **17,** 5625-5634 (2005).

28. Groner, M. D.; George, S. M.; McLean, R. S.; Carcia, P. F., *Applied Physics Letters* **88,** 3 (2006).

29. Liang, X. H.; King, D. M.; Li, P.; Weimer, A. W., *Journal of the American Ceramic Society* **92,** 649-654 (2009).

30. Yoshimura, T.; Ito, S.; Nakayama, T.; Matsumoto, K., *Applied Physics Letters* **91,**

(2007).

31. Du, Y.; George, S. M., *Journal of Physical Chemistry C* **111,** 8509-8517 (2007).

32. Peng, Q.; Gong, B.; VanGundy, R. M.; Parsons, G. N., *Chemistry of Materials* **21,** 820-830 (2009).

33. George, S. M.; Yoon, B.; Dameron, A. A., *Accounts of Chemical Research* **42,** 498-508 (2009).

34. Lee, B. H.; Ryu, M. K.; Choi, S. Y.; Lee, K. H.; Im, S.; Sung, M. M., *Journal of the American Chemical Society* **129,** 16034-16041 (2007).

35. Wang, Y. L.; Chang, Y. C., *Advanced Materials* **15,** 290-293 (2003).

36. Chang, Y. C.; Frank, C. W., *Langmuir* **14,** 326-334 (1998).

37. Park, K. J.; Parsons, G. N., *Applied Physics Letters* **89,** (2006).

38. Park, K. J.; Doub, J. M.; Gougousi, T.; Parsons, G. N., *Applied Physics Letters* **86,** (2005).

39. Tasis, D.; Tagmatarchis, N.; Bianco, A.; Prato, M., *Chemical Reviews* **106,** 1105-1136 (2006).

CHAPTER 5 is a reprint of a manuscript published in Thin Solid Films

CHAPTER 5. Low-Temperature Metal Oxide Film Deposition and Reaction Kinetics in Supercritical Carbon Dioxide

Qing Peng,[†] Daisuke Hojo,[†] Kie Jin Park[§] and Gregory N. Parsons[†*]

[†]Department of Chemical and Biomolecular Engineering,
North Carolina State University, Raleigh, North Carolina 27695, USA

[§]Novellus Systems, Inc.
4000 North First Street, San Jose, California 95134, USA

ABSTRACT

An effective method is developed for low temperature metal oxide deposition through thermal decomposition of metal diketonates in supercritical carbon dioxide ($scCO_2$) solvent. The rates of $Al(acac)_3$ (Aluminum acetyl acetonate) and $Ga(acac)_3$ (Gallium acetyl acetonate) thermal decomposition in $scCO_2$ to form conformal Al_2O_3 and Ga_2O_3 thin films on planar surfaces were investigated. The thermal decomposition reaction of $Al(acac)_3$ and $Ga(acac)_3$ were found to be initialized at ~ 150 °C and 160 °C respectively, in $scCO_2$ solvent compared to ~ 250 °C and 360 °C in analogous vacuum-based processes. By measuring the temperature dependence of the growth rates of metal oxide thin films, the apparent activation energy for the thermal decomposition of $Al(acac)_3$ in $scCO_2$ is found to be 68±6 kJ/mol, in comparison with 80-100 kJ/mol observed for the corresponding vacuum-based thermal decomposition reaction. The enhanced thermal decomposition rate in $scCO_2$ is ascribed to the high density solvent which effectively reduces the energy of the polar transition states in the reaction pathway. Preliminary results of thin film deposition of other metal oxides including ZrO_x, FeO_x, Co_2O_3, Cr_2O_3, HfO_x from thermal decomposition of metal diketonates or fluorinated diketonates in $scCO_2$ are also presented.

Keywords: *Supercritical carbon dioxide ($scCO_2$), Metal Oxides, Solvation Energy, Thermal decomposition, Metal Diketonates;*

CHAPTER 5 is a reprint of a manuscript published in Thin Solid Films

5.1 Introduction

Metal oxide thin films have important applications including dielectrics for semiconductor devices, thermal insulation, filtration, catalyst supports, coatings, sensors and others [1-4]. A wide range of processes have been developed to deposit metal oxide thin films, including chemical vapor deposition (CVD) [5-7], spray thermal decomposition [8], atomic layer deposition (ALD) [3, 9], and others. However CVD usually requires high reaction temperature (T>400 °C) to enable the metal-containing precursor to thermally dissociate at or near the growth surface, even in the presence of oxidizing agents such as O_2, O_3 and H_2O [5-7]. Atomic layer deposition can provide very conformal and uniform coatings, but it is not always amenable to low temperature processing, and deposition rates are relatively slow [3, 9]. Spray pyrolysis techniques are also of interest, but they typically suffer from an inherent inability to coat high aspect ratio structures [8].

Supercritical fluids have unique properties including zero surface tension, low viscosity and high diffusivity (analogous to vapors) and high density (similar to liquids) [10]. These unique properties allow supercritical fluids to wet high aspect ratio structures, dissolve metal organics, remove impurities from depositing surfaces, and enable conformal deposition of thin film coatings. In particular, supercritical carbon dioxide ($scCO_2$) has a reasonably accessible critical point (P_C=7.4 MPa, T_C=31 °C) and is non-toxic and environmentally benign. To date, a number of metal thin films including Pt, Cu, Co, Ni and others have been

deposited from $scCO_2$-based process using suitable precursors on different substrates [10-12]. However, the deposition of metal oxides in $scCO_2$ is much less studied [1, 4, 13, 14]. Recently, Uchida et al. [1] observed that the deposition of TiO_2 onto native oxide Si by pyrolysis of $Ti(O\textit{i}\text{-}Pr)_2(dpm)_2$ could be carried out at much lower deposition temperature (50-120 °C) in $scCO_2$-based process than in a conventional CVD process (>210 °C). However, no characterization or analysis of the enhanced TiO_2 deposition kinetics in $scCO_2$-based process was presented.

Previous work has shown that supercritical fluids (including $scCO_2$) can uniquely affect critical chemical reaction rates in homogeneous systems, as well as in heterogeneous catalysis [15-18]. For example, the work of Johnston and Haynes [19] helped clarify the extreme solvent effects in homogeneous reactions by analyzing in detail the homogeneous pyrolysis of α-chlorobenzyl methyl ether. That report showed a dramatic decrease in the homogeneous decomposition activation energy when the reaction was carried out in supercritical 1,1-difluoroethane as comparison to other liquid solvents such as carbon tetrachloride. The pronounced effect of pressure of supercritical fluids on the reaction rate constant was interpreted in term of a large negative activation volume within the solvent clustering theory [19].

While several studies have characterized solvent-enhancement effects in homogeneous reactions [15-18], there are few previous results demonstrating details of

supercritical solvent effects in heterogeneous film deposition reaction kinetics. In this article, the kinetics of low temperature pyrolysis of metal-organics is characterized in $scCO_2$, producing uniform coatings of metal oxide thin films. Specifically, Al_2O_3 and Ga_2O_3 deposition in $scCO_2$ from the pyrolysis of metal diketonates is analyzed as a model system to study the kinetics of heterogeneous $scCO_2$-based thin film deposition, and to understand the unique effects of $scCO_2$ solvent on the deposition process. We found that the $scCO_2$ solvent can help lower the energy barrier of the pyrolysis reaction and thus decrease the pyrolysis temperature of metal organics, when compared with the corresponding vacuum-based pyrolysis reaction [3, 5]. Moreover the observed effect of $scCO_2$ on the enhanced rate of pyrolysis of metal diketonates is consistent with theoretical understanding of solvent effects on homogeneous reaction kinetics [18-20], including Onsager's reaction field theory[18, 19]. The results and analysis presented here lead to an improved comprehension of heterogeneous thin film deposition reaction systems.

5.2 Experiment

Native oxide Si(100) wafers were used as substrates for deposition, and were prepared by wet cleaning in BakerClean® JTB-100 solution (Mallinckrodt Baker Inc), followed by rinsing in deionized water, then drying in a N_2 flow. Metal containing precursors utilized in this study including aluminum acetylacetonate (99 %) ($Al(acac)_3$) [$Al(C_5H_7O_2)_3$], $Ga(acac)_3$, $Fe(acac)_3$, $Zn(acac)_2$, $Zr(acac)_4$, $Co(acac)_3$, $Cr(acac)_3$, $Hf(acac)_4$, aluminum

CHAPTER 5 is a reprint of a manuscript published in Thin Solid Films

hexafluoroacetylacetonate ($Al(hfac)_3$) [$Al(C_5HO_2F_6)_3$] and $Zr(hfac)_4$, were used as received (Strem Chemicals). Coleman grade CO_2 (99.99 %) (National Welders) was used in experiments. Deposition reactions were carried out in a homemade stainless steel batch type reactor with a total volume of 110 milliliters as illustrated schematically in Figure 5.1.

In a typical experiment, a piece of pretreated native oxide Si substrate (~ 1 cm×1.5 cm) was fixed onto the heating block, which was attached to a gland fitting (Conax Buffalo Corp.), as shown in Figure 5.1. Three cartridge heaters (Tempco) were fit into the heating block, enabling substrate surface temperature to be controlled by using a feedback thermocouple fit through the gland fitting. A predetermined amount of precursor was weighed and placed in the reactor with the substrate holder before sealing. Air was purged from the reactor by flowing low pressure CO_2 through a vent valve for 5 min at a temperature of ~ 70-100 °C. The reactor was then pressurized with CO_2 and heated to the predetermined set point (P=21 MPa, T=100 °C). Subsequently, the system was kept stable for 2 h to allow the precursor to dissolve. The typical precursor concentration was approximately 170 μmol/L for $Al(acac)_3$ and 230 μmol/L for $Ga(acac)_3$. For some experiments, to examine the effect of oxidizing species, oxygen or water was intentionally added to the reaction. For these experiments, after the precursor was loaded into the clean vessel, the vessel was purged with low pressure CO_2 for ~ 10 min to remove ambient air. The vessel was then filled with high purity dry air or a small known volume of deionized water and subsequently sealed and filled

with high pressure CO_2. The concentration of oxidant was then estimated using the known volume of the system.

After the precursor dissolution time, the temperature of the substrate was increased to the growth temperature set point. This transition occurred relatively rapidly, typically within 1 min. After a predetermined reaction time, the cartridge heaters were turned off and the temperature of the substrate quickly decreased to <150 °C, typically within 1 min. For higher substrate temperatures, the reactor temperature was observed to increase above the set wall temperature of 100 °C during the first 20 min, but temperature generally stayed below ~ 190 °C. After the set deposition time, the effluent from the reactor was vented through an activated carbon bed, and fresh $scCO_2$ was used to purge the reactor to remove byproducts and remaining precursor in the system. The reactor was allowed to cool, and the samples were then removed from the reactor and characterized.

Growth rate was determined by measuring the sample thickness for the known growth time using ellipsometry (Rudolf/Auto EL) and/or surface profilometer (Tencor Alpha-Step 500). Ellipsometry was performed using 632.8 nm incident laser wavelength at an angle of 70^{o}, using n and k values of 1.79 and 0, respectively for Al_2O_3. Transmission Fourier transform infrared spectroscopy (FTIR) was used to characterize the film composition. A ThermoNicolet IR bench with a deuterated tri-glycine sulfate detector (KBr beam splitter) was used in the transmission mode. The typical measuring condition of FTIR

was 256 scans at 8 cm^{-1} resolution, and the measuring chamber was purged using purified dry air. A background spectrum was collected using the same wafer before the deposition. Auger electron spectroscopy with 5 keV primary electrons was used to measure the atomic composition of the deposited films. Film surface morphology was studied by a Nanoscope IIIa atomic force microscope (Digital Instruments) operated in tapping mode. Samples were measured with a scanning frequency of 1 Hz. Film roughness was characterized as root mean square (rms) values. Adhesion of deposited films was evaluated with the adhesive tape test.

5.3 Results

Figure 5.2 shows transmission FTIR results from a typical film deposited at 150 °C and 25-26 MPa for 30 min from pyrolysis of $Al(acac)_3$, before and after annealing in air at 600 °C for 15 min. The peaks generally confirm the presence of Al_2O_3 and some carbon contamination in the deposited film [2, 5, 13]. In the as-deposited film, the absorption peak near 1000 cm^{-1} from C-O-C vibration, peaks in the range of 1200-1750 cm^{-1} from C-O, C-C and C=C, and the peak around 2900 cm^{-1} from stretching vibration of $-CH_2$, $-CH_3$ or -CH, are likely due to carbon impurity from partially dissociated acetyl acetonate ligands [2, 5, 13]. The small broad peak at 3000-3600 cm^{-1} is due to the stretching modes of -OH related to H_2O molecules and -OH species [5, 13]. The stretching modes of Al-O-Al are visible as the broad peaks between 500 and 1000 cm^{-1} [5, 13]. After annealing the sample at 600 °C for 15 min in air, a decrease is observed in the carbonate related peaks at ~ 2900 cm^{-1} and between

1000 and 1800 cm^{-1}, and an increase is seen for the peaks of Al-O-Al. This is likely due to further decomposition of partially dissociated ligands at 600 °C in air to form more Al-O-Al bonding. At the same time Si-O peaks appear in the spectrum at ~ 1100 cm^{-1} because oxygen will diffuse to the Si substrate and form SiO_2 during the annealing [2, 5]. Carbon-containing contaminants observed in the IR before annealing are likely thermally decomposed to form carbon in the film that is not prominently visible in the IR spectrum or to form other carbon containing volatile byproducts.

An Auger electron spectrum (AES) of an Al_2O_3 film in the as-deposited state is presented in Figure 5.3(a). The film was deposited at 185 °C and 25-26 MPa for 50 min from pyrolysis of $Al(acac)_3$. The AES survey scan shows Al-KLL peaks at ~ 1300-1350 eV, O-KLL features at ~ 480-490 eV and C-KLL peaks at ~ 250-265 eV [21, 22]. As demonstrated in Figure 5.3(c), the primary Al-KLL peak is at 1350 eV, which is shifted from literature values for the Al-KLL peaks (~ 1360-1390 eV) [21], possibly due to carbon in the films or surface charging effects. No significant Si peak is detected at 96 eV, consistent with the expected film thickness of ~ 100 nm which is sufficient to block any Auger signal from the Si substrate. The Auger and FTIR data are qualitatively consistent, indicating Al-O-Al bonding as well as carbon at a level of ~ 10 atomic % in the as-deposited films. The C fraction was determined from the intensity of the C peak relative to that of the Ga and O peaks [21].

CHAPTER 5 is a reprint of a manuscript published in Thin Solid Films

Figure 5.3(a) also shows a typical AES survey scan for Ga_2O_3 thin films deposited from pyrolysis of $Ga(acac)_3$ at 200 °C and 28-32 MPa for 10 min with thickness ~ 150 nm. Peaks due to Ga-LMM (990-1070 eV), O-KLL (~ 450-480 eV) and C-KLL (~ 250-265 eV) Auger transitions are observed in the spectrum [21, 22]. In Figure 5.3(b), a high resolution scan in the Ga-LMM peak region provides evidence for the primary peak at ~ 1020 eV and Ga satellite peaks between 850 and 1070 eV. Auger spectra for the Ga_2O_3 film in Figure 5.3(a) and 5.3(b) indicate the film composition being primarily Ga_2O_3 with ~ 10 at.% carbon impurity.

Figure 5.4 shows the thicknesses of Al_2O_3 thin films deposited for several different reaction times at a range of deposition temperatures. Several sample measurements were made at each data point and error bars representing the typical uncertainty in film thickness are shown on representative data points. At the lower studied deposition temperatures (185 °C, 180 °C and 150 °C) the thickness of the deposited film increased linearly with reaction time up to ~ 40-50 min. For the higher deposition temperatures investigated (220 °C and 250 °C) the film thickness increases approximately linearly with reaction time at the early stage of deposition (<5 min). For longer deposition times, the film thickness continued to increase and eventually saturated. This saturation in film thickness at higher deposition temperatures is ascribed to the decrease of precursor concentration as the deposition reaction proceeds. This is consistent with the observed effect of precursor concentration on the growth

rate, shown in Figure 5.5 and described below. This interpretation is also in agreement with a simple mole-balance analysis of the precursor loaded in the reaction vessel. Specifically, if the complete mass of $Al(acac)_3$ precursor initially in the system (concentration ~ 170 μmol/L) leads to deposition on the area of the heated sample and substrate holder (~ 15 cm^2), at most ~ 500 nm of film deposition would result. This value is approximately a factor of two larger than the saturation thickness extrapolated from the trend in the growth data of high-temperature (200 °C and 250 °C) shown in Figure 5.4. The factor of two difference is consistent with the observation that at high temperatures, pyrolytic reaction of precursor occurred in the $scCO_2$ phase as well as on the reactor walls.

The effect of initial precursor concentration on the film growth rate is shown explicitly in Figure 5.5. Specifically, the amount of $Al(acac)_3$ precursor loaded into the reaction cell was varied, corresponding to concentrations ranging from 25 to 170 μmol/L, and the thickness of growth at 250 °C was measured after a fixed growth time (3 min). Thickness measurements were made on all the resulting samples, and typical error bars were included on representative data points. The growth rate is found to increase linearly with initial precursor concentration, and the linear regression shown in the figure results in an intercept at the origin. The results in Figure 5.5 indicate that the initial growth rate is determined by the precursor impingement flux on the surface, which is linearly proportional to the precursor concentration.

CHAPTER 5 is a reprint of a manuscript published in Thin Solid Films

Regarding effects of oxidizer addition, when ~ 10 μL of deionized H_2O was added to the $Al(acac)_3$ dissolved in $scCO_2$ at 120 °C, significant homogeneous reaction was observed. Specifically, the reaction produced a large amount of white particle precipitation, the solution color changed from yellow-brown to transparent, and no visible film deposition was observed on the substrate surface.

Measurements of thickness versus growth time were carried out for Ga_2O_3 deposition from pyrolysis of $Ga(acac)_3$ with no oxidizer present, and the initial growth rate is shown in an Arrhenius plot in Figure 5.6. For each data point several sample measurements from different experimental runs were averaged, and typical error bars are shown on representative data points. The slope of the lines in Figure 5.6 result in overall apparent activation energies of 68±6 kJ/mol and 84±7 kJ/mol for $scCO_2$-based deposition of Al_2O_3 and Ga_2O_3, respectively. The observed saturation of growth rate at higher temperature for Ga_2O_3 is ascribed to a transition from kinetically-limited growth to mass-transfer-limited growth. All of the Al_2O_3 and Ga_2O_3 films deposited on silicon oxide surfaces showed good adhesion (i.e. they remained intact upon an adhesive tape test) with a reflective and smooth surface texture, as confirmed by AFM measurement (rms is ~ 1-2 nm for a 170 nm as-deposited film)

In addition to $Al(acac)_3$ and $Ga(acac)_3$, pyrolysis reaction of other metal organics (listed in Table 5.1) were also investigated in the $scCO_2$ system. Routine deposition was not obtained for all precursors studied. Generally, the deposition rate was found to depend on the

nature of the precursor, including the degree of precursor solubility in $scCO_2$ and the precursor thermal stability. A summary of the results with other precursors is included in Table 5.1.

5.4 Discussion

The apparent kinetics of pyrolysis of $Al(acac)_3$ in vacuum-based processing has been investigated by several groups [23, 24]. Typically, in a vacuum-based process, pyrolysis of $Al(acac)_3$ initiates at temperatures of ~ 250 °C, and shows an apparent activation barrier of 80-100 kJ/mol [23, 24]. The results shown here in $scCO_2$ indicate that pyrolysis of $Al(acac)_3$ can take place at temperature as low as 150 °C with an overall kinetic barrier of 68±6 kJ/mol. For the case of $Ga(acac)_3$ pyrolysis in a vacuum process, detailed kinetic data for precursor thermal decomposition is not readily available. However, the results of atomic layer deposition (ALD) studies [3] using $Ga(acac)_3$ to form Ga_2O_3 indicate that the preferred deposition temperature is ~ 360 °C. In the ALD processes, adsorption and oxidation reactions of the precursor proceed sequentially under self-limiting conditions, and the preferred ALD temperature corresponds to the point where the precursor reacts with the surface but does not fully decompose. This suggests that in the vacuum-based process, substantial pyrolysis of $Ga(acac)_3$ will proceed only at temperatures in excess of 360 °C. In the $scCO_2$-based process reported here, deposition from the pyrolytic reaction of $Ga(acac)_3$ can be initialized in $scCO_2$ at a temperature as low as 160 °C. The results in Figure 5.6 show that the reaction barrier for

Ga_2O_3 deposition in the reaction rate limited regime at low temperature is 84±7 kJ/mol, and the barrier is ~ 20-30 kJ/mol at higher temperatures in the diffusion controlled regime.

Several possible mechanisms could be considered to understand the enhanced kinetics of heterogeneous thermal decomposition of the precursors in the $scCO_2$-based process. Firstly, the solvation effect of $scCO_2$ may enhance the rate of ligand removal from the growth surface resulting in an increased density of reactive sites available for growth compared to the solvent-free process at the same reaction temperature. However, since the reaction rate is linearly dependent on the homogeneous precursor concentration (as shown in Figure 5.5), one can infer that the surface ligand removal rate is not the rate determining step in the heterogeneous decomposition reaction. Another possibility is that oxygen impurities (including O_2 and/or H_2O) present in the $scCO_2$ solvent could affect the reaction kinetics. The CO_2 was known to contain some oxygen (O_2 + Ar <9 ppm) and H_2O (<10 ppm) impurities as delivered to the reactor from the source. For the reactor pressure and volume used, this corresponds to <10 μmol of total impurity in the reactor system, which is 10X less than the molar amount of oxygen present in the total mass of $Al(acac)_3$ precursor loaded into the reactor. While some oxygen may be present from the impurities, most of the film product is expected to result from pyrolysis of the precursor. Furthermore, the results of intentional oxidizer addition suggest that oxidizers promote homogeneous reactions at high density, supporting the conclusion that the observed film deposition proceeds primarily from direct

pyrolysis of metal diketonates on the substrate surface.

Based on the above results and discussion, we conclude that the relatively facile oxide deposition reaction observed at low temperature in $scCO_2$ proceeds because the supercritical fluid provides solvation energy that affects the transition state for the precursor pyrolysis reaction on the heated substrate surface. The detailed chemistry of pyrolysis of $Al(acac)_3$ has been previously studied in vacuum and atmosphere pressure systems [23-26]. It is generally understood that the molecules of $Al(acac)_3$ have an enol-keto equilibrium, and both the enol and keto types of $Al(acac)_3$ can be pyrolyzed to produce Al_2O_3 and other byproducts through a postulated polar transition state that is the rate-determining step as shown in Scheme 5.1 [23, 24]. During the pyrolytic reaction, the acetylacetonate ligands will break at the carbon-enolic O bond, leaving the metal (M)-O structure available to form metal oxides [23, 25, 27]. This reaction is favorable in most $M(acac)_x$ systems because the bonding energy of M-O is higher than the carbon-enolic oxygen [23, 24]. Moreover, since the $scCO_2$ solvent is inert and is not expected to react at temperatures <500 °C [10, 11, 14], the scheme for the pyrolytic reaction should be similar for the vacuum-based and $scCO_2$-based processes. Several theoretical analyses have predicted enhanced homogeneous and heterogeneous reaction rates for solvent-based catalysis and other systems [18, 20], where the activation barrier of the reaction is decreased by a factor ΔE_a with the presence of a solvent cluster around the solute. The value for ΔE_a can be estimated from Onsager's reaction field theory:

CHAPTER 5 is a reprint of a manuscript published in Thin Solid Films

$$\Delta E_a = \frac{\mu^2}{a^3}\frac{2(\varepsilon-1)}{2\varepsilon+1}$$

where μ is the dipole moment of the polar state of solute molecule in the cavity of radius a; and ε is the dielectric constant of the continuum medium. Assuming the vacuum-based and $scCO_2$-based processes for $Al(acac)_3$ pyrolysis proceed through the same polar transition state, the dielectric strength of the $scCO_2$ solvent ($\varepsilon \sim 1.2$) is expected to decrease the reaction barrier for decomposition by effectively reducing the free energy of the polar transition state. Furthermore, a local increase in the dielectric constant of the solvent due to molecular ordering around the polar transition state [18-20, 28], will further reduce the reaction activation energy as compared to a solvent-free vacuum-based process. A direct approach to test the Onsager theory is to change the dielectric strength of the solvent and observe the effect on deposition rate. Preliminary results in our lab show that the addition of 0.2 mol/L of ethanol co-solvent to the sc-CO_2 leads to an increase in the aluminum oxide growth rate. Since the dielectric constant for ethanol under the conditions used is larger than CO_2, the addition of the co-solvent is expected to increase in solvent overall dielectric strength and reduce the kinetic barrier, consistent with the observed increase in growth rate.

As shown in Figure 5.2 and Figure 5.3, the as-deposited films of Al_2O_3 and Ga_2O_3 in the $scCO_2$-based process, performed without optimization, have more carbon contamination compared to those formed at higher temperatures using oxygen reactants [3, 5], By further optimization of the reaction, for example using a co-solvent or a different oxidizer, the

carbon contamination may be further decreased. The preliminary results presented here for $scCO_2$-based deposition of metal oxides suggest another routes to promote materials fabrication at low temperature, especially in applications where integration with polymers, biomaterials and other thermal sensitive materials are of primary interest. Combined with the other unique properties of $scCO_2$, this process can be used to quickly coat uniform metal oxide films onto complex structure with high aspect ratio and high surface areas including, for example, carbon nanotubes.

5.5 Summary and Conclusions

A $scCO_2$ based low temperature deposition technique for thin films of metal oxides has been developed. Experimental results of deposition of metal oxide thin films in $scCO_2$ solvent demonstrates that $scCO_2$ can affect the reaction kinetics of pyrolysis of metal diketonates, allowing the coating processes of metal oxides to proceed at lower temperatures than in comparable vacuum-based pyrolytic reactions. Both $Al(acac)_3$ and $Ga(acac)_3$ are found to undergo pyrolysis at temperatures of ~ 150-160 °C in $scCO_2$ compared to ~ 250-360 °C in analogous vacuum-based processes. The apparent activation energy for the pyrolysis of $Al(acac)_3$ in $scCO_2$ is found to be 68±6 kJ/mol which is substantially reduced compared to 80-100 kJ/mol previously reported for the same reaction in the vacuum-based process. The enhanced kinetics for pyrolysis of metal diketonates is ascribed to the dielectric strength of the $scCO_2$ solvent which decreases the reaction barrier by effectively reducing the

free energy of the polar transition state in the pyrolytic reaction. While several studies have characterized solvent-enhancement effects in homogeneous reactions, there are few previous results demonstrating details of supercritical solvent effects in heterogeneous film deposition reaction kinetics. The experimental results afford valuable insight into the effect of $scCO_2$ on the thermal stability of metal organics of interest in low temperature material fabrication processes.

5.6 Acknowledgment. Support is acknowledged from the National Science Foundation Science and Technology Center for Environmentally Responsible Solvents and Processes at North Carolina State University under cooperative agreement CHE-9876674, and from NSF project CTS-0626256.

CHAPTER 5 is a reprint of a manuscript published in Thin Solid Films

REFERENCES

[1] A.O. Hiroshi Uchida, Kiyoshi Itatani and Seiichiro Koda, Jpn. J. Appl. Phys. 44/4A (2005) 1901.

[2] Q.T. Nguyen, J.N. Kidder, S.H. Ehrman, Thin Solid Films 410/1-2 (2002) 42.

[3] M. Nieminen, L. Niinisto, E. Rauhala, J. Mater. Chem. 6/1 (1996) 27.

[4] T.A. Crowley, K.J. Ziegler, D.M. Lyons, D. Erts, H. Olin, M.A. Morris, J.D. Holmes, Chem. Mater. 15/18 (2003) 3518.

[5] T. Maruyama, S. Arai, Appl. Phys. Lett. 60/3 (1992) 322.

[6] J.S. Kim, H.A. Marzouk, P.J. Reucroft, J.D. Robertson, C.E. Hamrin, Thin Solid Films 230/2 (1993) 156.

[7] H. Kumagai, K. Toyoda, K. Kobayashi, M. Obara, Y. Iimura, Appl. Phys. Lett. 70/18 (1997) 2338.

[8] M. Aguilar-Frutis, M. Garcia, C. Falcony, G. Plesch, S. Jimenez-Sandoval, Thin Solid Films 389/1-2 (2001) 200.

[9] J.W. Elam, S.M. George, Chem. Mater. 15/4 (2003) 1020.

[10] J.M. Blackburn, D.P. Long, A. Cabanas, J.J. Watkins, Science 294/5540 (2001) 141.

[11] A. O'Neil, J.J. Watkins, MRS Bulletin 30/12 (2005) 967.

[12] Y.F. Zong, J.J. Watkins, Chem. Mater. 17/3 (2005) 560.

[13] T. Gougousi, D. Barua, E.D. Young, G.N. Parsons, Chem. Mater. 17/20 (2005) 5093.

CHAPTER 5 is a reprint of a manuscript published in Thin Solid Films

[14] B.N. Hansen, B.M. Hybertson, R.M. Barkley, R.E. Sievers, Chem. Mater. 4/4 (1992) 749.

[15] S.C. Tucker, Chem. Rev. 99/2 (1999) 391.

[16] A. Baiker, Chem. Rev. 99/2 (1999) 453.

[17] P.E. Savage, S. Gopalan, T.I. Mizan, C.J. Martino, E.E. Brock, AIChE J. 41/7 (1995) 1723.

[18] O. Kajimoto, Chem. Rev. 99/2 (1999) 355.

[19] K.P. Johnston, C. Haynes, AIChE J. 33/12 (1987) 2017.

[20] J.F. Kauffman, J. Phys. Chem. A 105/14 (2001) 3433.

[21] B.A.C. Kenton D. Childs, Lori A. LaVanier, John F. Moulder F. P. F. Stickle, D. G. Watson, C. L. Hedberg, handbook of Auger Electron Spectroscopy, Physical Electronics, Inc., 1995.

[22] W. Koh, S.J. Ku, Y. Kim, Thin Solid Films 304/1-2 (1997) 222.

[23] A.F. Bykov, A.E. Turgambaeva, I.K. Igumenov, P.P. Semyannikov, J. Phys. IV 5/C5 (1995) 191.

[24] M.C. Rhoten, T.C. DeVore, Chem. Mater. 9/8 (1997) 1757.

[25] P.P. Semyannikov, V.M. Grankin, I.K. Igumenov, A.F. Bykov, J. Phys. IV 5/C5 (1995) 205.

[26] A.F. Bykov, A.E. Turgambaeva, I.K. Igumenov, Koord. Khim. 22/5 (1996) 422.

CHAPTER 5 is a reprint of a manuscript published in Thin Solid Films

[27] J. Vonhoene, R.G. Charles, W.M. Hickam, J. Phys. Chem. 62/9 (1958) 1098.

[28] C.A. Eckert, B.L. Knutson, Fluid Phase Equilib. 83 (1993) 93.

CHAPTER 5 is a reprint of a manuscript published in Thin Solid Films

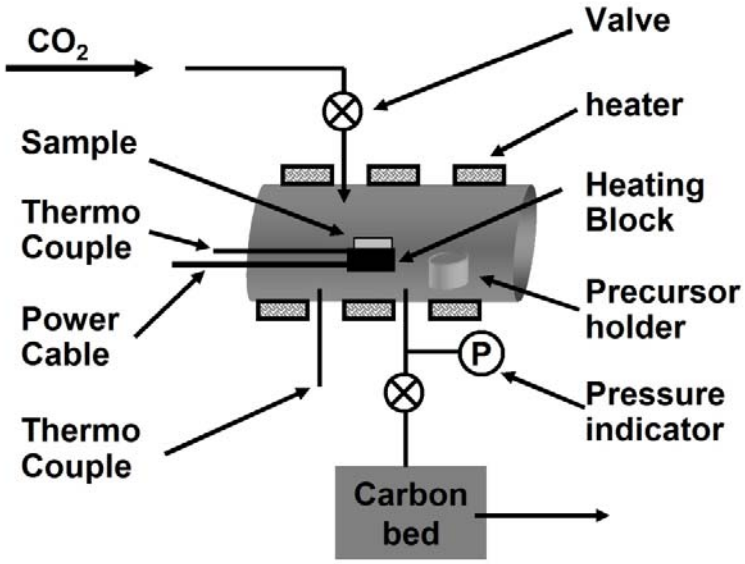


Figure 5.1. Schematic diagram of the experimental apparatus. The inner volume of the reactor is ~ 110 mL. The reactor wall temperature is typically held at 100 ^{o}C. The sample is located on a block that is heated independently from the reactor chamber wall.

CHAPTER 5 is a reprint of a manuscript published in Thin Solid Films

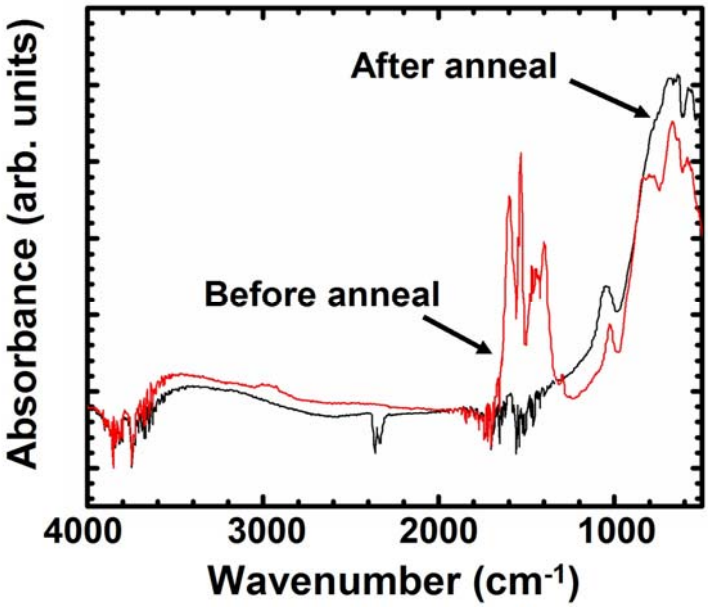


Figure 5.2. Transmission FTIR spectra for an Al_2O_3 film deposited from pyrolysis of $Al(acac)_3$ at 150 °C and 25-26 MPa on a Si substrate for 40 mins with film thickness ~ 23 nm. Before anneal: spectrum taken after deposition. After anneal: spectrum taken after the film was annealed at 600 °C in air for 15 mins.

CHAPTER 5 is a reprint of a manuscript published in Thin Solid Films

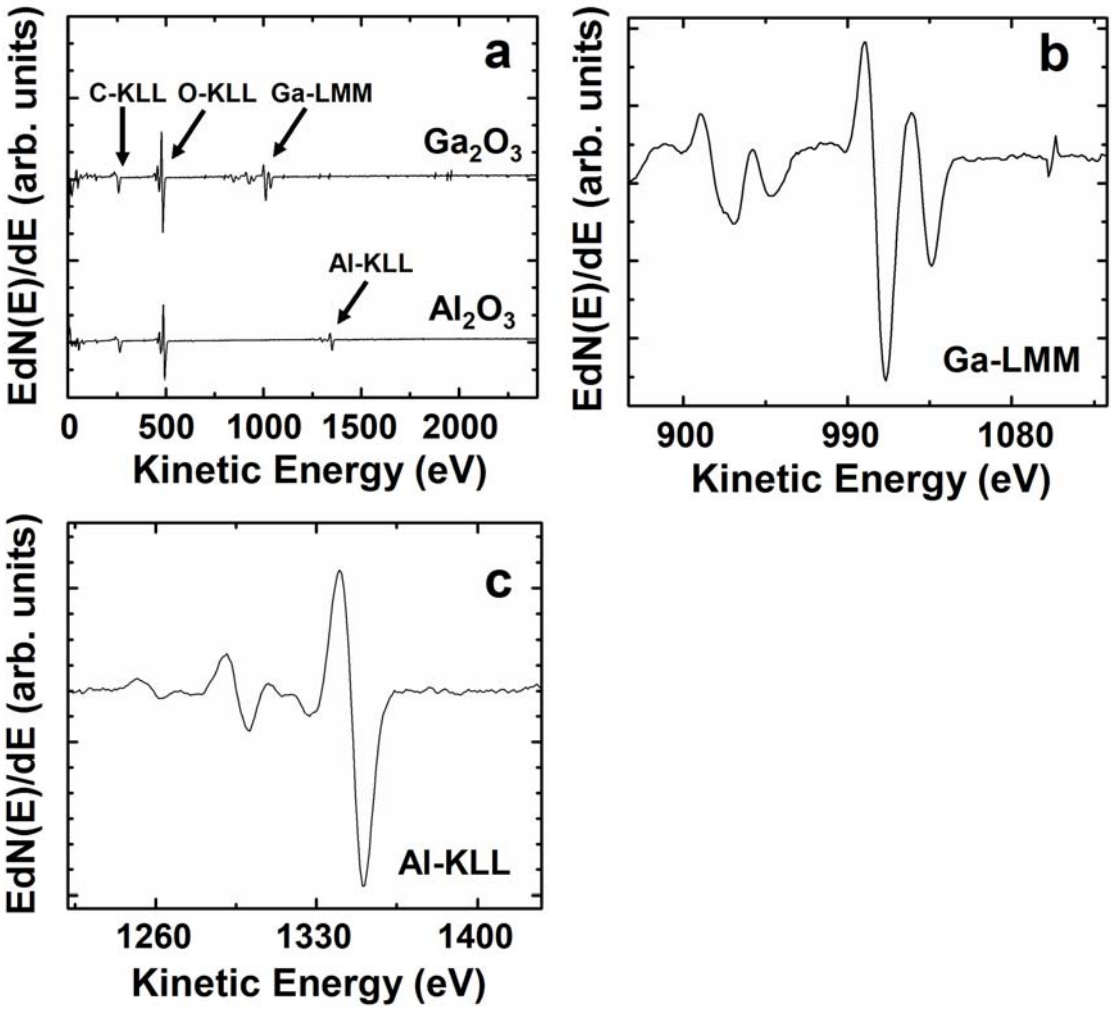


Figure 5.3. (a) Auger Electron Spectroscopy (AES) survey scan of Al_2O_3 and Ga_2O_3 films. Ga_2O_3 was deposited from pyrolysis of $Ga(acac)_3$ at 200 °C and 28-32 MPa, for 10 mins, resulting in a thickness of ~ 150 nm. Al_2O_3 was deposited from pyrolysis of $Al(acac)_3$ at 185 °C and 25-26 MPa for 50 mins, resulting in a thickness of ~ 100 nm. (b) The detailed AES spectrum of the Ga-LMM peaks. (c) The detailed AES spectrum of the Al-KLL peaks. The positions of Ga-LMM and Al-KLL peaks are consistent with the fully oxidized status of Ga and Al.

CHAPTER 5 is a reprint of a manuscript published in Thin Solid Films

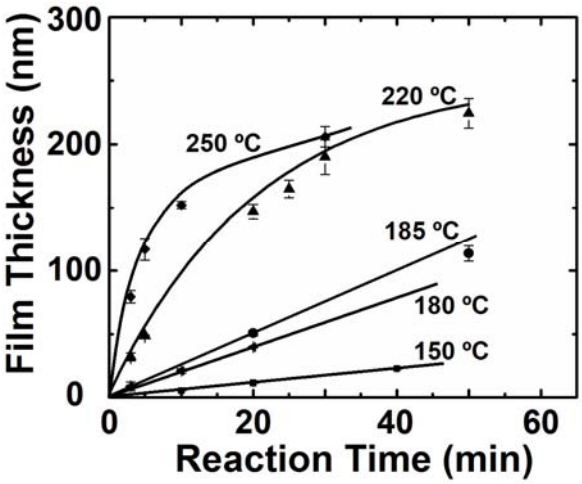


Figure 5.4. The Al_2O_3 film thickness measured as a function of deposition time at different reaction temperatures during the $scCO_2$-based pyrolysis of $Al(acac)_3$ with initial precursor concentration ~ 170 μmol/L. The straight lines are linear regressions and the curved lines are guides for the eye. At high temperatures (200 °C and 250 °C) for short deposition time (<5 mins), the films are observed to grow linearly with reaction time, followed by saturation of the film thickness at longer periods. At low temperatures (150 °C, 180 °C and 185 °C), the linear growth rate is observed for longer reaction times (measured up to 50 mins).

CHAPTER 5 is a reprint of a manuscript published in Thin Solid Films

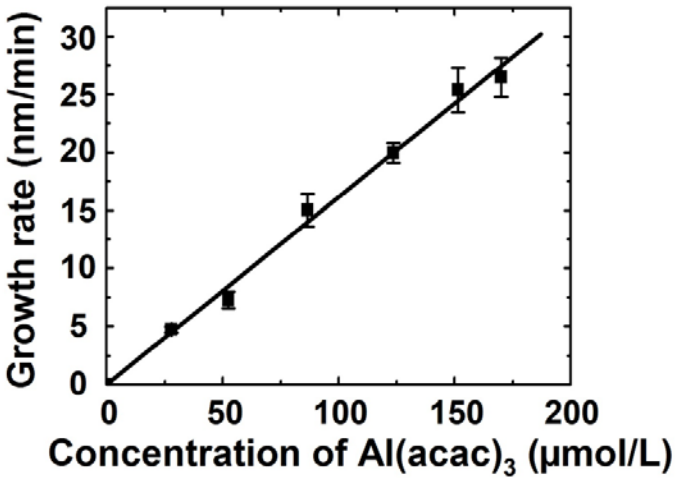


Figure 5.5. The effect of precursor concentration in the reaction system on the deposition rate of Al_2O_3 films in $scCO_2$-based process from pyrolysis of $Al(acac)_3$ at 250 °C. The solid line denotes a linear regression of the data points. The linear fit reveals that the growth rate is determined by the precursor concentration in the reaction system.

CHAPTER 5 is a reprint of a manuscript published in Thin Solid Films

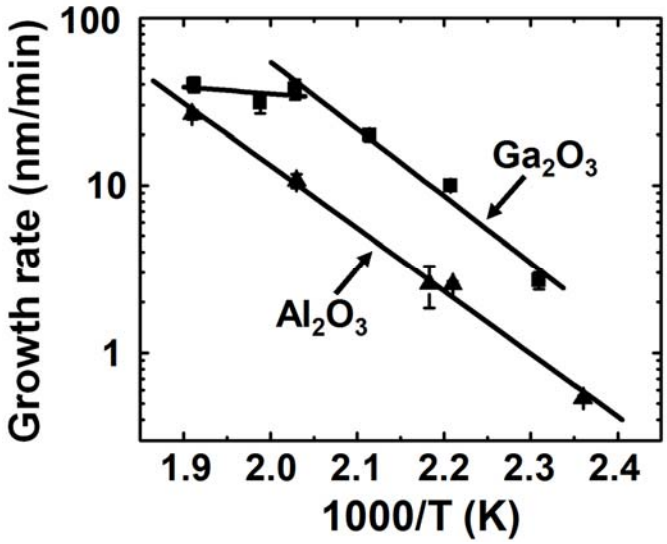


Figure 5.6. Apparent reaction kinetics of $scCO_2$-based deposition of Al_2O_3 films from pyrolytic reaction of $Al(acac)_3$ with initial concentration of 170 μmol/L. The slopes of the lines indicate that the overall energy barrier for Al_2O_3 deposition is 68±6 kJ/mol. And the apparent kinetics of $scCO_2$-based Ga_2O_3 deposition from pyrolysis of $Ga(acac)_3$ at initial concentration of 230 μmol/L. The kinetic barrier of Ga_2O_3 deposition is 84±7 kJ/mol. The solid lines represent linear regressions of the data points.

CHAPTER 5 is a reprint of a manuscript published in Thin Solid Films

Table 5.1. Experiment results of $scCO_2$-based deposition from pyrolytic reaction of different metal organics

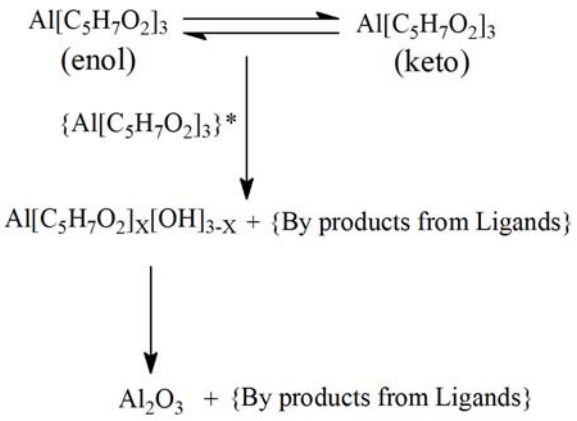
Precursor[A]	Amount	Solubility	Reaction T	Thickness/ Growth time[C]
$Al(hfac)_3$[B]	26.7 mg	Dissolved well	310 ºC	~ 650 nm/13 min
$Fe(acac)_3$	8.9 mg	Residue left	250 ºC	~ 110 nm/15 min
$Cr(acac)_3$	18.9 mg	Dissolve well	260 ºC	~ 20 nm/32 min
$Co(acac)_3$	6.9 mg	Hard to dissolve	250 ºC	< 10 nm/30 min
$Zr(acac)_4$	15.0 mg	Hard to dissolve	310 ºC	< 10 nm/30 min
$Zr(hfac)_4$	15.3 mg	Residue left	200 ºC	~ 75 nm/23 min
			310 ºC	~ 230 nm/5 min
$Zn(acac)_2$	8.0 mg	Hard to dissolve	200 ºC	No film
$Hf(acac)_4$	25.6 mg	Hard to dissolve	305 ºC	< 10nm/30 min

[A] All of these precursors dissolved at 100 °C, ~21 MPa;

[B] hfac: Fluorinated acetyl acetonate;

[C] For all as-deposited films, AES measurement shows corresponding Metal peak, O peak, C peak.

CHAPTER 5 is a reprint of a manuscript published in Thin Solid Films



Scheme 5.1. A simplified reaction mechanism for pyrolysis reaction of $Al(acac)_3$. The * denotes the postulated polar transition state.

CHAPTER 6 is a reprint of a manuscript published in JVST-B.

CHAPTER 6. Conformal Metal Oxide Coatings on Nanotubes by Direct Low-Temperature Metal-Organic Pyrolysis in Supercritical Carbon Dioxide

Qing Peng,[†] Joseph C. Spagnola,[‡] Hojo Daisuke,[†] Kie Jin Park[†] and Gregory N. Parsons[†*]

Departments of [†]Chemical and Biomolecular Engineering and
[‡]Materials Science & Engineering
North Carolina State University, Raleigh NC 27695, USA

Keywords: *supercritical carbon dioxide ($scCO_2$), multi-walled carbon nanotubes (MWCNTs), Gallium oxide, thermal decomposition, low temperature.*

[*]**Corresponding author:** parsons@ncsu.edu

ABSTRACT

We demonstrate that low temperature (<200°C) thermal decomposition of metal organic precursors dissolved in supercritical carbon dioxide ($scCO_2$) is an effective method to penetrate into dense three dimensional networks and deposit conformal metal oxide films with tunable thickness. Results specifically show that thermal decomposition of gallium acetylacetonate in $scCO_2$, leads to conformal coatings of gallium oxide on multi-walled carbon nanotube forests with a fast deposition rate (~3-4 nm/min), without the need for any co-solvent. Moreover, as-formed metal oxide/nanotube structures can be further conformally coated by metal atomic layer deposition to produce nanotube/oxide/metal nano-composites.

CHAPTER 6 is a reprint of a manuscript published in JVST-B.

6.1 Introduction

New tools and chemical processes for the synthesis of nano-scale materials will promote fabrication of new materials and constructs with unique electronic, optical, sensing, and catalytic capabilities.[1-3] In particular, there is significant interest in three-dimensional (3D) macro-structures consisting of nanostructures, including, for example, aerogels,[1] electrospun nanofibers,[4,5] and carbon nanotube forests and sheets.[3,6] In order to enable advanced function, it is necessary to uniformly modify or coat complex 3D nanostructure systems by film deposition techniques.[1-3,7-9] However, it is still a outstanding challenge to uniformly and conformably modify the complex 3D nanostructures.[1-3,7-9]

Due to the interesting properties and promising applications of metal oxide/carbon nanotubes,[3] to date, a variety methods, including atomic layer deposition (ALD)[10-12] and liquid solution based processes,[13-15] have been used to deposit metal oxides onto carbon nanotubes. Common solution-based processes have high surface tension and therefore have difficulty wetting the high surface areas in complex high aspect ratio structures, often resulting in poor conformality, collapse of the original shape and waste of organic solvent.[6,13-15]

As an environmentally benign solvent, supercritical carbon dioxide ($scCO_2$) has attracted much recent attention for chemical reaction because of its unique properties including liquid-like high density, gas-like high diffusivity, low viscosity and zero surface tension.[16-18] Because of those unique properties, it is possible for the $scCO_2$ based deposition processes to achieve conformal and uniform deposition in high aspect ratio structures. Especially, as a green solvent, $scCO_2$ can help remove byproducts and residue materials from the substrate

surface, which can reduce contaminants from the reaction environment.[17,19] Supercritical CO_2 has been investigated as an antisolvent agent to deposit metal oxide coatings onto nanotubes.[20-22] Herein, an environmentally benign pure $scCO_2$ based low temperature thermal decomposition chemistry of metal diketonates is developed to synthesize the coaxial nanostructure of gallium oxide coated multi-walled carbon nanotubes (MWCNT's), which could have potential applications in fields related to oxygen gas sensors,[23] optical systems,[24] catalysts,[25] coaxially-gated CNTs devices.[3] Furthermore, the coated nanotubes are further modified using atomic layer deposition of ruthenium metal at elevated temperature.

6.2 Experiment

For the gallium oxide deposition process, gallium acetylacetonate (99%) ($Ga(acac)_3$) [$Ga(C_5H_7O_2)_3$], (Strem Chemicals) was used as received. Coleman grade CO_2 (99.99%) (National Welders/Supply Company) was used for all experiments without further purification. Deposition experiments were carried out in a homemade 110 ml high-pressure stainless steel cold wall batch type reactor shown schematically in Figure 6.1.

MWCNTs were grown by catalytic chemical vapor deposition (CVD) process in a homemade quartz reactor at 500°C. Ethanol was used as the carbon source. Ar was bubbled through ethanol at room temperature with a flow rate of 1.5 standard liters per minute (SLM). The catalyst layer Fe(0.5nm)/Al_2O_3(10nm) was formed on the thermal oxide silicon wafer (SiO_2(500nm)/Si) by using sequential e-beam evaporation.

In a typical experiment, a Si substrate (size: ~1cm×1.5cm) having MWCNTs forest grown on it, was used as the deposition platform without further treatment. The sample was fixed onto the heating block, which was installed on the gland fitting (Conax Buffalo Corp.)

as shown in Figure 6.1. Three cartridge heaters (Tempco®) were fit into the heating block and the temperature of the heating block was controlled by a feedback thermocouple. One end of the reactor was sealed by the gland fitting. A known amount of precursor (corresponding to ~230 μmol/L) was loaded into the reactor with a sample before the reactor was sealed. Air was removed from the reactor continuously by flowing low pressure CO_2 through the reactor chamber for 10 minutes at a temperature of ~80°C. After purging, high pressure CO_2 was fed into the reactor and heated via a heating tape to the conditions desired for precursor dissolution (typically, P = 21MPa, T = 100°C). The system was kept stable at the set point for 1.5h to allow the precursor to be fully dissolved, as observed by inspection through the quartz window. The substrate was then rapidly heated (within 40 seconds) to the desired reaction temperature. Typical deposition temperatures were 160°C and 200°C, and the pressure ranged from 25-32 MPa. After a predetermined reaction time, the substrate heater was turned off and the temperature of substrate decreased to less than 150°C within 40 seconds, at which point the reaction ceased. The effluent from the reactor was then vented through an activated carbon bed filter and fresh $scCO_2$ was used to flush the reactor to remove reaction byproducts and any remaining precursor. The sample was then removed from the reactor and characterized.

The Ru ALD experiment was conducted in a home-made reactor system at 325°C by using bis(cyclopentadienyl)-ruthenium ($Ru(Cp)_2$) and O_2 as reactants.[26] The precursor and reactant were pulsed into reactor separately with pulsing time 3s and 6s respectively. Ar was used to purge the system for 20s after each precursor pulse. Argon was also used as a carrier gas for the $Ru(Cp)_2$ precursor.

CHAPTER 6 is a reprint of a manuscript published in JVST-B.

Auger electron spectroscopy (AES) was used to measure the atomic composition of the resulting materials using a 5 keV primary electron gun. Scanning electron microscopy (SEM) images were taken on the JEOL 6400F Field Emission SEM (FESEM). Complementary energy dispersive X-ray spectroscopy (EDS) analysis was performed with an Oxford ISIS system attached to JEOL 6400F FESEM. For TEM measurement, MWCNTs were dispersed in ethanol and sonicated for one minute. Several drops of the dispersion were pipetted onto copper TEM grids (Ted Pella, Inc), and the grids were dried at room temperature and then imaged using a Philips CM12 transmission electron microscope operating at 120 keV. No special preparation steps were necessary before coating MWCNTs. The same TEM grids were then exposed to the $scCO_2$ coating process and imaged again by using the same Philips CM12 TEM at 120keV. EDS analysis is also performed with a Oxford Instruments Inca Energy 100 system to ascertain the chemical composition of the oxide coated MWCNTs during the TEM measurement.

6.3 Results and discussion

Figure 6.2 shows results of AES spectra from pristine MWCNTs (top spectrum) and the same sample after gallium oxide coating in the supercritical CO_2 process (bottom spectrum). The AES spectrum of the as-grown pristine MWCNTs shows a dominant C-KLL (~250-265 eV) peak with a small O-KLL peak (~450-480 eV), which is ascribed to the absorbed oxygen from ambient exposure. Although the sample was positioned such that the electron beam was normal to the substrate surface, no peaks due to the substrate (Si/SiO_2) or CNT catalyst (Fe/Al_2O_3) were detected by AES analysis. The pristine MWCNTs were then treated by the $scCO_2$ based deposition process from thermal decomposition of $Ga(acac)_3$ at 200°C and 28-

32MPa for 10 minutes. In comparison with the uncoated pristine MWCNTs, the AES survey scan for the MWCNTs after oxide coating shows peaks from Ga-LMM (990-1070 eV), O-KLL (~450-480 eV) and C-KLL (~250-265 eV).[27] The prominent peaks of oxygen are mainly due to the oxygen atoms bonded with gallium atoms in the gallium oxide coating. There is a small C-KLL peak (corresponding to ~7 atomic % carbon) in the spectrum of the oxide coated MWCNTs, which is ascribed to adventitious carbon from atmospheric exposure and possibly some carbon residue in the as-deposited gallium oxide film. It is interesting to notice that the thermal decomposition temperature of $Ga(acac)_3$ in the $scCO_2$ process (200°C) is much lower than the typical 360°C used in vacuum-based deposition.[28] An enhanced low temperature growth rate has also observed for some other metal organics in sc-CO_2,[18,29] which is ascribed to solvation effects in modifying the energetics of precursor thermal dissociation in $scCO_2$.[18,30]

The appearance of Ga-LMM Auger transition with a relatively smaller C peak in the lower spectrum in Figure 6.2 is due to the conformal gallium oxide coating on the outside surface of MWCNTs in the MWCNT forest. This is confirmed by the resulting microstructure of the coated nanotubes shown in the FESEM images in Figure 6.3, and TEM images in Figure 6.4. Figure 6.3a is a FESEM image of pristine MWCNTs. The diameters of most uncoated MWCNTs are distributed in the range of 20-60nm. Compared with uncoated pristine MWCNTs, the oxide coated MWCNTs have larger diameters ~70-130 nm and the obvious morphology change is due to the conformal surface coating, as displayed in Figure 6.3b. Similar morphology was observed by FESEM measurement throughout the entire MWCNTs forest over a sample area of ~1 cm×1.5 cm. The average thickness of gallium

oxide coating is around 30nm after 10min deposition at reaction temperature 200˚C.

TEM images in Figure 6.4 provided further insight into the microstructure of MWCNTs before and after gallium oxide deposition performed at two different deposition temperatures. Figure 6.4a shows the TEM image of a single pristine MWCNT with a diameter of ~7nm. Figure 6.4b is a TEM image of MWCNTs exposed to gallium oxide deposition at 160°C for 7 mins showing non-uniform coating, with some sections showing no deposition as indicated by the arrow in Figure 6.4b. However, when the oxide deposition proceeded at 200°C for only 90 seconds, the MWCNTs were fully covered by gallium oxide with average thickness around 5-6nm as shown in Figure 6.4c. In Figure 6.4d, the interface between MWCNTs and the oxide coating can be clearly observed. The images in Figure 6.3b and 6.4d were collected from two samples deposited under the same conditions for different reaction times, which illustrate the thickness of gallium oxide increases with reaction time. Eventually, the growth rate will saturate upon consumption of the precursor. The ~230 μmol/L of precursor loaded in the reactor corresponds to ~$1.4x10^{19}$ molecules. With a typical film density of Ga_2O_3 of ~$5x10^{22}$ atoms/cm^3, this amount of precursor would enable a 30 nm film to be coated over an area of ~200 cm^2. The surface area of the reactor and carbon nanotube forest used in this experiment is roughly estimated to be <50cm^2, consistent with sub-saturation in the film growth rate. Further comparison between figure 6.4b and 6.4d indicates that deposition rate of gallium oxide coating increased with reaction temperature. The EDS spectrum of gallium oxide coated MWCNTs presented in Figure 6.4e revealed predominantly Ga and O, which confirmed the chemical composition of the gallium oxide coating. Compared with AES data, EDS spectra of nanotubes with oxide coating display a larger carbon fraction. This difference

is attributed to deeper penetration depth of the EDS method, therefore resulting in a larger carbon signal derived from the MWCNT.[21] The relative Auger signal intensities suggests carbon content ~7 atomic % in the gallium oxide. The EDS data reveals that the O/Ga atomic ratio in the gallium oxide is ~ 1.8, which exceeds the value of 1.5 in stoichiometric Ga_2O_3. The excess oxygen is ascribed to hydroxide and carbon (i.e. C-O) contamination likely present in the low-temperature deposited films. The AES data indicates the O/Ga atomic ratio is > 2.0, in agreement with a larger density of OH groups on the oxide surface. The as-formed gallium oxide coated carbon nanotubes could be calcined to remove the carbon and form gallium oxide nanostructures.

Further treatment by other techniques could be performed onto gallium oxide coated nanotubes to enable desired structure and material. For example, gallium oxide coated nanotube forest could be subsequently exposed to a thermally assisted atomic layer deposition (ALD) process to build up a coating of ruthenium metal, which is of interest as a metal gate electrode[26] and catalyst.[31] The ALD technique involves a vapor-phase self-limiting binary surface reaction sequence to form conformal thin-film coatings. Figure 6.5 displays a series of FESEM images of MWCNTs after various treatments, all shown at the same scale. Panel (a) shows an untreated MWCNT sample, and panel (b) is a similar sample after gallium oxide coating performed at 200°C for 10 minutes. The resulting gallium oxide coating is uniform and conformal, even for a helix structure in the MWCNT, as indicated by the arrow in Figure 6.5(b). Due to the zero surface tension of $scCO_2$, after the metal oxide deposition process, nanotube forest still maintains the original shape and there is no undesirable agglomeration/bundling or collapse geometry was observed, in contrast with

normal solvent-based process.[6] Figure 6.5(c) represents the results after exposing the oxide-coated MWCNTs to 150 ruthenocene/oxygen ALD cycles. The deposited ruthenium coating appeared uniform throughout the sample with no isolated Ru particles observed under the FESEM measurement. The EDS spectrum in Figure 6.5(d), shows that ruthenium ALD deposition successfully nucleate and grow onto the gallium oxide coated carbon nanotubes. Furthermore, a two point electrical evaluation of the nanotube forest shows metallic conductivity after Ru ALD deposition as compared to insulator properties with only oxide coating, which confirmed a continuous Ru film coating formed onto the oxide coated CNTs.

6.4 Conclusion

This study establishes that thermal decomposition of $Ga(acac)_3$ can provide a viable low temperature route to deposit conformal and uniform gallium oxide coating onto carbon nanotube forests with tunable coating thickness. The deposition reaction is found to proceed readily at low or co-solvents present.[20] Because of the unique properties of $scCO_2$, this coating process does not induced undesirable agglomeration or feature collapse. The gallium oxide coated CNTs can be further modified, for example by metal atomic layer deposition. Additionally, it is anticipated that this $scCO_2$ thermal decomposition process can be directly extended other metal oxide systems, including Al_2O_3, FeO_x, Cr_2O_3, and others[18] resulting in a variety of material systems for advanced devices. The method could be extended to modify other complex 3D systems, for example, aerogel[1] etc.

6.5 Acknowledgement

The STC program of the National Science Foundation under Agreement No. CHE-9876674 supported this work. Support is also acknowledged from NSF CTS-0626256. We

CHAPTER 6 is a reprint of a manuscript published in JVST-B.

also acknowledge Stephen Rossnagel and Ageeth Bol at IBM's TJ Watson research center for their help in imaging the samples by TEM and SEM.

CHAPTER 6 is a reprint of a manuscript published in JVST-B.

REFERENCES

[1] T. F. Baumann, J. Biener, Y. M. M. Wang, S. O. Kucheyev, E. J. Nelson, J. H. Satcher, J. W. Elam, M. J. Pellin and A. V. Hamza, Chem. Mater. **18**, 6106 (2006).

[2] M. Knez, K. Nielsch and L. Niinistö, Adv. Mater. **19**, 3425 (2007).

[3] R. H. Baughman, A. A. Zakhidov and W. A. de Heer, Science **297**, 787 (2002).

[4] S. V. Fridrikh, J. H. Yu, Brenner M. P. and Rutledge G. C., Phys. Rev. Lett. **90**, 144502 (2003).

[5] D. H. Reneker and I. Chun, Nanotechnology **7**, 216 (1996).

[6] X. R. Ye, L. H. Chen, C. Wang, J. F. Aubuchon, I. C. Chen, A. I. Gapin, J. B. Talbot and S. Jin, J. Phys. Chem. B **110**, 12938 (2006).

[7] M. Knez, A. Kadri, C. Wege, U. Gosele, H. Jeske and K. Nielsch, Nano Lett. **6**, 1172 (2006).

[8] G. K. Hyde, K. J. Park, S. M. Stewart, J. P. Hinestroza and G. N. Parsons, Langmuir **23**, 9844 (2007).

[9] Q. Peng, X. Y. Sun, J. C. Spagnola, G. K. Hyde, R. J. Spontak and G. N. Parsons, Nano Lett. **7**, 719 (2007).

[10] C. F. Herrmann, F. H. Fabreguette, D. S. Finch, R. Geiss and S. M. George, Appl. Phys. Lett. **87**, 123110 (2005).

[11] J. S. Lee, B. Min, K. Cho, S. Kim, J. Park, Y. T. Lee, N. S. Kim, M. S. Lee, S. O. Park and J. T. Moon, J. Cryst. Growth **254**, 443 (2003).

[12] Y. S. Min, E. J. Bae, K. S. Jeong, Y. J. Cho, J. H. Lee, W. B. Choi and G. S. Park, Adv. Mater. **15**, 1019 (2003).

CHAPTER 6 is a reprint of a manuscript published in JVST-B.

[13] C. N. R. Rao, B. C. Satishkumar and A. Govindaraj, Chem. Comm., **16**, 1581 (1997).

[14] B. C. Satishkumar, A. Govindaraj, M. Nath and C. N. R. Rao, J. Mater. Chem. **10**, 2115 (2000).

[15] W. Q. Han and A. Zettl, Nano Lett. **3**, 681 (2003).

[16] X. R. Ye, Y. H. Lin and C. M. Wai, Chem. Comm., **5**, 642 (2003).

[17] J. M. Blackburn, D. P. Long, A. Cabanas and J. J. Watkins, Science **294**, 141 (2001).

[18] Q. Peng, D. Hojo, K. J. Park and G. N. Parsons, Thin Solid Films **(published on-line, in press)** (2008).

[19] A. I. Cooper, Adv. Mater. **13**, 1111 (2001).

[20] Z. Y. Sun, X. R. Zhang, B. X. Han, Y. Y. Wu, G. M. An, Z. M. Liu, S. D. Miao and Z. J. Miao, Carbon **45**, 2589 (2007).

[21] L. Fu, Y. Q. Liu, Z. M. Liu, B. X. Han, L. C. Cao, D. C. Wei, G. Yu and D. B. Zhu, Adv. Mater. **18**, 181 (2006).

[22] Z. Y. Sun, H. Q. Yuan, Z. M. Liu, B. X. Han and X. R. Zhang, Adv. Mater. **17**, 2993 (2005).

[23] M. Ogita, K. Higo, Y. Nakanishi and Y. Hatanaka, Appl. Surf. Sci. **175**, 721 (2001).

[24] S. Sharma and M. K. Sunkara, J. Am. Chem. Soc. **124**, 12288 (2002).

[25] K. Nakagawa, C. Kajita, K. Okumura, N. Ikenaga, M. Nishitani-Gamo, T. Ando, T. Kobayashi and T. Suzuki, J. Catal. **203**, 87 (2001).

[26] K. J. Park, J. M. Doub, T. Gougousi and G. N. Parsons, Appl. Phys. Lett. **86**, 05193, (2005).

[27] D. C. Kenton, B. A. Carlson, L. A. LaVanier, J. F. Moulder, D. F. Paul, W. F. Stickle,

CHAPTER 6 is a reprint of a manuscript published in JVST-B.

D. G. Watson and C. L. Hedberg, *handbook of Auger Electron Spectroscopy*. (Physical Electronics, Inc., 1995).

[28] M. Nieminen, L. Niinisto and E. Rauhala, J. Mater. Chem. **6**, 27 (1996).

[29] H. Uchida, A. Otsubo, K. Itatani and S. Koda, Jpn. J. Appl. Phys. **44**, 1901 (2005).

[30] K. P. Johnston and C. Haynes, AIChE J. **33**, 2017 (1987).

[31] T. Mori, A. Miyamoto, N. Takahashi, M. Fukagaya, T. Hattori and Y. Murakami, J. Phys. Chem. **90**, 5197 (1986).

CHAPTER 6 is a reprint of a manuscript published in JVST-B.

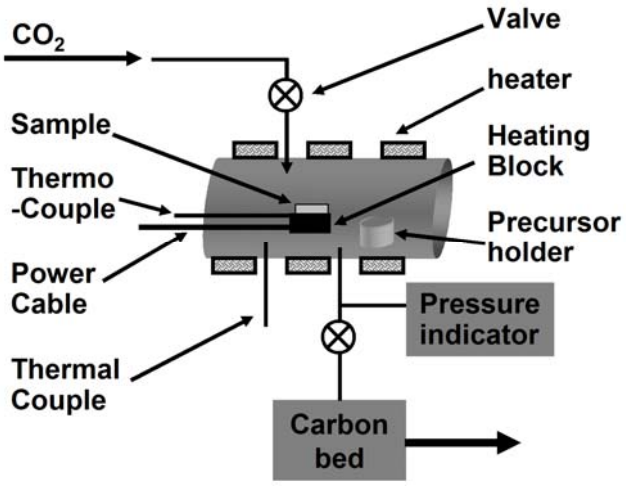


Figure 6.1. Schematic diagram of the experiment apparatus. Power cable was used to provide electricity for cartridge heaters in the heating block. The temperatures of sample and supercritical CO_2 solution were heated individually by different heaters and controlled by using different thermocouples. The inner volume of the reactor is around 110mL.

CHAPTER 6 is a reprint of a manuscript published in JVST-B.

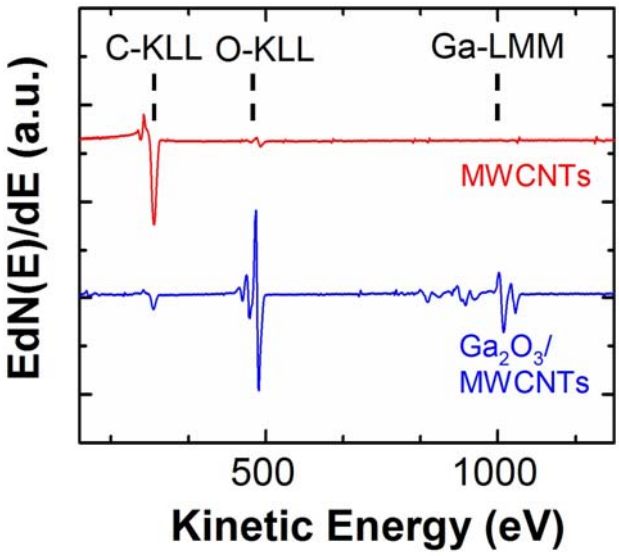


Figure 6.2. AES spectrum of untreated pristine MWCNTs (top spectrum) grown by catalytic chemical vapor deposition process at 500°C, with Fe (0.5nm)/Al_2O_3(10nm) as the catalyst on thermally grown silicon oxide. Gallium oxide coated MWCNTs (bottom spectrum) fabricated by thermal decomposition of $Ga(acac)_3$ in $scCO_2$ process at 200°C, 28-32 MPa for 10mins.

CHAPTER 6 is a reprint of a manuscript published in JVST-B.

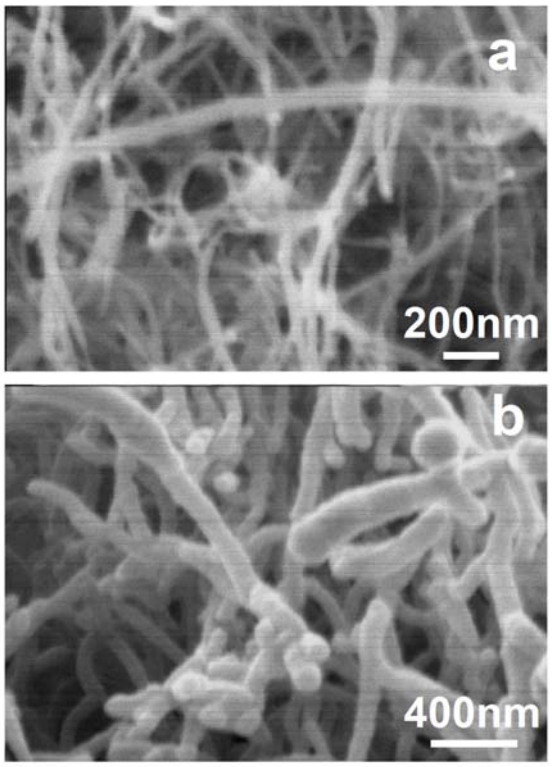


Figure 6.3. (a) FESEM image of untreated pristine MWCNTs. The diameters of the pristine MWCNTs are in the range of 20-60nm. (b) FESEM image of gallium oxide-coated MWCNTs. The gallium oxide coating was deposited by thermal decomposition of $Ga(acac)_3$ in $scCO_2$ process at 200°C, 28-32 MPa for 10mins. The diameters of the coated MWCNTs are in the range of 70-130 nm, which indicates the average thickness of the gallium oxide coating is around 30nm for 10mins.

CHAPTER 6 is a reprint of a manuscript published in JVST-B.

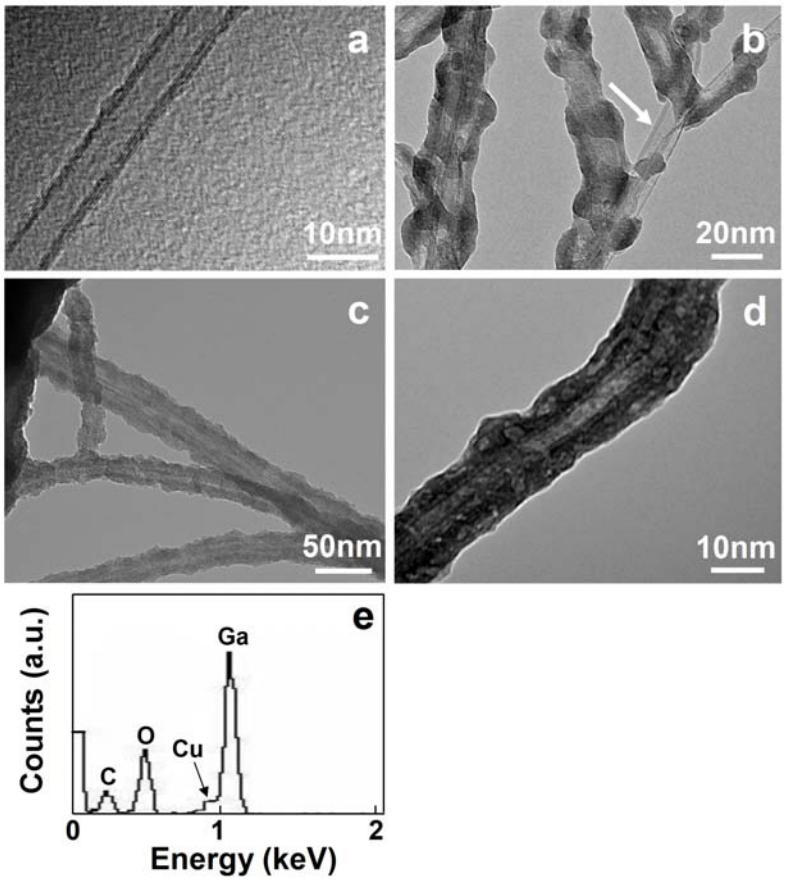


Figure 6.4. (a) TEM image of a single pristine MWCNT. (b) TEM image of MWCNTs coated by gallium oxide from thermal decomposition of $Ga(acac)_3$ at 160°C and 23MPa-24MPa for 7 mins. The arrow inside (b) shows the part of MWCNTs having no oxide coating. (c) TEM image of MWCNTs coated by gallium oxide from thermal decomposition of $Ga(acac)_3$ at 200°C and 28MPa for 1.5 mins. (d) Higher magnification TEM image of MWCNTs coated by gallium oxide from thermal decomposition of $Ga(acac)_3$ at 200°C and 28MPa for 1.5 mins. (e) A typical EDS spectrum of oxide coated MWCNTs. The gallium oxide deposition experiment was carried out at 200°C, 28-32MPa for 1.5 mins. The Ga and majority O peaks result from the gallium oxide coating, and the major carbon signal is ascribed to the MWCNTs with some contribution from carbon impurities and adventitious carbon. The tiny Cu peak is from the TEM grid.

CHAPTER 6 is a reprint of a manuscript published in JVST-B.

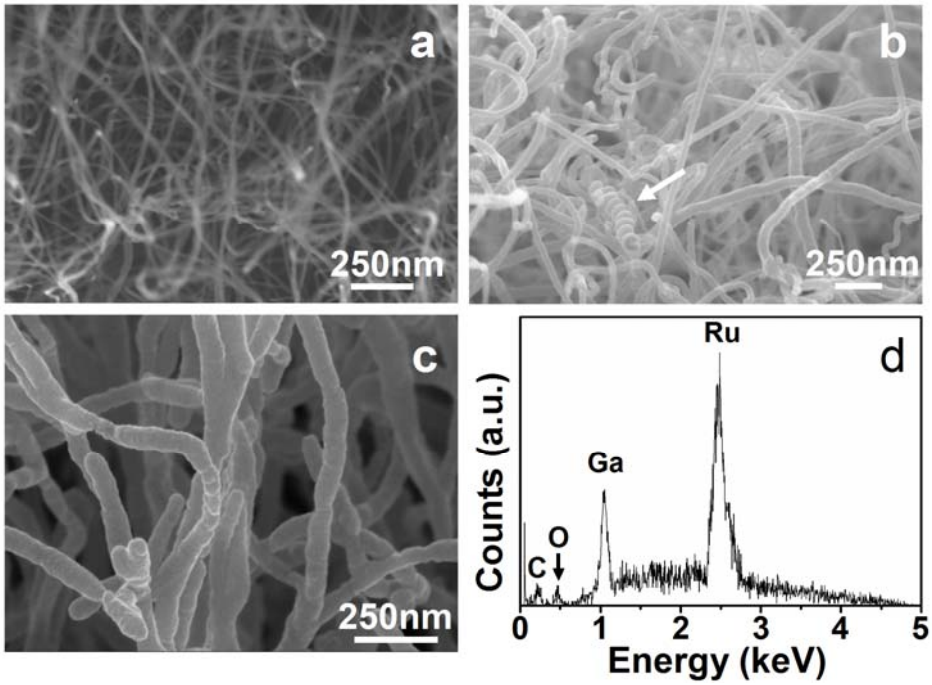


Figure 6.5. (a) FESEM image of untreated pristine MWCNTs. The diameters of the MWCNTs are in the range of 10-30nm. (b) FESEM image of MWCNTs coated by gallium oxide from pyrolysis of $Ga(acac)_3$ at 200°C, 28-30 MPa for 10 mins. The diameters of the MWCNTs are in the range of 60-100 nm The arrow in (b) indicates that the coating of gallium oxide can replicate the small helix feature of MWCNTs. (c) FESEM image of gallium oxide coated MWCNTs with relatively uniform Ru coating on the surface by atomic layer deposition from reaction between $Ru(Cp)_2$ and O_2 at 325°C for 150 cycles. (d) A typical EDS spectrum of oxide-coated MWCNTs with Ru ALD coating. The significant Ru peak is shown. The peak of Ga and O come from the gallium oxide under the Ru, and the tiny C peak probably comes from the carbon nanotube core, adventitious carbon from air and the as-deposited films.

CHAPTER 7 is a reprint of a manuscript published in Journal of the Electrochemical Society

CHAPTER 7. Self-Catalyzed Hydrogenolysis of Nickelocene: Functional Metal Coating of Three-Dimensional Nanosystems at Low Temperature

Qing Peng,[†] Joseph C. Spagnola,[‡] Gregory N. Parsons[†*]

Departments of [†]Chemical and Biomolecular Engineering and [‡]Materials Science & Engineering, North Carolina State University, Raleigh NC 27695, USA

Keywords: *self-catalyzed hydrogenolysis, low temperature, nickelocene, nickel, supercritical carbon dioxide (scCO$_2$)*

ABSTRACT

In this paper, we demonstrate the hydrogenolysis of Nickelocene can take place through a self-catalyzed process at low temperature (< 70 ˚C) in supercritical carbon dioxide to generate relatively uniform dispersed Ni (nickel) metal particles onto carbon nanotubes forests and Ni films on flat surfaces. The ability to form metal particles or films without a local catalyst at this low temperature is significant because it provides further insight into mechanisms for Ni deposition reactions, and it enables a new route for low temperature metal coating on a range of non-metal substrate materials with complex topography and nanostructure, for example to form Ni/polymer magnetic nanocomposites.

CHAPTER 7 is a reprint of a manuscript published in Journal of the Electrochemical Society

7.1 Introduction

The ability to fabricate unique three-dimensional (3D) macro-structures consisting of nanostructures will lead to new materials and constructs with unique electronic, optical, sensing, and protective capabilities. Forests and sheets of carbon nanotubes (CNTs),[1-3] electrospun nanofibers,[4,5] or nanostructured aerogels,[6] for example, could be used as platforms for advanced catalytic systems,[7,8] biomedical systems,[9] and energy storage or conversion systems[10,11] where the surface functionality of the nanostructures provides unique performance capabilities. Many studies have addressed the issues of surface coating and surface modification of nanostructures, including 3D surface in particular.[6,12,13] As a specific example, nickel (Ni) is an important catalyst, magnetic material and promising energy storage material,[3] and nickel (Ni)-CNTs nanocomposites have been synthesized by chemical vapor deposition (CVD),[14,15] wet chemical processing,[11,16] electroless plating,[17,18] and by direct incorporation of Ni nanoparticles catalysts into the as-grown CNTs.[14] Recently, supercritical carbon dioxide ($scCO_2$) has been successfully used as a green medium for chemical reaction because of its liquid-like high density, gas-like high diffusivity, low viscosity, and zero surface tension.[2,19] A number of different metal thin films including Pt, Pd, Ru, Au, Ni and Cu have been deposited by using $scCO_2$ process at modest temperature and pressure.[8,19-24] For example, Ni films were deposited onto silicon wafer in $scCO_2$ solvent using catalyst seed layers such as Pt, Pd, and Ni.[19] This previous work found this catalyst layer is critically important at temperatures less than 120 ˚C to initiate the deposition.[19] The requirement of a local surface catalyst to initiate deposition is expected to significantly limit

the formation of film coating in small features and uniform coatings on complex 3D surface topologies.

This article describes a new phenomenon of self-catalyzed hydrogenolysis of $Ni(Cp)_2$ in $scCO_2$ wherein Ni metal (including nanoparticles and films) can be generated from direct hydrogenolysis of nickelocene at 70 ˚C without addition of any catalysts. Using this method, dense Ni nanoparticles were anchored onto multi-walled CNTs (MWCNTs) throughout the MWCNTs forest without destroying the original structure of the carbon nanotube forest.

7.2 Experiment

Nickelocene [$Ni(Cp)_2$] (Strem Chemicals®) was used as the precursor and H_2 was used as the reducing agent. Coleman grade CO_2 (99.99%) and high purity H_2 (99.999%) (National Welders/Supply Company) were used without further purification. The experiment was carried out in a 110 ml homemade high-pressure reactor as shown in Figure 7.1. In a typical experiment, 70-90 mg $Ni(Cp)_2$ was loaded into the high pressure reactor, which was then sealed by sapphire windows on both sides, with a silicon wafer having MWCNTs forest grown on it. Following precursor loading, low-pressure fresh CO_2 was used to purge the system for 10 min (minute) at temperature ~ 70 ˚C in order to purge air out of the reactor. After purging, high-pressure CO_2 was fed into the reactor through a high-pressure syringe pump (Model 260D, Isco, Inc.). The temperature of the $scCO_2$ solution was stabilized by a heating tape at the dissolving condition (T=70 ˚C, P=17 MPa) for 4 h (hours) to form a uniform solution. During $Ni(Cp)_2$ dissolution, H_2 was fed into another clean, air-free high-pressure manifold vessel (43 ml), to the pressure of ~ 3.5 MPa at 60 ˚C. The vessel was then further charged with fresh CO_2 using the high-pressure syringe pump to the pressure of ~

34.5 MPa. This $H_2/scCO_2$ solution was kept stable at this condition for more than 2 h before injected into the high-pressure reactor. Upon $H_2/scCO_2$ injection, the pressure in the vessel dropped from ~ 34.5 to ~ 19.3 MPa, allowing the amount of H_2 fed into the reactor to be quantified. Normally the H_2 injection process will be repeated to obtain a 50-100X molar excess of hydrogen relative to nickelocene in the reactor system. Upon the addition of H_2, the $scCO_2$ solution containing $Ni(Cp)_2$ maintained a green color and the reaction system was left undisturbed at 70 ˚C, 17-18 MPa for several hours. After 7-8 h substantial Ni film and particles deposition was observed (as described in the experiment results section). Following each experiment, the reactor was prepared for another reaction sequence by removing the Ni deposition on the vessel walls. The reactor was scrubbed then sonicated in water, followed by deionized (DI) water flush and N_2 flow dry.

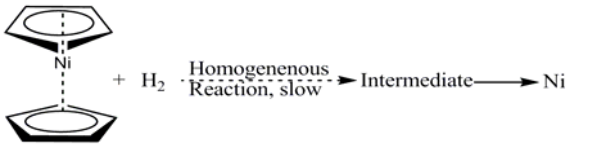
As substrates for deposition, MWCNTs forests were grown by catalytic CVD process in a homemade quartz reactor at 600 °C with ethanol as the carbon source. As the carrier gas, Ar was bubbled through ethanol at room temperature with a flow rate of 1.5 SLM (L/min, at 0 ˚C, 101.3 kPa). The catalyst layer of Fe (0.5 nm) on Al_2O_3 (10 nm) was fabricated on the thermal oxide silicon wafer (SiO_2(500 nm)/Si) by sputtering Al_2O_3 and e-beam evaporation of Fe sequentially. No further processes were taken to purify or open the end of the as-grown MWCNTs.

Imaging of the samples was performed using field emission scanning electron microscopy (FESEM) on a JEOL 6400F instrument at 5 kV. Transmission electron microscopy (TEM) images were taken on a Hitachi HF-2000 operated 200 kV. Energy dispersive X-ray spectroscopy (EDS) was carried out on an Oxford Instruments Inca Energy

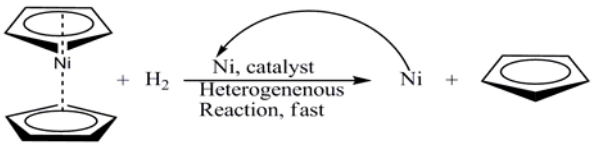
100 system attached onto the TEM to determine the chemical composition of the Ni nanoparticles decorated MWCNTs. For TEM measurement, Ni nanoparticles decorated MWCNTs were dispersed into ethanol and sonicated for one minute. Then several droplets of the dispersion were pipetted onto Lacey silicon TEM grids (Ted Pella, Inc.). The prepared samples were dried in room temperature overnight before the TEM measurement.

7.3 Results and Discussion

The deposition reaction was observed to be strongly time and temperature dependent. As shown in Figure 7.2(a), the starting homogeneous solution of $Ni(Cp)_2$ in $scCO_2$ is green in color. Without addition of H_2, the solution is stable and no reaction was observed after more than 24 h. With injection of H_2, no noticeable color change was observed, and no deposition reaction occurs for several hours. However, after 7-8 h incubation time at 70 $^{\circ}$C, the solution color changed very rapidly (within 1 to 2 min) from green to orange, as shown in Figure 7.2(b), then became transparent. The transition from orange color to transparent occurred over ~ 20 min, and corresponded to the completion of the deposition reaction. The orange color is ascribed to the reaction intermediates present during the reaction process. The reaction scheme for the homogeneous reaction is shown in Equation (1). This incubation time for the reaction decreased as the reaction temperature increased.



(1)



(2)

At 130 °C the reaction initiated immediately to form Ni metal and the solution color disappeared shortly after injection of H_2, which is in agreement with previous observations.[19,25] At low reaction temperature (such as 70 °C), it takes a long period for H_2 to reduce $Ni(Cp)_2$ to form intermediate products (orange color), which are subsequently converted to Ni nanoparticles. However once the Ni nuclei were formed and reached a critical size, they act to catalyze hydrogen dissociation[19,25] and promote rapid heterogeneous hydrogenation of nickelocene, resulting in Ni particle formation, as shown by the reaction Equation (2). On the surface of the MWCNTs where no catalysts such as Ni, Pt, Pd are present, a large amount of Ni nanoparticles are attached to the MWCNTs. Therefore, the Ni nanoparticles formation likely proceeds through an initial homogeneous reaction (Equation (1)) in the supercritical carbon dioxide solvent, followed by a faster heterogeneous catalytic reaction (Equation (2)) on the as-formed Ni nanoparticles.

A FESEM image of an untreated pristine nanotube substrate sample is shown in Figure 7.3a. The sample is a dense forest of aligned carbon nanotubes. The $scCO_2$-based Ni deposition process at 70 °C using 78 mg of $Ni(Cp)_2$ results in dense and dispersed Ni nanoparticles, which are anchored on the surface of the MWCNTs, as shown in a representative FESEM image in Figure 7.3b. Figure 7.3b also shows that after the deposition process the morphology of the nanotube structure maintains its original structure, with no undesired collapse or tube aggregation observed. Figure 7.3c shows a typical high resolution SEM image of resulting MWCNTs decorated with a number of Ni particles. The same morphology was observed across the entire sample surface with an area of 1×1.5 cm^2. After Ni deposition, the samples shown in Figure 7.3b-c were exposed to a sonication treatment (1

min in ethanol) to remove loosely bound particulates. Figure 7.3d shows a typical TEM image of Ni particles decorated MWCNTs after the sonication dispersal process. The diameters of Ni particles are in the range of 10-60 nm.

Figure 7.4 shows the energy dispersive X-ray spectrum of the MWCNTs sample after Ni deposition, showing clear evidence for the presence of nickel. The O peak probably results from the oxidation of Ni nanoparticles and MWCNTs with exposure to ambient air before EDS measurement. The C peak is ascribed to MWCNTs, and the Cu and Si peak are the consequence of the Lacey® Silicon TEM grid. The EDS spectrum of Ni decorated MWCNTs verified the chemical composition of Ni/MWCNTs nanocomposites.

CNTs with high structural perfection generally are inert for chemical reactions.[1] However, the MWCNTs produced catalytically by gas phase chemical vapor deposition have relatively high defect densities compared with those produced by other processes,[1] and those defects can promote island type growth and nanoparticle formation. It is possible in this study, therefore, that Ni metal deposition proceeded through nucleation on chemically active defects on the CVD MWCNTs. In contrast, on substrates such as planar SiO_2 and Al_2O_3, which have very high density of reactive sites, we found the Ni hydrogenation process resulted in thin film metal coatings as shown in Figure 7.5. This coating was also formed from the self-catalyzed heterogeneous growth mode. However, we find that the complex nucleation process for the Ni film on the SiO_2 and Al_2O_3 surfaces is relatively difficult to control.

CHAPTER 7 is a reprint of a manuscript published in Journal of the Electrochemical Society

7.4 Conclusions

Results clearly indicate that nickelocene hydrogenolysis process can proceed through a self-catalyzed process at low temperature (< 70 °C) in $scCO_2$ to generate relatively uniform dispersed Ni metal particles onto carbon nanotubes forests and Ni films on flat surfaces. The ability to form metal particles or films without a local catalyst at this low temperature is significant because it provides further insight into mechanisms for deposition reactions, and it enables a new route for low temperature metal coating on a range of non-metal substrate materials with complex topography and nanostructure. The low temperature $scCO_2$ based Ni deposition process described here could also have other applications, including metal deposition onto thermally sensitive substrates to form, for example, Ni/polymer magnetic nanocomposites.

7.5 Acknowledgments

This work was supported by the STC program of the National Science Foundation under agreement No. CHE-9876674. Support is also acknowledged from NSF CTS-0626256.

CHAPTER 7 is a reprint of a manuscript published in Journal of the Electrochemical Society

REFERENCES

[1] R. H. Baughman, A. A. Zakhidov and W. A. de Heer, Science **297**, 787 (2002).

[2] C. H. Yen, X. L. Cui, H. B. Pan, S. F. Wang, Y. H. Lin and C. M. Wai, J. Nanosci. Nanotechnol. **5**, 1852 (2005).

[3] G. G. Wildgoose, C. E. Banks and R. G. Compton, Small **2**, 182 (2006).

[4] S. V. Fridrikh, J. H. Yu, M. P. Brenner and G. C. Rutledge, Phys. Rev. Lett. **90**, 144502 (2003).

[5] D. H. Reneker and I. Chun, Nanotechnology **7**, 216 (1996).

[6] T. F. Baumann, J. Biener, Y. M. Wang, S. O. Kucheyev, E. J. Nelson, J. H. Satcher Jr., J. W. Elam, M. J. Pellin and A. V. Hamza, Chem. Mater. **18**, 6106 (2006).

[7] Z. Y. Sun, Z. M. Liu, B. X. Han, Y. Wang, J. M. Du, Z. L. Xie and G. J. Han, Adv. Mater. **17**, 928 (2005).

[8] Y. H. Lin, X. L. Cui, C. H. Yen and C. M. Wai, Langmuir **21**, 11474 (2005).

[9] S. G. Penn, L. He and M. J. Natan, Curr. Opin. Chem. Biol. **7**, 609 (2003).

[10] X. P. Gao, Y. Lan, G. L. Pan, F. Wu, J. Q. Qu, D. Y. Song and P. W. Shen, Electrochem. Solid-State Lett. **4**, A173 (2001).

[11] H. S. Kim, H. Lee, K. S. Han, J. H. Kim, M. S. Song, M. S. Park, J. Y. Lee and J. K. Kang, J. Phys. Chem. B **109**, 8983 (2005).

[12] G. K. Hyde, K. J. Park, S. M. Stewart, J. P. Hinestroza and G. N. Parsons, Langmuir **23**, 9844 (2007).

CHAPTER 7 is a reprint of a manuscript published in Journal of the Electrochemical Society

[13] Q. Peng, X. Y. Sun, J. C. Spagnola, G. K. Hyde, R. J. Spontak and G. N. Parsons, Nano Lett. **7**, 719 (2007).

[14] E. F. Kukovitsky, S. G. L'Vov and N. A. Sainov, Molecular Crystals And Liquid Crystals Science And Technology Section C-Molecular Materials **10**, 165 (1998).

[15] C. Pham-Huu, N. Keller, V. V. Roddatis, G. Mestl, R. Schlogl and M. J. Ledoux, Phys. Chem. Chem. Phys. **4**, 514 (2002).

[16] S. Arai, M. Endo and N. Kaneko, Carbon **42**, 641 (2004).

[17] F. Wang, S. Arai and M. Endo, Carbon **43**, 1716 (2005).

[18] L. M. Ang, T. S. A. Hor, G. Q. Xu, C. H. Tung, S. P. Zhao and J. L. S. Wang, Carbon **38**, 363 (2000).

[19] J. M. Blackburn, D. P. Long, A. Cabanas and J. J. Watkins, Science **294**, 141 (2001).

[20] Y. F. Zong and J. J. Watkins, Chem. Mater. **17**, 560 (2005).

[21] J. J. Watkins, J. M. Blackburn and T. J. McCarthy, Chem. Mater. **11**, 213 (1999).

[22] X. R. Ye, Y. H. Lin and C. M. Wai, Chem. Communi. **5**, 642 (2003).

[23] X. R. Ye, Y. H. Lin, C. M. Wang, M. H. Engelhard, Y. Wang and C. M. Wai, J. Mater. Chem. **14**, 908 (2004).

[24] X. R. Ye, Y. H. Lin, C. M. Wang and C. M. Wai, Adv. Mater. **15**, 316 (2003).

[25] E. T. Hunde and J. J. Watkins, Chem. Mater. **16**, 498 (2004).

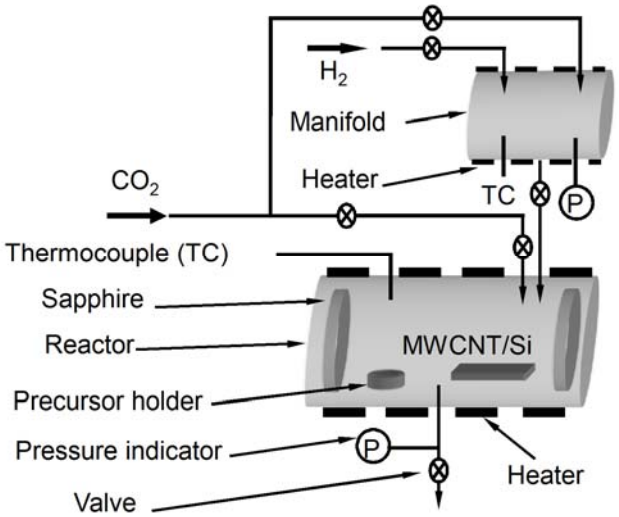


Figure 7.1. The diagram of reaction system. H_2 is mixed with $scCO_2$ in the manifold to form uniform solution. The temperature of the reactor and manifold are controlled by feedback thermal couples individually. The reaction system can be observed through the sapphire windows.

CHAPTER 7 is a reprint of a manuscript published in Journal of the Electrochemical Society

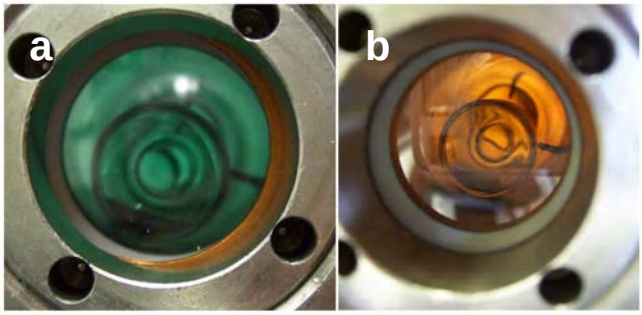


Figure 7.2. (a) A photo image of stable $Ni(Cp)_2$ in $scCO_2$ solution (Green) at 70 $^{\circ}$C. (b) A photo image of the solution after 7-8 h incubation time (Orange).

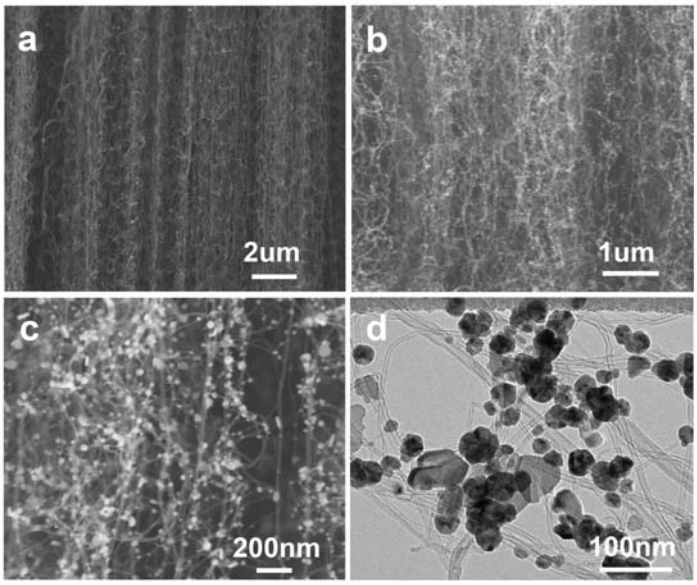


Figure 7.3. (a) FESEM image of pristine MWCNTs. (b) FESEM image of the Ni nanoparticles decorated MWCNTs after treated in the $scCO_2$ based direct hydrogenolysis reaction between $Ni(Cp)_2$ and H_2 at 70 $^{\circ}$C. (c) A typical TEM image of the Ni nanoparticles anchored MWCNTs. (d) High Resolution TEM image of Ni nanoparticles decorated MWCNTs.

CHAPTER 7 is a reprint of a manuscript published in Journal of the Electrochemical Society

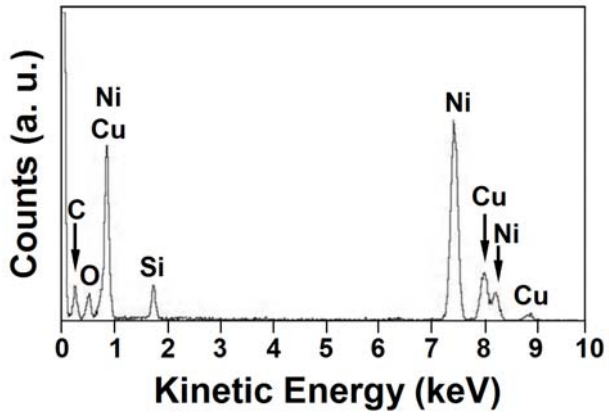


Figure 7.4. EDS spectrum of Ni nanoparticles decorated MWCNTs

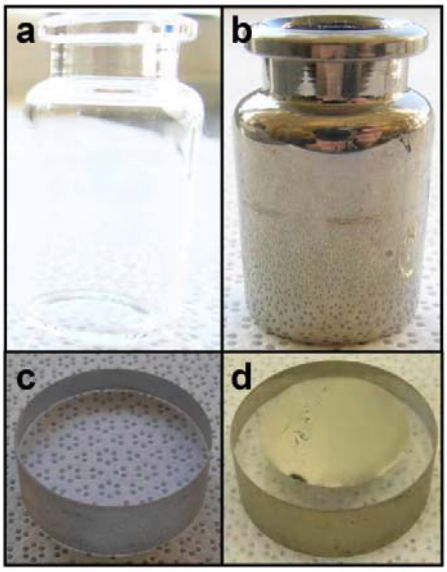


Figure 7.5. (a) A photo image of clean glass bottle which is transparent. (b) A photo image of glass bottle coated by Ni thin film by the direct low temperature supercritical carbon dioxide based hydrogenation process of Ni $(Cp)_2$ at 70 $^{\circ}$C. The gold color film is Ni. (c) A photo image of clean sapphire window which is transparent. (d) A photo image of sapphire window after Ni deposition from the direct low temperature supercritical carbon dioxide based hyrogenation process of $Ni(Cp)_2$ at 70 $^{\circ}$C.

CHAPTER 8 is a reprint of a manuscript published in Nano Letters

CHAPTER 8. Atomic Layer Deposition on Electrospun Polymer Fibers as a Direct Route to Al_2O_3 Microtubes with Precise Wall Thickness Control

Qing Peng,[†] Xiao-Yu Sun,[†] Joseph C. Spagnola,[‡] G. Kevin Hyde,[§]
Richard J. Spontak[†‡] and Gregory N. Parsons[†‡*]

Departments of [†]Chemical and Biomolecular Engineering, [‡]Materials Science & Engineering and [§]Textile Engineering, Chemistry and Science
North Carolina State University, Raleigh NC 27695, USA

Keywords: atomic layer deposition, electrospinning, aluminum oxide, microtubes, templating

ABSTRACT

Atomic layer deposition (ALD) of Al_2O_3 on electrospun poly(vinyl alcohol) microfiber templates is demonstrated as an effective and robust strategy by which to fabricate long and uniform metal-oxide microtubes. The wall thickness is shown to be precisely controlled within a molecular layer or so by adjusting the number of ALD cycles utilized. By judiciously selecting the electrospinning and ALD parameters, designer tubes of various sizes and inorganic materials can be synthesized.

CHAPTER 8 is a reprint of a manuscript published in Nano Letters

8.1 Introduction

Inorganic microtubes with precisely defined nanoscale walls have attracted considerable attention due to their potential application in technologies related, but not limited to, electronics, photonics, nanofluidics, medicine, sensing, catalysis, and controlled release.[1] A variety of different processes have been developed to fabricate such tubes from a variety of materials. Among those processes, the template-directed approach represents a straightforward and facile route to the fabrication of nano/microscale structures with hollow interiors. Nanorods,[2] carbon nanotubes[3,4] and porous media[5,6] have all been successfully used as templates in this vein. Such templates are, however, expensive and difficult to produce in large volume. Natural materials including cotton and paper[7,8] have also been used as templates, but the resultant nano/microscale structures are not easy controlled. In this work, we employ atomic layer deposition (ALD) on electrospun polymer fibers as a direct means by which to construct inorganic microtubes with well-defined nanoscale walls composed of Al_2O_3 after the templating polymer is removed. The results reported here indicate that this strategy provides an attractive, high-fidelity and low-cost route to inorganic microtubes, as well as nanoscale tubes and other complex shapes.

Electrospinning has become a valuable and versatile route by which to obtain exceptionally long polymer nano/microscale fibers possessing uniform diameter and good composition control.[9-14] Electrospun fibers are produced from polymer solutions as the electric field between a spinneret and a target is increased until the electrostatic force at the tip of the spinneret exceeds the surface tension of the solution drop. The Taylor cone that forms is transformed into a continuous jet that forms solid fibers as the solvent evaporates. In

combination with various surface modification tactics including physical vapor deposition (PVD),[15,16] chemical vapor deposition (CVD),[15] sol-gel processing,[7] and spin-on glass (SOG) incorporation,[16,17] electrospun templates have been used to fabricate metal,[15] metal oxide[7,16] and polymer[15,18] nanotubes. However each of these deposition methods is hindered by significant process limitations. For example, sol-gel chemistry has been successfully performed on electrospun fibers to generate TiO_2 nanotubes,[7] but uniform wetting of the huge surface area of the fiber matrix presents a significant and ongoing challenge for this method. In addition, PVD is a line-of-sight deposition technique that does not permit conformal deposition on fibers throughout the matrix. In CVD processes, depletion of precursor frequently limits uniform coating on large surface areas. Due to the limitations of these traditional deposition techniques, it is difficult to produce long nano/microtubes with smooth outer surfaces, uniform walls of controlled thicknesses at nanometer length scales.

In this work, atomic layer deposition (ALD)[19-22] has been applied to matrices of electrospun polymer fibers to fabricate Al_2O_3 microtubes with smooth wall surfaces and precisely controlled wall thickness. This strategy exploits a sequential, self-limiting deposition process that operates on the principle of alternating saturating surface reactions. During ALD, a specimen is exposed to a precursor vapor that forms a (sub)monolayer of the precursor on the substrate. After excess precursor is removed from the vapor phase by a purge gas (e.g., Ar), the reactant gas is subsequently pulsed onto the substrate, where it reacts with the adsorbed precursor layer to form a layer of the target film-forming material. Since no gas phase reaction occurs, the target film is grown layer-by-layer on the substrate, in which case the thickness of the deposited film can be accurately controlled by the number of

cycles the process is repeated, as illustrated in Fig. 8.1. Because of its unique process characteristics and controllability, ALD can be used to deposit conformal, uniformly thin films with precise thickness and composition control over large scales and onto substrates with complex topologies (including for example, fibers).[8,22,23] Moreover, ALD is chemically versatile and has been used to fabricate layers of metals,[24-26] metal oxides,[27] metal nitrides[22,24] and other materials. An additional benefit of ALD is that the deposition of Al_2O_3,[21,22] TiO_2[8] and TiN[24] can be conducted at relatively low temperatures (< 150˚C), thereby reducing, if not altogether eliminating, thermal damage to temperature-sensitive substrates such as organic media.

8.2. Experiment

Poly(vinyl alcohol) (PVA) with a molecular weight of 127 kDa and a degree of hydrolysis of 88% was purchased from Aldrich and used without further purification. A 7 wt% PVA aqueous solution was prepared by dissolving PVA in deionized water (DI H_2O) at 60˚C and stirring gently for 2 h. Electrospinning was performed using the parallel-plate setup described elsewhere.[14] A stable jet was formed at a flow rate of 7 μl/min and an electric field of 1 kV/cm. Representative electrospun PVA fibers were sputter-coated with Au/Pd prior to field-emission scanning electron microscopy (FESEM) analysis performed on a JEOL 6400F microscope operated at 5 kV. Coated fiber composites were fabricated by depositing thin Al_2O_3 films on the electrospun PVA fibers by ALD at 45˚C and a pressure of ~0.5 Torr. The aluminum precursor and oxygen reactant sources were $Al(CH_3)_3$ (TMA, 95%) and DI H_2O, respectively, and were delivered to the reactor as ambient-temperature vapors. During cycling, the TMA and DI H_2O were alternately introduced into the ALD chamber (base

pressure ~10^{-6} Torr) in pulses of 5 and 0.5 s, respectively. Purge times were 20 s for TMA and 60 s for DI H_2O. In conjunction with each ALD on PVA fibers, a piece of native oxide Si wafer (measuring ~1 cm × 1.5 cm, treated by JTB® Baker Clean, rinsed in DI water and then N_2 blown-dry) was used as a reference substrate for growth rate measurements on a planar surface under identical deposition conditions. To remove the organic constituent after ALD, the Al_2O_3-coated PVA fibers were heated in air at 400˚C for 24 h. After removing the PVA by calcination, the resultant microtubes were likewise characterized by FESEM under the same conditions listed above. Transmission electron microscopy (TEM) was conducted by sonicating Al_2O_3 microtubes in ethanol for 1 min. Several drops of the suspension were pipetted onto TEM grids, which were allowed to dry at ambient temperature and then imaged with a Hitachi HF-2000 microscope operated at 200 kV. Complementary energy-dispersive x-ray spectroscopy (EDS) was performed with an Oxford Instruments Inca Energy 100 system to ascertain the chemical composition of the microtubes under different ALD conditions.

8.3 Experiment results and discussion

A representative FESEM image of individual as-electrospun PVA fibers is presented in Fig. 8.2a. Depending on the duration of electrospinning, these fibers typically connect to form a self-supporting web. The diameters of most of the PVA fibers used in this study range from 200 to 400 nm. To reflect this size scale, we hereafter refer to the fibers as *microfibers*. In comparison with poly(L-lactide) (PLA) electrospun fibers, which have been traditionally used as templates by which to generate tubes by PVD and CVD,[15,28] PVA with surface hydroxyl groups capable of reacting with deposited precursor species is much less expensive

and likewise amenable to electrospinning from aqueous solution. These considerations are ultimately important in the mass production of high-quality templated microtubes. The resulting conformal deposition of Al_2O_3 on PVA fibers is shown in the FESEM images displayed in Figs. 8.2b and 8.2c, as well as in the TEM image included in Fig. 8.2d. Figure 8.2b indicates that the Al_2O_3 microtubes are connected together in a web, thereby preserving the original arrangement of the PVA electrospun fiber templates. This figure, which shows a large number of Al_2O_3 microtubes as only a very small part of the specimen investigated, also confirms that the ALD process yields uniform coverage over a relatively large area despite the apparent topological complexity. Most of the Al_2O_3 microtubes are observed to measure tens of micrometers in length, with many observed to extend into the millimeter range. The close-up FESEM image provided in Fig. 8.2c reveals the structure of the hollow Al_2O_3 microtubes formed after removal of the PVA core. It is apparent from this and related images that the outer surface of the microtubes after 475 ALD cycles is relatively smooth. In this case, the wall thickness of these Al_2O_3 nanometer tubes is estimated to be about 38 nm on the basis of TEM images such as the one displayed in Fig. 8.2d. As indicated by the arrow in this figure, the microtube replicates nanoscale features from the surface of the electrospun fiber. Attention is drawn here to a small neck in the PVA fiber, along with some small surface blemishes and a peripheral circular feature. A similar circular feature is likewise evident on the interior of a microtube produced after 300 cycles of ALD (cf. Fig. 8.3a).

Figure 8.3a is a TEM image of an Al_2O_3 replica of a PVA electrospun fiber template that was first exposed to Al_2O_3 ALD for 300 cycles prior to thermal treatment in air at 400˚C for 24 h. Despite their diameter (in excess of 200 nm), these microtubes appear electron

transparent when observed by TEM. The high-magnification TEM image provided in Fig. 8.3a demonstrates that the wall thickness of the microtubes is ~25 nm and is remarkably uniform along the length of a single tube. This observation extends to different tubes throughout the entire web. For comparison, Al_2O_3 microtubes formed after 150 ALD cycles are shown in the FESEM image in Fig. 8.3c. In this case, the wall thickness is only ~14 nm, according to TEM (cf. Fig. 8.3d). An EDS analysis performed on Al_2O_3 microtubes after 150, 300 and 475 ALD cycles and subsequent heating in air at 400°C for 24 h shows an Al:O ratio of 0.68:1 with 5% variation, thereby confirming that the elemental composition of the microtube walls is consistent with Al_2O_3. Carbonaceous residue has not been observed within the sensitivity of the EDS analysis (i.e., < 0.5%), as evidenced by the spectra provided in the Information in Fig. 8.5. Corresponding analysis of the ALD wall thickness under these conditions is displayed in Fig. 8.4. In this figure, the dependence of Al_2O_3 layer thickness on cycle number is discerned for (*i*) microtube walls on PVA fibers by TEM and (*ii*) planar films on Si wafers by ellipsometry. The average growth rate of Al_2O_3 on PVA fibers is ~0.08 nm/cycle, which is, within experimental uncertainty, virtually identical to the deposition rate (~0.07 nm/cycle) measured on the planar substrates under identical ALD conditions. A larger population of water molecules residing in the electrospun PVA fibers than on the Si substrate may explain the marginally higher growth rate on PVA.[21] The results shown in Fig. 8.4 indicate that the wall thickness of the Al_2O_3 microtubes generated here by ALD may be precisely (within a molecular layer or so) controlled by simply altering the number of deposition cycles.

CHAPTER 8 is a reprint of a manuscript published in Nano Letters

8.4 Conclusion

For microfluidic applications, the porosity and permeability of fabricated microtubes constitute important design concerns. Previous reports[29,30] of Al_2O_3 ALD performed on planar polymer substrates indicate that films measuring tens of nanometers thick (similar to those fabricated here) perform as high-quality gas barriers. Although the TEM images in Figs. 8.2 and 8.3 show evidence of breakage (presumably during calcination and/or sonication), the Al_2O_3 microtubes appear predominantly compact and smooth without discernible nanometer-size holes, suggesting that intact microtubes are most likely impermeable to liquids (e.g., water and organic solvents), while affording low permeability to gases. Even without process optimization, the results of this study unequivocally establish that ALD is an effective and robust strategy by which to fabricate long and uniform Al_2O_3 microtubes with precise control of wall thickness from electrospun PVA microfiber templates. By judiciously adjusting the electrospinning parameters, the diameter, alignment and structure of the templates can be further tuned as desired.[9-14] In similar fashion, the ALD process can be appropriately extended to synthesize designer microtubes of other inorganic materials such as TiO_2[8] and TiN.[24] Because ALD is a self-limiting vapor-phase process, it can be easily adapted to construct, via reactive layering, large numbers of tube structures with nanoscale-precision dimensions and controlled composition, thereby providing an attractive complement to physical self-assembly.[31]

8.5 ACKNOWLEDGMENTS

This work was supported by the STC Program of the National Science Foundation under Agreement No. CHE-9876674 (GNP) and the Department of Commerce through the

CHAPTER 8 is a reprint of a manuscript published in Nano Letters

National Textiles Center (RJS). GNP also acknowledges support from NSF under grant CTS-0626256.

CHAPTER 8 is a reprint of a manuscript published in Nano Letters

REFERENCES

1. Xia, Y. N.; Yang, P. D.; Sun, Y. G.; Wu, Y. Y.; Mayers, B.; Gates, B.; Yin, Y. D.; Kim, F.; Yan, Y. Q. *Adv. Mater.* **2003**, *15*, 353.
2. Lauhon, L. J.; Gudiksen, M. S.; Wang, C. L.; Lieber, C. M. *Nature* **2002**, *420*, 57.
3. Min, Y. S.; Bae, E. J.; Jeong, K. S.; Cho, Y. J.; Lee, J. H.; Choi, W. B.; Park, G. S. *Adv. Mater.* **2003**, *15*, 1019.
4. Lee, J. S.; Min, B.; Cho, K.; Kim, S.; Park, J.; Lee, Y. T.; Kim, N. S.; Lee, M. S.; Park, S. O.; Moon, J. T. *J. Cryst. Growth* **2003**, *254*, 443.
5. Martin, C. R. *Science* **1994**, *266*, 1961.
6. Steinhart, M.; Wendorff, J. H.; Greiner, A.; Wehrspohn, R. B.; Nielsch, K.; Schilling, J.; Choi, J.; Gosele, U. *Science* **2002**, *296*, 1997.
7. Caruso, R. A.; Schattka, J. H.; Greiner, A. *Adv. Mater.* **2001**, *13*, 1577.
8. Kemell, M.; Pore, V.; Ritala, M.; Leskela, M.; Linden, M. *J. Am. Chem. Soc.* **2005**, *127*, 14178.
9. Reneker, D. H.; Chun, I. *Nanotechnology* **1996**, *7*, 216.
10. Fridrikh, S. V.; Yu, J. H.; Brenner, M. P.; Rutledge, G. C. *Phys. Rev. Lett.* **2003**, *90*, 144502.
11. Li, D.; Xia, Y. N. *Adv. Mater.* **2004**, *16*, 1151.
12. Li, D.; Xia, Y. N. *Nano Lett.* **2004**, *4*, 933.
13. Li, D.; Ouyang, G.; McCann, J. T.; Xia, Y. N. *Nano Lett.* **2005**, *5*, 913.
14. Sun, X. -Y.; Shankar, R.; Börner, H. G.; Ghosh, T. K.; Spontak, R. J. *Adv. Mater.* **2007**, *19*, 87.

CHAPTER 8 is a reprint of a manuscript published in Nano Letters

15. Bognitzki, M.; Hou, H. Q.; Ishaque, M.; Frese, T.; Hellwig, M.; Schwarte, C.; Schaper, A.; Wendorff, J. H.; Greiner, A. *Adv. Mater.* **2000**, *12*, 637.

16. Czaplewski, D. A.; Kameoka, J.; Mathers, R.; Coates, G. W.; Craighead, H. G. *Appl. Phys. Lett.* **2003**, *83*, 4836.

17. Kameoka, J.; Verbridge, S. S.; Liu, H.; Czaplewski, D. A.; Craighead, H. G. *Nano Lett.* **2004**, *4*, 2105.

18. Dong, H.; Prasad, S.; Nyame, V.; Jones, W. E. *Chem. Mater.* **2004**, *16*, 371.

19. Gordon, R. G. *Abs. Am. Chem. Soc.* **2004**, *227*, U553.

20. Ferguson, J. D.; Weimer, A. W.; George, S. M. *Chem. Mater.* **2004**, *16*, 5602.

21. Groner, M. D.; Fabreguette, F. H.; Elam, J. W.; George, S. M. *Chem. Mater.* **2004**, *16*, 639.

22. Ritala, M.; Leskela, M.; Dekker, J. P.; Mutsaers, C.; Soininen, P. J.; Skarp, J. *Chem. Vap. Dep.* **1999**, *5*, 7.

23. Knez, M.; Kadri, A.; Wege, C.; Gosele, U.; Jeske, H.; Nielsch, K. *Nano Lett.* **2006**, *6*, 1172.

24. Kim, H. *J. Vac. Sci. Technol. B* **2003**, *21*, 2231.

25. Park, K. J.; Doub, J. M.; Gougousi, T.; Parsons, G. N. *Appl. Phys. Lett.* **2005**, *86*, 051903.

26. Park, K. J.; Parsons, G. N. *Appl. Phys. Lett.* **2006**, *89*, 043111.

27. Kim, H.; McIntyre, P. C. *J. Kor. Phys. Soc.* **2006**, *48*, 5.

28. Hou, H. Q.; Jun, Z.; Reuning, A.; Schaper, A.; Wendorff, J. H.; Greiner, A. *Macromolecules* **2002**, *35*, 2429.

CHAPTER 8 is a reprint of a manuscript published in Nano Letters

29. Groner, M. D.; George, S. M.; McLean, R. S.; Carcia, P. F. *Appl. Phys. Lett.* **2006**, *88*, 051907.

30. Carcia, P. F.; McLean, R. S.; Reilly, M. H.; Groner, M. D.; George, S. M. *Appl. Phys. Lett.* **2006**, *89*, 031915.

31. Zou, J.; Ji, B. H.; Feng, X. Q.; Gao, H. J. *Nano Lett.* **2006**, *6*, 430.

CHAPTER 8 is a reprint of a manuscript published in Nano Letters

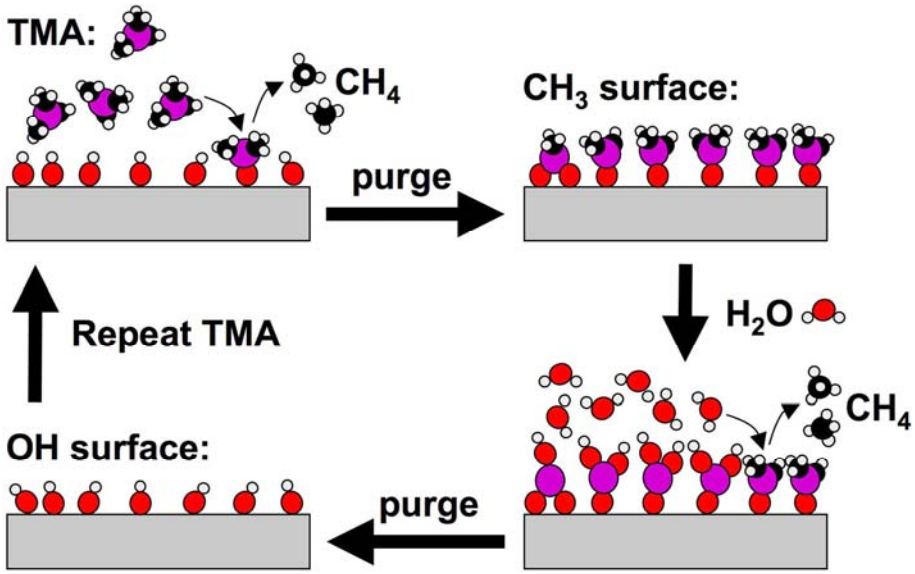


Figure 8.1. Schematic diagram of vapor-phase, self-limiting atomic layer deposition (ALD) illustrating the cyclic process by which an Al_2O_3 surface coating is controllably constructed layer-by-layer from TMA and H_2O precursors.

CHAPTER 8 is a reprint of a manuscript published in Nano Letters

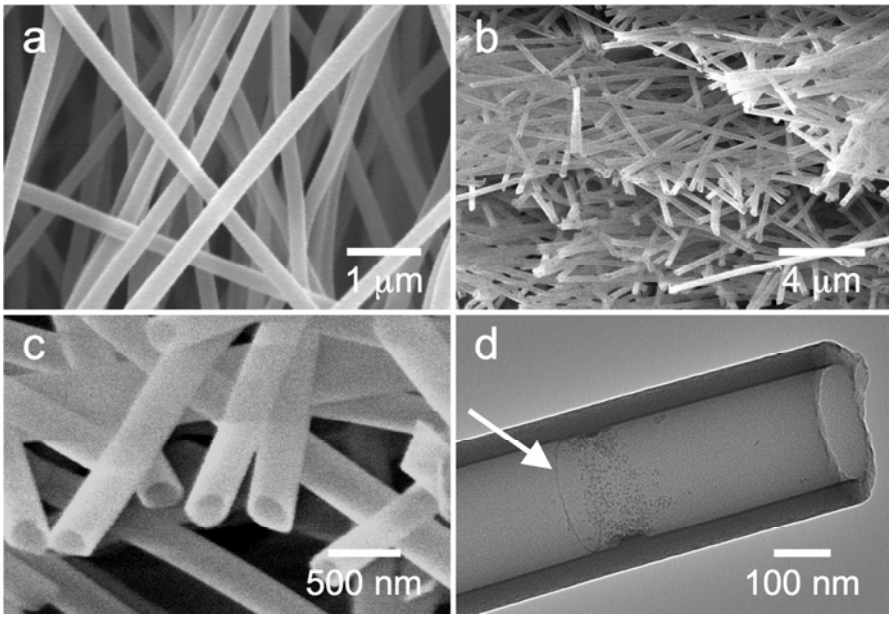


Figure 8.2. (a) FESEM image of electrospun PVA fibers. (b, c) FESEM images of Al_2O_3 microtube replicas prepared by ALD wherein the Al_2O_3 coating was deposited at 45˚C for 475 cycles. (d) TEM image of a corresponding Al_2O_3 microtube. The arrow in (d) identifies a peripheral circle formed inside the microtube near an apparent neck in the fiber template.

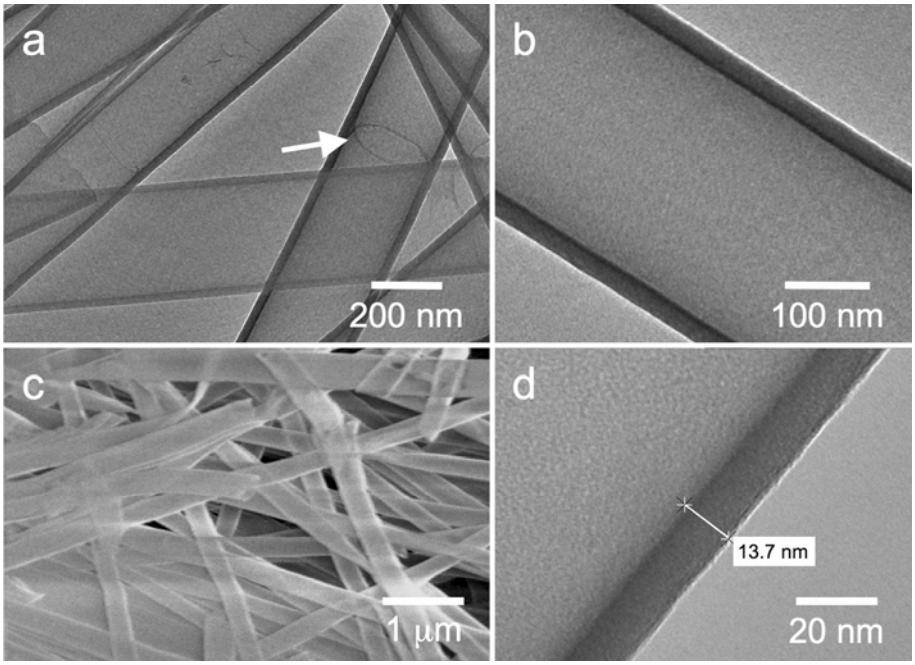


Figure 8.3. (a) FESEM image of an Al_2O_3 microtube in which ALD was performed on electrospun PVA fibers for 300 cycles at 45˚C. The arrow indicates a circle on the inside wall of the resultant microtube. (b) TEM image of the corresponding Al_2O_3 microtube illustrating the wall thickness. (c) FESEM and (d) TEM images of Al_2O_3 microtubes fabricated by ALD for 150 cycles at 45˚C. A wall thickness measurement is included in (d). In all cases, the electrospun PVA fiber templates were removed by heating in air at 400˚C for 24 h.

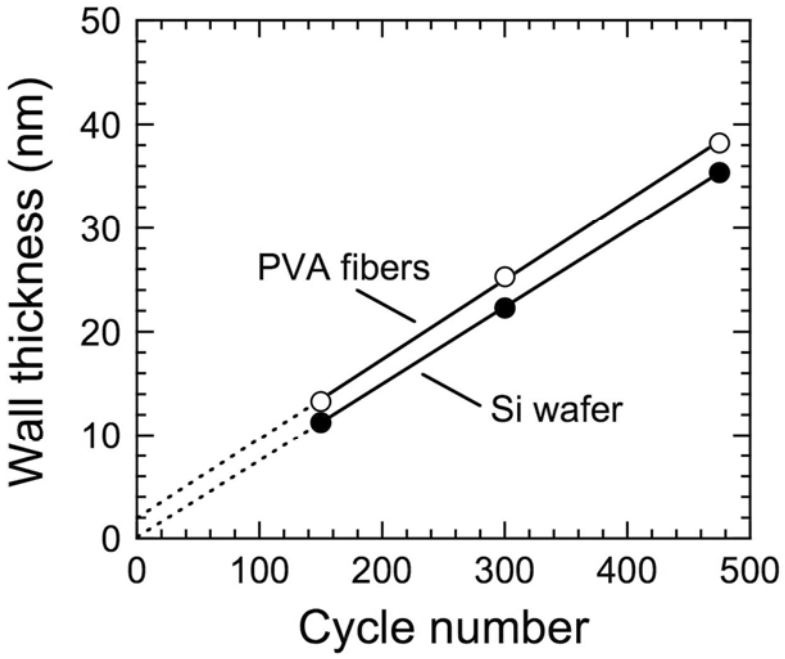


Figure 8.4. Wall thickness of Al_2O_3 microtubes prepared on electrospun PVA fibers (○) and measured by TEM as a function of ALD cycle number. Included for comparison is the Al_2O_3 film thickness on a planar Si substrate (●) measured by ellipsometry. The solid lines denote linear regressions of the data points. The corresponding average growth rates of Al_2O_3 are about 0.08 nm/cycle on the electrospun fibers and 0.07 nm/cycle on the Si substrate. Error bars (±1 standard deviation) deduced from analysis of 25 thickness measurements from each specimen are smaller than the symbols shown.

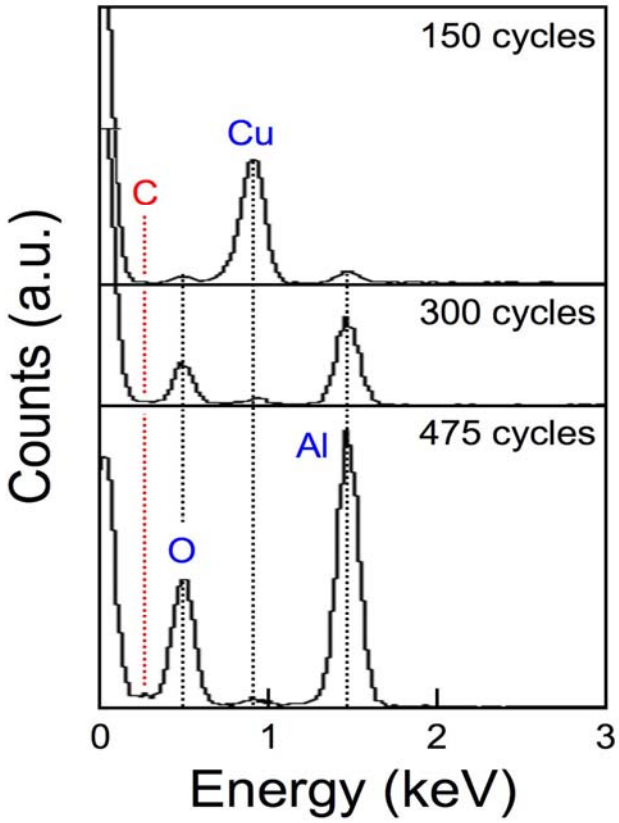


Figure 8.5. Representative EDS spectra acquired from the Al_2O_3 microtubes generated by ALD on electrospun polymer fibers after different cycle numbers (labeled). Note the presence of Al and O signals from Al_2O_3, as well as the absence of a discernible C peak from the polymer precursor (the instrument employed is capable of detecting C), after thermal treatment in air at 400°C for 24 h. The Cu signal is a consequence of the TEM grid and can be disregarded. The expected position for a signal due to C is also identified.

CHAPTER 9 is a reprint of a manuscript published in ACS Nano

CHAPTER 9. Bi-Directional Kirkendall Effect in Coaxial Microtube Nanolaminate Assemblies Fabricated by Atomic Layer Deposition

Qing Peng,[†] Xiao-Yu Sun,[†] Joseph C. Spagnola,[‡] Carl Saquing,[†] Saad A. Khan,[†] Richard J. Spontak,[†‡] and Gregory N. Parsons[†*]

Departments of [†]Chemical & Biomolecular Engineering and [‡]Materials Science & Engineering North Carolina State University, Raleigh NC 27695, USA

KEYWORDS: atomic layer deposition, electrospinning, aluminum oxide, zinc oxide, Kirkendall effect, tube-in-tube, microtube

[*]**Corresponding author:** parsons@ncsu.edu

ABSTRACT

The solid-state reaction within a coaxial Al_2O_3/ZnO/Al_2O_3 multilayered microtubular structure can be used to prepare discrete microtube-in-microtube $ZnAl_2O_4$ spinel assemblies through a Kirkendall void production mechanism at 700°C. In contrast with previous studies of the nano-scale Kirkendall effect, the reaction observed here proceeds through a bi-directional vacancy diffusion mechanism wherein ZnO species diffuse into inner- and outer-Al_2O_3 concentric layers, thereby resulting in vacancy supersaturation and void production between two isolated spinel microtubes. Low-temperature atomic layer deposition (ALD) of Al_2O_3 and ZnO enables the fabrication of complex coaxial multilayered microtubes with precise control of the starting film thicknesses and relative composition. When a molar excess of ZnO is present between two Al_2O_3 layers, electron microscopy images reveal incomplete ZnO consumption after annealing at 700°C. At higher initial Al_2O_3 mole fractions, however, complete reaction with ZnO is observed, and the size of the Kirkendall gap between isolated spinel microtubes appears to be directly influenced by the thickness of the ZnO layer.

CHAPTER 9 is a reprint of a manuscript published in ACS Nano

9.1 Introduction

Several interesting studies have recently demonstrated that the Kirkendall effect,[1] a well-known metallurgical process involving non-equilibrium counter-diffusion of two species through an interface, can be used to produce nanoscale objects including spherical shells,[2] nanotubes,[3-9] dendrites,[10] and other structures[11] with controlled dimensions and geometries. According to this mechanism, vacancies diffusing toward the region containing faster-diffusing species can either be annihilated at dislocations or, if the density or number of defects is sufficiently low, the vacancies can become supersaturated and condense to form voids. Production of such porous nanostructures often proceeds by exposing a small colloidal or nanocrystalline structure to a species or thin film coating of a complementary reactive compound. During subsequent reaction, accumulated vacancies will condense close to the interface and within the faster-diffusing core to form Kirkendall voids. The resulting voids can also enable surface diffusion of species, which, in turn, can accelerate the reaction kinetics.[5, 6] A wide range of complementary compounds have been identified and studied with regard to Kirkendall-related nanostructures.[2-14] The solid-state reaction and diffusion process that occurs between ZnO and Al_2O_3 in the formation of the spinel $ZnAl_2O_4$ is often used as a model system. For instance, quasi-one-dimensional ZnO nanowires or branched nanostructures generated by vapor-phase processes have been coated with highly conformal Al_2O_3 films of controlled thickness by atomic layer deposition (ALD).[4-8] The solid-state reaction between ZnO and Al_2O_3 progresses through fast outward diffusion of Zn or ZnO into the Al_2O_3 layer to form hollow microtubes of a single crystal or polycrystalline $ZnAl_2O_4$ spinel. [4-8]

CHAPTER 9 is a reprint of a manuscript published in ACS Nano

In all prior reports of the nanoscale Kirkendall effect induced in engineered assemblies, the nanoscale crystal "substrate" and complementary reactive coating or chemical species have been physically arranged in a bilayer (*e.g.*, Al_2O_3 on ZnO) so that the counter-diffusion process yields spinel in a single solid-state reaction zone (*e.g.*, between the ZnO and Al_2O_3 layers[4-8]). In this work, we demonstrate that, by using multilayer structures fabricated by successive ALD, the Kirkendall effect can be extended to produce alloys at multiple reaction interfaces, yielding a complex arrangement of multiple, isolated layers of a single alloy product. The resultant layers of spinel demonstrate that concurrent outward and inward diffusion of a fast-diffusing species can actively participate in Kirkendall void formation. Specifically, we show that when a trilayered Al_2O_3/ZnO/Al_2O_3 tubular nanostructure is prepared at material volumes that favor stoichiometric solid-state reaction, two spinel microtubes develop as a "microtube-in-microtube" structure wherein the microtubes are physically separated by a nanoscale gap (Kirkendall void). Moreover, by varying the volumes of the co-reactive species available at multiple binary junctions, the extent of each reaction and the thickness of the accompanying product layer can be independently controlled. This ability to tune multiple reaction fronts in a nanoscale Kirkendall process may open new opportunities for material design and function for a range of future nanotechnologies.

9.2 Experiment methods

The inorganic coaxial microtubes used in this study were prepared by coating electrospun poly(vinyl alcohol) (PVA) microfibers with Al_2O_3 and ZnO thin films deposited

by ALD. The fabrication processes regarding PVA electrospinning and ALD coating were described elsewhere. [15, 23] In the present work, Al_2O_3 ALD was conducted at 45˚C and ~0.9 Torr.[15] A modestly higher temperature (65°C) was used for ZnO ALD, also performed at ~0.9 Torr. The reactants included two organometallic precursors - trimethylaluminum ($Al(CH_3)_3$, TMA, 98%, Strem®) and diethyl zinc ($Zn(C_2H_5)_2$, DEZ, 96%, Strem®) and deionized water vapor (DI H_2O). All the species were delivered as ambient-temperature vapors into a custom-built hot-wall viscous flow tube reactor. High-purity Ar (99.999%) (National Welders Supply Co.) was used as the purge and carrier gas and further purified by a gas filter (DRIERITE Gas Purifier) before entering the reaction system. During cycling, the TMA and DI H_2O were alternately introduced into the ALD chamber (base pressure ~10^{-6} Torr) in pulses of 5 and 1 s, respectively. Corresponding purge times were 20 s (TMA) and 60 s (DI H_2O). For ZnO deposition, DEZ and DI H_2O were likewise injected into the reactor in pulses of 5 and 2 s respectively, and each purge time was 120 s. In conjunction with each ALD deposition on PVA microfiber mats, two pieces of silicon wafer (measuring ~1 cm × 1.5 cm, treated by JTB® Baker Clean, rinsed in DI water and then blown-dry with N_2) were used as reference substrates for growth rate measurements on a planar surface under identical deposition conditions. During deposition, the microfiber mat was positioned between the two Si wafers. The PVA microfiber templates were removed either by heating in air at 450˚C for 12 h or dissolution in DI H_2O for 12 h. In order to stimulate solid-state interfacial reaction, resultant specimens consisting of coaxial microtubes composed of Al_2O_3 and ZnO layers were subsequently annealed in a convective air furnace at 700˚C for 12 h. Microfibers and microtubes were examined by field-emission scanning electron microscopy (FESEM)

performed on a JEOL 6400F microscope operated at 5 kV. Microtube samples for transmission electron microscopy (TEM) analysis were first sonicated in ethanol for 1 min. Several drops of the suspension were pipetted onto carbon-coated TEM grids, which were allowed to dry at ambient temperature and then imaged with an FEI Tecnai G^2 Twin microscope operated at 160 kV. The crystal structure of the microtubes were characterized by X-ray diffractometry (XRD) performed on a Philips X'Pert PRO MRD HR diffractometer over an angular range of 5 to 85˚ (2θ) in intervals of 0.01˚ (2θ) and with a step duration of 1 s. For XRD, a mat of microtubes was attached to the sample holder by means of double-sided tape. The Al_2O_3 and ZnO ALD film thicknesses on Si wafer were discerned by ellipsometry using refractive indices of 1.79 and 2.00 for Al_2O_3 and ZnO, respectively. X-ray photoelectron spectroscopy (XPS) measurements were conducted on a Kratos Analytical AXIS ULTRA spectrometer outfitted with a monochromatic Al Kα source and operated at 15 kV. For all samples, the C 1s peak was normalized to 284.6 eV as the reference. In the survey and detail scans, the pass energies were maintained at 160 and 20 eV, respectively, and the data were analyzed and fitted using the CasaXPS software suite.

9.3 Results and discussions

Figure 9.1 is a schematic diagram of the synthesis procedure, based on atomic layer deposition chemistry, developed to generate coaxial $ZnAl_2O_4$ microtubes from sequentially layered Al_2O_3 and ZnO thin films. A matrix of electrospun poly(vinyl alcohol) (PVA) microfibers (Figure 9.1a) constitutes the initial substrate template. The fibers are coated with a conformal film of Al_2O_3 by ALD (Figure 9.1b), followed by ALD of ZnO (Figure 9.1c) and

another Al_2O_3 layer (Figure 9.1d) to form trilayered Al_2O_3/ZnO/Al_2O_3 coaxial nanostructures on a three-dimensional (3D) PVA microfiber mat. The ALD process allows the thickness of the deposited ZnO and Al_2O_3 coatings to be independently tuned with monolayer-scale precision by adjusting the number of ALD cycles used during fabrication.[15-17] After ALD film coating, the PVA core is eliminated by annealing at 450°C in air for 12 h (Figure 9.1e). Alternatively, the PVA core can be dissolved in deionized H_2O (DI H_2O) at ambient temperature. After PVA removal, the free-standing nano-laminated microtubes are further annealed at 700°C in air for an additional 12 h to induce species diffusion and solid-state reaction, as depicted in Figure 9.1f. The resulting unique nanostructure portrayed in Figure 9.1f is referred to as a "microtube-in-microtube" arrangement. Figure 9.1g schematically illustrates the difference between previous studies,[4-8] where the sample geometry promotes uni-directional vacancy diffusion from the slower- toward faster-diffusing species, and the present study, where a multilayer geometry enables bi-directional vacancy diffusion.

The approach used to deposit inorganic oxides on PVA microfibers, as well as the resulting film morphology and hollow microtubes, have been previously reported.[15] Microfibers of PVA coated by Al_2O_3 appear smooth and uniform, with the film thickness precisely controlled at the monolayer level and with film deposition proceeding during the first few ALD cycles without a detectible growth incubation period.[15] Figures 9.2a and 9.2b show PVA microfibers that have been sequentially coated by Al_2O_3 (212 ALD cycles) and ZnO (112 ALD cycles). These results confirm that successive ALD preserves the original 3D morphology of an electrospun PVA microfiber mat. An enlargement of a single PVA microfiber after coating with Al_2O_3 and ZnO is presented in Figure 9.2b. The dark core

corresponds to the PVA microfiber with a diameter of ~300 nm, and the bright shells correspond to coaxial Al_2O_3 and ZnO coatings. Figure 9.2c is a TEM image of an Al_2O_3/ZnO core-shell microtube formed after dissolving the PVA substrate in DI H_2O at ambient temperature for 12 h. It is interesting to note that the PVA substrate templated in this example consisted of two parallel microfibers fused longitudinally during electrospinning, and the ALD Al_2O_3/ZnO coating accurately retains the shape of the original substrate. Due to similar electron densities of Al_2O_3 and ZnO in this image, the precise thickness of each shell cannot be accurately determined. Similar concentric microtube morphologies are observed in all areas analyzed by TEM and are thus considered to be representative of the specimen. The surface of the outer ZnO shell is noticeably rougher than the comparable Al_2O_3 microtubes previously reported[4-7, 15] due presumably to the crystalline nature of ZnO ALD film. The bi/multilayered ALD coatings examined here consistently appear uniform along the length of each microtube, with no large defects detected by TEM measurement.

In the case of bilayered two-shell microtubes, removal of the PVA template by thermal calcination leads to significant breakdown of the microtubular morphology. After thermal calcination at 450˚C for 12 h, followed by sonication in ethanol, the ZnO coating is found to densify as it crystallizes into microtubes composed of aggregated ZnO nanoparticles measuring 10-30 nm across. In some cases, the inner Al_2O_3 shell deteriorates to form nanoscale plates (indicated by the arrows in Figure 9.2d), resulting in complete disintegration of the surrounding ZnO shell. These observations are ubiquitous and representative of the specimen. It is important to note that previous studies of PVA microfibers coated only by Al_2O_3 and annealed under similar conditions in our laboratory showed no evidence of

microtube disintegration.[15] The microtube deterioration exemplified in Figure 9.2d could be due to mechanical weak points introduced into the Al_2O_3 network by ZnO ALD. Such weak points can help to promote film disruption during thermal annealing and/or mechanical sonication.

X-ray photoelectron spectra collected from several ZnO films deposited by ALD on silicon wafers verify the presence of only Zn and O, with a relatively small amount (< 2.5 atom%) of C even for films deposited at temperatures as low as 65°C. The O1s spectrum shows evidence of oxide and O-H bonding, and peak integration indicates the -OH content comprises ~18% of the oxygen species present. Similar hydroxyl bonding is observed in infrared spectra of ZnO and Al_2O_3 layers deposited at low temperatures. We anticipate that any hydroxyl groups or carbon residue remaining after high-temperature annealing might influence the detailed energetics and kinetics of diffusion of the species/vacancy during spinel formation (*e.g.*, by enhancing vacancy formation or species diffusion rates), but the overall reaction process should not be significantly affected.

To explore mechanisms related to bi-directional vacancy diffusion, trilayered specimens consisting of three chemically distinct coatings were prepared by sequential ALD, thereby forming the Al_2O_3/ZnO/Al_2O_3/PVA coaxial microfiber morphology schematically depicted in Figure 9.1d. Upon removal of the inner PVA core by annealing at 450˚C in air for 12 h, (*cf.* Figure 9.1e), tri-shell Al_2O_3/ZnO/Al_2O_3 coaxial microtubes are obtained. Transmission electron micrographs of the resulting structures obtained after low temperature annealing are provided in panels a and b of Figures 9.3, 9.4 and 9.5. Each figure corresponds to samples prepared with different ALD layer thicknesses, and the number of ALD cycles

used to generate each layer is listed in Table 1. In sharp contrast to the previous bi-shell microtube morphology discussed with regard to Figure 9.2, the images in Figure 9.3, 9.4 and 9.5 demonstrate significantly less disintegration (implying improved stability) when the tri-shell assembly is calcinated at 450°C to eliminate the PVA core. It is reasonable to anticipate that, for the case of tri-shell assembly, the outer amorphous Al_2O_3 layer protects and reinforces the sandwiched semi-crystalline ZnO layer. Moreover, after heating to 450°C, the microtubes retain their compact tri-shell arrangement, as demonstrated, for example, in the high-resolution (HR), cross-sectional TEM image of an Al_2O_3/ZnO/Al_2O_3 coaxial microtube displayed in Figure 9.3b. In this image, three clearly defined shells are evident and appear intimately bound together with no voids located between the layers. Such HRTEM images provide a direct means by which to measure the thickness of each ALD layer in the tri-shell assembly, and the corresponding results are included in Table 1. The compact arrangement of the tri-shell Al_2O_3/ZnO/Al_2O_3 microtube layers affords complete confinement of the middle ZnO shell, which is able to react with both the inner and outer Al_2O_3 shells to form Kirkendall voids.

Annealing the trilayered coaxial microtubes at 700 °C initiates solid-state interfacial reaction and diffusion processes, and TEM images of the resultant morphologies are also presented in Figures 9.3, 9.4 and 9.5. Additional HRTEM images of samples after high temperature annealing are shown in Figure 9.6 and 9.7 as well. The composite materials studied here are unique compared to previous studies of the nanoscale Kirkendall mechanism in that all of the materials involved in the reaction are strategically deposited by ALD so that the relative composition of each reactant can be readily controlled by the number of ALD

cycles utilized to generate each layer. As alluded to and indicated in Table 1 earlier, the thicknesses of the ZnO and Al_2O_3 layers are different in each of the three specimen series displayed in Figures 9.3, 9.4 and 9.5. As indicated in panels c and d of Figure 9.3, the morphology of the microtubes changes dramatically upon annealing at 700°C for 12 h. The blotchy texture of the microtubes shown in Figure 9.3c suggests the formation of voids in the ZnO layer, and the TEM image provided in Figure 9.3d confirms the existence of Kirkendall voids in the ZnO layer below the outer Al_2O_3 shell. It is important to note that, before annealing at 700°C, the trilayered coaxial microtubes portrayed in Figure 9.3 possess a ZnO/Al_2O_3 film thickness ratio of about 21/(18 + 8.2) ≈ 0.80, which is larger than the molar volume ratio $\mathbf{V}_{ZnO}/\mathbf{V}_{Al_2O_3}$ of (14.5 cm^3/mol)/(25.7 cm^3/mol) ≈ 0.56. Although the mass density of ALD films deposited at low temperature may not be the same as bulk materials, the measured thickness ratio suggests that the sample in Figure 9.3 contained excess ZnO for the solid-state stoichiometric reaction $ZnO + Al_2O_3 \rightarrow ZnAl_2O_4$, which is consistent with the presence of ZnO after the solid state diffusion and reaction upon annealing at 700°C in air. For comparison, the samples discussed with regard to Figures 9.4 and 9.5 have a thinner ZnO inner shell and/or thicker Al_2O_3 outer shells, giving rise to a reaction excess of Al_2O_3 in those samples.

Figure 9.4 shows TEM images acquired from another set of trilayered $Al_2O_3/ZnO/Al_2O_3$ coaxial microtubes with film thicknesses of 18/10/25 nm, respectively. Relative to the specimen described in relation to Figure 9.3, this sample has a thinner (10 nm) ZnO layer and a thicker (25 nm) outer Al_2O_3 shell. Images in panels a and b of Figure 9.4 verify that the microtubes maintain a trilayered coaxial arrangement after calcination at

450°C. This arrangement is particularly striking in the HRTEM image of a broken microtube in Figure 9.4b, wherein the sandwiched ZnO middle layer appears dark relative to the brighter Al_2O_3 inner and outer shells. Corresponding images of microtubes annealed at 700°C for 12 h are displayed in panels c-f of Figure 9.4. While broken pieces of inner and outer shells are visible in Figure 9.4c, panels d-f provide evidence that the trilayer morphology largely remains intact after annealing. Note, however, that the middle layer now appears bright relative to the inner and outer shells, thereby revealing a gap that develops between the two shells. Close examination of the broken microtube edge in Figure 9.4f confirms the presence of a gap that results from the bi-directional solid-state reaction and diffusion process between the Al_2O_3 and ZnO layers. As before, HRTEM images permit direct assessment of thicknesses of the layer and gap, and the results are given in Table 1. The values reported here represent averages of more than 30 analysis points measured on several microtube samples. Two observations warrant mention here. The first is that the dimension of the gap is generally not uniform, possibly due to the relative proximity of the microtubes to each other, and surface roughness resulting from the polycrystalline nature of the inner and outer tubes. The second, expected from the solid-state reaction, is that high-temperature annealing promotes an increase in the inner and outer shell thicknesses. For the specimens shown in Figure 9.4, for instance, the inner shell is found to increase by 22% from 18 to ~22 nm, whereas the outer shell increases by 12% from 25 to ~ 28 nm. The arrow in Figure 9.4d identifies a broken shell piece that is ~28 nm thick. Existence of this isolated outer shell confirms that the adjacent shells are separated from each other after high-temperature annealing. Other broken shells from this sample set were further characterized

by HRTEM, and the images are shown in Figure 9.6. The layers show polycrystalline domains, with lattice spacings consistent with $ZnAl_2O_4$. X-ray diffraction data, shown in Figure 9.8, is also in agreement with this assignment. We also note from the HRTEM images in Figure 9.6 that the spinel $ZnAl_2O_4$ and amorphous Al_2O_3 are presented as separated phases in both inner (panels a and b) and outer (panels c and d) shells.

To further explore the versatility of this process and our capability to tune the extent of the bi-directional solid-state reaction and diffusion processes, the thickness of ZnO and Al_2O_3 shells have been further adjusted by sequential ALD to produce a larger Kirkendall gap. Images of the resulting morphologies are presented in Figure 9.5. Coaxial Al_2O_3/ZnO/Al_2O_3 microtubes formed after calcination are evident in panels a and b of Figure 9.5, while TEM images of those generated after annealing at 700°C are included in panels c and d. After heating to 450°C, the Al_2O_3(inner)/ZnO/Al_2O_3(outer) coaxial shells possess thicknesses of 18/21/38.5 nm, respectively, with the middle ZnO shell consistently appearing darker relative to both Al_2O_3 shells. After annealing at 700°C, a bright gap once again appears to be sandwiched by two darker shells. This gap, particularly clear in the HRTEM image in Figure 9.5d, measures 11.7±1.8 nm across, and the thicknesses of the outer and inner shells are 44.4±2.3 nm and 22.6±3.1 nm, respectively. It is important to recognize that this specimen is comparable to the sample portrayed in Figure 9.3 except for a thicker outer Al_2O_3 shell (38.5nm *versus* 8.5nm). The thicker Al_2O_3 shell allows consumption of all available ZnO during the solid-state reaction and diffusion processes upon annealing at 700°C, thereby producing a visible gap between the spinel microtubes. This signature feature

is absent in Figure 9.3. Densification can also be considered as a possible mechanism for void formation,[18] and the polycrystalline ZnO layers deposited at low temperature in the samples discussed with regard to Figures 9.3 and 9.5 are expected to undergo some degree of density change upon annealing. The very different final products displayed in Figures 9.3d and 9.5d cannot, however, be reconciled by considering only the densification of films. Rather, the difference between the two specimen series further corroborates the existence of a bi-directional vacancy diffusion mechanism.

The resulting physical separation between the inner and outer tubes is further visualized in the electron micrographs shown in Figure 9.7. These images were collected from a sample of microtubes with Al_2O_3/ZnO/Al_2O_3 of ~18/10/44 nm, respectively, after annealing at 700°C. The electron micrograph in Figure 9.7a shows a broken inner tube protruding from an outer tube, demonstrating clear physical separation between the tubes. The size of the gap is consistent with that shown in Figure 9.4 for samples with a similar starting thickness of ZnO. The TEM image also shows some nano-scale roughness of the spinel layers along the length of the tube, on the surface adjacent to the Kirkendall void. The HRTEM image in Figure 9.7b also reveals the polycrystalline nature of the tubes, consistent with inward and outward diffusion of Zn-related species into the Al_2O_3 layers, and the lattice spacings are consistent with $ZnAl_2O_4$ as well. No sharp interface is present between excess Al_2O_3 and the spinel shells.

In addition to the microtube structures shown here, it may be possible to extend this concept to planar or other three-dimensional nano- or micro-structures. For a planar

configuration, the bi-directional Kirkendall reaction for nano-laminated $Al_2O_3/ZnO/Al_2O_3$ films with suitable molar ratio is expected to result in two $ZnAl_2O_4$ layers. However there is no physical means to support a large area gap between these layers. Preliminary experiments suggest formation of two planar layers that may be physically separated, for example, by mechanical peeling.

The crystal structure of the microtubes displayed in Figure 9.4 have been analyzed by XRD after annealing at 450°C and 700°C, and results are provided in panels a and b, respectively, of Figure 9.8. The specimen annealed at 450°C shows only ZnO-related diffraction features, consistent with polycrystalline ZnO located between amorphous Al_2O_3 layers. The reflections present after annealing at 700°C, on the other hand, correspond to polycrystalline $ZnAl_2O_4$ spinel, providing direct evidence for the solid-state reaction between ZnO and Al_2O_3 in the coaxial microtubes assembly. In this case, the interfacial reaction appears to consume all the ZnO reactant in the middle shell. Previous results[19-21] show that thin ALD Al_2O_3 films show crystalline structure upon extended annealing at temperature above 800°C. The formation of segregated interfacial voids and microtube-in-microtube structures therefore demonstrates that the nanoscale Kirkendall effect can be directly extended to trilayered systems, where the solid-state reaction and diffusion simultaneously proceeds in two opposite directions across two spatially isolated interfaces.

The results shown in Figure 9.9 for samples in the microtube geometry, highlight the ability to tune the thickness of deposited films by sequential ALD and the size of reaction-induced Kirkendall gap that can develop between microtubes. The figure compares the

thicknesses of ALD coatings in microtube assmblies, as measured by TEM after annealing at 450°C, to those of ALD films deposited directly on planar silicon wafers, as determined by ellipsometry. As expected, the thickness of the ZnO and Al_2O_3 films deposited on a planar surface increases linearly with the number of ALD cycles at a growth rate of ~ 0.19 nm/cycle for ZnO and ~ 0.08 nm/cycle for Al_2O_3. Several cycles of growth incubation time may be required for ZnO ALD, which is consistent with previous reports.[16, 22] The TEM results gleaned from layers deposited under the same conditions on the fiber matrix indicate remarkably similar growth rate per cycle. The TEM data constitute mean values of more than 30 measurements, and the corresponding standard deviation is less than 7% on average. Figure 9.9 also shows the size of the gap between microtubes after annealing at 700°C. These results, obtained from TEM images such as those provided in Figures 9.3, 9.4, and 9.5, are plotted as a function of the cycle number used for ZnO ALD. Under conditions where there is sufficient Al_2O_3 present to react with the available ZnO (*i.e.,* the sample series displayed in Figures 9.4 and 9.5) the void dimension increases with increasing ZnO thickness, demonstrating that the Kirkendall gap size can be controlled by varying the ALD film thickness. It is important to note that the precise correspondence between the starting ZnO layer thickness and the ensuing void or gap size will depend on the reaction volume of the surrounding Al_2O_3 layers. When insufficient Al_2O_3 reactant is available and ZnO is in molar excess, discrete voids, rather than a distinct, contiguous gap, develop after annealing at 700°C for 12 h (*cf.* Figure 9.3).

CHAPTER 9 is a reprint of a manuscript published in ACS Nano

9.4 Conclusion

The experimental results reported here establish that Kirkendall voids can be formed between two $ZnAl_2O_4$ spinel microtubes through the solid-state reaction and diffusion processes between concentric Al_2O_3 and ZnO shells deposited by low-temperature ALD on fibrous templates. The resulting morphologies can be described as microtube-in-microtube $ZnAl_2O_4$ assemblies, where the individual spinel microtubes are separated by a continuous hollow gap. The process is understood in terms of a bi-directional vacancy diffusion mechanism, wherein ZnO diffuses into both inner and outer Al_2O_3 layers, resulting in vacancy accumulation and supersaturation between the two spinel microtubes. If the mole fraction of Al_2O_3 is insufficient for completion of the spinel formation reaction, excess ZnO crystallites remain in the reaction zone after annealing. For samples with an equal or excess Al_2O_3 mole fraction, the thickness of the Kirkendall gap between isolated spinel microtubes can be controlled in part by the thickness of the deposited ZnO layer. Fabrication of microtube-in-microtube assemblies is achieved using the precise control over layer thickness afforded by ALD of Al_2O_3 and ZnO thin layers at low deposition temperatures. This work demonstrates that complex material multilayers produced by ALD can enable vacancy diffusion in more than one direction. Extending this scheme to other materials and geometries will open new possibilities for complex nano-architecture synthesis and engineering, for a broad range of nano-technological applications.

CHAPTER 9 is a reprint of a manuscript published in ACS Nano

9. 5 Acknowledgments

This work was supported by the STC Program of the National Science Foundation under Agreement No. CHE-9876674. Support is also acknowledged from NSF CTS-0626256 (GNP), the Nonwovens Cooperative Research Center (GNP) and the National Textile Center (RJS).

CHAPTER 9 is a reprint of a manuscript published in ACS Nano

REFERENCES

1. Smigelskas, A. D.; Kirkendall, E. O., Zinc Diffusion in Alpha-Brass. *Transactions of the American Institute of Mining and Metallurgical Engineers* **1947,** *171*, 130-142.
2. Yin, Y. D.; Rioux, R. M.; Erdonmez, C. K.; Hughes, S.; Somorjai, G. A.; Alivisatos, A. P., Formation of Hollow Nanocrystals Through the Nanoscale Kirkendall Effect. *Science* **2004,** *304*, 711-714.
3. Tu, K. N.; Gosele, U., Hollow Nanostructures Based on the Kirkendall Effect: Design and Stability Considerations. *Appl. Phys. Lett.* **2005,** *86*.
4. Fan, H. J.; Knez, M.; Scholz, R.; Nielsch, K.; Pippel, E.; Hesse, D.; Zacharias, M.; Gosele, U., Monocrystalline Spinel Nanotube Fabrication Based on the Kirkendall Effect. *Nature Mater.* **2006,** *5*, 627-631.
5. Fan, H. J.; Gosele, U.; Zacharias, M., Formation of Nanotubes and Hollow Nanoparticles Based on Kirkendall and Diffusion Processes: A Review. *Small* **2007,** *3*, 1660-1671.
6. Fan, H. J.; Knez, M.; Scholz, R.; Hesse, D.; Nielsch, K.; Zacharias, M.; Gosele, U., Influence of Surface Diffusion on the Formation of Hollow Nanostructures Induced by the Kirkendall Effect: The Basic Concept. *Nano Lett.* **2007,** *7*, 993-997.
7. Yang, Y.; Kim, D. S.; Knez, M.; Scholz, R.; Berger, A.; Pippel, E.; Hesse, D.; Gosele, U.; Zacharias, M., Influence of Temperature on Evolution of Coaxial ZnO/Al_2O_3 One-Dimensional Heterostructures: from Core-Shell Nanowires to Spinel Nanotubes and Porous Nanowires. *J. Phys. Chem. C* **2008,** *112*, 4068-4074.

CHAPTER 9 is a reprint of a manuscript published in ACS Nano

8. Yang, Y.; Kim, D. S.; Scholz, R.; Knez, M.; Lee, S. M.; Gosele, U.; Zacharias, M., Hierarchical Three-Dimensional ZnO and Their Shape-Preserving Transformation into Hollow $ZnAl_2O_4$ Nanostructures. *Chem. Mater.* **2008,** *20*, 3487-3494.

9. Qiu, Y.; Yang, S., Kirkendall Approach to the Fabrication of Ultra-Thin ZnO Nanotubes with High Resistive Sensitivity to Humidity. *Nanotechnology* **2008,** *19*, 265606-1– 265606-7.

10. Ng, C. H. B.; Tan, H.; Fan, W. Y., Formation of Ag_2Se Nanotubes and Dendrite-Like Structures from UV Irradiation of a CSe_2/Ag Colloidal Solution. *Langmuir* **2006,** *22*, 9712-9717.

11. Li, Q.; Penner, R. M., Photoconductive Cadmium Sulfide Hemicylindrical Shell Nanowire Ensembles. *Nano Lett.* **2005,** *5*, 1720-1725.

12. Yin, Y. D.; Erdonmez, C. K.; Cabot, A.; Hughes, S.; Alivisatos, A. P., Colloidal Synthesis of Hollow Cobalt Sulfide Nanocrystals. *Adv. Funct. Mater.* **2006,** *16*, 1389-1399.

13. Henkes, A. E.; Vasquez, Y.; Schaak, R. E., Converting Metals into Phosphides: A General Strategy for the Synthesis of Metal Phosphide Nanocrystals. *J. Am. Chem. Soc.* **2007,** *129*, 1896-1897.

14. Chiang, R. K.; Chiang, R. T., Formation of Hollow Ni_2P Nanoparticles Based on the Nanoscale Kirkendall Effect. *Inorg. Chem.* **2007,** *46*, 369-371.

15. Peng, Q.; Sun, X. Y.; Spagnola, J. C.; Hyde, G. K.; Spontak, R. J.; Parsons, G. N., Atomic Layer Deposition on Electrospun Polymer Fibers as a Direct Route to Al_2O_3 Microtubes with Precise Wall Thickness Control. *Nano Lett.* **2007,** *7*, 719-722.

CHAPTER 9 is a reprint of a manuscript published in ACS Nano

16. Elam, J. W.; George, S. M., Growth of ZnO/Al_2O_3 Alloy Films Using Atomic Layer Deposition Techniques. *Chem. Mater.* **2003,** *15*, 1020-1028.

17. Elam, J. W.; Sechrist, Z. A.; George, S. M., ZnO/Al_2O_3 Nanolaminates Fabricated by Atomic Layer Deposition: Growth and Surface Roughness Measurements. *Thin Solid Films* **2002,** *414*, 43-55.

18. Striemer, C. C.; Gaborski, T. R.; McGrath, J. L.; Fauchet, P. M., Charge- and Size-Based Separation of Macromolecules Using Ultrathin Silicon Membranes. *Nature* **2007,** *445*, 749-753.

19. Jakschik, S.; Schroeder, U.; Hecht, T.; Gutsche, M.; Seidl, H.; Bartha, J. W., Crystallization Behavior of Thin ALD-Al_2O_3 Films. *Thin Solid Films* **2003,** *425*, 216-220.

20. Scarel, G.; Hyde, G. K.; Hojo, D.; Parsons, G. N., Berreman Effect in Infrared Absorption Spectroscopy of Ionic Oxide Coatings Formed by Atomic Layer Deposition on Three-Dimensional Structures. *J. Appl. Phys.* **2008,** *104*, 094314-1–094314-9.

21. Afanas'ev, V. V.; Stesmans, A.; Mrstik, B. J.; Zhao, C., Impact of Annealing-Induced Compaction on Electronic Properties of Atomic-Layer-Deposited Al_2O_3. *Appl. Phys. Lett.* **2002,** *81*, 1678-1680.

22. Yousfi, E. B.; Fouache, J.; Lincot, D., Study of Atomic Layer Epitaxy of Zinc Oxide by In-Situ Quartz Crystal Microgravimetry. *Appl. Surf. Sci.* **2000,** *153*, 223-234.

CHAPTER 9 is a reprint of a manuscript published in ACS Nano

23. Sun, X. Y.; Shankar, R.; Borner, H. G.; Ghosh, T. K.; Spontak, R. J., Field-Driven Biofunctionalization of Polymer Fiber Surfaces during Electrospinning. *Adv. Mater.* **2007,** *19*, 87-91.

CHAPTER 9 is a reprint of a manuscript published in ACS Nano

Table 9.1 Characteristic dimensions of initial ALD layers and post-reaction spinel layers and Kirkendall gaps.

Figure	Inner Al_2O_3	ZnO	Outer Al_2O_3	Spinel / Gap / Spinel[b]
9.2	18 (212)	21 (112)	–	–
9.3	18 (212)	21 (112)	8.5 (100)	N/A
9.4	18 (212)	10 (55)	25 (300)	22 ± 0.8 / 6.4 ± 1.5 / 28 ± 1.0
9.5	18 (212)	21 (112)	39 (450)	23 ± 3.1 / 12 ± 1.8 / 44 ± 2.3

[a] Presented as thickness, in nm (number of ALD cycles).

[b] Presented as thickness, in nm. Uncertainties represent 1 standard deviation from ~30 measurements.

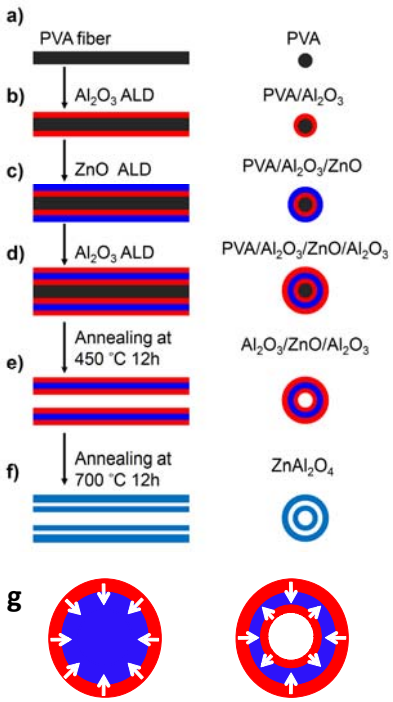


Figure 9.1. Schematic diagram of the procedure developed here for the fabrication of coaxial $ZnAl_2O_4$ microtube-in-microtube coaxial assemblies: (a) electrospinning is used to produce PVA microfibers; (b) a thin, conformal Al_2O_3 coating is applied to the PVA fibers by low-temperature ALD; (c) a successive ZnO coating is applied by ALD; (d) a second Al_2O_3 coating is applied by ALD, resulting in trilayered $PVA/Al_2O_3/ZnO/Al_2O_3$ microcables; (e) the PVA core is removed by calcination at 450°C in air for 12 h; (f) the resultant $Al_2O_3/ZnO/Al_2O_3$ coaxial microtubes are annealed at 700˚C to form coaxial $ZnAl_2O_4$ microtubes separated by a nanometer-scale gap resulting from accumulation of Kirkendall voids. (g) White arrows show the direction of vacancy diffusion for a typical nanoscale Kirkendall-effect experiment in which Al_2O_3 is coated onto a ZnO crystal (left), as well as for the experimental procedure described here, where diffusion occurs in two directions to produce an internal nanoscale gap (right).

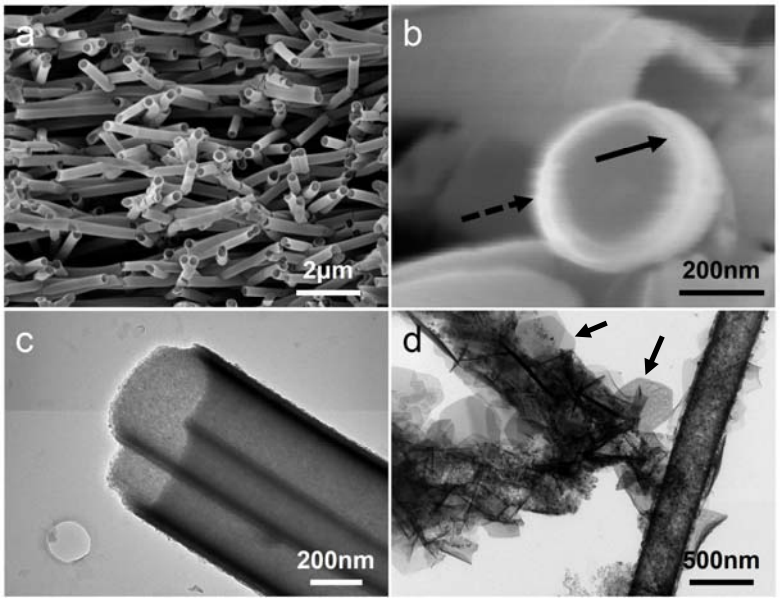


Figure 9.2. SEM (a and b) images of PVA electrospun fibers coated with an Al_2O_3(inner)/ZnO(outer) bilayer deposited by low-temperature ALD. Film thicknesses and the number of ALD cycles used in this and subsequent specimens are provided in Table 1. The SEM image in (b) shows a single PVA fiber with the coaxial bi-layer coating (Al_2O_3, solid arrow; ZnO, dashed arrow). TEM (c and d) image of the coaxial Al_2O_3/ZnO microtubes obtained after removal of the PVA by dissolution in water, which is displayed in (c), whereas microtubes produced after PVA calcinations, which are evident in (d).

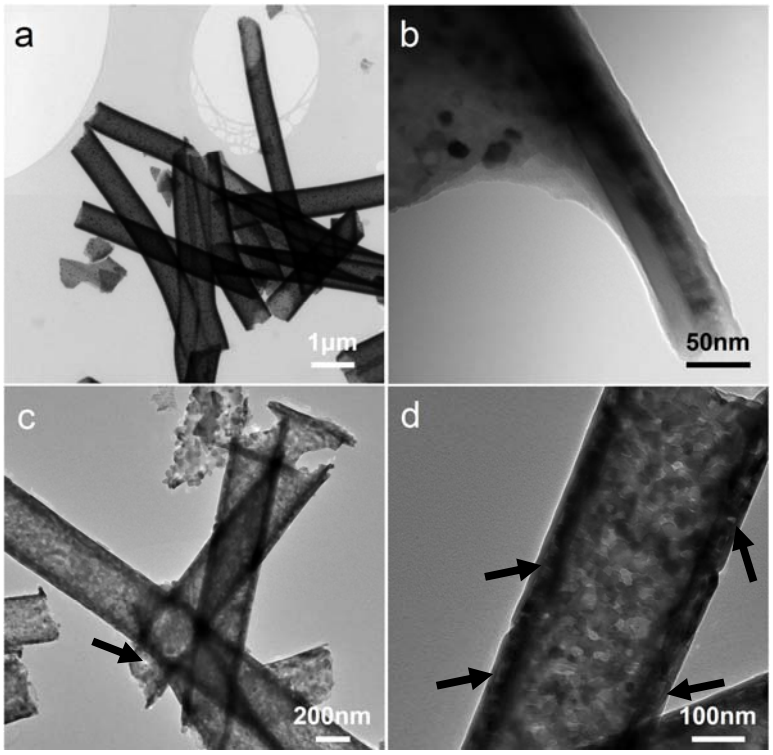


Figure 9.3. Representative TEM images of $Al_2O_3/ZnO/Al_2O_3$ microtubes formed by ALD on PVA microfibers. The images in (a) and (b) were obtained after annealing at 450˚C in air. The image in (b) permits direct visualization of the trilayered morphology consisting of a dark polycrystalline ZnO middle layer and lighter amorphous Al_2O_3 shells. The images in (c) and (d) were obtained after annealing at 700°C for 12 h. Light spots (arrows in c and d) indicate void formed within the tubular structure. Unreacted excess ZnO partitions between the inner and outer shells.

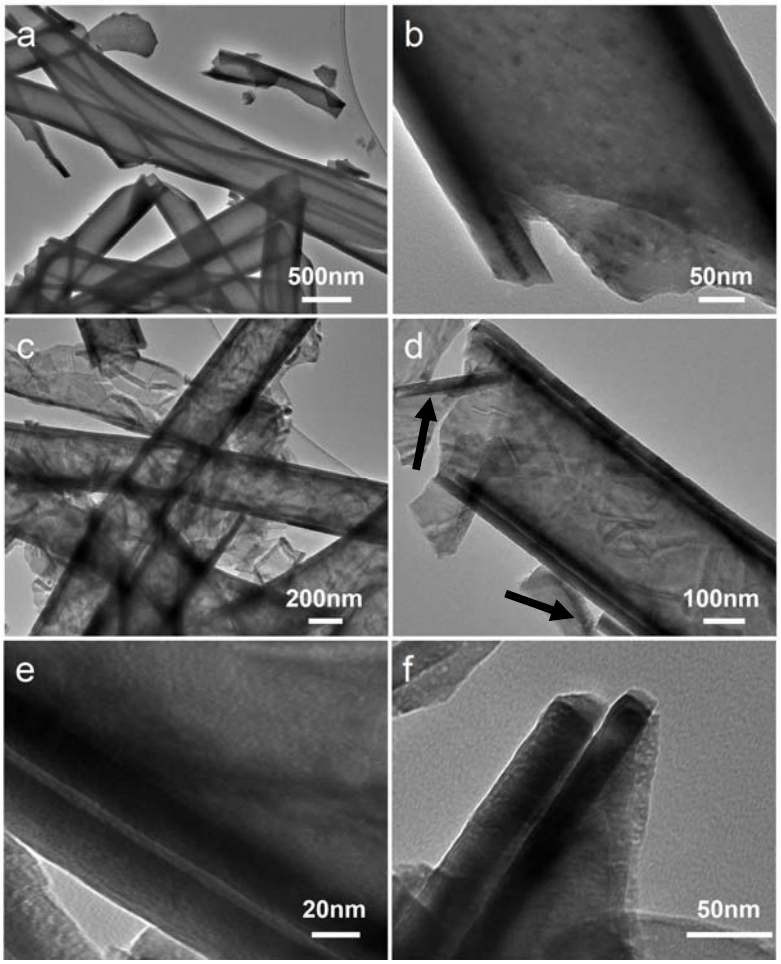


Figure 9.4. TEM images of $Al_2O_3/ZnO/Al_2O_3$ microtubes: (a), (b) after annealing in air at 450°C; The HRTEM image in (b) shows the thin dark ZnO middle layer sandwiched between two lighter Al_2O_3 layers. (c) – (f) after further annealing at 700°C for 12 h. Compared to samples in Figure 9.3, these samples contained a thinner (~10 nm) ZnO layer, with a thicker (~25 nm) outer Al_2O_3 layer. The arrows in (d) identify isolated pieces of the inner or outer shells as a consequence of microtube fracture. In (e) and (f), HRTEM images reveal a light middle layer located between two darker layers, indicating the formation of a thin gap between two polycrystalline $ZnAl_2O_4$ layers.

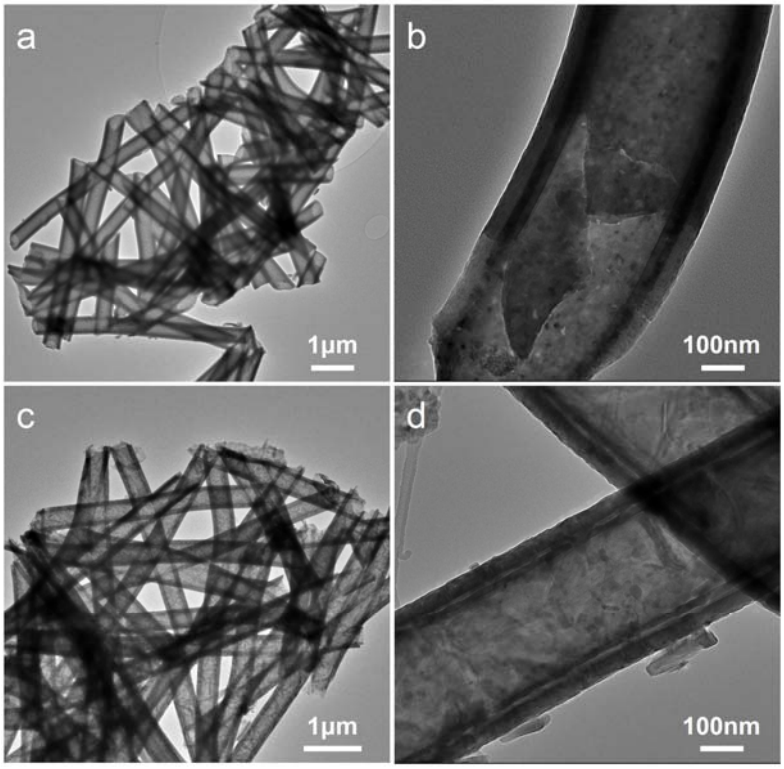


Figure 9.5. TEM images of $Al_2O_3/ZnO/Al_2O_3$ microtubes similar to those shown in Figure 9.4, with thicker ZnO (~21 nm) and outer Al_2O_3 (~39 nm) layers: (a), (b) annealed at 450˚C in air; (c), (d) annealed at 700°C for 12 h. Image contrast (and reversal) is identical to that observed in Figure 9.4. A continuous Kirkendall gap is evident in (d).

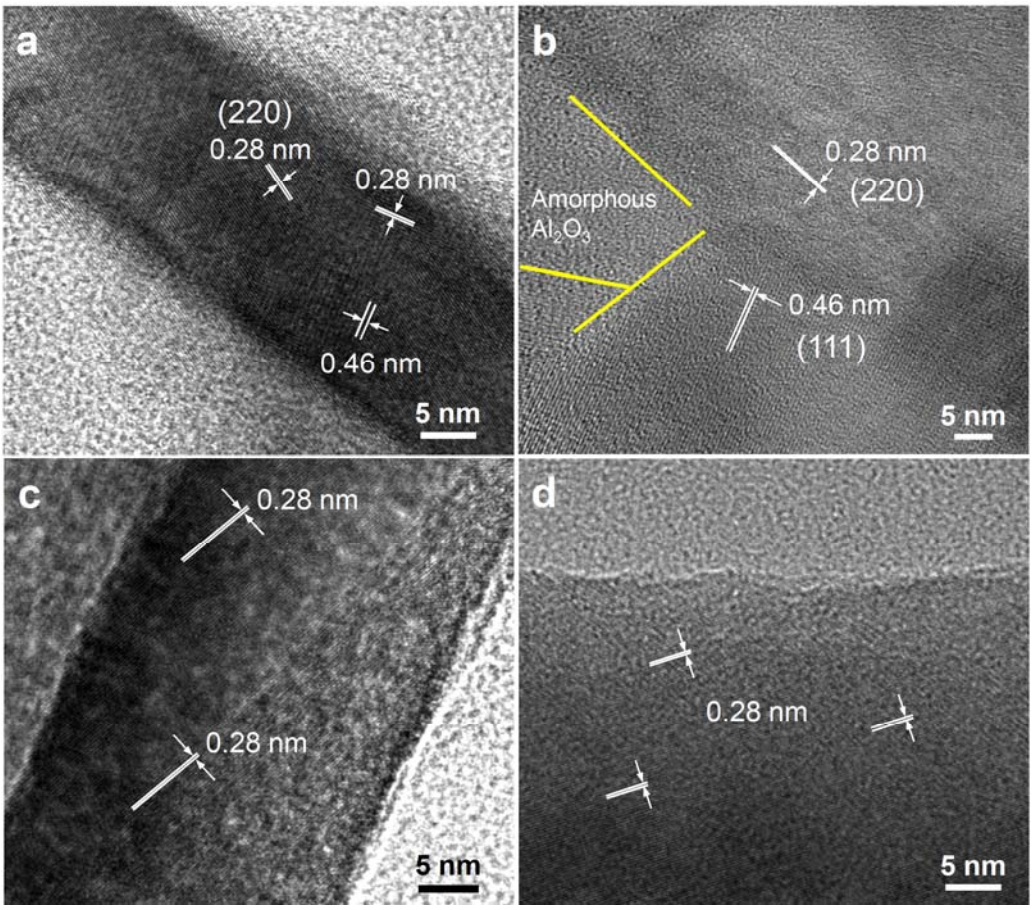


Figure 9.6 HRTEM images of a) a section of isolated inner tube wall, showing polycrystalline structures, b) a part of inner tube shell showing polycrystalline $ZnAl_2O_4$ and amorphous Al_2O_3 region (within the yellow line region), c) a section of outer tube wall consisting mainly of $ZnAl_2O_4$ crystal, d) a section of outer tube wall having $ZnAl_2O_4$ crystalline and amorphous Al_2O_3. The inner and outer microtubes obtained from the sample batch shown in Figure 9.4 after 700°C for 12 h. Lattice spacing is 0.46 and 0.28 nm corresponding to the 111 and 220 planes of $ZnAl_2O_4$ respectively.

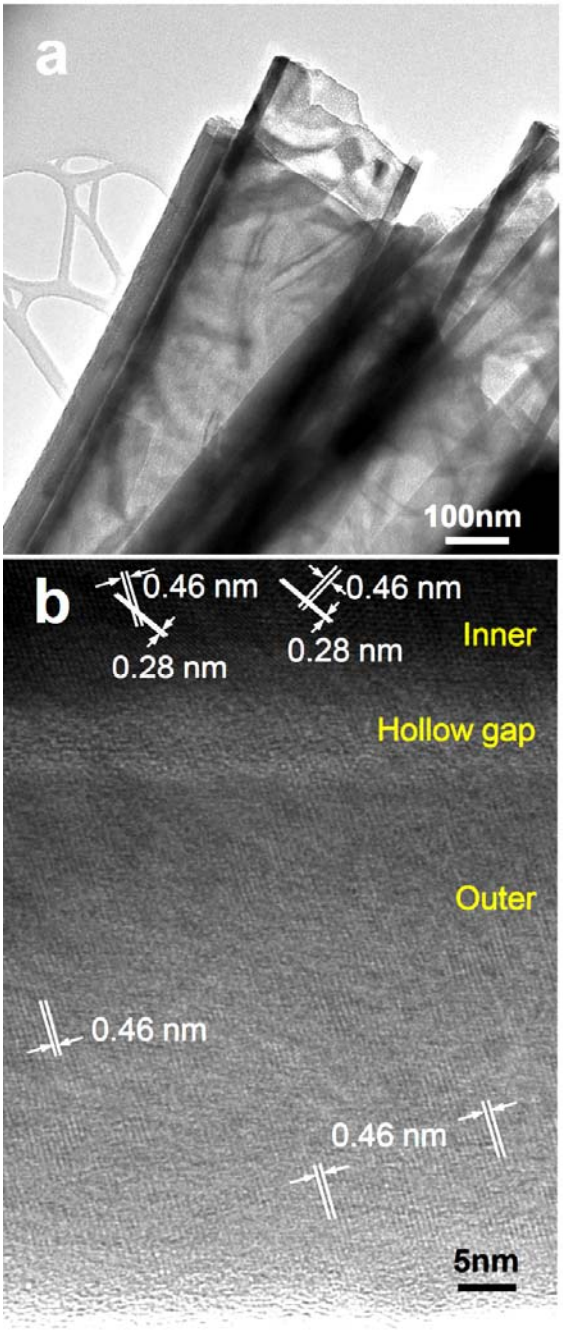


Figure 9.7. Typical TEM image of $Al_2O_3/ZnO/Al_2O_3$ microtubes (~18/10/44nm) annealed at 700°C for 12h. a) The broken tubes reveal clear physical separation and delineation between the inner and outer tubes. The image reveals roughness of the spinel layers along the length of the tube, on the surfaces adjacent to the Kirkendall void. A process break during the final Al_2O_3 coating step resulted in the thin line visible in the thick outer Al_2O_3 layer. b) HRTEM image of the tube set in panel a, showing the outer tube, hollow gap and inner tube. The lattice spacing and orientation are consistent with polycrystalline $ZnAl_2O_4$ distributed randomly in an amorphous Al_2O_3 matrix. The lattice signal becomes weaker along the radial direction toward the outer surface of the outer shell. The width of the hollow region between the tubes is consistent with that shown in Figure 9.4, with a similar starting thickness of ZnO.

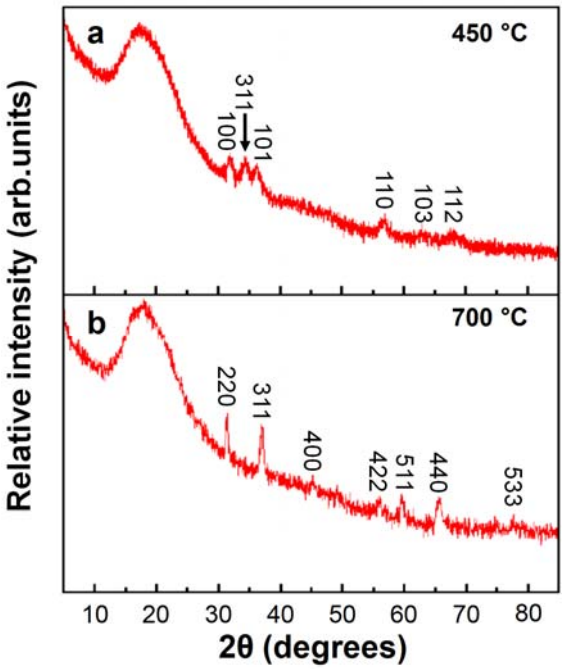


Figure 9.8. XRD patterns of the coaxial microtubes portrayed in Figure 9.4: (a) after calcination at 450°C in air for 12 h, and (b) after annealing at 700°C for 12 h. The reflections marked in (a) correspond to the ZnO lattice, whereas those in (b) correspond to features associated with $ZnAl_2O_4$. There is no evidence of crystalline ZnO in the diffraction pattern acquired after high-temperature annealing, which is indicative of complete reaction consumption of the ZnO layer.

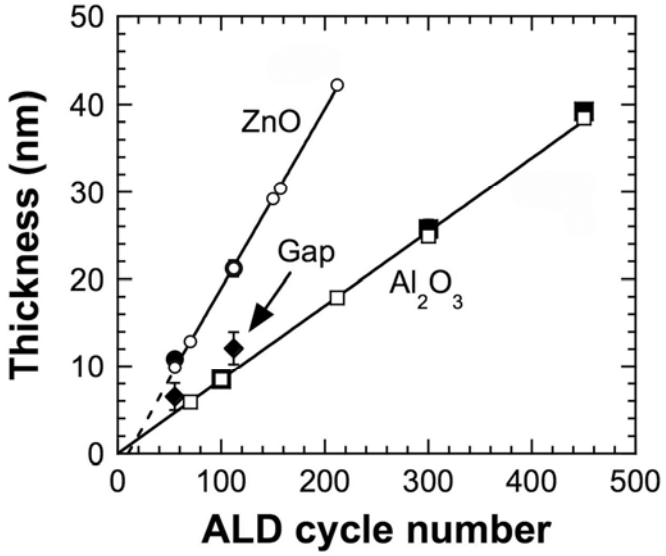


Figure 9.9. ALD layer thicknesses of ZnO and Al_2O_3 deposited on planar silicon wafers (measured by ellipsometry, open symbols) and microfibers (measured by TEM, filled symbols) after annealing at 450°C in air. Included is the Kirkendall gap thickness from two Al_2O_3/ZnO/Al_2O_3 microtubular specimen series (shown in Figure 9.4 and 9.5) annealed at 700°C and plotted as a function of the ALD cycle number for the ZnO layer. The error bars represent one standard deviation in the data.

CHAPTER 10 is a reprint of a manuscript published in Chemistry of Materials

CHAPTER 10. "Zincone" Zinc Oxide–Organic Hybrid Polymer Thin Films formed by Molecular Layer Deposition

Qing Peng, Bo Gong, Ryan M. VanGundy and Gregory N. Parsons*

Department of Chemical and Biomolecular Engineering, North Carolina State University, Raleigh NC 27695, USA

Abstract

Hybrid organic–inorganic polymer thin films of the form $(–O–Zn–O–C_2H_4–)_n$, have been deposited from diethyl zinc and ethylene glycol using molecular layer deposition (MLD) over a range of substrate temperatures between 100 and 170°C. Infrared transmission confirms that the films consist of Zn–O and ethylene–oxide units. In analogy with known alucone polymers of the form $(–O–Al–O–R–)_n$, the zinc based hybrid material is an example of a "zincone" polymer. In-situ quartz crystal microbalance analysis indicated that the sequential surface reactions of diethyl zinc and ethylene glycol are sufficiently self-limiting and saturating to enable well–controlled MLD growth. Quantitative analysis of in–situ quartz crystal microbalance and film thickness results indicate that ethylene glycol molecules can undergo a "double reaction" where the OH groups on both ends of the diol react with available $–Zn–C_2H_5$ surface sites to produce a relatively inert bridging alkane. The mass uptake per MLD cycle during Zn–hybrid film deposition decreased with increasing reaction temperature. Infrared transmission also shows that Zn–organic hybrid films are stable in dry air. However, the as-deposited ZnO-hybrid material could be hydrolyzed by H_2O (for example, in ambient) resulting in films consisting of zinc oxide and zinc hydroxide with some carbon remnants. Spectroscopic ellipsometry indicated the thickness of hydrolyzed

CHAPTER 10 is a reprint of a manuscript published in Chemistry of Materials

films increased linearly with reaction cycles, and scanning probe and transmission electron microscopy images show the hydrolyzed ZnO-hybrid film coating is uniform and conformal. The transmission electron micrographs also show the hydrolyzed Zn-hybrid films contain nano–scale porosity. These results suggest new pathways to fabricate organic–inorganic hybrid materials, including metal–organic framework structures.

CHAPTER 10 is a reprint of a manuscript published in Chemistry of Materials

10.1 Introduction

Advances in chemical synthesis and thin film processing techniques are opening new approaches to prepare functional materials with well–defined composition, uniformity and conformality. Atomic layer deposition (ALD),[1-5] for example, employing a repeated binary sequence of self–limiting monolayer deposition reactions, has been applied to a variety of inorganic metals and metal compounds for advanced electronic and optical applications.[6-12] Molecular layer deposition (MLD) expands upon the chemical concepts of ALD to integrate organic monomer and molecular building blocks into oligomeric and polymeric thin film structures with precise control of film thickness.[13-18] Recently, a combination of ALD and MLD approaches has been used to deposit several examples of hybrid organic–inorganic thin films, including compounds of aluminum, silicon, titanium, and others.[19-22] Some organic–inorganic hybrid materials are referred to as coordination polymers, or metal–organic framework solids, built up of repeating metal–ligand–metal (M–L–M) connectivity,[23] where the L denotes a functional organic ligand, commonly containing C–O units linking to the metal center. Molecular layer deposition can also result in formation of planar or one–dimensional extended inorganic hybrid materials[21] with continuous metal–oxygen–metal (M–O–M) binding units.[23] Hybrid organic–inorganic materials, however, are most widely synthesized using solution–based hydrothermal chemistry (for example, see reviews by Yaghi et al.,[24] Cheetham et al.,[23] and Rao et al.[25] The extension into vapor–phase fabrication could open up significant new applications for hybrid materials. Vapor–phase methods, however, require precursors to be sufficiently volatile for transport without decomposition,

and the reactant must provide terminal groups that enable spontaneous exothermic surface reactions.

Vapor–phase molecular layer deposition has recently been investigated to form poly (aluminum ethylene glycol) materials[19, 22] of the form $(–O–Al–O–R–)_n$. These alkyl–aluminum oxide network solids are known as "alucone" polymers,[19, 26, 27] and were initially

Scheme I: ZnO ALD:

$$-OZn(OH)_{(s)} + Zn(C_2H_5)_2 \rightarrow -OZn(C_2H_5)_{(s)} + C_2H_6 \quad (1)$$

$$-OZn(C_2H_5)_{(s)} + H_2O \rightarrow -OZn(OH)_{(s)} + C_2H_6 \quad (2)$$

Scheme II: Zn-hybrid MLD

$$-OZn(O–R–OH)_{(s)} + Zn(C_2H_5)_2 \rightarrow -O–R–OZn(C_2H_5)_{(s)} + H–R–H \quad (3)$$

$$-OZn(C_2H_5)_{(s)} + HO–R–OH \rightarrow -OZn(O–R–OH)_{(s)} + C_2H_6 \quad (4)$$

formed as preceramic polymers using solution–based sol–gel reaction processes. Preliminary studies of molecular layer deposition using diols and diethyl zinc have also reported formation of related "Zn–hybrid" or "zincone" polymers[28, 29] of the form $(–O–Zn–O–R–)_n$.

The ALD process for ZnO utilizes alternating doses $Zn(CH_2CH_3)_2$ and H_2O, and previous in–situ IR and QCM studies suggest it closely follows the typical ALD reaction sequence indicated in Scheme I.[6, 30, 31] An analogous reaction scheme for organic–inorganic polymer MLD can be devised using a metal alkyl and a bifunctional organic monomer.[19] For example, a hypothetical scheme for reaction of diethyl zinc (DEZ) and a diol to obtain steady–state deposition of a M–L–M network $(–O–Zn–O–R–)_n$ zincone thin film is shown in

Scheme II. We report here an investigation of MLD surface reactions using ethylene glycol and diethyl zinc to form zincone poly (zinc ethylene glycol) hybrid organic–inorganic thin films. The growth behavior of zincone is quantified using in–situ quartz crystal microbalance (QCM) and several ex–situ characterization tools, and differences between growth initiation on ZnO and steady–state hybrid material deposition are observed and analyzed. The chemical and physical properties of the resulting zincone film are also of interest, including bonding structure and reactivity of the as-formed hybrid material upon exposure to ambient, and these properties are characterized by ex–situ spectroscopic and imagine analysis. Transmission electron microscopy indicates that the zincone structure could be a precursor layer for fabrication of nano–porous thin films with well–controlled thickness.

10.2 Experimental

A. ALD and MLD Precursors

Diethyl zinc ($Zn(C_2H_5)_2$) (95%) was obtained from Strem Chemicals Inc. and used without further treatment. Deionized water (DI–H_2O) was used as the water source for ZnO ALD deposition. Anhydrous ethylene glycol, EG (OHC_2H_4OH) (99.8%) (Sigma-Aldrich) was used as the organic material source without further purification. High purity Ar (99.999%) (National Welders Supply Co.) was used as the purge gas and carrier gas for reactants.

CHAPTER 10 is a reprint of a manuscript published in Chemistry of Materials

B. Reactor and QCM Setup for ZnO ALD and Zincone MLD

Atomic layer deposition of ZnO and molecular layer deposition of the zincone material were carried out in the same homemade viscous flow vacuum reactor. A schematic of the deposition equipment is shown in Figure 10.1. The reaction system is composed of stainless steel tube ~3.5 cm in diameter connected to gas inlet and pumping ports by conflat flanges. A resistively heated jacket surrounding the system is used to achieve the desired temperature. A controlled temperature gradient was maintained along the entire gas flow path to prevent precursor condensation. Ultrahigh-purity Ar gas was used as the carrier gas and further purified by using a gas filter (DRIERITE Gas Purifier) before entering the reaction system.

For a typical ZnO deposition cycle, the gas exposure time for the DEZ and H_2O was 2 and 4 seconds (s) respectively, with an Ar purge time of 42 s between each reactant pulse. This process cycle is denoted as DEZ/Ar/H_2O/Ar = 2/42/4/42 s. The flow rate of Ar carrier gas is ~120 standard cubic centimeters per minute (sccm) with a steady-state process pressure of ~0.9 Torr monitored by a Baratron pressure gauge (MKS Instrument Inc.). The reaction system was pumped using a rotary mechanical pump. As shown in the reactor schematic in Figure 10.1, the gas effluent during the EG or H_2O cycle was directed through a liquid nitrogen trap to eliminate reaction with excess DEZ in the pump. The sample substrates and the QCM crystal were heated by convection and radiation from the heated reactor wall. The substrate samples were silicon wafer pieces, prepared by wet cleaning in BakerClean® JTB-100 solution (Mallinckrodt Baker Inc), followed by rinsing in DIH_2O and

blown-dry with N_2, which results in a thin chemical oxide surface. Sample substrates were fixed onto an aluminum sample boat before loading into the reaction chamber. The in-situ QCM was installed onto the deposition reactor system through the inlet of the reactor as show in Figure 10.1. Polished QCM crystal sensors with Au coating (Colorado Crystal Corp.) were mounted in the Maxtek BSH-150 bakeable sensor head. The sensor head was modified to allow ~10 sccm of Ar flow over the back side of the sensor, and the crystal was sealed to the QCM housing using conductive epoxy to prevents material from depositing onto the backside of the crystal surface.[32] The mass change signals were detected by a monitor (Maxtek TM-400), and recorded using a home designed LABVIEW program.

C. Precursor Delivery System.

The DEZ precursor was stored in a stainless steel bottle and evaporated at room temperature (~25˚C). The DI–H_2O and EG were also stored in stainless steel containers and evaporated at room temperature and 80˚C respectively. The DI–H_2O and DEZ vapors were bled into the reactor using Ar carrier gas through a computer–controlled ALD solenoid valve in series with a needle valve. The amplitude of the pressure increase during the DEZ and H_2O pulses is ~ 50 mTorr. The EG container was connected to the system using only a solenoid valve, and the pressure increase during EG dose is also ~50 mTorr. The reactant dose amount was adjusted by either changing pulse time or by changing the flow through the needle valve orifice. The organic and metal organic precursors were pumped through separate exhaust lines, which were controlled separately using computer-controlled gate valves. As illustrated by the schematic in Figure 10.1, the reactor was designed to allow

simple transitions between deposition of ZnO ALD and MLD of zincone materials by switching easily between H_2O and EG reactant flow.

D. Ex-situ Film Characterization.

The composition of synthesized material was analyzed using transmission Fourier transform infrared spectroscopy (FTIR). A ThermoNicolet IR bench with a deuterated triglycine sulfate detector (KBr bean splitter) was used in the transmission mode with 2048 scans at 4 cm^{-1} resolution. The measuring chamber was continuously purged with purified dry air (ambient without water moisture). A background spectrum was collected using the starting Si wafer before the deposition. X-ray photoelectron spectroscopy (XPS) analysis was performed with a Kratos Analytical Axis Ultra equipment with a monochromatic Al Kα source operated at 15kV. For all samples, the C 1s peak (–C–H_2) was normalized to 284.6 eV as the reference. For the survey and detail scans, 160 and 20 were used for the pass energy respectively. Before spectrum collection, the sample surfaces were cleaned in–situ with 3 minutes of Ar sputtering at 5 kV.

Surface morphology of films was analyzed by a Nanoscope IIIa atomic force microscope (Digital Instruments) operated in tapping mode with a scanning frequency of 0.5 Hz. X-ray diffraction spectra were obtained using a Bruker AXS D-5000 x-ray diffractometer equipped with GADDS area detector. All measurements were taken by using a generator with a voltage of 40 kV and a current of 30 mA.

Film thickness and refractive index were measured using variable-angle spectroscopic ellipsometry (J. A. Woollam). Measurement was carried out over a spectrum from 400 to

1100 nm using incident angles of 65, 70, and 75 degrees. A three-layer Cauchy model (hybrid/nativeSiO_2/Si) was used to fit the experiment data to derive the refractive index and film thickness. In the model, thickness of native oxide and Si substrate were set at 15Å and 1mm, respectively.

The deposited Zn-hybrid material was also examined by transmission electron microscopy (TEM). For this analysis, TEM grids (Ted Pella, Inc.) were loaded with Al_2O_3 microtubes fabricated by ALD, then used as the substrate for the zincone deposition. For this process, Al_2O_3 microtubes were fabricated by coating a polyvinyl alcohol (PVA) electrospun fiber template with 500 cycles Al_2O_3 ALD at 45°C, followed by calcination in ambient at 400°C for 24 h to remove the PVA.[11] The as-formed Al_2O_3 microtubes were dispersed in ethanol and sonicated for 1min. Several droplets of the dispersion solution were pipetted onto the carbon film coated TEM grid, and grids were dried at room temperature overnight, then heated to the reaction temperature in vacuum for 1h before being exposed to the MLD deposition process. The samples were removed from the reactor and imaged with an FEI Tecnai G^2 Twin microscope operated at 160 kV. All samples were exposed to ambient for more than 12h before TEM analysis.

10.3 Experimental Results

A. In-situ QCM Analysis of ZnO ALD

In-situ quartz crystal microbalance results obtained during ZnO ALD are shown in Figures 10.2 and 10.3. Figure 10.2(a) shows the mass uptake data from ZnO ALD using DEZ/Ar/H_2O/Ar = 2/42/4/42 s at 120°C over a large number of cycles on the gold–coated

quartz crystal. The ZnO film growth is linear with the number of deposition cycles, with an average mass gain of about 125±3 ng/(cm^2•cycle), where the error reflects the standard deviation. Ellipsometry analysis of deposited films indicates a growth rate of ~2.25 Å/cycle at 120°C for deposition up to 1000 ALD cycles, consistent with literature reports of 120-140 ng/(cm^2•cycle) and 2.1-2.8 Å/cycle,[6, 30] respectively for ZnO ALD. Moreover, the film density estimated from the mass uptake rate and growth rate is (125ng/cm^2)/(0.225nm/cycle) ~ 5.56 g/cm^3, in good agreement with the literature value[6, 30] of 5.61 g/cm^3.

A detailed view of QCM results obtained during ZnO ALD at 120°C is shown in Figure 10.2(b), where the dashed regions refer to the reactant pulsing steps. The QCM results display a large mass uptake of ~125 ng/(cm^2•cycle) during the DEZ exposure and a small mass loss of ~ 3 ng/(cm^2•cycle) upon reaction with H_2O, consistent with previous QCM analyses of ZnO ALD.[6, 30] Note that when the DEZ exposure is repeated without a H_2O step, a much smaller mass uptake of ~15 ng/(cm^2•cycle) is followed by a slow mass decrease during subsequent Ar purge, concluding with virtually no net mass uptake. This result is consistent with a chemically saturated -OZn$(C_2H_5)_{(s)}$ surface after one pulse 4 s DEZ exposure. The QCM data also shows that after the three DEZ exposure steps on the saturated -OZn$(C_2H_5)_{(s)}$ surface, the regular ZnO ALD growth can be readily re–started with the same mass uptake per cycle as the steady-state growth by exposing the saturated surface to H_2O/Ar/DEZ/Ar cycles.

CHAPTER 10 is a reprint of a manuscript published in Chemistry of Materials

B. Ethylene Glycol Adsorption on the ALD ZnO Surface

Vapor–phase ethylene glycol was used in place of water in the ZnO ALD reaction sequence, and QCM was used to monitor th mass changes and surface saturation. These studies have two points of interest. First, it is important to determine to what extent EG can react with the surface–bonded $–OZn(C_2H_5)_{(s)}$ ligands, on the ZnO ALD substrate. Second, it is important to characterize the extent to which DEZ can react with the surface bonded $–Zn(OC_2H_4OH)_{(s)}$ ligands generated during the EG exposure. While the QCM results may not confirm the detailed surface reaction stoichiometry implied in the given Schemes, QCM will allow quantitative analysis of the relative mass uptake during surface exposure sequences. Specifically, after confirming steady-state ALD growth of ZnO on the QCM crystal, the $–OZn(C_2H_5)_{(s)}$ ligand saturated ALD ZnO surface was exposed to EG molecules and the mass gain was monitored by QCM. Data in Figure 10.3a initially shows two full cycles of DEZ/Ar/H_2O/Ar, with average mass uptake of ~127 ng/(cm^2•cycle), which agrees well with the results shown in Figure 10.2. The first two DEZ/H_2O cycles are followed by two Ar/DEZ cycles (88/2 s) and a longer (132 s) Ar exposure, then this surface is exposed to three ethylene glycol vapor pulses of 4 s each. The two Ar/DEZ exposure steps again show evidence for surface saturation, consistent with formation of a $-OZn(C_2H_5)_{(s)}$ saturated ALD ZnO surface. Upon exposing the $–OZn(C_2H_5)_{(s)}$ saturated ZnO surface to EG (near t~ 6280 s in Fig. 10.3a), the QCM results show a mass uptake of ~ 33 ng/cm^2. The next two EG/Ar exposure steps show some evidence for physisorption, but no net mass gain, consistent with surface saturation. This surface was then exposed to DEZ for 2 s (near t = 6600 s), and the mass uptake was ~ 16 ng/cm^2. After the DEZ exposure and Ar purge steps, exposure to EG

results in a mass uptake of ~ 3 ng/cm^2, which is also less than that observed for the first EG exposure on the –OZn$(C_2H_5)_{(s)}$ saturated ZnO surface.

Figure 10.3b shows another set of representative QCM results similar to Figure 10.3a, where the -OZn$(C_2H_5)_{(s)}$ terminated ALD ZnO surface is exposed to three EG/Ar exposure cycles at 120°C. This second set of data collected separately from that in Figure 10.3a, is included in part to demonstrate the reproducibility of the data collection. The first EG/Ar exposure (near t=5470 s) results in a net mass uptake of ~ 34 ng/cm^2, similar to the 33 ng/cm^2 observed in Figure 10.3a. Again, exposing this surface to additional pulses EG resulted in virtually no net mass uptake, consistent with a reaction–saturated surface. The three short EG exposures are followed by three DEZ/Ar/H_2O/Ar cycles (starting at t ~ 5690 s). The overall mass uptake during the first three ZnO ALD cycles on the EG–exposed surface is significantly reduced as compared to steady–state ZnO ALD. Further QCM analysis indicates that continuing the DEZ/Ar/H_2O/Ar exposure sequence results in a slow increase in mass uptake per cycle, returning to the full steady–state ZnO growth rate after ~40 cycles. Results in Figures 10.3a and 10.3b also show that, when the ALD ZnO surface is exposed to EG (after the DEZ exposure half–cycle) the mass uptake is larger than that observed during steady–state Zincone MLD. The same result was observed at other temperatures studied.

One may expect that since the saturated –OZn$(OH)_{(s)}$ surface generated during ZnO ALD is not reactive to further H_2O exposure, then it will also not be reactive with EG. Figure 10.4 shows QCM results where a -OZn$(OH)_{(s)}$ terminated surface formed during steady–state

Scheme III: EG on –OZn(OH)$_{(s)}$

$$–OZn(OH)_{(s)} + OHC_2H_4OH \rightarrow –OZn(OC_2H_4OH)_{(s)} + H_2O \quad (5)$$

ZnO ALD was exposed to H_2O/Ar (2/86 s) exposure (at t ~ 2310 in Figure 10.4), followed by EG exposure and Ar purge. As expected, the second sequential H_2O exposure resulted in no mass uptake. However, the first EG exposure results in a net mass gain of ~33 ng/cm^2, and this mass increase is stable during an extended Ar purge. A subsequent EG/Ar exposure resulted in no observed mass gain, consistent with a saturated surface. The mass uptake during EG exposure is attributed to the dehydration reaction shown in Scheme III, where the surface Zn–OH reacts with vapor–phase HO–(C_2H_4)–OH to produce Zn–O–(C_2H_4)–OH + H_2O.[33] Further insight into surface reactions can be gained by analysis of steady-state Zn–hybrid growth.

C. QCM Analysis of Steady-state Zn-hybrid MLD

Steady–state MLD growth of Zn–hybrid films was analyzed by QCM, and representative results are shown in Figure 10.5. The average net mass uptake during the DEZ and EG pulse, measured during the purge cycle after stabilization, is ~20.4±1.3 ng/(cm^2•cycle) and ~4.8±1.4 ng/(cm^2•cycle) respectively. The uncertainty values represent the standard deviation of more than 50 mass uptake values measured during steady–state deposition, and is ascribed to the mass resolution in the QCM, as well as small variations in flow or temperature during processing.

CHAPTER 10 is a reprint of a manuscript published in Chemistry of Materials

Following many cycles of steady-state growth, the surface generated during EG/Ar (2/42 s) half–cycle, is exposed to three DEZ/Ar half–cycles (2/88 s). Repeating the DEZ exposure (at t ~ 17600 and 17700 s in Figure 10.5) results in mass uptake, followed by a slow decrease, with no net mass increase obtained. The slow mass decrease during the purge step followed the DEZ exposure is consistent with physisorption of DEZ on the growth surface, or diffusion into the near–surface region of the growing film.[19] Results in Figure 10.5 indicate that one 2 s DEZ exposure during steady–state growth is sufficient for surface saturation in the MLD process.

The data in Figure 10.6 examines more closely the surface saturation after EG exposure during steady–state growth. The figure shows one full DEZ/Ar/EG/Ar (4/42/4/42) cycle (t ~ 8870 to 8906 s), followed by another similar cycle with a longer 86 s Ar purge after the EG exposure (between t ~ 8960 and 9090 s). The EG exposure is estimated to be ~100 mTorr•s during the 4 s EG pulse step. The QCM generally shows initial mass gain, followed by a slower mass loss, with a net mass uptake of ~3.5 ng/(cm^2•cycle) after the 42s purge. The cycle with the longer Ar purge generally shows a similar net mass uptake within the uncertainty of QCM measurement. When the EG/Ar (4/86 s) cycle was repeated (between t ~ 9090 and 9180 s), the QCM showed adsorption and desorption with nearly no net mass uptake. The effect of purge time and temperature on the surface saturation is quantified in more detail below.

In-situ QCM results obtained over many cycles at several deposition temperatures during steady-state Zn-hybrid film growth are shown in Figure 10.7. The deposition rate

decreases slightly with increasing deposition temperature, and overall average mass uptake rate decreased from ~24.3±1.4 ng/(cm^2•cycle) to ~17.4±2.8 ng/(cm^2•cycle) as the reaction temperature increased from 120 ˚C to 165 ˚C. The data collected at 165 ˚C shows some variation of the mass uptake rate during the deposition, which may be due to small temperature fluctuations during the QCM measurement.[34] The decrease in film growth rate with increasing temperature indicates kinetically controlled surface reactions during the hybrid MLD deposition,[30] including for example an enhanced rate of precursor desorption with increasing temperature.[16] Dameron et al.[19] found that during alucone MLD, film deposition rate decreased with increasing temperature, except during the first 2–5 alucone MLD cycles on Al_2O_3 where the rate was nearly independent of temperature. For our studies, data was not collected during film nucleation, and Figure 10.7 shows data normalized to the origin from an arbitrary starting time.

To further analyze the effect of precursor adsorption, the effect of gas purge time on the overall mass uptake rate was analyzed using in–situ QCM at temperatures between 105 and 165˚C, and results are summarized in Figure 10.8. Increasing the Ar purge time after DEZ and EG pulses from 12 to 42 s resulted in a decrease in net mass uptake rate, consistent with removal of physisorbed reactants. No significant difference is observed by extending purge times from 32 to 42 s, which is in agreement with surface saturation and self-limiting MLD type growth. In order to ensure consistent self-limiting MLD, the 42 s purge time was used to obtain the films used for characterization discussed below.

CHAPTER 10 is a reprint of a manuscript published in Chemistry of Materials

D. FTIR Results and Stability of Zn-hybrid Films

Chemical composition and bonding in the Zn–hybrid films after deposition were examined using FTIR. Generally, the films were observed to be sensitive to ambient laboratory air, and the film thickness decreased upon exposure to ambient, as discussed below. For IR analysis, as-formed zincone films were transferred immediately from the reactor into the dry air–purged analysis chamber. Characterization of Zn-hybrid films with short (<2 min) and long (several hours) exposures to ambient was performed in order to illustrate the instability mechanisms of the Zn-hybrid materials. Figure 10.9 shows representative FTIR spectra of a Zn–hybrid film deposited with 800 cycles at 120˚C: (a) in dry air for 1 min; (b) in dry air for 3 days; (c) in ambient for 1 hour; (d) in ambient for 12 hours; and (e) after further annealing in ambient at 100˚C for 2 hours. For reference, spectrum (f) in Figure 10.9 shows IR absorption for a ~ 45 nm ZnO ALD film deposited at 120˚C for 200 cycles. The as–deposited Zn–hybrid film in spectra (a) and (b) shows peaks primarily in the range of 2600-3000 cm^{-1} and 800-1600 cm^{-1}. The modes at 2921, 2868, 2840, and 2690 cm^{-1} are ascribed to antisymmetric, symmetric and combination C–H modes in $–CH_2–$ units.[19, 35-39] Similar differentiation of $–CH_2–$ IR modes in ethylene glycol is observed upon covalent grafting, depending on the chemical environment of the surface bound ligand.[38] The relatively small peaks at 1462, 1454, 1370, 1353, and 1240 cm^{-1} are ascribed to $-CH_2-$ scissor, twist and wag modes.[19, 35-39] Peaks at 1181 and 1145 cm^{-1} are related to C–C stretch, and the large peak at 1075 cm^{-1}, and the shoulder at 1053 cm^{-1}, are ascribed to C–O vibrations in C–C–O and Zn–O–C bonding units. The peak at 895 cm^{-1} is associated with combined $–CH_2–$ vibrations. These IR peaks confirm the successful covalent

incorporation of ethylene glycol to form the metal–organic hybrid thin film polymer (–O–Zn–O–C_2H_4–)$_n$. No detectable characteristic peaks from other organic components were found in the FTIR spectra of the as-formed Zn-hybrid materials.

Spectrum (b) in Figure 10.9 was obtained after storing the sample for several days in dry air in the FTIR analysis chamber. The IR absorbance appears the same as the as–deposited film, indicating good stability in dry air. However, exposure to relatively humid laboratory air for one hour resulted in significant change of the IR spectrum, as shown in spectrum (c). The C–H stretching and deformation modes of –CH_2– are significantly reduced, and the features associated with C–O modes become nearly indiscernible, indicating significant reaction, likely with water in the ambient. Significant –OH bonding appears near ~3300 cm^{-1}, consistent with water vapor inserting into the ethoxy linkage and releasing volatile glycol species. Ambient exposure also results in a decrease in total film thickness, consistent with material volatilization and visible color change. The metal M–O–R bonding in the zincone material (where R is the organic ligand) is generally unstable. The Si–O–C bonding in 3-aminopropyltriethoxysilane or other ethoxylsilanes or methoxysilanes, as well as bonds in Zn methoxyethoxide, are readily hydrolyzed by moisture from the ambient. Extended ambient exposures up to 12 hours resulted in no further significant change in the IR spectrum, as shown in spectrum (d) in Figure 10.9, indicating the reaction between the Zn-hybrid film and moisture from ambient proceeded relatively quickly. Similar instability was observed for zincone films deposited at other temperatures, and it has also been reported for alucone films deposited by MLD.[19] Ambient–exposed samples were also annealed in ambient at temperatures up to 100°C. As shown in spectrum (e), annealing at 100°C for 2

hours resulted in a decrease in hydroxide bonding and an increase in features related to Zn–O bonding near 400 cm^{-1}, consistent with a structure similar to that observed for the ALD ZnO shown in spectrum (f). In the discussion below, the resulting films after ambient exposure are referred to as "hydrolyzed Zn-hybrid" material.

E. Thickness dependence of FTIR and Ellipsometry results

Figure 10.10 shows FTIR spectra of Zn-hybrid films with different thicknesses deposited at 120°C. The characteristic IR peaks associated with C–H and C–O modes in ethylene oxide are observed to increase with the number of deposition reaction cycles, consistent with the QCM data shown in Figure 10.5-10.7. As mentioned above, the film thickness was observed to be unstable with time. To observe the thickness change, part of a freshly–deposited ZnO–hybrid film was covered with a glass slide and the sample left in laboratory air overnight. The uncovered film visibly changed, and step profilometry confirmed that the thickness of the exposed film had decreased. Similar measurements on other samples indicated that the film reacted with moisture within one to two hours upon ambient exposure. Due to this instability, reliable thickness measurements of as–deposited films were difficult to obtain. However, thickness values obtained from spectroscopic ellipsometry analysis of fully hydrolyzed Zn-hybrid films, shown in Figure 10.11, indicate that the thickness increased linearly with the number of deposition cycle, with a deposition rate of ~0.57 Å/cycle at 120 ˚C, and ~0.39 Å/cycle at 165 ˚C. The spectroscopic ellipsometry measurement data can be readily fit with the three layer Cauchy model using a refractive index of 1.55±0.05 for the hydrolyzed Zn-hybrid film.

CHAPTER 10 is a reprint of a manuscript published in Chemistry of Materials

F. X–Ray Photoelectron Spectroscopy of Hydrolyzed Zn-hybrid Films

Typical ALD ZnO and fully hydrolyzed Zn-hybrid films were characterized using X–ray photoelectron spectroscopy. The transfer of samples from the reactor to the XPS chamber precluded analysis of materials before ambient exposure. Survey scans of the hydrolyzed Zn-hybrid material show features similar to the control ZnO ALD film. High resolution scans of the O 1s and C 1s spectra for a hydrolyzed Zn-hybrid film (800 DEZ/EG cycles at 120˚C, ~ 45nm) are shown in Figure 10.12 (a) and (b) (top panels). Results obtained from an ALD ZnO film (200 DEZ/H_2O cycles at 120 ˚C, ~45 nm) are shown in Figures 10.12 (c) and (d) (bottom panels). The O 1s spectrum of the hydrolyzed Zn-hybrid film shows peaks at 531.5 eV corresponding to Zn–hydroxide, and at 529.7 eV related to Zn–O bonding, consistent with the IR results. The integrated intensity of the Zn–OH and Zn–O modes indicate that nearly 55% of the O is bound as Zn–OH. The hydrolyzed Zn-hybrid shows peaks at 284.6, 285.7 and 289.4eV in the C 1s spectrum corresponding to –C-H_2, –C–OH and –O–C=O respectively, likely due to residue from EG species. The carbon content in the hydrolyzed Zn–hybrid film estimated from XPS is ~ 5.6 at. %. The spectra from the ALD ZnO film in panels (c) and (d) show a significantly smaller hydroxide and C–H_2 peaks, corresponding to < 2 atomic % carbon, with negligible –C–OH and –O-C=O bonding.

G. Surface morphology and X–ray Diffraction of Hydrolyzed and Annealed Zn-hybrid films

The surface morphology of hydrolyzed Zn-hybrid thin films were characterized using scanning probe microscopy, and a representative image of a film deposited using 800 cycles

at 120˚C with thickness of 45 nm is shown in Figure 10.13a. The overall root mean square (RMS) roughness of the hydrolyzed Zn-hybrid film is ~ 0.8 nm. Features consistent with holes in the film with average diameter ~20–30 nm are observed, with excess material present at the edge of the features. These hole structures likely formed during post–deposition reaction with the ambient. Upon annealing at 100˚C in air for 2 h, the thickness of the hydrolyzed films decreased from ~ 45 nm to ~ 30 nm as measured by ellipsometry, and the roughness increased to 1.4 nm. It is interesting to note that the morphology becomes less well discerned after the thermal annealing process as shown by the scanning probe image in Figure 10.13b. X–ray diffraction results of the ZnO films deposited at 140°C show the characteristic 100 and 002 diffraction peaks of ZnO. An organic–inorganic hybrid film deposited at 140°C and measured after air exposure, shows only broad features, characteristic of an X–ray amorphous structure.

H. Transmission Electron Microscopy of Hydrolyzed Zn-hybrid films.

Zn–hybrid film samples for transmission electron microscopy were prepared by performing Zn–hybrid MLD onto Al_2O_3 microtubes. The microtubes were formed using 500 ALD cycles of Al_2O_3 onto polyvinyl alcohol fibers, followed by calcination.[11] The microtubes were then mounted on TEM grids and exposed to the Zn-hybrid MLD process for 528 cycles at 165°C. The resulting coated tubes were open to ambient at room temperature for more than 12 hours before TEM imaging. A representative TEM image is shown in Figure 10.14. The image shows two coated tubes oriented approximately perpendicular to each other. The cross–sectional view of the horizontal hollow tube (toward the left side of the image) shows a

42 nm Al_2O_3 shell (denoted by the white lines) surrounded by ~20 nm of hydrolyzed Zn-hybrid coating on the inside and outside of the tube. The outer coating is most easily discerned because of better electron contrast when imaging through only the single film layer. The film thickness obtained from the image of the outer layer agrees well with the thickness values of similar films deposited on planar Si wafers and measured by spectroscopic ellipsometry. The horizontal tube is broken revealing a region (toward the right side of the image) allowing a plan–view image of the Zn–hybrid/Al_2O_3/Zn–hybrid structure, showing non–uniform electron contrast. The TEM image shows that the hydrolyzed Zn-hybrid coating is uniform and conformal on both the inner and outer surfaces of the microtube. The contrast observed in the outer layer in both cross section and plan–view indicates a spatially non–uniform film density, consistent with nano–scale porosity in the hydrolyzed Zn-hybrid layer. The white arrow indicates one of several points in the plan–view image corresponding to a hollow hole through the film. These results suggest that the MLD hybrid organic/inorganic films may be useful as a precursor material to form well–defined conformal porous inorganic films and membranes.

10.4 Discussion:

The results presented above show that while steady state self–limiting deposition is achieved during cyclic exposures of diethyl zinc and ethylene glycol, the DEZ mass uptake (~20.4 ng/cm^2) is significantly less than the 125 ng/cm^2 obtained during DEZ exposure for ZnO ALD at 120°C. This suggests that the density of reactive surface sites produced during the EG step in the steady–state MLD process is considerably less than that produced during H_2O exposure during steady–state ZnO ALD. In addition, the estimated saturated growth

rate of the Zn–hybrid material (< 2Å/cycle) is considerably less than the length of ethylene glycol (5.3Å), further confirming that the Zn–hybrid film does not grow as a series of fully–extended organic monolayers. It is important to note, however, that the ratio of the mass uptake measured during DEZ and EG exposure throughout steady state Zn–hybrid film growth (20.4/4.8, in ng/cm^2/cycle) was close to the ratio expected from Scheme II (93/31, in g/mol/cycle), taking into consideration the relatively large uncertainty in the QCM measurements for small mass changes. This self–consistent mass uptake ratio indicates that film growth is steady with time, and there is no net buildup of one reactant, or evolution of the film composition over time. Film growth has been extended to more than 800 cycles, showing long–term steady–state film deposition.

A summary of the mass uptake results is presented in Table 10.1, including values obtained during steady–state ZnO and Zn–hybrid deposition, and for the initial dose of EG on ZnO (after DEZ exposure) and for the initial dose of DEZ on ZnO (after exposure to one EG cycle). The mass uptake of DEZ in the Zn–hybrid film deposition is approximately the same during steady state and initial steps, but the EG shows a distinctly larger mass uptake in the early growth cycle as compared to steady state growth. When there is a significant density of reactive surface sites, for example after DEZ exposure during ZnO ALD, it is likely that a significant fraction of the glycol molecules undergo a "double reaction", where both hydroxyl moieties react with adjacent –OZn(C_2H_5)$_{(s)}$ surface sites to produce non–reactive Zn–ethylene oxide "bridging" groups, as shown in Scheme IV. This double reaction follows the same scheme proposed by Dameron et al. to account for mass uptake in aluminum/organic hybrid film deposition.[19]

The double reaction allows some EG molecules to passivate more than one active surface site. For a flat and dense ZnO ALD surface with material bulk density of ~5.6 g/cm^3, the reactive site density is expected to be ~1.2x10^{15} cm^{-2} or approximately 3.2Å between sites. Considering that the length of an EG molecule is ~5.3Å, then a molecule that has reacted at only one end can access other available -Zn(C_2H_5)$_{(s)}$ surface sites within ~5Å to complete the double reaction, leaving isolate EG molecules separated by more than 5.3Å. This corresponds to a surface site density of less than ~3x10^{14} cm^{-2} for the subsequent EG/DEZ surface reaction. Any dehydration reactions between single–reacted glycols, bound close enough to react with each other, will tend to further increase this mean separation distance and decrease the surface site density. This reduction in surface site density for the DEZ/EG reaction compared to the DEZ/H_2O process is evident in the QCM results. If the DEZ/EG reaction following Scheme II could achieve vertical self–assembly without significant double reaction, a mass gain of 124 grams per mole of surface sites would be expected, which is larger than the 79 g per mol from the DEZ/H_2O reaction in Scheme I. Therefore, under fully–dense vertically–aligned film formation, the mass gain ratio would be approximated as (DEZ/EG)/(DEZ/H_2O) = 124/79 (in g/mol/cycle) ≈ 1.6. However, the actual mass gain ratio is measured to be (DEZ/EG)/(DEZ/H_2O) = 24/125 (in ng/cm^2/cycle) ≈ 0.2 during the steady–state DEZ/EG deposition reaction, consistent with the double reaction in the DEZ/EG process (Scheme IV) acting to decrease the number of available reactive surface sites.

It is important to note that other mechanisms beyond the double reaction could be important in affecting the mass uptake rates. For example, the ethylene ligands can contribute

steric effects, to effectively block available reactive sites.[16] It is also instructive to compare mass uptake values reported during alucone MLD[19] to those observed here. Because of the higher coordination of Al versus Zn and higher atomic density of Al_2O_3 versus ZnO, the TMA adsorption could be expected to produce a higher density of surface sites for EG adsorption as compared to DEZ. The mass uptake reported for EG adsorption during steady–state alucone MLD is between 8 and 17 ng/cm^2/cycle at 135 and 105°C, which is larger than the value of ~4.8 ng/cm^2/cycle reported here during MLD of zincone at 120°C, consistent with a higher density of reactive surface sites for EG adsorption in the alucone MLD process.

10.5 Conclusions:

Infrared transmission and quartz crystal microbalance analysis confirms that thin films of ZnO–organic hybrid polymer $(–O–Zn–O–C_2H_4–)_n$ material can be deposited from DEZ and ethylene glycol using an atomic/molecular layer deposition process over a range of substrate temperatures. In-situ QCM analysis indicated that the sequential surface reactions of EG and DEZ are self-limiting and saturating, and the Zn hybrid material deposition proceeds linearly, and film thickness increases with the number of deposition cycles. The mass uptake rate during Zn–hybrid film deposition decreased with increasing reaction temperature. The QCM results also indicate that the reaction mechanism of Zn hybrid films involves a significant of "double reaction" where the OH groups on both ends of the diol react with available $–Zn(–C_2H_5)_{(s)}$ surface sites to produce a relatively inert bridging alkane. The quantified mass uptake is consistent with a factor of ~10 reduction in active surface site density during Zn–organic hybrid film deposition compared to ZnO ALD at the same deposition temperature.

CHAPTER 10 is a reprint of a manuscript published in Chemistry of Materials

Infrared transmission demonstrates that Zn–organic hybrid films are stable in dry air. IR, XPS and ellipsometry results indicate that the materials react when exposed to humid laboratory air, releasing volatile organics resulting in ZnO films that are physically thinner, and contain C and OH reaction remnants. AFM and TEM analysis of the hydrolyzed Zn hybrid films show the material to be uniform and conformal, even in high aspect ratio structures, and the morphology of the TEM images indicate that the hydrolyzed Zn hybrid films contain uniform nano–scale porosity.

This work describes fundamental surface processes during atomic/molecular layer deposition of an example hybrid metal oxide–organic thin film. This method can be readily extended to other material systems including other diols, triols, or dicarboxylic acids reacting with a range of metal alkyls and other metal organics. These results suggest new pathways to fabricate organic–inorganic hybrid materials, including metal–organic framework structures, with well defined conformality and film thickness, to enable many novel thin film materials with significant new applications.

10.6 Acknowledgments

This work was supported by the National Science Foundation under grant CTS-0626256, and by the STC Program of the National Science Foundation under Agreement No. CHE-9876674. We are grateful to Ali Evren Ozcam, Shafi Mahmud Arifuzzaman and Prof. Jan Genzer for spectroscopic ellipsometry measurements, Jeong-Seok Na for AFM measurements, Seymen Aygun, Michelle D. Casper and Prof. J. P. Maria for XRD measurement, and Prof.'s Jan Genzer and Christopher Gorman for helpful discussions.

CHAPTER 10 is a reprint of a manuscript published in Chemistry of Materials

REFERENCES

1. Lujala, V.; Skarp, J.; Tammenmaa, M.; Suntola, T. In *Atomic Layer Epitaxy Growth of Doped Zinc-Oxide Thin-Films from Organometals*, 3rd International Symposium on Atomic Layer Epitaxy and Related Surface Processes (ALE-3), Sendai, Japan, May 25-27, 1994; Elsevier Science Bv: Sendai, Japan, **1994**; pp 34.
2. Tammenmaa, M.; Koskinen, T.; Hiltunen, L.; Niinisto, L.; Leskela, M. *Thin Solid Films* **1985**, *124*, 125.
3. Ahonen, M.; Pessa, M.; Suntola, T. *Thin Solid Films* **1980**, *65*, 301.
4. George, S. M.; Ott, A. W.; Klaus, J. W. *J. Phys. Chem.* **1996**, *100*, 13121.
5. Ritala, M.; Leskela, M. Atomic Layer Deposition. In *Handbook of Thin Film Materials*, Nalwa, H. S., Ed. Academic Press: San Diego: **2001**; *Vol. 1*, 103.
6. Elam, J. W.; George, S. M. *Chem. Mater.* **2003**, *15*, 1020.
7. Leskela, M.; Ritala, M. *Angew. Chem. Int. Ed.* **2003**, *42*, 5548.
8. Chen, P.; Mitsui, T.; Farmer, D. B.; Golovchenko, J.; Gordon, R. G.; Branton, D. *Nano Lett.* **2004**, *4*, 1333.
9. Kim, H. *J. Vac. Sci. Technol. B* **2003,** *21*, 2231.
10. Gordon, R. G.; Becker, J.; Hausmann, D.; Suh, S. *Chem. Mater.* **2001**, *13*, 2463.
11. Peng, Q.; Sun, X. Y.; Spagnola, J. C.; Hyde, G. K.; Spontak, R. J.; Parsons, G. N. *Nano Lett.* **2007**, *7*, 719.
12. Knez, M.; Knielsch, K.; Niinisto, L. *Adv. Mater.* **2007**, *19*, 3425.
13. Yoshimura, T.; Tetsuura, S.; Sotoyama, W. *Appl. Phys. Lett.* **1991**, *59*, 482.

CHAPTER 10 is a reprint of a manuscript published in Chemistry of Materials

14. Kubono, A.; Okui, N.; Tanaka, K.; Umemoto, S.; Sakai, T. *Thin Solid Films* **1991**, *199*, 385.

15. Kim, A.; Filler, M. A.; Kim, S.; Bent, S. F. *J. Am. Chem. Soc.* **2005**, *127*, 6123.

16. Putkonen, M.; Harjuoja, J.; Sajavaara, T.; Niinisto, L. *J. Mater. Chem.* **2007**, *17*, 664.

17. Du, Y.; George, S. M. *J. Phys. Chem. C* **2007**, *111*, 8509.

18. Adarnczyk, N. M.; Dameron, A. A.; George, S. M. *Langmuir* **2008**, *24*, 2081.

19. Dameron, A. A.; Seghete, D.; Burton, B. B.; Davidson, S. D.; Cavanagh, A. S.; Bertrand, J. A.; George, S. M. *Chem. Mater.* **2008**, *20*, 3315.

20. Jiang, Y. B.; Xomeritakis, G.; Chen, Z.; Dunphy, D.; Kissel, D. J.; Cecchi, J. L.; Brinkertt, C. J. *J. Am. Chem. Soc.* **2007**, *129*, 15446.

21. Lee, B. H.; Ryu, M. K.; Choi, S. Y.; Lee, K. H.; Im, S.; Sung, M. M. *J. Am. Chem. Soc.* **2007**, *129*, 16034.

22. Nilsen, O.; Klepper, K. B.; Nielsen, H.; Fjellvag, H. Organic inorganic hybrid materails by ALD. In University of Oslo: San Diego, 2007.

23. Cheetham, A. K.; Rao, C. N. R.; Fellera, R. K. *Chem. Commun.* **2006**, 4780.

24. Yaghi, O. M.; O'Keefe, M.; Ockwig, N. W.; Chae, H. K.; Eddaoudi, M.; Kim, J. *Nature* **2003**, *423*, 705.

25. Rao, C. N. R.; Cheetham, A. K.; Thirumurugan, A. *Journal of Physics: Condensed Matter* **2008**, *20*, 083202.

26. Rees, W. S.; Hesse, W. Preceramic Polymers for Aluminum Oxide. In *Chemical Perspectives of Microelectronic Materials II*, Iterrante, L. V.; Jensen, K. F.; Dubois,

L. H.; Gross, M. E., Eds. Materials Research Society: Pittsburgh, **1991**; *Vol. 204*, pp 563.

27. McMahon, C. N.; Alemany, L.; Callender, R. L.; Bott, S. G.; Barron, A. R. *Chem. Mater.* **1999**, *11*, 3181.
28. Peng, Q.; VanGundy, R. M.; Hyde, G. K.; Parsons, G. N. Atomic Layer Deposition of Zinc Oxide/Organic Hybrid Material from Diethyl Zinc and Ethylene Glycol In *2008 AVS International Topical Conference on Atomic Layer Deposition (ALD2008), Bruges Belgium*, AVS, Chico CA: , **2008**.
29. Yoon, B.; O'Patchen, J. L.; Davidson, S. D.; Segheste, D.; Cavanagh, A. S.; George, S. M. Molecular Layer Deposition of Hybrid Organic-Inorganic Polymers Based on Metal Alkyl and Diol Reactants. In *2008 AVS International Topical Conference on Atomic Layer Deposition (ALD2008), Bruges Belgium*, AVS, Chico CA:, **2008**.
30. Yousfi, E. B.; Fouache, J.; Lincot, D. *Appl. Surf. Sci.* **2000**, *153*, 223.
31. Ferguson, J. D.; Weimer, A. W.; George, S. M. *J. Vac. Sci. Technol. A* **2005**, *23*, 118.
32. Elam, J. W.; Groner, M. D.; George, S. M. *Rev. Sci. Instrum.* **2002**, *73*, 2981.
33. Hausmann, D.; Becker, J.; Wang, S. L.; Gordon, R. G. *Science* **2002**, *298*, 402.
34. Rocklein, M. N.; George, S. M. *Anal. Chem.* **2003**, *75*, 4975.
35. Harder, P.; Grunze, M.; Dahint, R.; Whitesides, G. M.; Laibinis, P. E. *J. Phys. Chem. B* **1998**, *102*, 426.
36. Aranda, P.; Ruiz-Hitzky, E. *Appl. Clay Sci.* **1999**, *15*, 119.
37. Tunney, J. J.; Detellier, C. *Clays Clay Miner.* **1994**, *42*, 552.

CHAPTER 10 is a reprint of a manuscript published in Chemistry of Materials

38. Guimaraes, J. L.; Marangoni, R.; Ramos, L. P.; Wypych, F. *J. Colloid Interface Sci.* **2000**, *227*, 445.

39. Wypych, F.; Schreiner, W. H.; Marangoni, R. *J. Colloid Interface Sci.* **2002**, *253*, 180.

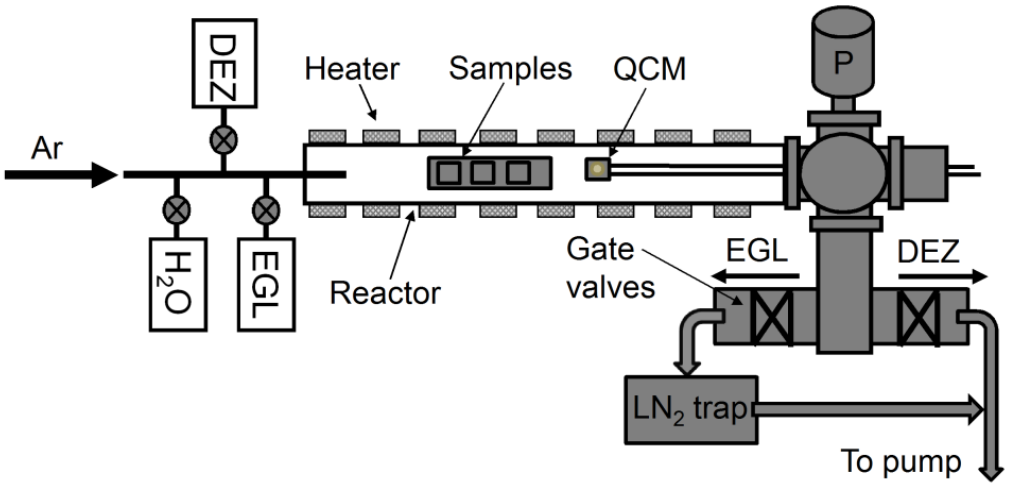


Figure 10.1 A schematic view of the viscous flow ALD/MLD reactor. The precursors are delivered into the reactor with Ar carrier gas. On the reactor exhaust line, computer controlled gate values are used to direct the exhaust from the EG pulse into a liquid nitrogen trap before entering the pump.

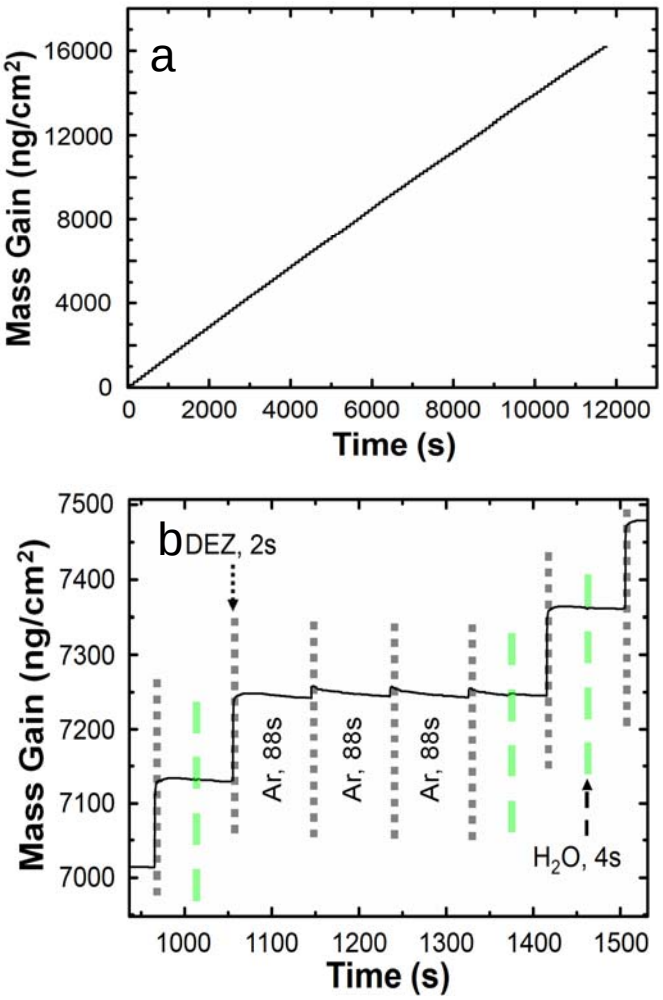


Figure 10.2 (a), (b) In–situ QCM results for ZnO ALD at 120 ˚C using DEZ/Ar/H_2O/Ar exposure times of 2/42/4/42 seconds. Panel (a) shows linear mass gain for more than 130 ALD cycles. The average mass uptake rate is ~125 ng/cm^2•cycle with standard deviation of 3 ng/cm^2•cycle. Panel (b) shows an interrupted ZnO ALD sequence at 120˚C, showing the effect of three sequential DEZ/Ar (2/88 s) ALD half–cycle exposures. The DEZ dose time is indicated by the dotted line, and the H_2O dose is indicated by the dashed line. Repeating the DEZ exposure results in a small mass uptake, followed by a slow mass decrease, consistent with some reactant physisorption.

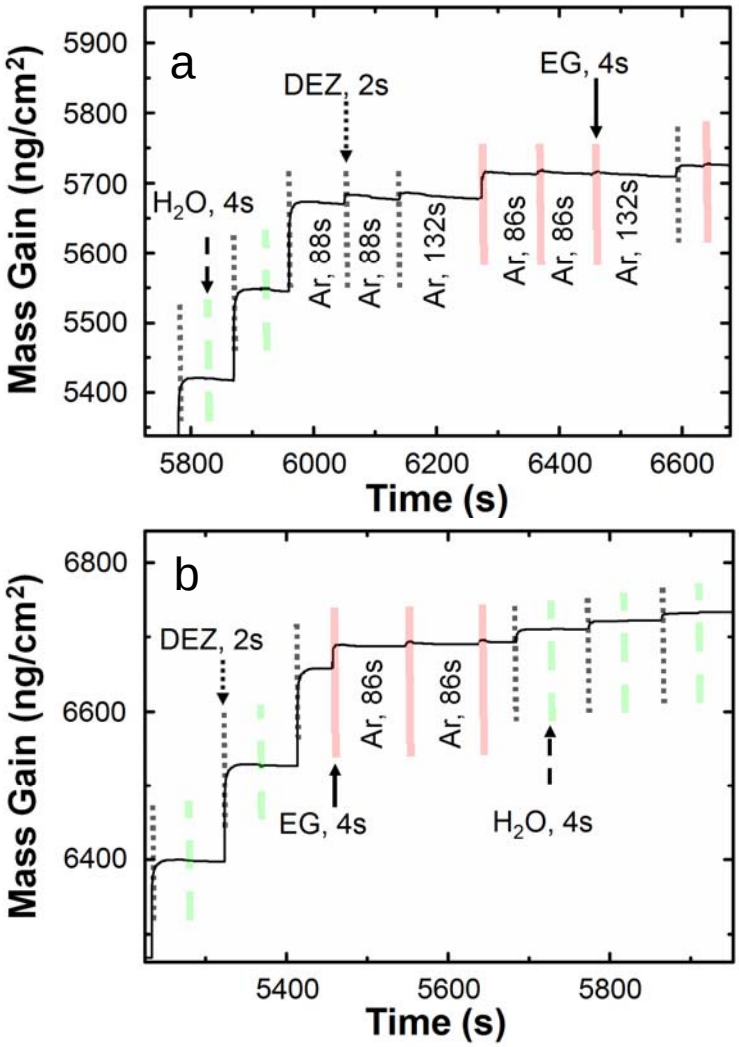


Figure 10.3 In-situ QCM results at 120˚C showing the effect of EG exposure on the -OZn$(C_2H_5)_{(s)}$ saturated surface produced during ZnO ALD. Two data sets are shown from two separate experiments. The DEZ dose is indicated by the dotted line, and the H_2O dose is indicated by the dashed line. The EG dose is shown with the shaded solid line. The first EG exposure result in mass uptake and surface saturation. The EG exposure results in significantly decreased mass uptake for subsequent DEZ exposure steps.

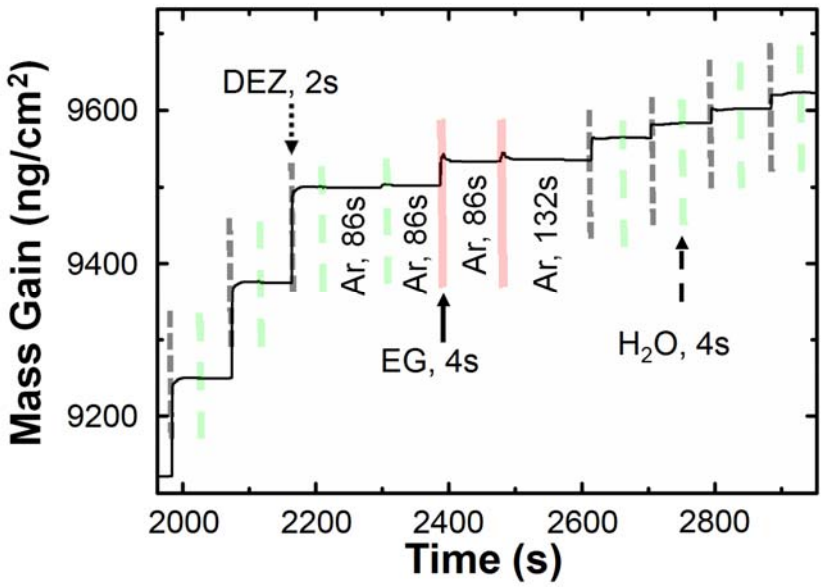


Figure 10.4 In-situ QCM results at 120 ˚C showing the effect of EG exposure on the -OZn(OH)$_{(s)}$ saturated surface produced during ZnO ALD. The DEZ dose is indicated by the dotted line, and the H_2O dose is indicated by the dashed line. The EG dose is shown with the shaded solid line. Exposing the –OH terminate surface to EG results in a mass uptake of ~33 ng/cm^2.

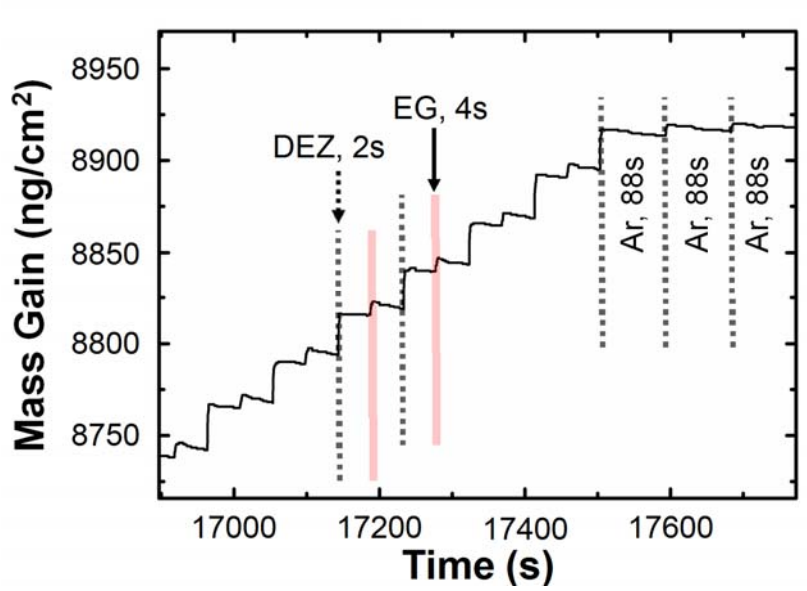


Figure 10.5 In-situ QCM results at 120˚C during steady–state molecular layer deposition. The DEZ dose is indicated by the dotted line, and the EG dose is shown with the shaded solid line. After an EG/Ar half cycle, the DEZ/Ar (2/88 s) half–cycle was repeated 3 times, resulting in mass uptake followed by approximately equivalent mass loss, indicative of DEZ physisorption/desorption.

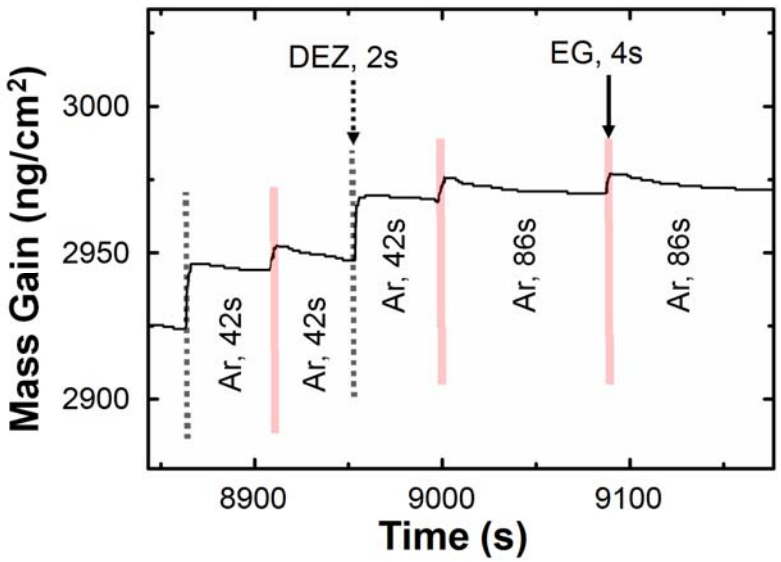


Figure 10.6 In-situ QCM results at 120˚C during steady–state molecular layer deposition using the same conditions shown in Figure 10.5. After a DEZ/Ar half cycle, the EG/Ar (4/86 s) half–cycle was repeated 2 times, resulting in mass uptake followed by approximately equivalent mass loss, indicative of reactant physisorption/desorption. No net mass gain is observed during the repeated EG/Ar half cycles.

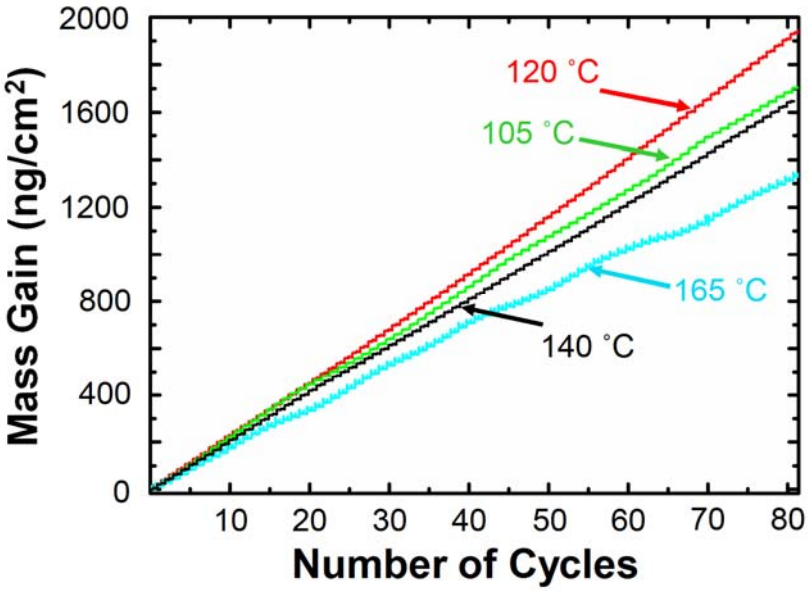


Figure 10.7 In-situ QCM results at various temperatures during steady–state molecular layer deposition using DEZ/Ar/EG/Ar: 2/42/4/42 s. The mass uptake rate decreased with increasing temperature, resulting in an average mass uptake of ~24.3 ng/(cm^2•cycle) at 120˚C and ~17.4 ng/(cm^2•cycle) at 165˚C. Data was not collected during film nucleation, so data from an arbitrary starting time was normalized to the origin.

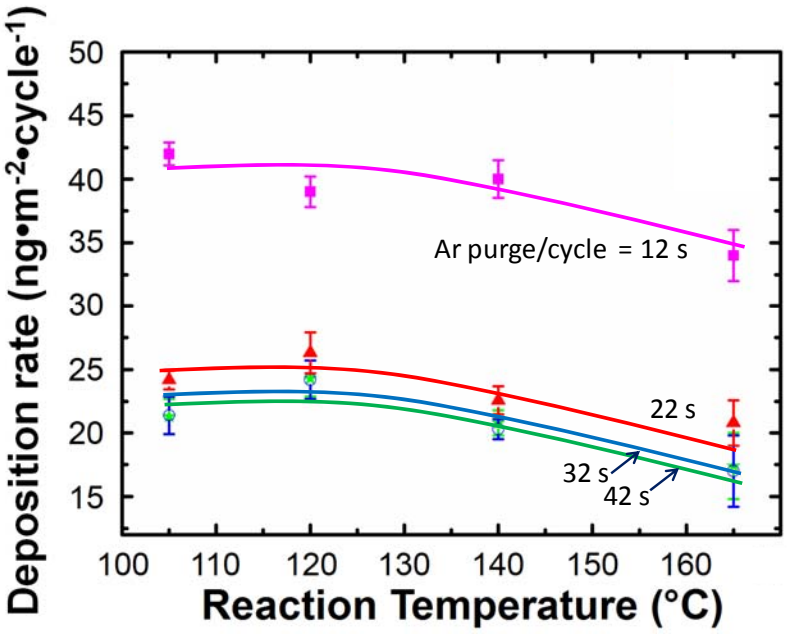


Figure 10.8 A plot of the net mass uptake rate at versus deposition temperature for various Ar purge times: DEZ/Ar/EG/Ar = 2/n/4/n s, where n is 12, 22, 32, or 42 seconds. The mass uptake rate of Zn hybrid MLD decreases with the increasing the purge time and the reaction temperature. The error bars were deduced from the corresponding QCM measurements, and the lines are a guide for the eye. The data at 32 and 42 s are statistically indistinguishable for all studied temperatures.

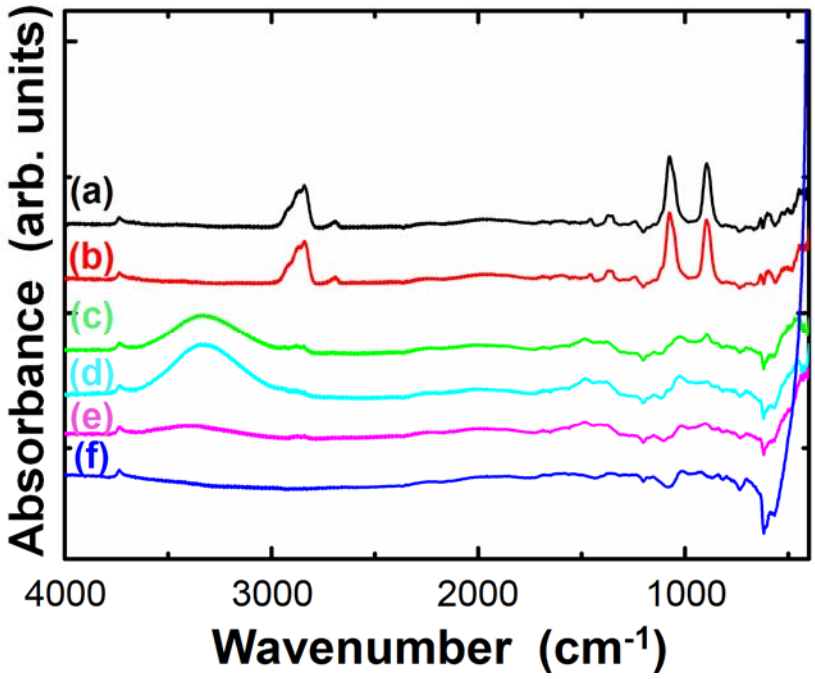


Figure 10.9 FTIR spectra collected from an example Zn-hybrid MLD film deposited using 800 cycles at 120˚C: (a) after immediate transfer to dry air; (b) in dry air for 3 days; (c) after exposure to ambient for 1 h; (d) after ~ 12 h in ambient; and (e) after annealing in ambient at 100 ˚C for ~ 2 h. Spectrum (f) is obtained from a ~ 45 nm thick ALD ZnO film deposited using 200 cycles at 120 ˚C.

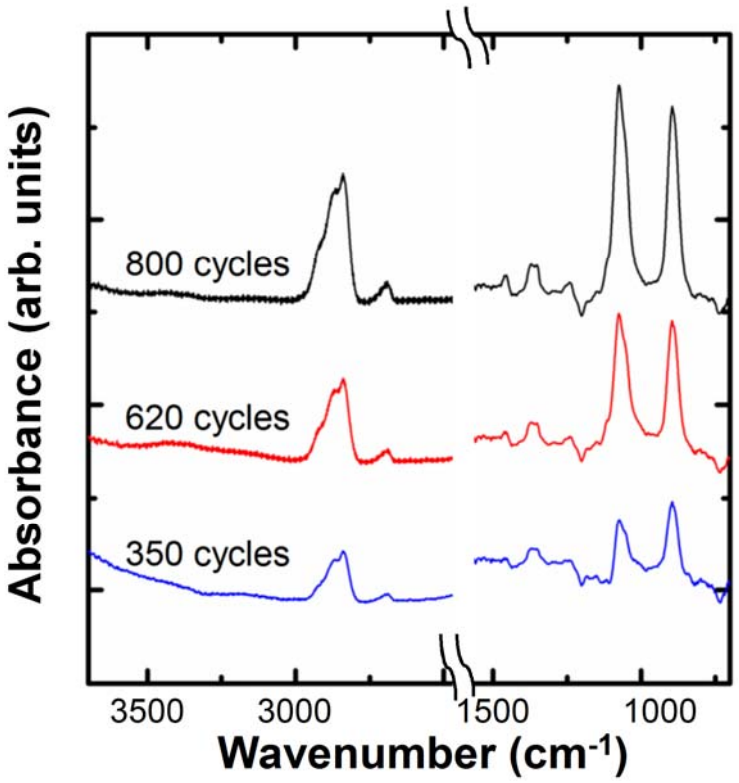


Figure 10.10 FTIR spectra obtained from three Zn-hybrid MLD films deposited at 120°C using different numbers of MLD cycles. All samples received a similar brief ambient exposure before analysis. The intensity of the characteristic EG peaks increase with the number of deposition cycles.

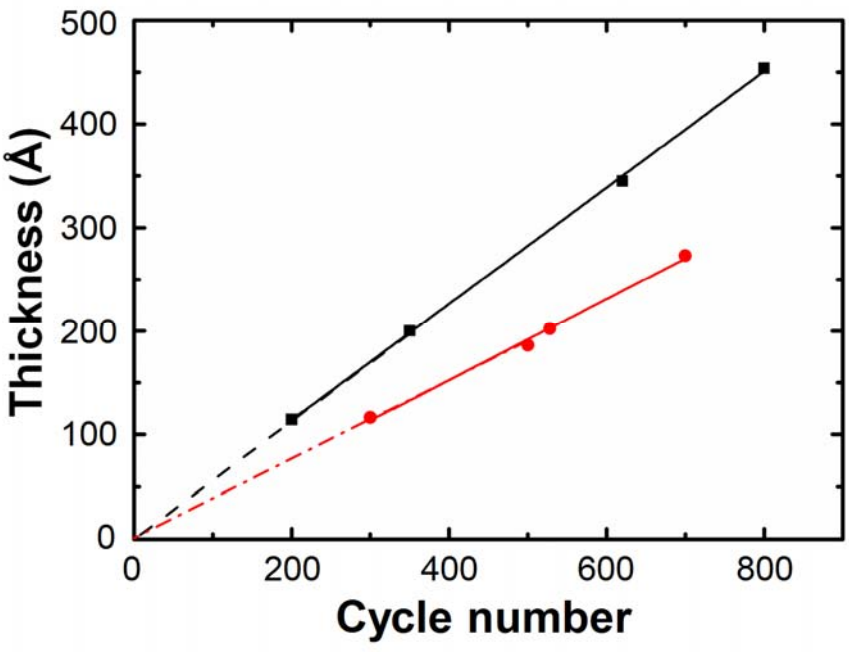


Figure 10.11 Film thickness of hydrolyzed Zn-hybrid films obtained from spectroscopic ellipsometry, plotted versus number of MLD cycles for films deposited on oxidized silicon. The typical uncertainty in each measurement is ~1–2%. The solid lines give linear fits corresponding to a deposition rate of 0.57 Å/cycle at 120°C (■) and 0.39 Å/cycle at 165°C (●).

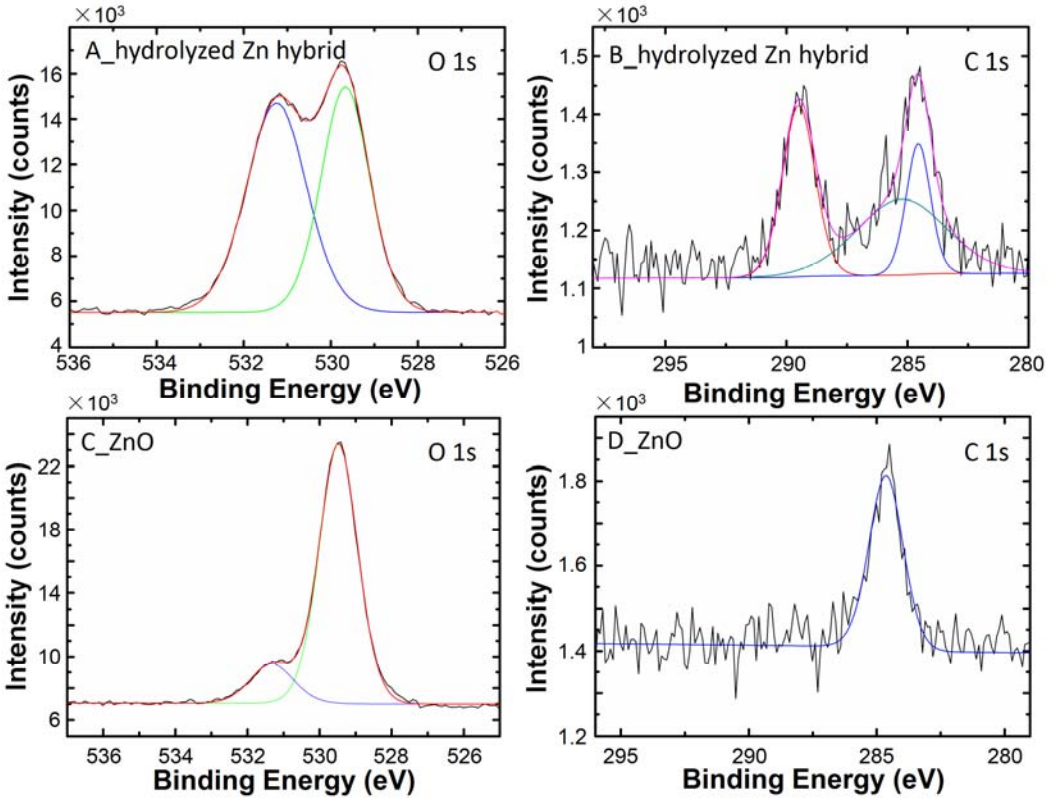


Figure 10.12 a), b) O1s and C1s XPS spectra collected from a hydrolyzed MLD Zn-hybrid film (~45 nm, 800 cycles, at 120˚C). The O1s signal shows features at 531.5 eV 529.7 eV corresponding to zinc hydroxide (54.5%) and zinc oxide (45.5%) respectively. The C1s signal includes components 284.6 eV, 285.7 eV and 289.4 eV related to –C–H_2, –C–OH and –O–C=O respectively. c), d) O1s and C1s XPS spectra collected from an ALD ZnO film (~45 nm, 200 cycles, at 120˚C). The carbon content is ~2 atomic %. Ar sputtering (5 KeV for 3 min) was used to remove surface contamination before spectra collection. Gaussian curve fits are included.

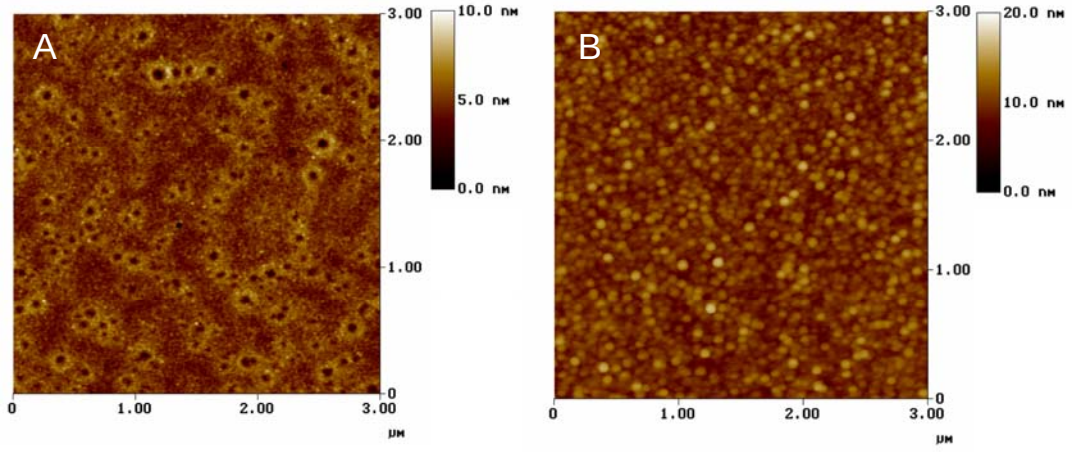


Figure 10.13 Image (a) is a scanning force micrograph of a MLD Zn-hybrid film deposited at 120 ˚C for 800 cycles after prolonged air exposure. The film thickness is ~45 nm and root mean square (RMS) roughness is 0.8 nm. The surface features with diameter of 20–30 nm are cavities or holes in the film. Image (b) was acquired after annealing the film in image (a) in ambient for 2 h at 100 ˚C. The film thickness decreased to ~30 nm and RMS increased to 1.4 nm. The surface appears more homogeneous without obvious voids or holes at the scale imaged.

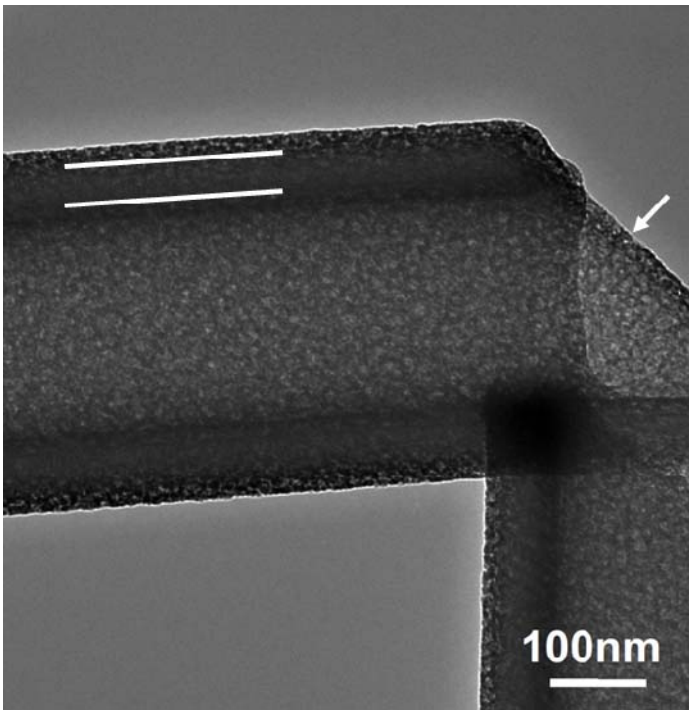


Figure 10.14 A transmission electron micrograph obtained from a hydrolyzed Zn - hybrid film deposited at 165 °C for 528 cycles onto two Al_2O_3 microtubes. The white lines depict the outline of the starting Al_2O_3 shell, and the right side of the image shows a region where the tube is broken allowing plan–view through the Zn–hybrid/Al_2O_3/Zn–hybrid laminate. The hydrolyzed Zn–hybrid MLD film is conformal and uniform with thickness ~20 nm. The white arrow indicates a point with high contrast suggesting through–holes present in the hydrolyzed film.

CHAPTER 10 is a reprint of a manuscript published in Chemistry of Materials

Table 10.1. Summary of mass uptake results obtained from QCM analysis during various ALD and MLD half–cycles on starting surfaces of interest.

Conditions	**Exposure**	**Mass uptake at 120 °C (ng/cm^2)**	**Data**
ZnO ALD Steady state	H_2O	~ -3	Fig. 4
	DEZ	~ 125 ± 3	Fig's 2, 3, 4
ZnO ALD surface –OZn-OH saturated	H_2O	~ 0	Fig. 4
	EG	~33	Fig. 4
ZnO ALD surface –OZn-C_2H_5 saturated	DEZ	~ 0	Fig. 2b
	EG	~ 33	Fig's 3a, 3b
ZnO ALD surface –OZnO–C_2H_4OH saturated	EG	~0	Fig's 3a, 3b
	DEZ	~ 16	Fig's 3a, 3b
MLD (-OZnO-C_2H_4-)$_n$ Steady state	DEZ	~ 20.4±1.3	Fig's 5-7
	EG	~ 4.8±1.4	Fig's 5-7

CHAPTER 11. Surface Functionalization with Aminosilane by Atomic Layer Deposition

Chemical and Biomolecular Engineering Department
North Carolina State University

Contact author: gnp@ncsu.edu

ABSTRACT

Chemical modification of substrates with functional reactive molecular layers, especially the amino (-NH_2) terminated layers, attract a lot of interests due to the wide range of applications in electronics, biology, catalyst, energy etc. Currently one of the major methods is to chemically assemble amino terminated silanes onto substrates, for example metal oxides, which are bearing -OH groups. As a well-known method, atomic layer deposition has been widely used to deposit highly conformal and uniform metal oxide films (Al_2O_3, ZnO, Fe_2O_3, SiO_2, TiO_2 etc) onto different substrates, including complex three dimensional nanostructures and inert surfaces at relatively low temperatures. In this study, sequential low temperature atomic layer deposition of metal oxides and amino silane self-assembly monolayer (SAM), is demonstrated as a new method to modify inert surface with amino group. Specifically, the deposition behavior of ALD of aminosilane (specifically γ-aminopropyl triethoxysilane: APTES) with H_2O on the in-situ generated Al_2O_3 ALD film is monitored by in-situ quartz crystal microbalance (QCM) at different deposition temperatures (120 and 150 ˚C). The QCM data shows that on Al-OH surface, the chemical adsorption of APTES/H_2O ALD is saturated after ~10 cycles. The ex-situ X-ray photoelectron spectroscopy measurement confirmed the N components on the surface, which is about 2.5 atomic percentages at reaction temperature of 120 ˚C. Moreover, in-situ QCM measurement

also confirmed that APTES could react with Al-CH_3 terminated Al_2O_3 ALD film surface. Detail analysis from in-situ Fourier transform infrared spectroscopy is included as well to illustrate the detail surface reaction chemistry. Moreover the APTES/H_2O ALD cycles are also studied on ZnO ALD film by QCM and other techniques. Furthermore the application of this technique on modification of the inert three dimensional fiber systems is presented as well.

11.1 Introduction

Functionalization of substrate surface with desired chemically active groups, especially amino group, attracts a lot of interests due to the wide range applications in fields including electronics,[1, 2] biomedicine and biochemistry,[3-6] catalyst,[7, 8] sensors,[9] chemical analysis,[10] optics[11] and mechanics[12]. Currently one of the major methods is to chemically assemble alkoxysilanes onto metal oxides substrates, which are bearing active -OH groups. For most of other substrates including polymers, generally a layer of metal oxides would be formed onto the inert substrates to incorporate active metal hydroxide ligands for the following silanization attachment.[6] However due to the surface tension, homogeneous reaction, it is difficult for the sol-gel process to form a conformal active metal oxide coating onto substrates with complex three dimensional structures. Although the surface sol-gel process was developed to get more uniform and conformal coatings,[6, 13] the long process time and unsolved surface tension issues presents a significant and ongoing challenge for this method.[13] Moreover, the assembly processes of silanes are usually performed in liquid phase as well, which rinse the concerns about nonuniform modification induced by the surface tension and contamination from organic solvent usage. The tedious washing steps involved in the solvent based sol-gel process and self assembly process is another big concern for actual application and environmental issue.

In this work, atomic layer deposition is presented as a promising solution for those problems mentioned above. Atomic layer deposition is a sequential, self-limiting gas phase deposition process that operates on the principle of alternating saturating surface reactions. A variety of different metal oxides including Al_2O_3,[14] SiO_2,[15-17] ZnO,[18] Fe_2O_3,[19] TiO_2[20] etc

could be deposited by ALD process with precisely controlled thickness, even into complex 3-dimensional nanostructures at relative low temperatures due to the self-limiting growth mechanism.[21, 22] Recently it was demonstrated by several groups that atomic layer deposition could also be performed onto inert surfaces (for example, polystyrene, polyethylene, polyimide, polypropylene, Teflon, etc) without reactive sites.[23-28] This unique nucleation and growth behavior of ALD growth of metal oxide films enable the incorporation of the metal hydroxide ligands onto the inert substrate, which would be accessible by the following silane treatment to allow surface engineering on the inert substrates. On the mean time, the atomic layer deposition of self assembly monolayer of amino silanes on silica substrates were studied and proved as a easy and controllable way to form high-density of amino silane monolayer on the surface.[29] In this study, sequential low temperature atomic layer deposition of metal oxides and amino silane self-assembly monolayer (SAM), is demonstrated as a promising method to modify inert surface with amino group. Specifically in-situ quartz crystal microbalance (QCM) and in-situ Fourier transmission infrared spectroscopy (FTIR) were used to illustrate the deposition behavior of 3-aminopropyl triethoxy silane (APTES)/H_2O ALD on the low temperature Al_2O_3 ALD films. Surface modification of polypropylene nonwoven fiber through this process is included as well.

11.2 Experiments

Metal oxides ALD deposition experiments and APTES/H_2O ALD process were carried out in a homemade hot wall vacuum reactor equipped in-situ QCM tools, which has been described in detail previously.[30] In-situ QCM was used to monitor the surface

deposition behavior during the ALD processes. During the QCM experiment, the ALD processes were performed at normal continuous mode of dose/purge/dose/purge.

Infrared spectra were collected by an in-situ FTIR spectrometer equipped with MCT-A detector.[31] The unpolarized IR beam were directed from FTIR spectrometer into and out of the reactor though two CsI windows, which were isolated by two gate valves from the reaction chamber in order to prevent materials from being deposited onto the windows. The optical paths out of the vacuum chamber were purged with dry air, which is CO_2-free as well. In the reactor, the IR beam is transmitting through the substrate. In order to get enough infrared signal during the transmission IR analysis, high surface area anodic aluminum oxide (AAO) porous membranes (Whatman®) were used as the substrates, which is 60 μm in thickness and have average pore diameters around 100 nm. All of the IR spectra were referenced to the spectrum of the very last generated substrate as the background. For each measurement, 200 scans are averaged at 4 cm^{-1} resolution.

Trimethyl aluminum (Strem, 98%), diethyl zinc (Strem, 96%) and deionized water (DI H_2O) were used as the reactants for Al_2O_3 and ZnO ALD process. Trimethyl aluminium (TMA) and diethyl zinc (DEZ) and DI H_2O were introduced into the reactor as room temperature vapor. 3-aminopropyl triethoxy silane (Sigma, 99%) is used the precursor for the amino silane atomic layer deposition process. APTES was heated to ~110 ˚C and introduced into the reactor by direct injecting into the carrier gas. High purity Ar (99.999%) (National Welders Supply Co.), purified with a gas filter (Gatekeeper®), was used as the purge gas and carrier gas for reactants.

40 nm Au colloids solution, which were stabilized by sodium citrate, were purchased from Ted Pella. Its pH value was adjusted to ~5.5 by acetic acid. For the Au colloids electrostatic adsorption experiment, substrates were incubated in the Au colloid solutions for 24 hours. After the adsorption experiment, the as-formed fiber matrix will be rinsed in DI water several times and then dried in air before analysis.

X-ray photoelectron spectroscopy (XPS) analysis was performed on Kratos Analytical Axis Ultra equipment with a monochromatic Al Kα source operated at 15 kV. For all samples, the C 1s peak ($–C–H_2$) was normalized to 284.6 eV as the reference. For the survey and detail scans, 160 and 20 eV were used for the pass energy respectively.

Surface morphology of films was analyzed by a Nanoscope IIIa atomic force microscope (Digital Instruments) operated in tapping mode with a scanning frequency of 0.5 Hz. The morphology of the resulted samples was analyzed by scanning electron microscopy (FEI XL30 SEM-FEG) operated at 5 keV.

11.3 Experiment results

Figure 11.1 shows the in-situ QCM measurement of the deposition behavior of atomic layer deposition of APTES/H_2O on the Al-OH terminated Al_2O_3 ALD film surface at 120 ˚C. For both Al_2O_3 ALD and APTES/H_2O ALD process, the ALD sequence of 2/40/2/40 s was used. In the Figure, the dose step (2s) of TMA, H_2O and APTES were labeled as solid line, dash line and dot line, respectively. Generally, purge time 40s is used between each dose steps. Before the APTES/H_2O ALD process, more than 100 cycles of Al_2O_3 ALD deposition were performed onto the QCM crystal surface in order to get the stabilized saturated Al_2O_3 ALD growth and cover the crystal surface completely with Al_2O_3. The QCM data of last several cycles of Al_2O_3 ALD was shown by the first stage of the data in Figure 11.1. According to the QCM data, the net mass uptake for the TMA steps (dose/purge, 2/40 s) is ~35 ng/cm^2. During H_2O half cycles (dose/purge, 2/40 s) in steady state Al_2O_3 ALD, the net mass uptake is around 6 ng/cm^2. Those mass uptake data of Al_2O_3 ALD is consistent with the literature reported values.[32] During the last cycle of Al_2O_3 ALD, the TMA dose step was skipped and only H_2O dose step was performed. The negligible mass uptake during this H_2O half cycle indicates that TMA dose is necessary for continuous Al_2O_3 ALD process. After the final half cycle of H_2O in the Al_2O_3 ALD process, the TMA dose was switched to the APTES dose. During the first pulse of the APTES dose, there is a big mass uptake followed by mass decrease in the purge step. Net mass uptake of ~ 68 ng/cm^2 was obtained for the first half cycle of APTES. The following water pulse does not affect the mass uptake much. For the 2nd APTES half cycle, the mass uptake is much smaller than 1st half cycle of APTES. Unlike the Al_2O_3 ALD process, the mass uptake for each cycle of APTES/H_2O is not

constant. The total mass uptake of 9 cycles of APTES/H_2O ALD process saturated at 88 ng/cm^2. It indicates that the majority of surface reaction between the surface bonded Al-OH ligands with APTES takes place at the first pulse of APTES. This self-limited growth behavior of APTES/H_2O ALD confirmed that there is no gas phase reaction during the process, which is consistent with the atomic layer deposition scheme. It also indicates that 40s purge time is enough for removing physical absorbed APTES and byproducts out of the reactor. After 9 cycles of APTES/H_2O ALD process, the Al_2O_3 ALD was then performed onto the APTES monolayer covered surface. According to the QCM data, the initial cycles Al_2O_3 ALD deposition on APTES covered surface has smaller mass uptake per cycle than the steady state growth rate, which indicates the passivation effect of the APTES layers.

The in-situ QCM measurement of deposition behavior of APTES/H_2O ALD process at 150 ˚C on Al-OH terminated Al_2O_3 ALD film is presented in Figure 11.2. During the steady state Al_2O_3 ALD deposition, the average mass uptake from TMA half cycle (2/40 s) and H_2O half cycle (2/40 s) is ~ 35 ng/cm^2 and 5 ng/cm^2 respectively, which are consistent with the results from Figure 11.1. In the similar fashion as the experiment performed in Figure 11.1, APTES/H_2O ALD process was then performed onto the QCM crystal surface, which has been covered by Al_2O_3 film terminated with Al-OH ligands. The mass uptake for the first half cycle of APTES is around 78 ng/cm^2. During the following H_2O half cycle, there is a small mass drop, which is due to the hydrolysis of the ethoxy group by H_2O. The total mass uptake after 11 cycles of APTES/H_2O ALD is saturated at ~138 ng/cm^2 and most of them are contributed from the first 4 cycles. It indicates that the surface reaction is almost saturated after 5 ALD cycles of APTES/H_2O. This self-limited growth behavior of

APTES/H_2O ALD confirmed that there is no gas phase reaction during the process. Similar as the Figure 11.1, the mass uptake rate of initial cycles of Al_2O_3 ALD on the APTES layer covered surface is smaller than the steady state growth rate of the Al_2O_3 ALD.

The representative IR spectra of the anodic aluminum oxide porous substrates after Al_2O_3 ALD, APTES/H_2O ALD process are shown in Figure 11.3. All the IR spectra are obtained by using the previous substrate as the background reference. The in-situ IR experiments were performed at 100 ˚C. The detail peaks assignments for each spectrum are listed in Table 11.1. The TMA spectrum in Figure 11.3a shows the representative infrared spectrum obtained after dose of TMA onto Al_2O_3 ALD film coated porous substrate. Spectrum shows clear negative -OH peak (broad peak from 3800-3000 cm^{-1}) and a positive peak of C-H stretch mode (at 2942, 2898, 2834 cm^{-1}) due to the surface bonded CH_3-Al surface ligands. The typical H_2O spectrum taken after the H_2O half cycle in Al_2O_3 ALD exhibits a negative infrared absorbance of the C-H stretching vibration of -CH_3 and a positive -OH peak from Al-OH ligands. These typical IR spectra taken during the Al_2O_3 ALD cycles are consistent with the literature reported data[31] and confirmed the surface reaction chemistry during the alternative pulsing of TMA and H_2O onto the substrate. After the final pulse of H_2O and the following purge step in Al_2O_3 ALD, one pulse of APTES was dosed onto the Al-OH terminated porous substrate. The resulted IR spectrum of APTES after purge, shows negative -OH peak and positive C-H stretching mode. The C-H stretching mode is different and more complex than the C-H mode in TMA spectrum. This complexity of C-H mode is due to the complex C-H bondings existed in the surface attached APTES ligands, which have -OCH_2CH_3- and -CH_2-CH_2-. Furthermore, signature signals of -CH_3 deformation mode (1442

and 1380 cm^{-1})[33, 34] and bending mode of the -CH_2- (1293 cm^{-1})[33, 34] is clearly observed in the APTES spectrum. Moreover, the stretching mode and scissor mode of N-H is visible around 3300 cm^{-1} and around 1580 cm^{-1} respectively.[33, 35] Those N-H modes provided direct evidence for APTES functionalization. Figure 11.3a also displays changes in the infrared absorption spectra of the porous substrate after water pulse followed the APTES purge step. It shows that the negative peaks of C-H stretching mode from 3000-2800 cm^{-1} and CH_3 deformation mode. At the mean time, there is a very small positive peak of –OH (broad peak from 3800-3000 cm^{-1}). This spectrum indicates that some of the ethoxyl ligands are removed by the water hydrolysis process.

Figure 11.3b presents the infrared spectra taken for the 2^{nd}-4^{th} cycles of APTES/H_2O on the Al_2O_3 ALD film coated porous substrate. Generally, after APTES exposure, the positive signal of -CH_3 and -CH_2 and negative –OH peak show up. The opposite phenomena were observed after H_2O exposure. The spectra taken after APTES for the 2^{nd}-4^{th} cycles resemble the shape of the spectrum taken after 1^{st} half cycle of APTES exposure except that the signal intensities of -CH_3 and -CH_2 adsorption decrease with cycle number increase.

Figure 11.3c shows that after 10 cycles of APTES/H_2O, the spectra taken for APTES and H_2O half cycles exhibits no obvious signals. It indicates the saturation of the surface reaction for the ALD of APTES/H_2O and self-limiting deposition behavior of APTES/H_2O ALD, which is consistent with the in-situ QCM data. The detail reaction chemistry will be discussed below. The surface chemistry of the Al_2O_3 ALD on the APTES covered substrate was also studied by performing TMA and H_2O ALD cycles after the APTES/H_2O ALD

process saturated. Spectrum of 1st TMA shows small negative –OH peak (broad peak from 3800-3000 cm^{-1}) and an positive C-H stretch mode (at 2990-2825 cm^{-1}). It is interesting that there is small positive peak at around 1580 cm^{-1}, which may come from the N-H scissor mode. However the reason is unclear. The spectrum is different than the TMA spectrum taken during the Al_2O_3 ALD process, which indicates different surface chemistry on the APTES covered substrate. After the H_2O half cycle, the spectrum shows small positive –OH peak and negative CH stretching mode. Interesting, there is a small negative peak at 1580 cm^{-1}. The detail surface reaction mechanism is discussed in the Discussion section.

The representative XPs analysis of the atomic composition of silicon substrate, which has been treated with 100 cycles of Al_2O_3 ALD followed by 10 cycles of APTES/H_2O ALD, is shown in Figure 11.4. The atomic concentration of N is around 2.5 at. %. The detail scan of N 1s is also presented in Figure 11.4, which shows the two chemical status of N. The one associated with 398.8 eV is assigned to non-H bonded amino groups. The one at 400.2 eV is assigned to the H-bonded amino groups.[36]

The sequential ALD process of Al_2O_3 (100 cycles) and APTES/H_2O (10 cycles) was applied onto polypropylene (PP) nonwoven fiber matrix, which has three dimensional complex fiber structures, as shown by the SEM image of pure nonwoven PP fiber matix in Figure 11.5a. The PP fibers are randomly laying on each other. The structure of the fiber matrix is complex and irregular. Figure 11.5b presents the microtube replica prepared by ALD wherein the sequential ALD processes of Al_2O_3 (100 cycles) and APTES/H_2O (10 cycles) were performed at 120 ˚C. The replica is prepared by removing PP fiber template

through calcination at 500 ˚C in air for 24 hours. The replica resembles the original complex structure of the PP nonwoven fiber matrix, which indicates successful conformal coverage formed onto the fibers by ALD process although the PP fibers do not have reactive sites for the ALD process. After the sequential ALD processes, the as-treated PP fiber matrix were then immersed into the 40 nm Au nanoparticle colloid solution for 24 hours in order to form electrostatic assembled Au nanoparticles layers onto the -NH_2 functionalized fiber surface. After the Au colloid solution treatment, visually the fiber matrix turns into deep red color, which does not decay after rinsing in DI-water several times. In contrast, pure PP fiber matrix and the ones with only Al_2O_3 ALD or APTES/H_2O ALD treatment at the same reaction conditions maintained their white color, which indicates no attachment of Au colloids. The SEM images presented in Figure 11.5c and 11.5d, provided direct evidence for the dense attachment of Au nanoparticles. As shown in the enlarged image in Figure 11.5d, the Au nanoparticle attachment is on every single fiber. Those results provided strong evidence that the -NH_2 terminated APTES monolayer were successfully incorporated onto the Al_2O_3 ALD covered PP fibers and its functionality as negative ions bonding sites.

The APTES/H_2O ALD process could also be performed sequentially with ALD process of other metal oxides including SiO_2, ZnO, TiO_2, SnO_2 etc. Figure 11.6 presents the results of the QCM data of the sequential ALD process of ZnO and APTES/H_2O ALD. In that experiment, more than 200 cycles of ZnO ALD (DEZ/Ar/H_2O/Ar: 2/40/2/40 s) were performed onto the QCM crystal to form a conformal coverage of the ZnO film. The steady state growth of ZnO ALD was achieved after ~ 50 cycles. The first stage of the data in Figure 11.6 shows the deposition behavior of typical ZnO ALD process. The Majority of mass

uptake during ZnO ALD is from DEZ half cycle, which is consistent with the reaction chemistry and previous reported values.[30] After the last half cycle of H_2O in ZnO ALD process, the surface were covered by Zn-OH ligands. Then the APTES dose was performed and a net mass increase (~ 60 ng/cm^2) was observed for the first half cycle of APTES. There is a small mass decrease observed in the following half cycle of H_2O. After repeating the APTES/H_2O cycles for 5 cycles, no more mass uptake was achieved, which indicates that the majority of reaction between APTES and surface bonded Zn-OH ligands was completed in the first cycle of APTES/H_2O. It demonstrated that the APTES SAM could also be formed onto the Zn-OH terminated ZnO ALD film as well.

Recently the non-hydrolytic metal oxide ALD process attracts a lot of interests.[17, 37, 38] Moreover, the interesting surface reaction chemistry was observed for ALD of APTES/H_2O onto the Al-CH_3 terminated Al_2O_3 ALD surface. As shown in Figure 11.7a, a representative in-situ QCM data at 150 ˚C shows that APTES could chemically react with the Al-CH_3 terminated surface. The mass uptake of 1st pulse of APTES on Al-CH_3 terminated surface is around 78 ng/cm^2. During the water dosing step, it is interesting to observe that the mass decrease first, followed by mass increase. The 2nd APTES half cycle also contributes ~ 20 ng/cm^2. The mass uptake of ALD APTES/H_2O nearly saturated after 5-6 cycles. The reaction chemistry during this process was also monitored by in-situ FTIR technique. The spectra are presented in Figure 11.7b. The spectra after TMA and H_2O half cycles in Al_2O_3 ALD process resemble the corresponding spectra in Figure 11.3a. Obviously the positive –OH peak and negative -CH_3 peaks are shown in the spectrum after H_2O dose/purge. On the opposite way, the negative -OH peak and positive -CH_3 were observed in after TMA pulsing during the

Al_2O_3 ALD process. On the Al-CH_3 toped porous substrates, the 1st dose of APTES and the following purge was performed. The resulted spectrum shows positive C-H stretching mode (3000-2800 cm^{-1}), C-H deformation mode (1442, 1380 and 1293 cm^{-1}) and -NH_2 stretch and scissor mode (center at 3300 cm^{-1} and 1580 cm^{-1}) suggested that APTES covalently bonded onto the substrate. Note, there is no clear negative peak of –OH in the spectrum at 3750cm^{-1} and 3800-3000 cm^{-1}, which confirm there is no –OH group on the TMA last substrates. After the APTES lasted substrates exposed to H_2O, the IR spectrum show positive -OH peak (broad peak 3800-3000 cm^{-1}) and negative -CH mode. The positive –OH mode is due to the hydrolysis reaction between the unreacted Al-CH_3 ligands and H_2O. It also contributes the negative C-H mode. At the mean time, the reactions between H_2O and surface bonded Si-O-C_2H_5 ligands release -CH_x ligands. The detail surface reaction chemistry is discussed in the following text.

11.4 Discussion

As illustrated in Figure 11.1 and Figure 11.2, the deposition behavior of APTES/H_2O ALD on Al-OH topped Al_2O_3 ALD film at different reaction temperatures is similar with each other in an overall view. For both cases, the mass uptake comes from the first half cycle of APTES is much bigger than the ones from following cycles. It suggests that the reaction between the APTES and Al-OH ligands is fast. The total mass uptake from the many APTES/H_2O cycles eventually saturated, which indicates the self-limiting and saturation deposition mode and consistent with the proposed and simplified reaction path as discussed in Scheme 11.1.[29, 39]

Scheme 11.1 illustrates the reaction mechanism of APTES/H_2O ALD on the Al_2O_3 ALD films coated substrates with Al-OH terminal groups. First of all, the substrate was coated by Al_2O_3 ALD film, which brings dense Al-OH ligands onto the substrates.[40] Following Al_2O_3 ALD process, one pulse APTES was dosed onto the substrates and reacted with the Al-OH ligands to form Si-O-Al bondings with -NH_2 attached and stick out of the substrate surface. However, due to the limited number of reactive -OH ligands on the surface as well as the steric hindrance effect of the large ethoxide groups (-O-C_2H_5), there are still some non-hydrolyzed -Si-O-C_2H_5 bondings on the surface bonded APTES molecules as shown in Scheme 11.1. During the following purge step, all physical adsorbed APTES molecules would be removed from the chamber before the H_2O pulse in order to eliminate the homogeneous gas phase reaction. After that, a pulse of H_2O dose was used to hydrolyze all of the non-hydrolyzed Si-O-C_2H_5 ligands and convert them into Si-OH ligands, which act as the hydrolysis agent for the 2nd APTES pulse following the purge step for H_2O. After repeating this APTES/H_2O cycle for several times, the substrate surface will be eventually saturated with a denser APTES monolayer, which is agree with the literature report of APTES/H_2O ALD on the silicas.[29, 39]

Although the general reaction scheme at different reaction temperatures follows the reaction Scheme 11.1, according to the QCM data in Figure 11.1 and Figure 11.2, the temperature effect on the APTES/H_2O ALD is apparent, beside the similarity of these two sets of data. First of all, in comparison with the 138 ng/cm^2 obtained at 150 ˚C, the saturated mass uptake from APTES/H_2O ALD at 120 ˚C is ~88 ng/cm^2. Second of all, the 1st half cycle of H_2O resulted in a clear mass drop at 150 ˚C, which is not observed in the process

performed at 120 ˚C. Moreover, the contribution of mass uptake from the 2nd, 3rd and 4th cycles is larger for reaction at 150 ˚C compared with the one performed at 120 ˚C. Those data indicate that higher molecular density in APTES monolayer is formed with deposition performed at 150 ˚C. All of those differences are due to the temperature dependent hydroxylation of alkoxy groups during the water half cycles. The degree of the hydrolysis of ethoxy ligands in the water half cycle increases with reaction temperature. As evidenced at higher reaction temperature (150 ˚C), there is a detectable mass decrease in the H_2O half cycle, which is not that obviously in the lower reaction temperatures 120 ˚C. It is well recognized that the ethoxy group of APTES could be hydrolyzed in the presence of water at low temperature (room temperature) due to the self catalytic effect of amino groups, especially with longer exposure (> 1hr). However it is not practical to perform the H_2O pulsing step for one hour in the ALD process in order to achieve higher degree of hydrolysis of ethoxy ligands at relatively low reaction temperature. On the other hand, the clear –CH stretch mode during the H_2O half cycles at 100 ˚C was observed to be negative, which indicates that the hydrolysis reaction do occur at low reaction temperature as well, except the lower extent of this reaction.

a. The density of APTES ligands:

Due to the complexity of the bonding conditions of the actual APTES molecules on the substrate surface, it is difficult to precisely calculate the $-NH_2$ ligand density based on the QCM measurement. The APTES molecules could bond on the surface through one, two or three Si-O-Al and left the other ethoxides group intact, then the mass uptake on the surface

contributed from one mole of such kind of surface bonded APTES molecules is 176g, 131g and 86g. Based the mass uptake date of 1st half cycles of APTES at 120 ˚C, the -NH_2 density generated from that is 2.3-4.7/nm^2. Calculated at the same way, the -NH_2 density generated from 1st half cycle of APTES onto Al-OH topped Al_2O_3 film at 150 ˚C is about 2.7-5.7/nm^2. This-NH_2 group density data is consistent with the previous study of APTES adsorption of on the Al-OH surface.[41] After the surface saturated with APTES molecules with consecutive APTES/H_2O cycles, the -NH_2 density resulted from 120 ˚C and 150 ˚C is around 3-6/nm^2 and 4.8-10/nm^2. Those values are generally higher than the reported -NH_2 density on the silica substrate with the similar APTES/H_2O ALD cycles,[29] which is probably due to the higher density of the hydroxyl group (> 7/nm^2)[40] in the in-situ generated Al-OH surface at the lower deposition temperatures (<200 ˚C) compared with the silica substrate used in the literature (< 6.5 /nm^2). However in order to illustrate the discrepancy of the density data, more analysis experiment in the future is necessary.

The surface reaction mechanism of ALD APTES on Al-CH_3 terminated Al_2O_3 surface is presented in Scheme 11.2. The reaction between APTES and Al-CH_3 is a nonhydrolysis process with byproducts of $CH_3CH_2CH_3$ released from the surface. However due to the steric hindrance effect, there are still some Al-CH_3 ligands left over after the reaction. So when next water pulse dosed onto the substrate surface, all of the unreacted Al-CH_3 ligands were converted into the Al-OH ligands, which will add more mass onto the substrate surface. At the meantime the unreacted Si-O-C_2H_5 were hydrolyzed into Si-OH ligands and cause mass decrease. Due to these two effects, the QCM measurement shows that mass decreased first and then increased in the 1st half cycle of H_2O in the APTES/H_2O ALD

according to the data in Figure 11.7a. In the corresponding in-situ IR spectrum of the 1st half cycle of H_2O, the positive –OH peak (3800-3000 cm^{-1}) and negative peak of CH modes (3000-2800 cm^{-1}) provide further evidence for the simultaneous hydrolysis reactions between the Al-CH_3 ligands and H_2O molecules and ethoxy groups with H_2O. The QCM data from the 2nd cycle of APTES/H_2O resembles the data of APTES/H_2O ALD cycles in Figure 11.2. It indicates the reaction chemistry would be the same as the one performed on the Al-OH terminated substrate surface, which is shown in Scheme 11.1.

11.5 Conclusions

Sequential Al_2O_3 ALD and APTES/H_2O ALD were performed at different temperatures. By using in-situ QCM and FTIR methods, the deposition behavior and surface reaction chemistry of the sequential Al_2O_3 ALD and APTES/H_2O ALD was studied. This method is demonstrated as a promising way to functionalize substrate with amino active groups. The material growth from APTES/H_2O ALD process saturates within 10 cycles with a higher surface coverage density of $–NH_2$ groups than the one generate from only one pulse of the APTES dose. This sequential ALD process of Al_2O_3 and APTES/H_2O was successfully applied onto inert polypropylene nonwoven fiber matrix, which has three dimensional complex structures, to generate reactive $–NH_2$ ligands throughout the matrix. This method could also be adapted to other silane chemistries[29, 39, 42, 43] and metal oxide ALD processes to form designer functional reaction sites into the complex structures, as evidenced by in-situ QCM data of the sequential ALD of ZnO and APTES/H_2O. This sequential ALD

process of metal oxides and silanes provides a general strategy with which to design and produce well tuned and controlled surface reactive layers.

11.6 Acknowledgement.

This work was supported by the National Science Foundation under grant CTS-0626256, and by the STC Program of the National Science Foundation under Agreement No. CHE-9876674.

REFERENCES

1. Kobayashi, S.; Nishikawa, T.; Takenobu, T.; Mori, S.; Shimoda, T.; Mitani, T.; Shimotani, H.; Yoshimoto, N.; Ogawa, S.; Iwasa, Y., *Nature Materials* **3,** 317-322 (2004).
2. DiBenedetto, S. A.; Facchetti, A.; Ratner, M. A.; Marks, T. J., *Advanced Materials* **21,** 1407-1433 (2009).
3. Subramanian, A.; Kennel, S. J.; Oden, P. I.; Jacobson, K. B.; Woodward, J.; Doktycz, M. J., *Enzyme and Microbial Technology* **24,** 26-34 (1999).
4. Hsiao, V. K. S.; Waldeisen, J. R.; Zheng, Y. B.; Lloyd, P. F.; Bunning, T. J.; Huang, T. J., *Journal of Materials Chemistry* **17,** 4896-4901 (2007).
5. Robinson, P. J.; Dunnill, P.; Lilly, M. D., *Biochimica Et Biophysica Acta* **242,** 659-& (1971).
6. Huang, J. G.; Ichinose, I.; Kunitake, T., *Angewandte Chemie-International Edition* **45,** 2883-2886 (2006).
7. Brunel, D., *Microporous and Mesoporous Materials* **27,** 329-344 (1999).
8. LizMarzan, L. M.; Giersig, M.; Mulvaney, P., *Langmuir* **12,** 4329-4335 (1996).
9. Buso, D.; Palmer, L.; Bello, V.; Mattei, G.; Post, M.; Mulvaney, P.; Martucci, A., *Journal of Materials Chemistry* **19,** 2051-2057 (2009).
10. Grabar, K. C.; Freeman, R. G.; Hommer, M. B.; Natan, M. J., *Analytical Chemistry* **67,** 735-743 (1995).
11. Cooper, T. M.; Campbell, A. L.; Crane, R. L., *Langmuir* **11,** 2713-2718 (1995).
12. Tsukruk, V. V.; Bliznyuk, V. N., *Langmuir* **14,** 446-455 (1998).

13. Ichinose, I.; Senzu, H.; Kunitake, T., *Chemistry of Materials* **9,** 1296-& (1997).

14. Peng, Q.; Sun, X. Y.; Spagnola, J. C.; Hyde, G. K.; Spontak, R. J.; Parsons, G. N., *Nano Letters* **7,** 719-722 (2007).

15. Burton, B. B.; Boleslawski, M. P.; Desombre, A. T.; George, S. M., *Chemistry of Materials* **20,** 7031-7043 (2008).

16. Bachmann, J.; Zierold, R.; Chong, Y. T.; Hauert, R.; Sturm, C.; Schmidt-Grund, R.; Rheinlander, B.; Grundmann, M.; Gosele, U.; Nielsch, K., *Angewandte Chemie-International Edition* **47,** 6177-6179 (2008).

17. Hausmann, D.; Becker, J.; Wang, S. L.; Gordon, R. G., *Science* **298,** 402-406 (2002).

18. Peng, Q.; Sun, X. Y.; Spagnola, J. C.; Saquing, C.; Khan, S. A.; Spontak, R. J.; Parsons, G. N., *Acs Nano* **3,** 546-554 (2009).

19. Bachmann, J.; Jing, J.; Knez, M.; Barth, S.; Shen, H.; Mathur, S.; Gosele, U.; Nielsch, K., *Journal of the American Chemical Society* **129,** 9554-+ (2007).

20. Kim, G. M.; Lee, S. M.; Michler, G. H.; Roggendorf, H.; Gosele, U.; Knez, M., *Chemistry of Materials* **20,** 3085-3091 (2008).

21. Leskela, M.; Ritala, M., *Angewandte Chemie-International Edition* **42,** 5548-5554 (2003).

22. Knez, M.; Niesch, K.; Niinisto, L., *Advanced Materials* **19,** 3425-3438 (2007).

23. Sinha, A.; Hess, D. W.; Henderson, C. L., *Journal of Vacuum Science & Technology B* **25,** 1721-1728 (2007).

24. Lee, S. M.; Pippel, E.; Gosele, U.; Dresbach, C.; Qin, Y.; Chandran, C. V.; Brauniger, T.; Hause, G.; Knez, M., *Science* **324,** 488-492 (2009).

25. Kemell, M.; Farm, E.; Ritala, M.; Leskela, M., *European Polymer Journal* **44,** 3564-3570 (2008).

26. Wilson, C. A.; Grubbs, R. K.; George, S. M., *Chemistry of Materials* **17,** 5625-5634 (2005).

27. Groner, M. D.; George, S. M.; McLean, R. S.; Carcia, P. F., *Applied Physics Letters* **88,** 3 (2006).

28. Liang, X. H.; King, D. M.; Li, P.; Weimer, A. W., *Journal of the American Ceramic Society* **92,** 649-654 (2009).

29. Ek, S.; Iiskola, E. I.; Niinisto, L.; Vaittinen, J.; Pakkanen, T. T.; Keranen, J.; Auroux, A., *Langmuir* **19,** 10601-10609 (2003).

30. Peng, Q.; Gong, B.; VanGundy, R. M.; Parsons, G. N., *Chemistry of Materials* **21,** 820-830 (2009).

31. Dillon, A. C.; Ott, A. W.; Way, J. D.; George, S. M., *Surface Science* **322,** 230-242 (1995).

32. Groner, M. D.; Fabreguette, F. H.; Elam, J. W.; George, S. M., *Chemistry of Materials* **16,** 639-645 (2004).

33. Pasternack, R. M.; Amy, S. R.; Chabal, Y. J., *Langmuir* **24,** 12963-12971 (2008).

34. Kuznetsova, A.; Wovchko, E. A.; Yates, J. T., *Langmuir* **13,** 5322-5328 (1997).

35. Kim, A.; Filler, M. A.; Kim, S.; Bent, S. F., *Journal of the American Chemical Society* **127,** 6123-6132 (2005).

36. Kallury, K. M. R.; Macdonald, P. M.; Thompson, M., *Langmuir* **10,** 492-499 (1994).

37. Ritala, M.; Kukli, K.; Rahtu, A.; Raisanen, P. I.; Leskela, M.; Sajavaara, T.; Keinonen, J., *Science* **288,** 319-321 (2000).

38. Rauwel, E.; Clavel, G.; Willinger, M. G.; Rawel, P.; Pinna, N., *Angewandte Chemie-International Edition* **47,** 3592-3595 (2008).

39. Ek, S.; Iiskola, E. I.; Niinisto, L., *Langmuir* **19,** 3461-3471 (2003).

40. Puurunen, R. L., *Journal of Applied Physics* **97,** 52 (2005).

41. Kurth, D. G.; Bein, T., *Angewandte Chemie-International Edition in English* **31,** 336-338 (1992).

42. Ek, S.; Iiskola, E. I.; Niinisto, L.; Pakkanen, T. T.; Root, A., *Chemical Communications***,** 2032-2033 (2003).

43. Ek, S.; Iiskola, E. I.; Niinisto, L.; Vaittinen, J.; Pakkanen, T. T.; Root, A., *Journal of Physical Chemistry B* **108,** 11454-11463 (2004).

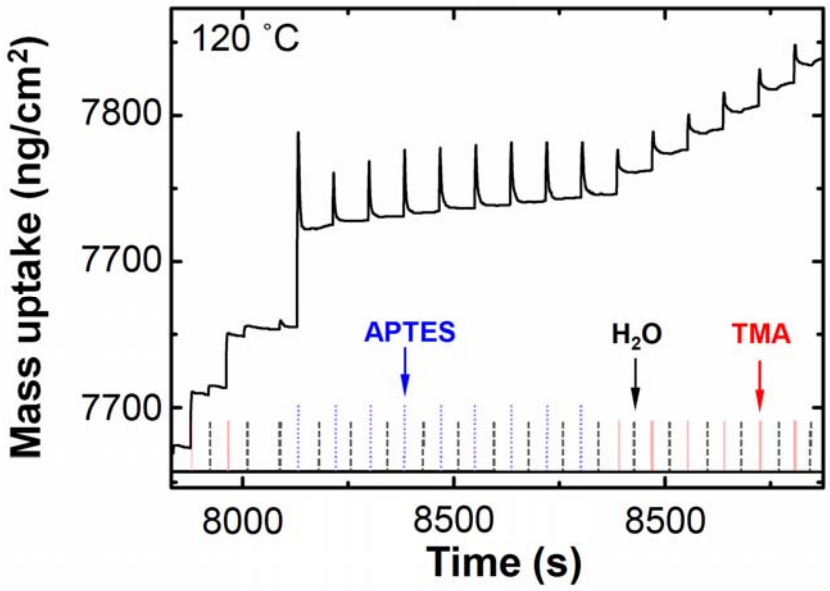


Figure 11.1 In-situ QCM measurement of APTES/ H_2O ALD (2/40/2/40 s) on Al_2O_3 ALD film. It shows steady state Al_2O_3 ALD process (2/40/2/40 s) at 120 ˚C, which has a mass uptake of ~35 ng/cm^2 for TMA dose, ~6 ng/cm^2 for H_2O dose. The mass uptake of the 1st cycle of APTES on Al_2O_3 ALD film is ~68 ng/cm^2. The following 8 cycles of APTES/H_2O contribute ~20 ng/cm^2. The surface reaction is completed after 5 cycles. The following Al_2O_3 ALD on APTES covered surface has a smaller mass uptake than steady state growth rate of Al_2O_3 ALD.

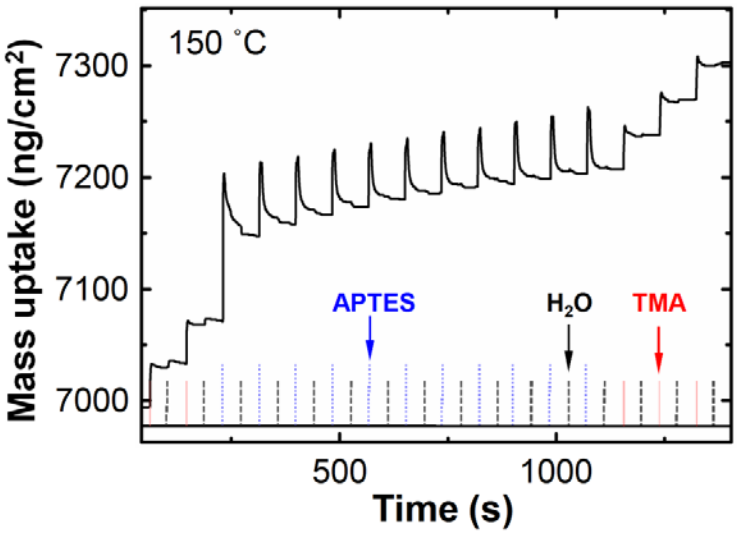


Figure 11.2 In-situ QCM measurement at 150 ˚C: Al_2O_3 ALD, APTES/H_2O ALD cycles (2/40/2/40 s) on Al-OH terminated Al_2O_3 ALD film, Al_2O_3 ALD on APTES covered surface. It shows steady state Al_2O_3 ALD process (2/40/2/40 s) at 150˚C, which has a mass uptake of ~35 ng/cm^2 for TMA dose, ~5 ng/cm^2 for H_2O dose. The mass uptake of the 1st cycle of APTES on Al_2O_3 ALD film is ~78 ng/cm^2. The mass uptake from 11 cycles of APTES/H_2O is saturated at ~138 ng/cm^2. The mass uptake of TMA on the APTES covered surface is ~28 ng/cm^2, which is smaller than the steady state mass uptake rate of Al_2O_3 ALD.

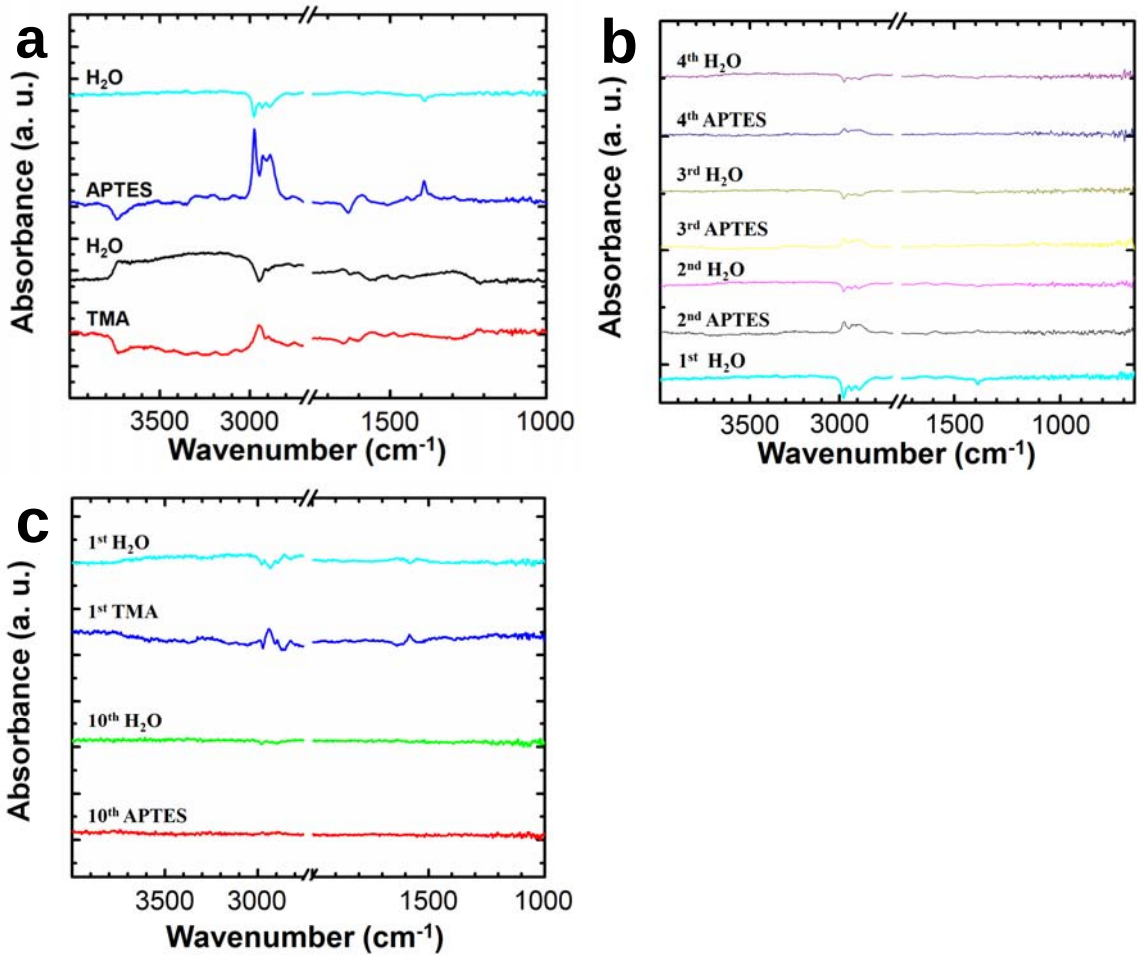


Figure 11.3 Representative in-situ FTIR spectra of the Al_2O_3 ALD film (with Al-OH surface bonded ligands) coated AAO substrate at 100 ˚C: A) after sequential TMA half cycle, H_2O half cycle, APTES half cycle, then the H_2O half cycle. B) The No. 2 to No. 4 cycles of APTES/H_2O after the 1st cycle of APTES/H_2O. C) The No. 10 cycle of APTES/H_2O, followed by TMA and H_2O dose at same temperature. All spectra were taken after more than 1mins purge time to make sure that all physical absorbed molecules were removed.

Table 11.1 Infrared spectral assignment of APTES functionalized Al_2O_3 ALD film and the surface generated after TMA and H_2O half cycles in Al_2O_3 ALD process.

Al_2O_3 ALD	Frequency (cm^{-1})
CH_3asym stretch	2942
CH_3 sym stretch	2898
CH_3 bending	2834
Isolated Al-OH	3735
CH_3 sym deform	1221
APTES/H_2O ALD	Frequency (cm^{-1})
OH stretch	Broad peak from 3800-3000
NH_2 and NH stretch	Center at 3300
CH_3 and CH_2 stretch	3115, 3023, 3005, 2975, 2928,2917, 2899, 2888
NH_2 scissor	1580
CH_3 deformation	1442
CH_3 sym deformation	1380
CH_2 in-plane bend	1293
Al_2O_3 ALD on APTES covered surface	Frequency (cm^{-1})
OH stretch	Broad peak from 3800-3000
CH_3 Stretch	2990, 2943, 2896, 2822
NH_2 and NH stretch	Center at 3300
NH_2 scissor	1578

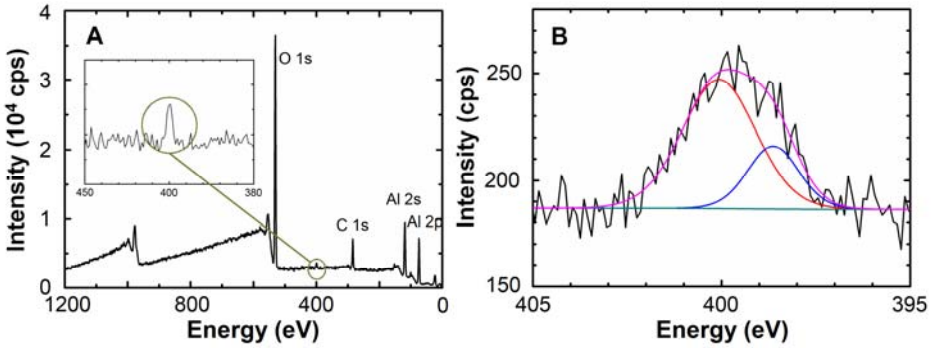


Figure 11.4 XPS analysis of Al_2O_3 ALD film (deposited at 120 ˚C) with 10 cycles of APTES/H_2O (2/40/2/40 s) at 120 ˚C. A) The survey scan of the APTES functionalized Al_2O_3 film. The N atomic concentration is ~2.5 %, which is similar as the Si atomic ratio in the film. It shows that N 1s peak in the film. B) The detail scan of the N 1s peaks (in black), which is fitted with Gaussian curve. According to the fitting, there are two components of Nitrogen were observed in the APTES monolayer.

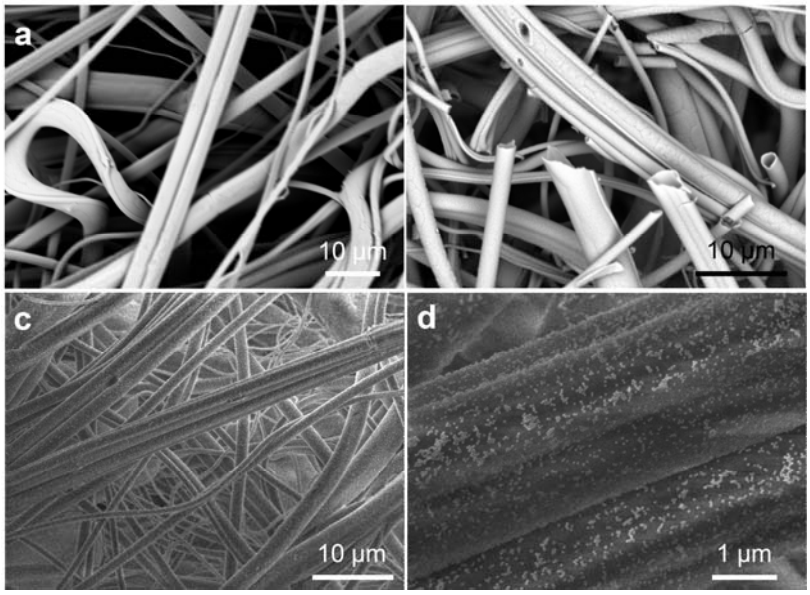


Figure 11.5 a) The nonwoven polypropylene fiber matrix coated by Al_2O_3 ALD 100 cycles and 10 cycles of APTES/H_2O ALD process at 120 ˚C. b) The replica resulted by removing template of nonwoven PP fiber matrix through annealing in air at 500 ˚C for 24 hours. c) The overall view of the PP fibers with 40 nm Au NP attachment. The resulted fibers from (a) were dipped into the 40nm Au colloid solutions for 24 hours. d) The higher magnification view of PP fibers coated with Au NPs.

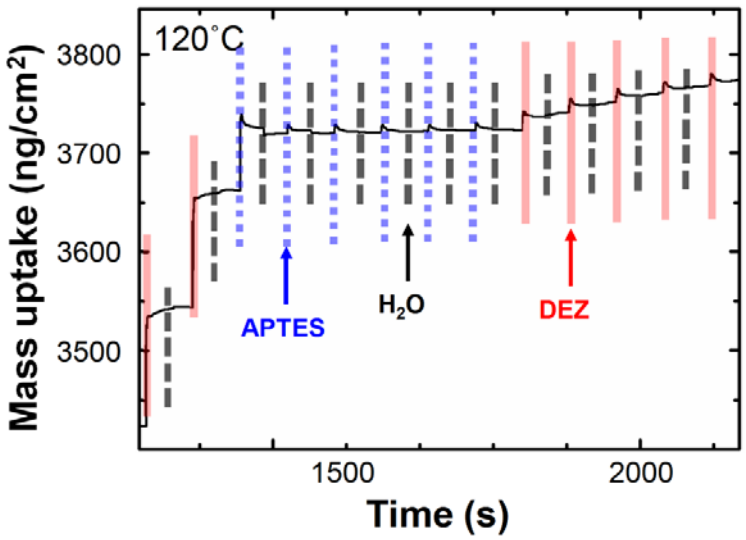


Figure 11.6 In-situ QCM measurement of APTES/H_2O cycles (2/40/2/40 s) on ZnO ALD films. The mass uptake of the 1st pulse of APTES on ZnO ALD film is around 60ng/cm^2. There is a small net mass decrease in the 1st water half cycle. Virtually there is no mass uptake in the following 5 cycles of APTES/H_2O. Steady state ZnO ALD process has a mass uptake ~ 120 ng/cm^2 for each cycle.

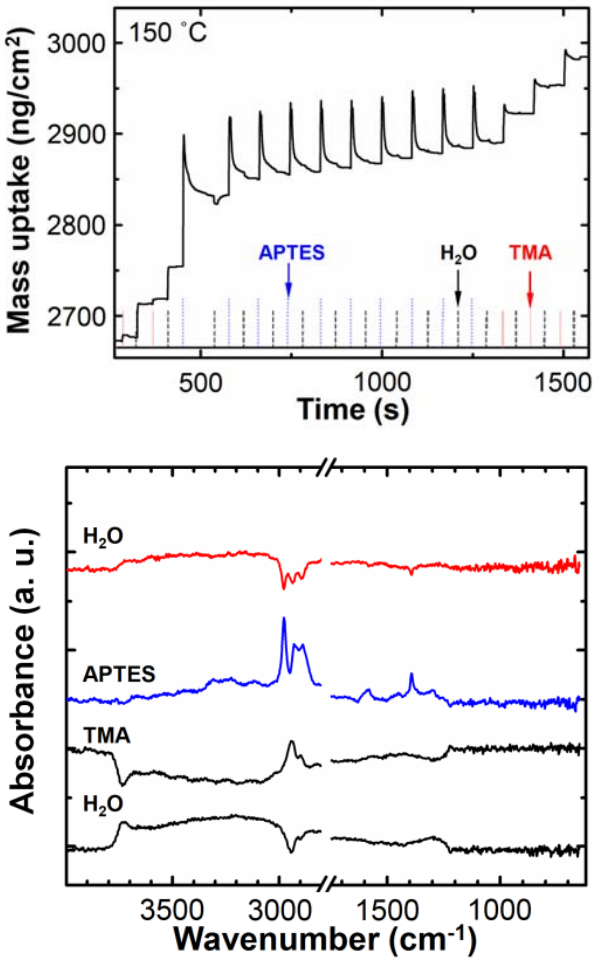
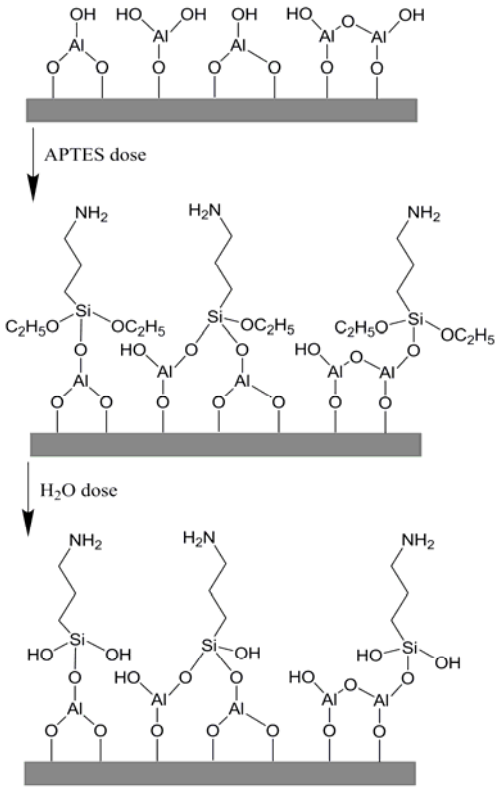
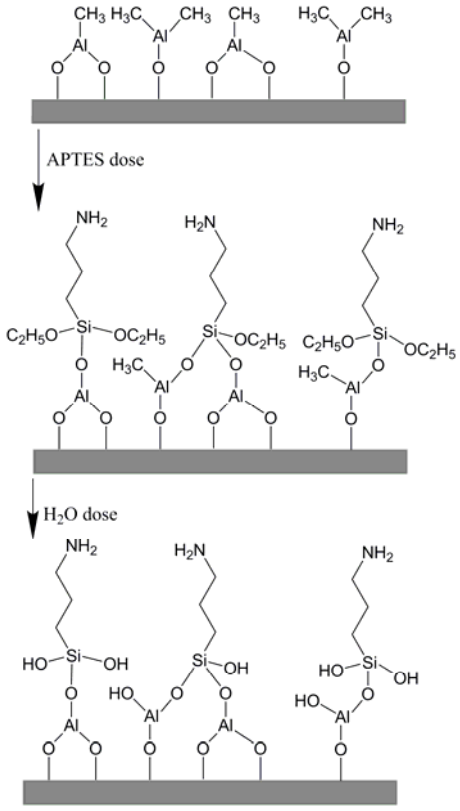


Figure 11.7 In-situ QCM measurement of mass uptake of APTES/H_2O ALD cycles (2/40/2/40 s) on Al-CH_3 terminated Al_2O_3 ALD film. It shows steady state Al_2O_3 ALD process (2/40/2/40 s) at 150 ˚C, which has a mass uptake of ~35 ng/cm^2 for TMA dose, ~5 ng/cm^2 for H_2O dose. APTES on the Al-OH terminated Al_2O_3 ALD film. The mass uptake of the 1st cycle of APTES on Al_2O_3 ALD film is around ~78ng/cm^2. The following 9 cycles of APTES/H_2O contribute around ~55ng/cm^2. The surface reaction is completed after 10 cycles. B) Representative in-situ FTIR spectra of the Al_2O_3 ALD film coated AAO substrate at 100 ˚C: A) after chemical absorption of TMA, H_2O in the Al_2O_3 ALD process, after APTES, H_2O onto the Al-CH_3 terminated Al_2O_3 ALD film.



Scheme 11.1 Reaction scheme of the APTES on the Al-OH terminated Al_2O_3 ALD film surface. It is possible the one, two or even three of the ethoxyl ligands reacted with -OH groups through a hydrolytic sol-gel reaction to form Si-O-Al bondings. The following H_2O pulsing step will hydrolyze the unreacted ethoxy groups and generate new -OH groups for hydrolysis reaction with the following APTES pulse. By repeating this APTES/H_2O ALD process, the surface will be covered by a monolayer of APTES with -NH_2 terminal group.



Scheme 11.2 Reaction scheme of the APTES on the Al-CH_3 terminated Al_2O_3 ALD film surface. It is possible the one, two or even three of the ethoxyl ligands reacted with Al-CH_3 through an nonhydrolytic sol-gel reaction to form Si-O-Al bonding. The following H_2O dose step will convert the unreacted ethoxy group and CH_3 ligands to –OH ligands, which will be available for the hydrolysis reaction with the next pulse of APTES. By repeating the APTES/H_2O ALD cycles, the Al_2O_3 ALD film surface will be eventually covered by one monolayer of APTES SAM with NH_2 terminals.